

ABSTRACT

JAYAPRAKASH, ARJUN. Recommendations for Durability and Seismic Design of an External Socket Connection in Steel Bridge Substructures. (Under the direction of James Nau, Mohammad Pour-Ghaz, and Mervyn Kowalsky.)

A substructure system consisting of driven steel piles that double as columns above ground is a prominent choice for structures such as marginal wharves, piers, and bridges. External socket connections, such as the grouted shear stud (GSS) connection, offer a simple and cost-efficient option for connecting these pile-columns to the cap-elements. The GSS connection is formed by a larger diameter pipe stub socket directly welded to the cap-element into which the columns can be inserted. The annular region thus formed can then be filled with high-strength grout to complete the connection. Welded shear studs inside the connection provide resistance to column pull out. Although the GSS connection has been shown to exhibit exceptional structural performance under laboratory conditions, there were a few issues that required consideration before widespread deployment of the connection in practice.

The study discussed in this dissertation was undertaken to address the following issues. First was the issue of connection durability. Since the Alaska Department of Transportation and Public Facilities (AKDOT) is interested in using this connection in their bridges, there was a need to investigate its long-term durability in extreme cold climates. Second, to implement this connection in engineering practice, standard structural design guidelines were deemed necessary. And third, since the state of Alaska also happens to fall in an active seismic zone, the design guidelines also required to include recommendations for estimating non-linear structural response of bridge piers with the GSS connection.

To determine the long-term durability of the GSS connection, it was sufficient to establish either that commonly available grouts are durable themselves, or that grout deterioration does not compromise the structural integrity of the connection. First, four commonly available commercial grouts were chosen to determine their vulnerability to freeze and

thaw damage and their propensity to cracking under restrained shrinkage. Experiments suggested that some grouts are indeed vulnerable to freeze and thaw degradation while others show exceptional performance.

Since material durability tests were inconclusive, the next step was to determine if grout deterioration would impair the structural capabilities of the GSS connection. Four large scale steel bridge pier specimens incorporating the GSS connection were structural tested. To determine the consequences of grout deterioration, the performance of specimens with deteriorated GSS connections was compared to that of a control specimen. Connection deterioration was achieved by mixing expanded polystyrene (EPS) aggregates in the grout, which reduced the compressive strength and elastic modulus of the grout. Direct comparison between the global structural behavior of the piers with deteriorated connections and the control specimen indicated that grout deterioration does not compromise the structural integrity of the GSS connection.

To provide guidelines for optimum design, there was a need to better understand the force transfer mechanism within the connection. Large scale experimental data was subsequently used to investigate the force transfer mechanism. The embedment length of the column inside the connection was found to be the most important parameter for a successful design. Subsequently, a model was developed to calculate the lower bound capacity of the GSS connection.

Seismic design procedure for bridges demands that the designer can estimate the total displacement of piers at important limit states. In the case of steel bridge piers with socket connections, estimation of limit state displacements is not trivial because of additional flexibility in the system attributable to cap-beam flexure and socket connection rotation. Using the data collected from the large-scale tests, finite element modeling, and parametric studies, a semi-empirical model was developed to establish essential limit state displacements and the rate of strength degradation in these bridge piers.

© Copyright 2020 by Arjun Jayaprakash

All Rights Reserved

Recommendations for Durability and Seismic Design
of an External Socket Connection in
Steel Bridge Substructures

by
Arjun Jayaprakash

A dissertation submitted to the Graduate Faculty of
North Carolina State University
in partial fulfillment of the
requirements for the Degree of
Doctor of Philosophy

Civil Engineering

Raleigh, North Carolina

2020

APPROVED BY:

Mervyn Kowalsky
Co-chair of Advisory Committee

Charles Balik

James Nau
Co-chair of Advisory Committee

Mohammad Pour-Ghaz
Co-chair of Advisory Committee

DEDICATION

To

Amma, who never discouraged the skeptic in me.

and

Achan, who I deeply miss.

BIOGRAPHY

The author was born in Kochi, India but spent most of his life in Kozhikode, India, which he calls home. He went to *Kendriya Vidyalaya No.1*, Kozhikode for his basic schooling from 1996 to 2007. Later, he completed his Bachelors (B.Tech) degree in Civil Engineering from the National Institute of Technology Calicut, Kozhikode in 2011. After graduation, he first worked as a construction engineer, and then as a structural engineer, before moving to the United States of America to pursue a Masters degree.

He arrived in Raleigh, North Carolina, which he calls his second home, in August 2014. He was awarded the Master of Civil Engineering (MCE) degree from North Carolina State University in 2016. Immediately after graduation, he re-enrolled in the same university to pursue his Doctorate.

His research interests are in the areas of performance-based seismic design, large-scale structural testing, computational modeling, and implementation of probabilistic methods in earthquake engineering. Following his Doctoral degree, he plans to contribute to the field of natural hazards engineering and risk mitigation.

ACKNOWLEDGEMENTS

The research work discussed in this dissertation was made possible by the financial support I received from Alaska Department of Transportation and Public Facilities (AKDOT&PF) and the Department of Civil, Construction, and Environmental Engineering at North Carolina State University. I acknowledge their contribution gratefully.

I would like to thank Dr. James Nau for his constant support in every way possible, even to the extent of jackhammering high-strength grout out of the GSS connections. I thank Dr. Mervyn Kowalsky for accepting me into his research group, inspiring me with his work, and inviting all of us to the many house parties, which were state-of-the-art. I also thank Dr. Mohammad Pour-Ghaz for introducing me to a completely new area of research, providing intelligent feedback, and never failing to concoct witty remarks.

None of the experimental work would have been completed in time if not for the technical staff at the Constructed Facilities Laboratory, Dr. Greg Lucier, Jerry Atkinson, Johnathan McEntire, and Ben Smith. Equally important was support from my fellow graduate students Emrah, Chris, Zakariya, Guillermo, Francisco, Zach, Mike, Jessi, Kareem, Payam, and Hussam, and undergraduates Daniel, Cade, Anthony, Taylor, Luis, Oscar, Naesh, Thomas, and Joey who have helped me in constructing and executing my large-scale tests.

Special acknowledgement goes to Elmer Marx and Nicholas Murray of AKDOT&PF for providing us with timely feedback through frequent meetings. In addition, I would like to acknowledge Mike Pulley of NCDOT for his weld inspection of the test specimens, Neil Bain and Joe Blalock of the BAE shop for their timely specimen fabrication.

Last, I would like to thank the two most important people in my life. My wife, Indu, who has been a constant source of support, even assisting me with late night freeze-thaw tests! My mother, Ajitha Jayaprakash, for believing in me unconditionally. I hope that I make you proud.

TABLE OF CONTENTS

LIST OF TABLES	viii
LIST OF FIGURES	ix
Chapter 1 Introduction	1
1.1 Background	7
1.2 Advantages of the GSS connection	9
1.3 Motivation for this study	13
1.3.1 Durability in Cold Climates	14
1.3.2 Investigation of the Force Transfer Mechanism	15
1.3.3 Seismic Design	16
1.4 Research Approach	16
1.5 Chapter Summary	20
Chapter 2 Durability of Cementitious Grouts in Cold Climates	22
2.1 Introduction	22
2.2 High-Strength Cementitious Grouts	25
2.3 Freeze and Thaw Cracking	31
2.3.1 Mechanisms of Freeze-Thaw Damage	31
2.3.2 A Review of Freeze-Thaw Testing Methods	37
2.4 Freeze and Thaw Resistance of Commercial Grouts	42
2.4.1 ASTM C666 Test Procedure	42
2.4.2 Exploratory Investigation	47
2.4.3 Freeze-Thaw Tests on Multiple Commercial Grouts	51
2.4.4 Closure to Freeze and Thaw testing	56
2.5 Shrinkage Cracking in Cementitious Grouts	60
2.5.1 Introduction	60
2.5.2 A Literature Review of the Ring Test	61
2.6 Restrained Ring Test on Cementitious Grouts	66
2.7 Chapter Summary, Recommendations, and Concluding Remarks	79
2.7.1 Chapter Summary	79
2.7.2 Recommendations	80
2.7.3 Concluding Remarks	82
Chapter 3 Simulating Grout Deterioration for Large Scale Tests	83
3.1 Introduction	83
3.2 Physical Damage Simulation	87
3.2.1 Exploratory Study	87
3.2.2 Preventing EPS migration	89
3.2.3 Mock Connection	95
3.2.4 Level of Deterioration for Large Scale Tests	99
3.3 Chapter Summary	102

Chapter 4 Structural Consequences of Grout Deterioration	104
4.1 Introduction	105
4.2 Large Scale Experiments on Two-Column Bridge Piers - Part 1	107
4.2.1 Research Approach	107
4.2.2 Large Scale Experimental Setup	109
4.2.3 Large Scale Test 1	113
4.2.4 Large Scale Test 2	128
4.3 Chapter Summary and Conclusions	141
4.3.1 Summary	141
4.3.2 Concluding remarks	142
4.3.3 Relevant results from Large Scale Test 3	145
Chapter 5 Force Transfer Mechanism in the GSS Connection	146
5.1 Introduction	146
5.2 Background	148
5.2.1 Large Scale Test 0	150
5.3 Large Scale Experiments on Two-Column Bridge Piers - Part 2	156
5.3.1 Introduction	156
5.3.2 Large Scale Test 3	157
5.3.3 Large Scale Test 4	169
5.4 Limit States from Experimental Observations	177
5.4.1 Cracking at the Neutral Axis	177
5.4.2 Socket Detachment	178
5.4.3 Grout Spalling	183
5.4.4 Pile Wall Buckling	183
5.4.5 Pile Wall Rupture	185
5.5 Chapter Summary and Conclusions	189
Chapter 6 Analytical Model for Design of the GSS Connection	192
6.1 Introduction	192
6.2 Literature Review	193
6.3 GSS Force Transfer Mechanism	197
6.4 Analytical Model	199
6.5 Application of the Analytical Model to Large-Scale Experiments	208
6.6 Parametric Study and Design Equations	213
6.7 Chapter Summary	221
Chapter 7 Limit State Displacements of Steel Substructures with the GSS Connection	222
7.1 Direct Displacement-Based Design	224
7.2 Material and Section Behavior of Hollow Steel Sections	228
7.3 Displacement Limits of Cantilever Columns	237
7.3.1 Yield Limit State	238
7.3.2 Local Buckling Limit State	240
7.3.3 Buckling Moment and Force	249

7.3.4	Post-buckling Limits and Strength Degradation	250
7.4	Fiber-based Computational Model for Limit-state Prediction	250
7.4.1	Total Displacement of a Bridge Pier System	252
7.4.2	Development of the Numerical Model	255
7.5	Displacement Limits of Two-column Bridge Piers	276
7.5.1	Cap beam flexibility: Condition 2 versus Condition 1	277
7.5.2	Connection flexibility: Condition 3 versus Condition 2	283
7.6	Strength Degradation Rate	285
7.7	Model Validation	288
7.8	Chapter Summary	290
Chapter 8	Conclusions and Recommendations	292
8.1	Durability of the GSS connection in Cold Climates	293
8.1.1	Durability of Cementitious Grouts	294
8.1.2	Structural Consequences of Grout Deterioration	295
8.2	Structural Design of the GSS Connection	296
8.3	Limit State Displacements of Bridge Piers with GSS Connections	298
8.4	Recommendations for Connection Design and Maintenance	299
8.4.1	GSS Durability Recommendations	299
8.4.2	Design Recommendations	300
8.4.3	Maintenance Recommendation	303
8.5	Recommendations for Seismic Design	303
BIBLIOGRAPHY	305	
APPENDICES	311	
Appendix A	Equations for Estimating the Cyclic Backbone Response of Two-Column Bridge Piers	312
Appendix B	Mill Certificates	318
Appendix C	Weld Specification Details	334

LIST OF TABLES

Table 2.1	Material used, bag weights, and the amount of water added in each mixture	26
Table 2.2	Summary of the results - average compressive strengths	27
Table 2.3	Summary of the results - coefficients of variation for average compressive strengths	27
Table 2.4	Comparison between the measured and manufacturer specified compressive strength values for cementitious grouts.	28
Table 2.5	Grout mixtures tested under ASTM C666.	47
Table 2.6	Test matrix and results for restrained shrinkage ring tests	68
Table 3.1	Trial and error test matrix to determine required EPS volume percentages.	88
Table 4.1	Test matrix used to determine consequences of grout deterioration on the structural performance of the GSS connection.	109
Table 5.1	Test matrix used to determine the force transfer mechanism of the GSS connection.	157
Table 6.1	Step-wise calculation of the capacity and demand in the GSS connections in tests 3 and 4.	209
Table 6.2	Input variables and their values used in the parametric study.	217
Table 7.1	Large-scale experiments performed on hollow circular steel columns connected to the GSS connection.	234
Table 7.2	Section details and their strain limits for local buckling as determined using British Standards model.	241
Table 7.3	Independent variables in the numerical experimental study matrix.	245
Table 7.4	Average values of k_p to calculate the plastic hinge length.	248
Table 7.5	Comparison of estimated limit state displacements of the experimental specimen calculated using different models.	255
Table 7.6	Comparison of yield displacement, buckling displacement, and rate of strength degradation between experiments and numerical models.	263
Table 7.7	Comparison of rate of strength degradation between numerical models in Fulmer et al. [Ful10b] and this study.	273
Table 7.8	Independent variables in the parametric study to evaluate γ_{cb}	280

LIST OF FIGURES

Figure 1.1	Structures where steel piles are commonly used.	3
Figure 1.2	Examples of existing bridges that use hollow steel piles connected to steel cap beam.	4
Figure 1.3	Possible column to cap element connections, as described by Harn et al. [Har10].	5
Figure 1.4	Test set up from Fulmer et al. [Ful10a; Ful10b] to test directly welded connections.	8
Figure 1.5	Typical brittle failure observed in Cookson [Coo09], Fulmer et al. [Ful10b], and Fulmer et al. [Ful10a] on directly welded connections.	8
Figure 1.6	Stages of the GSS connection: (a) Constituent components, (b) Connection before grouting, (c) Connection after grouting, (d) Failure by plastic hinge relocation.	10
Figure 2.1	Comparison of cube strength and cylinder strength for all the tested grouts.	29
Figure 2.2	All average cube strengths versus average cylinder strengths.	30
Figure 2.3	A sample plot showing dynamic elastic modulus vs degree of saturation for concrete specimens tested in five different laboratories [Fag77b].	34
Figure 2.4	A sample plot showing mean values of capillary degree of saturation vs time of water uptake [Fag77b].	36
Figure 2.5	Photographs of various steps during the FT resistance testing procedure.	43
Figure 2.6	Typical cycles of the two control specimen temperatures and the environmental chamber air temperature.	44
Figure 2.7	A typical time domain and frequency domain pair of specimen acceleration responses.	46
Figure 2.8	Results from exploratory investigation of FT resistance of grout material CG1: (a) with 9 lbs. water, and cured under water (b) with 8.5 lbs. water, and sealed cured.	50
Figure 2.9	Results from ASTM C666 FT tests on multiple commercial grout (Good performance). Grout: CG1, Water per bag: 8.5 lbs.	52
Figure 2.10	Results from ASTM C666 FT tests on multiple commercial grout materials (Good performance).: (a) Grout: CG2, Water per bag: 8.4 lbs., (b) Grout: CG3, Water per bag: 6.6 lbs.	53
Figure 2.11	Results from ASTM C666 FT tests on multiple commercial grout materials (Poor performance).: (a) Grout: CG4, Water per bag: 9.3 lbs., (b) Grout: PG1, w/c ratio: 0.46.	54
Figure 2.12	A comparison of results of the exploratory study performed on CG1 with 9 lbs. water per bag, and cured under water to the results of the same when repeated: (a) Exploratory (b) Repeat.	57

Figure 2.13	A comparison of results of the exploratory study performed on CG1 with 8.5 lbs. water per bag, and cured under sealed conditions to the results of the same when repeated: (a) Exploratory (b) Repeat.	58
Figure 2.14	Restrained ring specimens: (a) top and bottom drying, and (b) circumferential drying, and their corresponding stress profiles as shown in Hossain & Weiss [HW06]	63
Figure 2.15	Restrained ring test specimen cross section schematic: Circumferential drying specimen (Left) and sealed specimen (Right).	67
Figure 2.16	Restrained ring test specimens under circumferential drying conditions in the environmental chamber.	69
Figure 2.17	Results from restrained ring tests tests on CG1 under two different drying conditions: Circumferential drying (Left) and Sealed (Right) conditions.	71
Figure 2.18	Results from restrained ring tests tests on CG2 under two different drying conditions: Circumferential drying (Left) and Sealed (Right) conditions.	72
Figure 2.19	Results from restrained ring tests tests on CG3 under two different drying conditions: Circumferential drying (Left) and Sealed (Right) conditions.	73
Figure 2.20	Degrees of restraint plotted against column diameter for a GSS connection outer-to-inner diameter ratio of 1.5.	75
Figure 2.21	Restrained ring test specimen cross section schematic: 3/4" dia. shear studs (Left) and 1" dia. shear studs (Right).	76
Figure 2.22	Results from ring tests performed on specimens with shear studs: (a) 3/4" dia. shear studs (b) 1" dia. shear studs.	77
Figure 3.1	Variation of compressive strength with age and EPS volume for concrete added with fly ash [Bab05].	85
Figure 3.2	Variation of split tensile strength with compressive strength for EPS concrete added with fly ash [Bab05].	86
Figure 3.3	Expanded Polystyrene (EPS) beads.	88
Figure 3.4	Elastic modulus normalized to value at 0% EPS plotted against EPS volume replacements for trial and error mixtures.	89
Figure 3.5	Migration of EPS aggregates observed in cylindrical grout samples.	90
Figure 3.6	Premature failure observed in two different samples of grout mixed with 18% EPS. This corresponds to a 20% reduction of elastic modulus compared to standard grout.	91
Figure 3.7	Compressive strength cylindrical specimens cast in 2" layers with 18% EPS.	92
Figure 3.8	Compressive strength cylindrical specimens cast in 1" layers with 18% EPS.	93
Figure 3.9	Uniform distribution of EPS aggregates observed in cylindrical grout samples under the 1"-layered casting scheme.	94
Figure 3.10	Formwork for the mock GSS connection.	95

Figure 3.11	The layered scheme used to cast the mock connection and the corresponding 4"×24" PVC pipes.	97
Figure 3.12	The locations of ultrasonic pulse velocity measurements along the height and around the section of the mock connection.	97
Figure 3.13	Results of the UPV test to measure relative elastic modulus along the height of the mock connection.	98
Figure 3.14	Results of elastic modulus measurements using disc samples along the height of the mock connection.	98
Figure 3.15	Results of compressive strength measurements using cylindrical samples along the height of the mock connection.	99
Figure 3.16	Results of grout properties from the GSS connection of test 2 (a) Compressive strength profile obtained from cubic samples (b) Dynamic elastic modulus profile obtained from disc samples.	100
Figure 3.17	Results of grout properties from the GSS connection of test 3 (a) Compressive strength profile obtained from cubic samples (b) Dynamic elastic modulus profile obtained from disc samples.	101
Figure 4.1	Laboratory large scale experiment setup	111
Figure 4.2	A typical three cycle set loading history.	112
Figure 4.3	Fabrication details for the cap-beam stub assembly of Tests 1 through 4.	114
Figure 4.4	Fabrication details for the hollow circular columns used in Tests 1 through 4.	115
Figure 4.5	Columns erected and ready for cap-beam assembly.	116
Figure 4.6	Photographs showing (a) the cap-beam stub assembly being lowered onto the columns and (b) one of the columns afterwards.	116
Figure 4.7	Photographs showing (a) the grout pump and (b) the pumping process.	117
Figure 4.8	Photographs showing the arrangement of shear studs in (a) the stub pipe on the cap-beam, and (b) the pile columns.	119
Figure 4.9	The force-displacement hysteretic response of Test 1.	121
Figure 4.10	Grout spalling observed at (a) North column, South side, and (b) South column, South side (Ductility: 1.5, Cycle: -3, Force: 143.7 kips, Displacement: -4.1 in.).	122
Figure 4.11	Pile wall outward local buckling on the (a) south face of north pile (Ductility: 3, Cycle: +1, Force: 136.3 kips, Displacement: 8.62 in.) and, (b) north face of south pile during the first negative cycle of ductility 3 (Ductility: 3, Cycle: -1, Force: -132.2 kips, Displacement: -8.65 in.).	124
Figure 4.12	Pile wall rupture in the plastic hinge region on the north face of south pile during the first positive cycle of ductility 5 (Ductility: 5, Cycle: +1, Force: 51.0 kips, Displacement: 9.32 in.).	125
Figure 4.13	The test specimen experienced a maximum drift of 9% (Ductility: 4, Cycle: +3, Force: 82.2 kips, Displacement: 11.60 in.).	126

Figure 4.14	Comparison of the force-displacement response of Test 0 (SG-96) and Test 1 (SG-32).	127
Figure 4.15	Detachment of the column from the surrounding grout ring on the tension side of the connection.	127
Figure 4.16	Results of grout properties from the GSS connection of Test 2 (a) Compressive strength profile obtained from cubic samples (b) Dynamic elastic modulus profile obtained from disc samples.	130
Figure 4.17	Layering scheme used to obtain uniform EPS distribution in GSS connections for physical damage simulation.	131
Figure 4.18	(a) Transverse cracking observed at the neutral axis of the GSS connection (Ductility: F_y , Cycle: +1, Force: 97.8 kips, Displacement: 2.53 in.), and (b) the observed gap between the column and surrounding grout ring (Ductility: 3, Cycle: +1, Force: 142.1 kips, Displacement: 8.64 in.).	133
Figure 4.19	Pile wall local buckling (Ductility: 3, Cycle: +1, Force: 142.1 kips, Displacement: 8.64 in.)	134
Figure 4.20	Pile wall local buckling (Ductility: 4, Cycle: +1, Force: 112.2 kips, Displacement: 11.50 in.)	135
Figure 4.21	Pile wall local buckling (Ductility: 5, Cycle: +1, Force: 84.1 kips, Displacement: 14.21 in.)	135
Figure 4.22	Structure drift of 11% (Ductility: 5, Cycle: +1, Force: 84.1 kips, Displacement: 14.21 in.)	136
Figure 4.23	A comparison of the force-displacement hysteretic responses: Test 1 (SG-32) v Test 2 (DG-32)	137
Figure 4.24	Comparison between hysteretic loops of Test 1 (SG-32) and Test 2 (DG-32) at different ductilities: (a) F_y (b) μ_2	139
Figure 4.25	Comparison between hysteretic loops of Test 1 (SG-32) and Test 2 (DG-32) at different ductilities: (a) μ_3 (b) μ_4	140
Figure 4.26	A comparison of the force-displacement hysteretic responses: Test 1 (SG-32) v Test 3 (DG-16)	142
Figure 4.27	Comparison between hysteretic loops of Test 1 (SG-32) and Test 3 (DG-16) at different ductilities: (a) F_y (b) μ_2	143
Figure 4.28	Comparison between hysteretic loops of Test 1 (SG-32) and Test 3 (DG-16) at different ductilities: (a) μ_3 (b) μ_4	144
Figure 5.1	Shear stud detail and constituent elements of the specimen in Test 0.152	
Figure 5.2	Force-displacement hysteresis of the two-column bridge bent specimen tested by Fulmer et al. [Ful10b], referred to as Test 0 in this report	153
Figure 5.3	Observed local buckling initiation pile wall (Ductility: 2, Cycle: -3, Force: -132 kips, Displacement: -5.62").	154
Figure 5.4	Observed grout spalling and tear marks on the pile wall (Ductility: 4, Cycle: 3, Force: 85 kips, Displacement: 11.25").	154
Figure 5.5	Specimen failure mode of pile wall rupture (Ductility: 6, Cycle: -1, Force: -54 kips, Displacement: -16.88").	155

Figure 5.6	Drift of 12% was observed at termination of Test 0 [Ful10b] (Ductility: 6, Cycle: 1, Force: 75 kips, Displacement: 16.88")	155
Figure 5.7	Result of the bend test on a sample 1" diameter shear stud.	159
Figure 5.8	Comparison of the locations of shear studs in each of the first three large scale tests (Not to scale).	159
Figure 5.9	Cracks observed at the neutral axis of the GSS connection (Ductility: 1, Cycle: 1, Force: 111 kips, Displacement: 2.79")	161
Figure 5.10	The gap between the column wall and the grout ring. (Ductility: 3, Cycle: 1, Force: 145.1 kips, Displacement: 8.39")	161
Figure 5.11	GSS connection at ductility 3; No grout spalling was observed in Test 3. (Ductility: 3, Cycle: 1, Force: 145.1 kips, Displacement: 8.39") .	162
Figure 5.12	Minor buckling observed on the north column. (Ductility: 3, Cycle: 1, Force: 145.1 kips, Displacement: 8.39")	162
Figure 5.13	Minor buckling observed on the north column. (Ductility: 4, Cycle: 1, Force: 119.1 kips, Displacement: 11.19")	163
Figure 5.14	Minor buckling observed on the north column. (Ductility: 5, Cycle: 3, Force: -77.5, Displacement: -14.18")	163
Figure 5.15	Final drift of 11% achieved by the test 3 specimen.	164
Figure 5.16	A comparison of the force-displacement hysteretic responses: Test 2 (DG-32) and Test 3 (DG-16)	165
Figure 5.17	A comparison of the force-displacement hysteretic responses: Test 0 (SG-96) and Test 1 (SG-32)	166
Figure 5.18	Comparison of the slip in the force-displacement response in ductility 1 cycle.	167
Figure 5.19	Comparison of the slip in the force-displacement response in ductility 2 cycle.	167
Figure 5.20	Comparison of the slip in the force-displacement response in ductility 3 cycle.	168
Figure 5.21	Comparison of the slip in the force-displacement response in ductility 4 cycle.	168
Figure 5.22	Hypothesized force transfer mechanism within the GSS connection.	170
Figure 5.23	Specimens for large scale tests: (a) Test 3 (b) Test 4.	172
Figure 5.24	(a) Grout spalling initiated (Ductility: 1, Cycle: 1, Force: 80.4 kips, Displacement: 2.87") (b) The first row of shear studs visible (Ductility: 1, Cycle: 3, Force: 74.4 kips, Displacement: 2.88").	174
Figure 5.25	Gap opening up between the pile and grout ring (Ductility: 2, Cycle: 1, Force: 107.9 kips, Displacement: 5.46").	175
Figure 5.26	Bent shear stud (Ductility: 2, Cycle: 3, Force: 85.5 kips, Displacement: 5.49").	175
Figure 5.27	Column remaining straight under lateral loading (Ductility: 3, Cycle: 1, Force: 96.1 kips, Displacement: 8.48").	176
Figure 5.28	A comparison of the force-displacement hysteretic responses: Test 3 (DG-16) v Test 4 (DG-16-SS)	176

Figure 5.29	Grout cracking observed in the GSS connection transverse to the direction of loading in (a) Test 1 at $\mu_{1.5}$, (b) Test 2 at μ_1 , and (c) Test 3 at μ_1	179
Figure 5.30	A schematic to explain cracking observed at the neutral axis, and the socket detachment limit state of the GSS connection.	180
Figure 5.31	Socket detachment observed in the GSS connection on the tension side of the column under bending (a) Test 1 at $\mu_{1.5}$, (b) Test 2 at $\mu_{1.5}$, and (c) Test 3 at $\mu_{1.5}$	181
Figure 5.32	Socket detachment observed in the GSS connection on the tension side of the column under bending (a) Test 1 at μ_3 , (b) Test 2 at μ_3 , and (c) Test 3 at μ_3	182
Figure 5.33	Grout spalling observed in a GSS connection in (a) Test 1 at μ_2 , and (b) Test 2 at μ_3 (c) No spalling was observed in Test 3.	184
Figure 5.34	Visible pile wall buckling in (a) Test 1 at μ_2 , and (b) Test 2 at μ_3 (c) Test 3 at μ_3	186
Figure 5.35	Permanent pile wall buckling in (a) Test 1 at μ_3 , and (b) Test 2 at μ_4 (c) Test 3 at μ_4	187
Figure 5.36	Excessive pile wall buckling in (a) Test 1 at μ_4 , and (b) Test 2 at μ_5 (c) Test 3 at μ_5	188
Figure 5.37	Pile wall rupture in (a) Test 1 at μ_4 , and (b) Test 2 at μ_5 (c) Test 3 at μ_5	190
Figure 6.1	Embedment stress block as per PCI handbook [Han99]	194
Figure 6.2	Illustration of Moment Capacity Calculation by Xiao et al. [Xia06].	195
Figure 6.3	Hypothesized force transfer mechanism within the GSS connection.	198
Figure 6.4	A typical profile of bending moment on a bridge pier under lateral loading.	200
Figure 6.5	A schematic showing the strut-and-tie mechanism of force transfer in a single column.	202
Figure 6.6	A 3-D representation of the assumed 2-D strut formation around the hollow column.	203
Figure 6.7	Free body diagram of half of the outer ring of the GSS connection providing confinement to the grout contained within.	204
Figure 6.8	Free body diagrams of points in the strut-and-tie model shown in Figure 6.5: (a) Point A; and (b) Point B.	206
Figure 6.9	Comparison of the strut-and-tie model for tests 3 and 4.	210
Figure 6.10	D/C ratio versus the shear force demand in each column of tests 3 and 4.	212
Figure 6.11	Comparison of the force-displacement backbone response of tests 3 and 4.	213
Figure 6.12	Sensitivity of D/C ratio with respect to the variables in the parametric study.	214
Figure 6.12	Sensitivity of D/C ratio with respect to the variables in the parametric study (cont.)	215
Figure 6.12	Sensitivity of D/C ratio with respect to the variables in the parametric study (cont.)	216

Figure 6.13	(a) D/C ratio versus L_e/L_t ratio from the parametric study. (b) Probability density of L_e/L_t ratios that led to optimum GSS connection design.	219
Figure 6.14	(a) D/C ratio versus L_e/D ratio from the parametric study. (b) Probability density of L_e/D ratios that led to optimum GSS connection design.	220
Figure 7.1	Fundamentals of DDBD [Pri07].	225
Figure 7.2	Stress-strain diagrams of API 5L X52 PSL2 steel material: (a) Full (b) Zoomed-in.	229
Figure 7.3	Stress-strain diagrams of ASTM A500 Gr. B steel material: (a) Full (b) Zoomed-in.	230
Figure 7.4	Optotruk instrumentation schematic for measurement of strain at buckling.	233
Figure 7.5	Applied force versus strain at critical sections during cyclic loading: (a) Fulmer et al. Test 2 Column 1 South face and (b) This Study Test 2 Column 1 North Face.	235
Figure 7.6	Empirical compressive strains prior to local buckling.	236
Figure 7.7	Simplified force-displacement response.	238
Figure 7.8	Moment area method for the calculation of yield displacement.	240
Figure 7.9	Plastic hinge method for the calculation of displacement at local buckling.	243
Figure 7.10	(a) Implemented fiber-based model of cantilever column and (b) stress-strain response of steel material employed in the model.	246
Figure 7.11	Typical results from pushover analysis of a cantilever column: (a) Strain versus Curvature and (b) Strain versus Displacement.	247
Figure 7.12	Coefficient (k_p) to estimate the plastic hinge length.	248
Figure 7.13	(a) Bi-linear factor (r) versus D/t ratio and (b) Comparison between the value of force at local buckling (F_b) obtained from pushover analysis and that calculated using proposed equations.	251
Figure 7.14	Illustration of displacement components in a bridge pier: (a) A typical bridge pier under lateral loading; (b) System displacement due to column flexure; (c) Modified displacement due to cap-beam flexibility; (d) Modified displacement due to socket action.	253
Figure 7.15	Comparison of force-displacements responses of numerical models: (a) Three conditions 1, 2, and 3 shown in Figure 7.14 and (b) same curves superimposed on the corresponding experimental cyclic response.	256
Figure 7.16	Fiber element model summary.	258
Figure 7.17	Moment-rotation rule for rotational spring.	260
Figure 7.18	Comparison of initial stiffness between five different large scale tests.	261
Figure 7.19	Comparison between experimental and simulated force-displacement backbone response until buckling.	262
Figure 7.20	Comparison between experimental and simulated force-displacement backbone response from full cyclic pushover analyses.	264

Figure 7.21	<i>Hysteretic Material</i> model from OpenSees: (a) Idealized; (b) From pushover analysis.	266
Figure 7.22	Comparison between experimental and simulated cyclic force-displacement response.	267
Figure 7.23	Idealized force displacement envelopes of hollow columns illustrating the impact of D/t ratio.	269
Figure 7.24	Comparison between backbone envelopes of bridge piers modeled by Fulmer et al. and this study.	274
Figure 7.25	Evaluation of the strength degradation rate for numerical models with D/t ratio = 20 and axial load ratio = 5%: (a) FEM and (b) Fiber model	275
Figure 7.26	Schematic comparison: Condition 1 versus Condition 2.	278
Figure 7.27	Cap-beam flexibility coefficient ($\gamma_{cb-yield}$) for yield displacement calculation as a function the relative stiffness of cap-beam, K_{rcb}	281
Figure 7.28	Cap-beam flexibility coefficient ($\gamma_{cb-buckling}$) for displacement at local buckling as a function of K_{rcb} , D/t-ratio, and ALR.	282
Figure 7.29	Schematic comparison: Condition 2 versus Condition 3.	284
Figure 7.30	Cap-beam flexibility coefficient for (a) yield displacement ($\gamma_{sc-yield}$) and (b) displacement at local buckling ($\gamma_{sc-buckling}$) as a function the column D/t ratio.	286
Figure 7.31	Strength degradation rate of hollow circular columns as a function of D/t ratio and axial load ratio.	288
Figure 7.32	(a) Comparison of the proposed model with experimental results. (b) Variation of the force versus displacement behavior of hollow steel columns with the same diameter but different wall thickness.	289
Figure A.1	Idealized force versus displacement response.	313

CHAPTER

1

INTRODUCTION

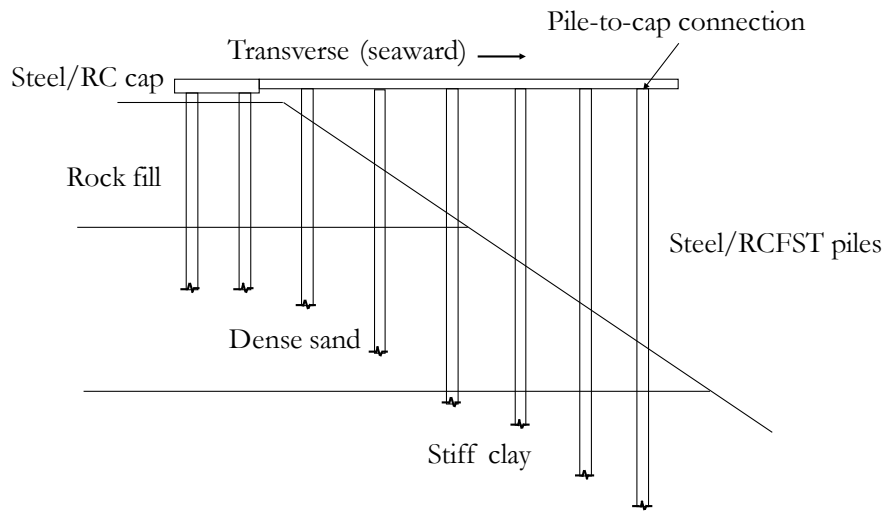
The use of structural systems consisting of hollow circular steel piles doubling as columns above ground has been widespread. Such systems have been used, most prominently, in three different types of structures, namely, marginal wharves, piers, and bridges. Marginal wharves and piers are structures commonly used in seaports to berth ships and are differentiated by the direction of their longitudinal axis. A marginal wharf has its major axis parallel to the shoreline, whereas a pier has its long axis perpendicular to the shore. Typical transverse cross-sections of marginal wharves and piers are shown in Figures 1.1a and

1.1b, respectively. In these structures, hollow or concrete-filled steel cross-sections are often used as piles that act both as foundation and columns supporting the superstructure. These piles are driven into the ground and the top of each pile is cut at the same elevation before connecting to the cap-elements. The cap-elements are either made of structural steel or reinforced concrete. In bridges, these pile-columns are used as part of a bridge bent, also known as a bridge pier. Bridge piers are located at intermittent points along the length of the bridge, often marking the endpoints of bridge girders. Such bridge bents typically consist of pile-columns that are larger than those used in port structures, but fewer in number, as shown in Figure 1.1c.

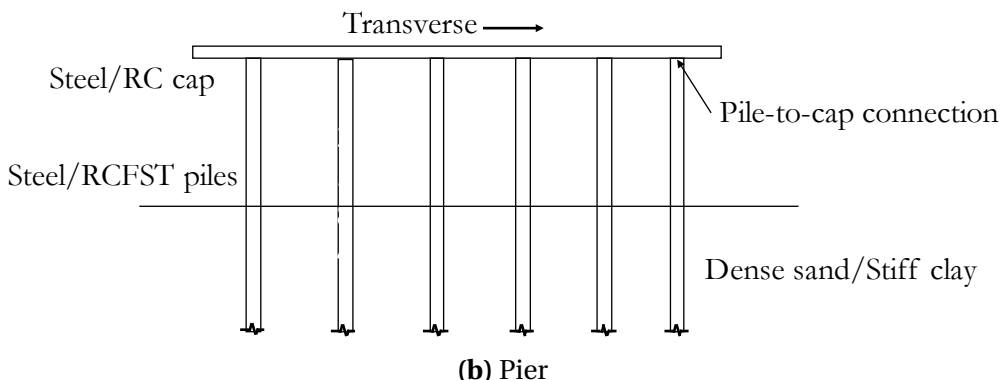
Lifeline structures, such as ports and bridges located along the western coast of the United States, are susceptible to damage from earthquakes. In these areas, all of the aforementioned substructure types must also act as the dominant lateral load resisting system. Previous earthquakes (1989 Loma Prieta, 1995 Great Hanshin, 1999 Kocaeli, and others) have demonstrated that, in such structural systems, locations that are most vulnerable are the pile-to-cap connections.

For connecting steel piles to steel cap-elements, the general approach is to directly weld the two members together. Figure 1.2 shows examples of bridges in Alaska which use this detail. On the other hand, when the cap element is fabricated from reinforced concrete (RC), many more options arise. Harn et al. [Har10] list the different construction approaches generally implemented to build these substructure systems. Figure 1.3 shows a number of these different connection types involving steel pile-columns. Among these, the most common connection detail is the embedded pile [Xia06; Lar13; Gri17; Ham17].

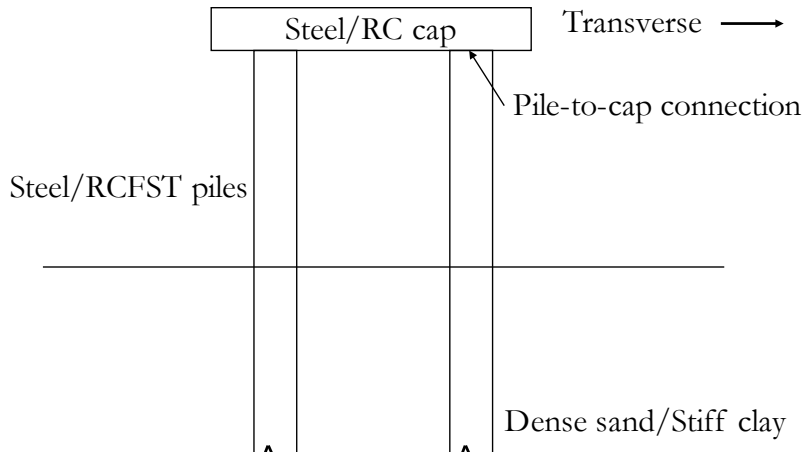
Notwithstanding the type of the cap-element, directly connecting the steel piles to the



(a) Marginal wharf



(b) Pier



(c) Bridge bent

Figure 1.1 Structures where steel piles are commonly used.



(a)



(b)



(c)

Figure 1.2 Examples of existing bridges that use hollow steel piles connected to steel cap beam.

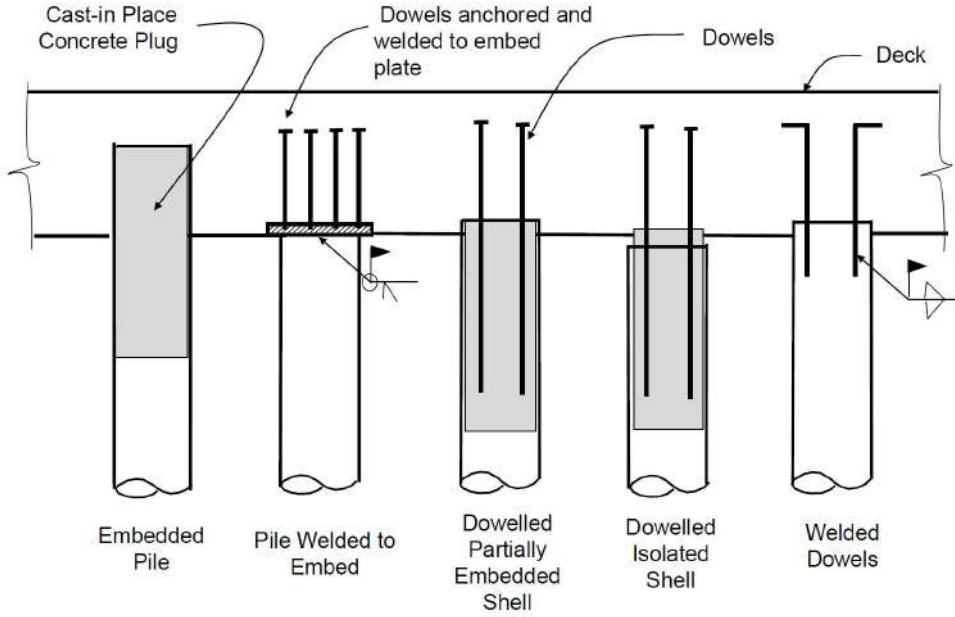


Figure 1.3 Possible column to cap element connections, as described by Harn et al. [Har10].

cap can lead to unsatisfactory performance under cyclic lateral loads, such as those developed during earthquakes. Directly welded connections have been shown to undergo the brittle failure mode of weld fracture even at low levels of inelastic action [Coo09; Ful10b]. Piles embedded in RC cap elements can cause premature spalling of the concrete surrounding the pile, resulting in reduced capacity and inability to mobilize plastic hinging [Har10]. Successfully avoiding premature failure in embedded pile connections is predicated on the embedment length. The longer the embedment length, the better. However, achieving a long embedment length can sometimes be difficult because of heavy cap-element reinforcement. Furthermore, past studies which have investigated the optimum embedment length are few, exacerbating the lack of confidence in these connections.

External socket-type connections have emerged as superior alternatives for fabricat-

ing the connection between piles and cap-elements. Typically these involve a structural socket attached to the exterior of the cap-element into which the piles can be inserted. The annular void thus generated can then be filled with some type of grout material. It is important to distinguish external sockets from internal sockets, which are formed into the cap-element during its construction. Both forms of socket connections have been shown to provide adequate seismic performance. However, there are some key advantages to utilizing external sockets over internal sockets.

External sockets can theoretically be used for both RC and steel cap-beams or footings, while internal sockets can only be used for RC cap-elements. As the column diameter increases, the required embedment length into the socket also increases. For internal sockets, this can lead to a large cap-beam depth. However, the depth of the cap-beam remains unchanged for external sockets. A consequence of containing large RC cap-beams in these types of structures is larger mass concentrated at the superstructure, which in turn leads to greater seismic demands.

One example of an external socket-type connection is the grouted shear stud connection, developed at North Carolina State University. The primary focus of the work described in this dissertation is the grouted shear stud connection in developing recommendations for its durability and structural performance, and establishing simplified models to perform the displacement-based seismic design procedure for substructure systems incorporating this connection.

1.1 Background

The grouted shear stud (GSS) connection for steel bridge substructures was developed by Fulmer et al. [Ful15] as a ductile alternative to directly welded column to cap-beam connections. Fulmer et al. [Ful10a; Ful10b] investigated multiple weld configurations to connect the pipe columns to cap-beams, including the fillet weld, complete joint penetration (CJP) weld, CJP weld with a reinforcing fillet outside the pipe, and CJP weld with reinforcing fillets both inside and outside the pipe. They tested large scale two-column steel bents fabricated using the aforementioned weld details (Figure 1.4). The specimens were tested under cyclic quasi-static lateral loading until failure. Irrespective of the weld configuration, they observed undesirable brittle cracking at the weld or heat affected zones in the pile (Figure 1.5). They concluded that while welding steel pipe columns to cap-beams may be acceptable for non-seismic regions, designing such a connection in seismic regions without explicit consideration for protection of welded regions results in undesirable brittle cracking. The GSS connection shifts the failure mode to the desirable plastic hinge formation in the column section, thereby preventing premature damage at the weld or the heat affected zone.

The GSS connection is an external socket-type connection and consists of a prefabricated cap beam (double wide HP was used by Fulmer et al. [Ful15]) to which a stub pipe section is welded, as shown in Figure 1.6a. The stub pipe, larger in diameter than the column, acts as a socket into which the column can be inserted. In Figure 1.6a, the cap beam is shown on the left, resting on its top surface. The inner wall of the stub pipe contains 12 vertical lines of $\frac{3}{4}$ inch diameter shear studs. Similarly, the top of each pile section has 12



Figure 1.4 Test set up from Fulmer et al. [Ful10a; Ful10b] to test directly welded connections.



Figure 1.5 Typical brittle failure observed in Cookson [Coo09], Fulmer et al. [Ful10b], and Fulmer et al. [Ful10a] on directly welded connections.

lines of studs, as shown in Figure 1.6a.

In the field, shear studs are welded to the pile after driving and cutting it at the proper elevation. No field welding (other than installation of the shear studs) is required in the construction of the GSS connection. After inserting the pile in the stub (Figure 1.6b), the moment resisting connection is completed by pumping a high-strength, non-shrink flowable grout into the annular region (Figure 1.6c). Fulmer et al. [Ful15] tested two-column steel bents that use the GSS connection detail by subjecting them to cyclic quasi-static lateral loading. These tests showed the proof of concept that the GSS connection can successfully protect the welded region by relocating the plastic hinge formation to the steel column (Figure 1.6d) below the larger diameter pipe stub. The GSS connection also provided increased system displacement capacity when compared to the directly welded connections.

1.2 Advantages of the GSS connection

Seismic resistance

The primary motivation that led to the development of the GSS connection was enhanced performance under seismic conditions. The GSS connection enables a designer to make efficient use of the column moment and ductility capacity. By using capacity design principles, the connection and the cap-beam can be protected resulting in the column being the weakest link. As a consequence, the GSS connection eliminates premature brittle failure modes such as cracking at the weld or in the heat affected zones.

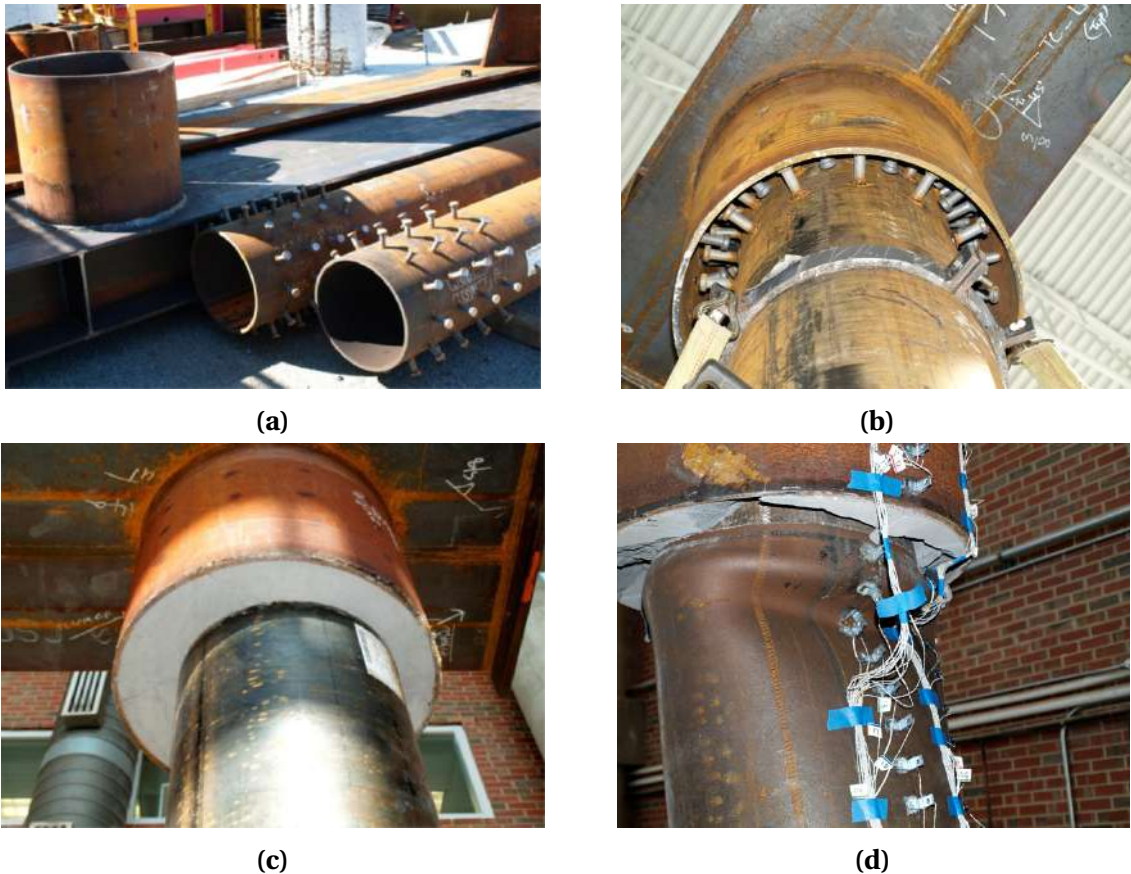


Figure 1.6 Stages of the GSS connection: (a) Constituent components, (b) Connection before grouting, (c) Connection after grouting, (d) Failure by plastic hinge relocation.

Accelerated bridge construction

Accelerated bridge construction (ABC) has received increasing attention over the last several years. The goal of ABC is to improve quality and reduce the duration of bridge construction. Rapid, high quality construction is especially important in regions that have short construction seasons, such as cold climate regions. The interest in ABC has led to studies in socket and pocket style details of column connections. The majority of the previous studies have focused on precast concrete. There have also been a few studies on steel bridge substructures for seismic applications. The GSS connection can be employed as part of ABC for steel bridge substructures. The cap-beam with pipe stub sockets can be prefabricated and brought to the site where it can be lowered onto driven piles until the bottom of the cap-beam bears on the pile top. The connection can then be formed and pumped with commercially available grout in little time to complete the construction process. The time required for field welding and welding inspection under conventional construction processes is essentially eliminated with the GSS connection.

Retrofitting option

Although the GSS connection was developed for new construction, it can be readily adapted for retrofit of steel bridges in which the pipe column to cap-beam connections are deficient. To accomplish this retrofit, the stub pipe is cut longitudinally to produce two semi-circular stub pipe sections. Shear studs are welded to these stub pipe sections and to the top section of the existing pipe column. The stub pipe sections are then welded to the existing cap beam, and finally the two halves of the stub are welded together before grouting. While there is field welding to be performed, these welds are capacity protected, ensuring

their satisfactory performance, provided there is adequate inspection.

Redundant load paths

The results of large scale experiments discussed in this dissertation indicate that multiple load transfer mechanisms are mobilized within the GSS connection to resist the axial force, shear force, and bending moment demands on the connection. This redundancy of load paths is desirable in structures. Conventional directly welded connections only provide a single load path, i.e., through the weld, for the same demand. A full qualitative description of the components that contribute to the capacity of the connections is provided in Chapter 4.

Low sensitivity to construction tolerance

A high degree of quality control is necessary during the construction of directly welded connections, because these welds are critical to the structural integrity of the system. This leads to high costs of welding. The structural performance of systems incorporating the GSS connection has a higher tolerance to construction errors. Fulmer et al. [Ful15] compared the performance of two systems with the GSS connection, where the first system had concentric columns and stubs, while the second system had the columns offset with respect to the stub. Both systems performed essentially identically under cyclic quasi-static lateral loading protocols. In one of the large scale experiments performed as part of the present study, the specimen had an out of plane inclination because one of the columns was inclined due to a fabrication error. The structural performance of this test was also comparable to the performance of the control test. These results indicate a higher allow-

able tolerance in the construction of the GSS connection.

Suitability for any system

The underlying mechanism of the GSS connection is plastic hinge relocation. The column to cap-beam interface is capacity protected to ensure plastic hinging in the column section. This mechanism is independent of the structural system. The GSS connection can hence be employed in steel, reinforced concrete, or reinforced concrete filled steel tube columns.

1.3 Motivation for this study

The GSS connection is relatively in its infancy compared to conventional approaches of connecting steel bridge columns to cap-beams. An understanding of the full set of implications of its use in practice required further study. This work was funded by the Alaska Department of Transportation and Public Facilities (AKDOT) to produce initial guidelines and recommendations for the design and maintenance of the GSS connection in Alaska. At the beginning of this work, a few areas that required attention to understand the implications of using the GSS connection were:

1. Ascertaining the durability of the connection
2. Achieving a reasonable understanding of the force transfer mechanism within the connection for design
3. Formulating a seismic design model for substructure systems that incorporate this connection

This study was undertaken to address each one of the aforementioned areas of inquiry.

1.3.1 Durability in Cold Climates

A geographical area of interest for practical application of the GSS connection is the state of Alaska, United States. It is widely known that Alaska is in a seismically active zone. Hence, the GSS connection is a good option to be used as it forces plastic hinge formation into the pile/column section as well as to provide adequate ductility capacity. However, the climate of Alaska is dominated by sub-zero temperatures for significant portions of the year. It was, therefore essential to characterize the durability of the GSS connection in cold climates.

To assess the durability of the GSS connection, it was necessary to investigate the durability of the constituent materials (structural steel and high-strength grout). One possible concern regarding the low temperature performance of the columns was the undesirable brittle fracture of steel. AKDOT prefers to use high quality steel, grade API 5L X52 PSL2, for pipe columns in new construction of bridge substructures. The mill certificates for the pipes that were ordered showed that all of them had Charpy V-notch (CVN) toughness values exceeding 200 ft-lb at 32° F, which is typical of all API 5L PSL2 pipes. This high value of CVN toughness will be sufficient for the satisfactory performance of the steel in the low temperature climate in Alaska [Bjo05]. A good summary of realistic performance requirements for structural steel is provided by Bjorhovde [Bjo05].

The use of grout makes the construction of the GSS connection rapid, which is desirable because of the short construction seasons in Alaska. However, during the service life of a bridge, these connections are exposed to a large number of freeze-thaw (FT) cycles, low temperature events, and large thermal gradients. These environmental conditions may

adversely affect the performance of the connection due to mechanical degradation, i.e., cracking of the grout. In addition, the geometry of the connection and the presence of the shear studs might contribute to degradation of the grout as they provide restraint against shrinkage. The thermal strain mismatch between the grout and shear studs, and between the grout and the steel pipe pile may also cause cracking. Properly designed grouts can withstand a large number of FT cycles without degradation. Therefore, one of the goals of this study was to investigate whether the factors listed above posed significant concerns to the durability of the GSS connection.

1.3.2 Investigation of the Force Transfer Mechanism

The design recommendations for the GSS connection provided by Fulmer et al. [Ful15] make many conservative assumptions, as discussed later. AKDOT was interested in optimizing the design for this connection. In doing so, the aim was to reduce the total number of shear studs used to fabricate this connection. Yet another variable of interest was the embedment length and what an optimum value might be. Therefore, the second goal of this study was to perform large scale experimental tests to possibly determine the force transfer mechanism and relevant variables that impact it. Throughout the project, it was realized that the force transfer mechanism that transpires within the connection was different from what was assumed earlier, which will be evident from a later discussion. Consequently, one of the motivations became formulating the new force transfer mechanism and corresponding design equations.

1.3.3 Seismic Design

Since the ultimate goal of the GSS connection is its application in real structures to resist seismic forces, a design procedure was required. Most of the seismically active regions in the United States are currently subscribing to the displacement based seismic design philosophy, which emphasizes the use of structural displacement as the primary design variable. As a result, the estimation of structural displacement at various limit states is of utmost importance. Therefore, the final objective of this work was to develop a simplified model that can be used by engineers to estimate the displacement of bridge pier systems at key limit states.

1.4 Research Approach

To answer the questions posed earlier, this study approaches the problem using three different phases:

1. Grout Durability Tests
2. Large Scale Steel Bridge Pier Tests
3. Test Data Analysis and Computational Modeling

Phase 1: Grout Durability Tests

In a journal article in 1980 [Lit80], Litvan commented:

“A statement concerning durability is meaningful only in the context of specified geographical areas and particular applications.”

To evaluate grout durability, it was therefore essential to identify the specific geographical area and the practical application. Results and conclusions from the experiments discussed here are concerned with the application of the grout material in the GSS connection in cold climate regions. From this perspective, the physical processes that cause concern are

1. Freeze and Thaw (FT) cracking
2. Early age shrinkage cracking

These concerns are discussed in detail in Chapter 2. Chapter 2 also provides a full discussion of damage inducing mechanisms, standardized tests for evaluation, test results, and conclusions. Investigation to determine the durability of cementitious grouts is referred to as Phase 1 in this dissertation. The objective of Phase 1 was to identify the behavior of some readily available commercial grouts with respect to aforementioned durability concerns. During Phase 1, typical characteristics of common cementitious grouts under short- and long-term exposure to cold climates were also observed and are reported in Chapter 2.

Although it would have been ideal to be able to specify and control the durability of the grout used in the GSS connection, Phase 1 results suggested that this may not be possible. In Phase 1, there were cases where specimens of a specific batch of a certain commercial grout performed well under freeze and thaw, while a different batch of the same grout showed poor results. There were also grouts from different manufacturers with similar bag labelled properties that showed highly variable results, ranging from excellent to poor, under freeze and thaw. All of the above led to the conclusion that specifying an “ideal” grout for the GSS connection was likely impossible.

Before delving deeper into the material level properties of cementitious grout, Phase 2 of the project was pursued to investigate whether grout durability significantly impacts the overall structural performance of the system in use.

Phase 2: Large Scale Experiments

To determine the consequences of grout durability damage on their overall structural performance, three large scale two-column steel bridge bent specimens employing the GSS connection were tested. These were representative of typical steel bridge bents above the point of contraflexure under in-plane bending. The first test used standard unaltered high-strength grout to fill the annular space in the GSS connections. The second and third tests used the same high-strength grout, but with its compressive strength and elastic modulus artificially reduced to 40% and 70% of initial by adding a low density admixture. This reduction simulated an effective state of damage equivalent to grout exposed to multiple years of service in extreme cold climates. If grout durability significantly impairs adequate structural performance of the GSS connection, the tests employing connections with simulated damage should have resulted in poorer performance compared to the control test. However, this was not the case. All three tests showed similar structural behavior, which led to the conclusion that grout durability is of little concern for the long-term performance of the GSS connection.

After completion of the first two tests, a meeting with the Alaska Department of Transportation and Public Facilities (AKDOT) introduced a minor change of scope in the overall project. The remaining two large scale tests were subsequently used to better understand the force transfer mechanism within the GSS connection. It was found that the dominant

force transfer mechanism that resists the bending moment demand on the connection is the action of two equal and opposite normal forces developed within the connection. These forces act as a moment couple to resist the moment demand on the connection. It was also found that a long stub length, as described later in this report, is necessary to achieve successful relocation of the plastic hinge into the columns. Moreover, the role of the number of shear studs present in a connection was found to be less impactful than was previously assumed.

The method of artificial damage simulation, through which a grout damage state was achieved representative of years of service life, is discussed in Chapter 3. The large scale tests performed to determine the consequences of grout damage on the structural performance of the GSS connection is discussed in detail in Chapter 4. The investigation conducted to better understand the force transfer mechanism in the GSS connection is discussed in Chapter 5.

Phase 3: Experimental Data Analysis and Computational Modeling

After the successful completion of four large scale structural tests, the focus shifted to the retrieval of experimental data and its evaluation to propose meaningful models that can be useful for the structural design of the GSS connection. First, an a priori strut-and-tie based model was used to explain the force transfer inside the socket. This model was able to estimate the maximum capacity of the GSS connection when columns are under flexural loading. These capacity estimates matched the results from the large scale tests. The development of this model is discussed in Chapter 6.

The large scale test specimens were also instrumented with LED markers, which could

be sensed by high definition Optotrak cameras to record real-time 3-D displacement data. This data was post-processed to provide local strain data on the critical cross-sections of each test specimen. Computational models developed in OpenSees were then able to replicate this local strain data and the global displacement data, simultaneously. These models were then used to perform parametric studies, which led to the development of a set of equations that could estimate an idealized non-linear backbone curve for any two-column steel bridge pier with the GSS connection and hollow circular column cross-section. The development of this model that can estimate displacement limit states of these systems is described in Chapter 7.

1.5 Chapter Summary

This chapter introduced the grouted shear stud connection, also referred to as the GSS connection. The GSS connection was developed as a ductile alternative to directly welded connections in steel bridge substructures. In addition to its superior seismic performance, the GSS connection scores highly in its potential to be used within the framework of accelerated bridge construction. It is suitable for use as a connection detail for structural steel, reinforced concrete, or reinforced concrete filled steel tube bridge bent systems. Unlike directly welded connections, the GSS connection provides redundant load paths for force transfer. Construction of systems with the GSS connection offer higher tolerances compared to directly welded connections. Furthermore, the GSS connection can also be deployed as a retrofitting option for deficient bridge systems.

The primary motivation for this study can be summarized by asking three questions:

1. *Can the GSS connection be used in cold climates?*
2. *Can the force transfer mechanism in the GSS connection be determined?*
3. *Can the structural displacements at key limit states of systems incorporating the GSS connection be predicted?*

To answer these questions, the project was divided into three phases. Phase 1 investigated the durability at the material level, i.e., durability of cementitious grouts that could potentially be used in the GSS connection. Phase 2 investigated at the system level and had two objectives; whether grout durability matters from the perspective of long-term structural performance and whether the design of the GSS connection can be optimized. Phase 3 compiled all of the available empirical data on the GSS connection to develop design recommendations. This dissertation discusses all of these phases in detail.

CHAPTER

2

DURABILITY OF CEMENTITIOUS GROUTS IN COLD CLIMATES

2.1 Introduction

The GSS connection is a composite connection composed of a hollow steel socket, an inner steel pipe, steel shear studs, and a high-strength cementitious grout. The force transfer between the column pipe and cap-beam takes place through the grout ring and hence

it is important to characterize the properties of cementitious grout. Tests performed on GSS connections by Fulmer et al. [Ful15] have shown that a high-strength grout can successfully transfer the forces and relocate the plastic hinge to the column section. However, these tests were performed in laboratory conditions on specimens with standard grout. In reality, bridges are exposed to a variety of extreme environments for many years. If engineers were to use the GSS connection in practice, they must expect some amount of grout deterioration. The amount of deterioration that could be expected is currently unknown, as few studies have investigated the durability of cementitious grouts, let alone in the specific setting of the GSS connection. Our objective for Phase 1 of this project was to obtain information in this regard through various experimental means.

In porous materials, water is generally involved in every form of deterioration, and with cementitious materials, the ease of penetration of water into the solid usually determines the rate of deterioration. Durability under one set of conditions does not equate to durability under another, and therefore it is important to specify a target environmental condition before proceeding with durability determination. Phase 1 of this project evaluated the durability of commercially available cementitious grouts in extreme cold climates.

Durability of concrete has been widely studied, and there exist standard test procedures to evaluate the durability of different concrete mixtures. The assumption in this study is that grouts are different from concrete only with respect to the absence of coarse aggregates. Both are porous materials, and therefore the standard test methods to evaluate degradation of one can be applied to the other. In the specific application of the GSS connection, two major issues that can potentially cause degradation and in turn cracking of the grout material in Alaskan cold climates are freeze and thaw cracking, and restrained

shrinkage cracking. Cementitious materials are prone to damage under repeated freezing and thawing when they contain water at or above a critical degree of saturation. The major focuses of this chapter are to (1) explain the mechanisms of frost damage, (2) describe different test methods that are prevalent to assess freeze-thaw (FT) resistance of cementitious materials, (3) describe tests performed as part of this study, and (4) provide conclusions.

Due to the complex geometry and the presence of embedded steel shear studs, the GSS connection may cause considerable early age restrained shrinkage cracking. Early age cracking is important since it can result in the reduction of service life of the grout, and in turn of the connection by allowing water and contaminants to enter the cracks causing corrosion to occur furthering grout cracking and deterioration.

In this chapter, a study carried out to determine the compressive strengths of some commonly available high-strength cementitious grouts is discussed. After introducing the different grouts used in this study, mechanisms of FT damage are discussed followed by a review of some of the most used test methods to assess FT resistance of porous materials. Following this discussion, the results of the tests performed as part of this study are provided.

The materials that performed well under FT testing were chosen to perform restrained shrinkage tests (ring tests) to investigate their early age cracking potential. To assess the impact of the presence of shear studs in the GSS connection on the shrinkage cracking behavior, the ring tests were then performed on specimens with shear studs embedded in them. These specimens simulated actual geometrical conditions within a real GSS connection. Before discussing the results of all the restrained ring tests, a review of the latest literature on the ring test is presented. This chapter is then concluded with a section sum-

marizing the inquiry into assessing the durability of commercial grouts. A set of qualitative recommendations are provided regarding good practices for choosing, mixing, and placing of the grout.

2.2 High-Strength Cementitious Grouts

Cementitious grouts are proportioned Portland cement based mixtures prepared by combining Portland cement, fine aggregate, and some combination of mineral and chemical admixtures, that are sold commercially in bags for instant use. Normally, these bags are mixed, in situ, with a manufacturer specified amount of water. These grouts are proportioned so that they exhibit good flowability and workability. Over the years, high-strength cementitious grouts have been used in a multitude of applications such as crack injection, anchorage sealing, and post-tensioning applications [Kha99; Tou99]. Lately, high performance grouts are also being used for structural repair and retrofit of bridges [Sha02b]. The GSS connection is yet another example of cementitious grouts making their way into large scale applications.

Before moving to the durability aspects of commercial grouts, a small study was undertaken to ascertain the strength characteristics of cementitious grouts to gauge the current state-of-practice. As part of testing the compressive strengths of the grout filler being used in the large scale tests, the scope was again expanded to include a series of compressive strength tests performed on four different high strength cementitious grout materials. Tests were performed on both 2"× 2" cubic samples and 4"× 8" cylindrical samples. The objectives of the tests were to investigate the following:

1. Variability of compressive strength values for cubic samples.
2. Differences between cylinder strength and cube strength of cementitious grouts.
3. Compare compressive strengths of typical high strength grouts.

All the different grout materials that were tested are given in Table 2.1. These were labelled CG1 to CG4. The size and testing protocol for testing cylindrical samples followed ASTM C39 [Asta]. ASTM C109 [Astb] specifies the cubes to be cured in lime water after 24 hours whereas the specimens tested here were sealed cured. The standard does not specify the use of polymer pad caps over the loading faces. However, such caps were used to test these samples. Samples were tested on their 3rd, 7th, 28th and 90th day after casting.

Table 2.1 Material used, bag weights, and the amount of water added in each mixture

Material	Bag Weight (lbs.)	Water added per bag (lbs.)	Consistency label*
CG1	55	8.5	-
CG2	50	8.4	Flowable
CG3	50	6.6	Flowable
CG4	50	9.3	Flowable

* Label specified by manufacturer corresponding to the amount of water

The average strengths of cube and cylinder samples at different ages are provided in Table 2.2 . The coefficients of variation of each value in Table 2.2 are provided in Table 2.3 .

Overall, cylinder strength values showed less variation compared to cube strength values. This was expected as cylinders, being large samples, are more homogeneous along the length-scale as compared to the smaller cubes. The average coefficients of variation

Table 2.2 Summary of the results - average compressive strengths

Grout	Average Strengths (ksi)							
	3-day		7-day		28-day		90-day	
	Cube	Cylinder	Cube	Cylinder	Cube	Cylinder	Cube	Cylinder
CG1	8.44	7.84	10.20	8.80	11.47	10.60	12.27	11.04
CG2	7.19	7.16	8.93	8.04	9.91	9.05	10.44	9.60
CG3	10.21	8.10	10.41	8.91	10.41	9.86	-	-
CG4	6.47	5.60	7.15	7.42	8.60	8.43	10.76	9.44

Table 2.3 Summary of the results - coefficients of variation for average compressive strengths

Grout	Coefficients of Variation							
	3-day		7-day		28-day		90-day	
	Cube	Cylinder	Cube	Cylinder	Cube	Cylinder	Cube	Cylinder
CG1	0.05	0.03	0.03	0.00	0.07	0.07	0.04	0.07
CG2	0.02	0.04	0.04	0.04	0.05	0.02	0.10	0.05
CG3	0.05	0.01	0.03	0.03	0.08	0.03	-	-
CG4	0.11	0.02	0.12	0.02	0.09	0.05	0.08	0.04

for cubes and cylinders were 0.06 and 0.03, respectively. Figure 2.1 provides a graphical representation of the data. Note that the cubes for CG3 show almost equal strength at all ages, a result which is not consistent with the cylinders from the same batch. A likely reason for this is improper curing. Cubes of CG3 grout were not sealed after demolding due to misplacement. Drying ensued preventing further hydration. This halted strength gain. The authors would like to emphasize the importance of curing for strength test samples, especially for cubic specimens since they can lose significant amount of moisture rapidly. Data from other grouts, which were cured without moisture loss, show an increase in strength with age. The error bars indicate one standard deviation above and below the mean of the sample data. Compressive strengths of cubes are higher than those of cylinders, on av-

erage. This conforms to expectations as specimens with higher aspect ratios show lower strengths due to localization [MM17]. Cube and cylinder samples had an aspect ratio of 1 and 2 respectively. Both classifications of strength show the same pattern of increase with age, which indicates that measuring strength of grout cubes can be a valid alternative to measuring strength of grout cylinders, if all steps of testing are performed properly. CG1 and CG3 showed high strengths very early and kept increasing up to 90 and 28 days respectively. CG2 and CG4 had comparatively lower early age strength and a lower 90-day strength compared to CG1 and CG3. A comparison between the measured and manufacturer specified values of compressive strength are provided in Table 2.4. Note that the measured strengths equal or exceed the manufacturer specified strength.

Table 2.4 Comparison between the measured and manufacturer specified compressive strength values for cementitious grouts.

Material	Water added per bag (lbs.) ¹	Specified Strength (ksi) ²	Measured Strength (ksi) ³
CG1	8.5	8.0	10.6
CG2	8.4	8.0	9.1
CG3	6.6	10.0	9.9
CG4	9.3	8.0	8.4

¹ Amount of water corresponds to flowable consistency.

² Specified by the manufacturer for corresponding consistency.

³ 4"×8" cylindrical samples.

All the average cylinder strengths are compared to their corresponding average cube strengths in Figure 2.2. Any point on the red line are points of equal strength. Cube strengths are almost always greater than cylinder strengths as can be observed from the fact that al-

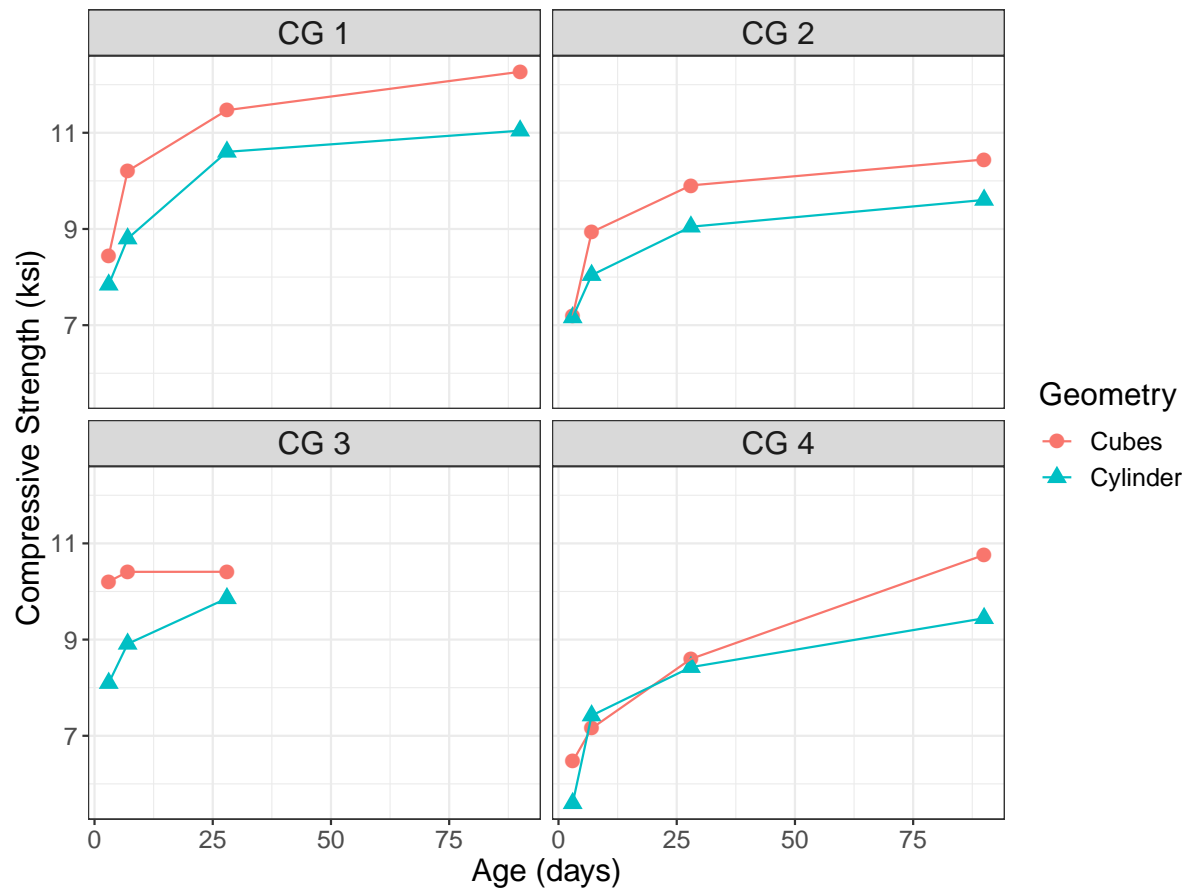


Figure 2.1 Comparison of cube strength and cylinder strength for all the tested grouts.

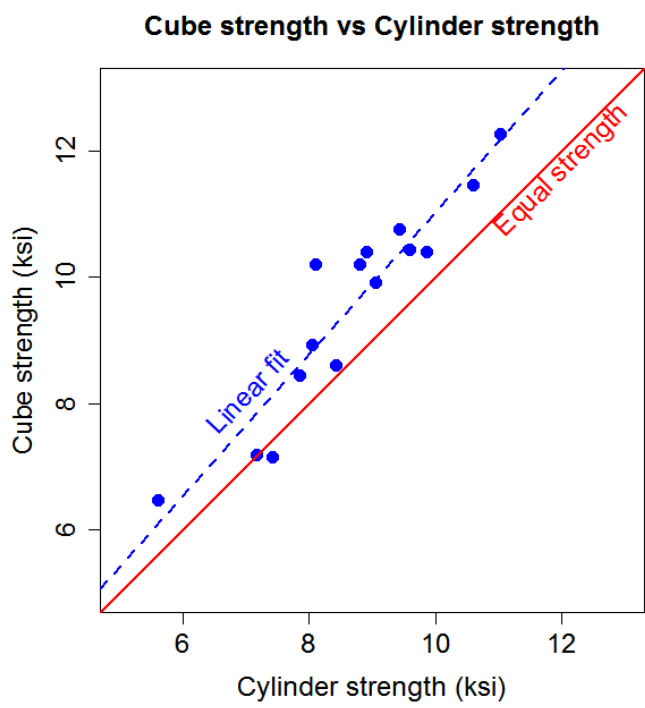


Figure 2.2 All average cube strengths versus average cylinder strengths.

most all points lie above the red line. The data is also suggestive of a linear correlation between cube and cylinder strengths. A linear fit to the data is shown in Figure 2.2.

To summarize, high-strength cementitious grouts are Portland cement based mixtures that can be readily used by mixing with water. They have high flowability and workability to be able to fill structural cracks, post-tensioned cable sleeves, anchor holes etc. They generally develop high early age strength which can be measured using either cylindrical or cubical samples. For sufficient strength development, good curing practices are crucial.

2.3 Freeze and Thaw Cracking

2.3.1 Mechanisms of Freeze-Thaw Damage

Concrete is made up of four main components: cement, water, fine aggregates, and coarse aggregates. Cement in combination with water (also called as cement paste) binds the aggregates together to form structural concrete. Cyclic freezing and thawing can result in damage and degradation of concrete in the presence of a sufficient amount of moisture in its pore structure. The component of concrete largely vulnerable to freeze and thaw damage is the cement paste. The main mechanism by which formation of ice damages cement paste is the repeated expansion and accumulation of water during FT cycles. A large body of literature exists regarding frost damage mechanisms in porous materials. The two most accepted mechanisms for FT damage in concrete are:

1. The hydraulic pressure mechanism due to ice formation, and
2. The microscopic ice body growth

The hydraulic pressure mechanism is caused by the 9% volume increase when water transforms to ice [Bag10]. In a saturated pore system, this leads to an increase in the water pressure which, if greater than the tensile strength of the surrounding cement paste matrix, results in crack formation. According to the microscopic ice body formation theory, ice forms as micro lenses in the pores. Such micro lenses in porous materials act in two opposing ways [Set99]:

1. The free pore water moves towards the micro ice lenses which will therefore grow and exert pressure on the surrounding pore walls, leading to an increase in volume of the paste.
2. On the other hand, the driving forces that cause the water to move towards these ice lenses also may draw water from the gel pores resulting in shrinkage of the paste.

The resulting damage is believed to be a cumulative effect of the two processes which may depend upon a number of other factors such as the critical degree of saturation (discussed later), availability of external water, rigidity of the microstructure gel [Set99] etc. Any volume dilation due to ice formation in the freeze cycle can propagate cracks which can then be filled with more water in the subsequent thaw cycle. With each successive FT cycle, damage accumulates [Set99].

It has also been found over the years that there are common factors that influence frost damage in any porous cementitious material [Lit80] such as:

1. Flow Distance (D)
2. Degree of Saturation (S)

3. Cooling Rate

Flow distance is an approximate measure of the greatest distance that water must travel to the nearest air-filled space (or the surface) without causing damage. Damage occurs when the flow distance is greater than the critical flow distance (D_{cr}). In theory, if water could leave the capillary pores of the material during the cooling period, ice forms outside the capillary pores or within large empty air voids, causing no damage. Due to a high cooling rate, high degree of saturation, or a long diffusion path, if water cannot escape and solidifies inside the capillary pores, mechanical damage ensues. Any porous material can be destroyed by enough freezing and thawing by saturating it above the critical degree of saturation. This means that for frost resistance testing, there is a need to assess the FT resistance of the material under representative exposure conditions.

Degree of saturation (S) is the ratio of the total volume of water/moisture to the total volume of voids present in the porous material. A fully saturated system will experience significant damage even in a single FT cycle [Lit88]. In general, FT damage occurs when the degree of saturation is greater than the critical degree of saturation (S_{cr}). The critical degree of saturation (S_{cr}) is considered as the point (or a region) along the saturation axis beyond which considerable damage occurs, measured usually by the decline in the elastic modulus. Figure 2.3 shows an example plot from several experiments collected by Fagerlund [Fag77b]. The decline in elastic modulus can be clearly seen for tests done on different specimens in different labs. It is also worthwhile to note that most S_{cr} values lie within a common region (the striped region in Figure 2.3). This was found to be approximately within 0.86-0.88 degree of saturation. A simplistic way to understand this is by using the idea of volume expansion of water when frozen. Water expands by about 9%

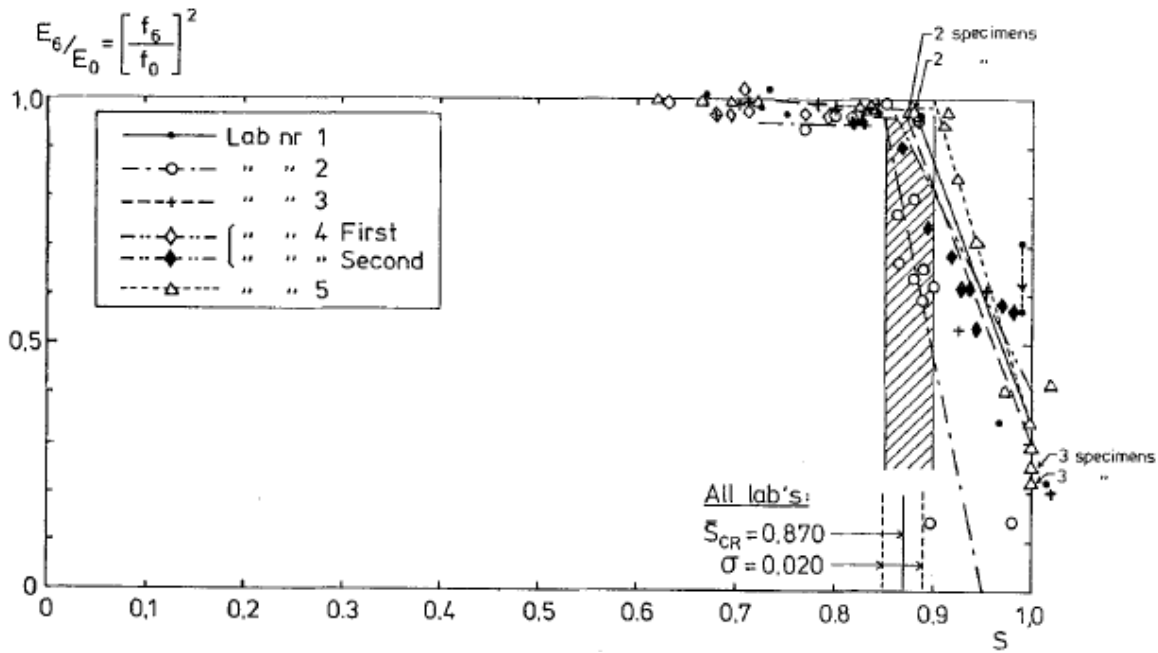


Figure 2.3 A sample plot showing dynamic elastic modulus vs degree of saturation for concrete specimens tested in five different laboratories [Fag77b].

when frozen. After allowing for this expansion, the critical degree of saturation should become 0.91. This is close to the measured values between 0.86 to 0.88. The water expansion model is a simplified model and the deviation from the measured values can be attributed to more complex mechanisms.

Li et al. [Li11] studied the effect of water ingress and the role of air content in FT damage of pavement joints. It was found that water ingress had deleterious effects on the concrete, corroborating earlier observations of Litvan [Lit80]. It was also found that air entrainment, which is a widely accepted method of preventing frost damage, provides resistance by delaying the attainment of the critical degree of saturation (S_{cr}). This means that the value of S_{cr} is more or less fixed for cementitious materials. This value also helps in many ways

to determine the potential of frost damage and also, to an extent, predict the service life of the material.

Water uptake is another measure that can be related to frost damage. It is normally measured by having a thin slice of the material in contact with the surface of water. Weight measurements can be made at regular intervals to determine water uptake. Water uptake or absorption potential depends on the capillary system formed within the material. There are two different aspects of water uptake that have interested researchers. One is the absorption without undergoing FT cycling and the second is the absorption under FT cycling. Fagerlund [Fag77b] introduced a term called capillary degree of saturation (S_{cap}) which proved to be a convenient parameter to estimate the frost resistance of concrete. If a concrete specimen is subjected to a test in which its ability to absorb water is measured, its absorption rate can be monitored, and a point in time is reached when this rate declines drastically, as shown in Figure 2.4. The degree of saturation of the specimen at this point is called the capillary degree of saturation (S_{cap}). For each type of concrete, each environment can be translated to a certain water uptake time or S_{cap} value. The difference between S_{cr} and S_{cap} for a material can be used as a good indicator of potential FT resistance of the material.

2.3.1.1 Reducing the w/c ratio

The w/c ratio is the ratio of the amount of water by weight, to the amount of cement in a mixture. Water in the cement mixture is mostly consumed in the chemical reaction of cement hydration which forms the hardened microstructure. However, the excess water that is not consumed ends up as capillary pores within the material microstructure. The larger

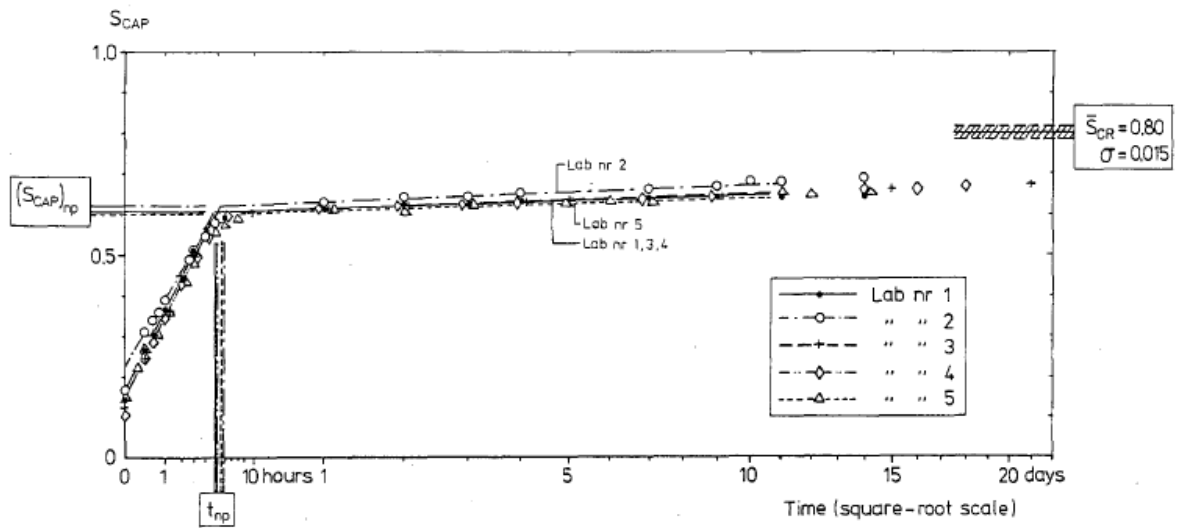


Figure 2.4 A sample plot showing mean values of capillary degree of saturation vs time of water uptake [Fag77b].

the amount of excess water, the larger the pore volume inside the material. The water inside these pores expands when freezing which in turn causes cracking inside the material. Hence, reducing the w/c ratio of the mixture is one way to reduce FT vulnerability.

2.3.1.2 Increasing the air content

Air entrainment is an alternate way of increasing the FT resistance of cementitious materials. Air voids when introduced into the microstructure allow space for water to expand into, thus reducing the tensile stress on the rest of the microstructure. However, air entrainment only delays FT damage. When all the air voids are filled by the cumulative effect of FT cycling, subsequent cycles can damage induce damage.

2.3.1.3 Decreasing paste content

This method is only effective in concrete, not grout, as it has the additional component of coarse aggregates in its microstructure. The water in concrete is held as part of the hardened cement paste. This cement paste is the most vulnerable component to FT damage. An indirect way of increasing FT resistance of concrete is by reducing the cement paste content. This can be achieved by increasing the volume fraction of the coarse aggregate in the design mix.

2.3.2 A Review of Freeze-Thaw Testing Methods

A large number of FT test methods exist in the literature. Albeit different in other aspects, they all follow the same core principle. Concrete specimens are subjected to a predetermined freezing and thawing cycle for a specified number of cycles. Based on the requirement of the application, different variations have emerged over time. The most widely used FT test is the ASTM C666 [Aste].

ASTM C666 provides an accelerated test method in which specimens are subjected to a maximum of 300 FT cycles. The damage in the specimens is monitored by measuring the dynamic elastic modulus after a predetermined number of cycles. This test may be terminated before 300 cycles if the reduction in elastic modulus is greater than 40%. The 40% value is derived from empirical observations correlated to the point where visible cracking is observed in FT specimens. In this test, specimens are subjected to FT cycles between 40°F (4°C) and 0°F (-18°C). The specimens are prismatic (12" × 3" × 3") and are cured for 14 days in saturated lime water after demolding. The outcome of a single test is a dimensionless Durability Factor (DF) which is based on the terminal relative dynamic modulus

of elasticity and the total number of FT cycles. Further details of ASTM C666 test method is provided later in this report.

According to Janssen [Jan02], a good assessment of FT resistance should be based on three factors:

1. Internal cracking of the paste,
2. Internal cracking of aggregates, and
3. Surface scaling.

Among these factors, only the internal cracking of the paste is relevant to the durability of the GSS connection because sound fine aggregates, i.e., aggregates resistant to degradation, as defined by ASTM C88 [Astf], are used in the mixture. Due to the small exposed surface of the GSS connection grout, surface scaling is also not of concern. Janssen [Jan02] also added that it is vital to have a good simulation of the exposure conditions that include temperature exposure, moisture availability, and drying conditions. Specifically, to closely simulate the microstructural damage of the cementitious material that corresponds to damage in field exposure conditions, “some” method of specimen conditioning that includes cycles of drying and rewetting, is required.

Generally, FT resistance for cementitious materials is achieved by

1. Reducing the water-to-cement (w/c) ratio of the mixture,
2. Increasing the air content, and/or
3. Decreasing the paste content (increasing the aggregate content).

According to Auberg [Aub02], estimation of service life can only be accomplished by knowing the expected environmental loading on the material. The duration and temperature range of the test should therefore be representative of the actual exposure conditions. The actual degree of saturation at the beginning of frost attack and the additional water absorption in the thawing phases are the main parameters that should be considered in investigating FT durability.

Over the years, ASTM C666 has been criticized for specifying a severe exposure that does not represent normal field exposure. Furthermore, the specimens are tested immediately after the curing period and hence no specimen conditioning is carried out. Since the outcome of ASTM C666 is only a Durability Factor (DF), a complete picture of the frost resistance and service life of the material cannot be obtained. Quantities such as the critical degree of saturation (S_{cr}) and water uptake potential, not obtained from the ASTM C666 testing protocol, are more meaningful in assessing material durability. Nevertheless, ASTM C666 is a simple and straightforward test to compare the FT performance of different materials. The scope of this study is limited to investigating the current state of high-strength cementitious grouts with respect to applicability in the GSS connection under cold environmental conditions. Hence, it was established as the standardized test of choice for this study.

Among other alternatives, two test methods are discussed next for completeness in presenting past literature. These test methods are: the Critical Degree of Saturation method [Fag77a] and the Capillary suction, Internal damage, and freeze-thaw (CIF) test [Set04]. Although these test methods provide more information regarding FT resistance of a material, they require more complicated test setups compared to ASTM C666, and both require sig-

nificantly more time. Furthermore, application of these test methods to the GSS connection is impractical due to the required measurements of degree of saturation as a function of time, critical degree of saturation, and water sorption characteristics of the material as further described below. Both of these tests have been part of RILEM (International Union of Laboratories and Experts in Construction Materials, Systems, and Structures) recommendations in the years 1977 and 2004, respectively, and their relevance is discussed in some detail here.

2.3.2.1 Critical Degree of Saturation method

This method, proposed by Fagerlund [Fag77a; Fag77b], is based on the existence of critical moisture contents or degrees of saturation beyond which materials experience damage during freezing. The test is carried out in two parts, first the critical degree of saturation (S_{cr}) is determined and second, the determination of the capillary degree of saturation (S_{cap}). S_{cr} is determined by a test in which sealed specimens containing different amounts of water are subjected to a few FT cycles. Other specimens of the same material type are subjected to a test in which their ability to absorb water is measured. The FT resistance, F , is then defined by:

$$F = S_{cr} - S_{cap} \quad (2.1)$$

S_{cr} is essentially independent of outer climatic conditions. Theoretically, for each type of concrete, each environment can be translated to a certain S_{cap} . Therefore, F expresses the potential FT resistance of a certain concrete type used in different environments. The fundamental difference between this method and other traditional methods is that tradi-

tional methods investigate specimens of only a single degree of saturation and indicate whether the concrete is damaged at that particular water content. In other words, traditional methods such as ASTM C666 evaluate the material at the most severe degree of saturation which may not represent true exposure conditions, and a material that may fail the test may still perform well under actual conditions.

In the S_{cr} method, the initial degree of saturation of specimens is varied and the corresponding damage after equal numbers of cycles is plotted. This means that one can consult these plots to estimate the expected damage for any initial degree of saturation. While the initial degree of saturation may be important to estimate the expected damage, it is unknown and difficult to determine. Therefore, the initial degree of saturation is not a consideration in this study of the durability of the GSS connection. The risk for an increase of water content can also be judged from the experimentally determined water absorption curves such as those provided by Fagerlund [Fag77a; Fag77b]. Hence, all materials can be tested and evaluated in exactly the same way, irrespective of where and how they are used. However, this method of testing is elaborate and requires a significant amount of work to perform.

2.3.2.2 Capillary suction, Internal damage, and Freeze-thaw (CIF) Test

The CIF test was proposed to obtain a large amount of information regarding durability of a concrete material from a single test. This test incorporates conditions representative of the realistic exposure conditions. The aim is to conduct a test from which it would be possible for designers to predict FT durability and service life of a material. The test method is combined with the measurement of surface scaling. Although the duration of the test is

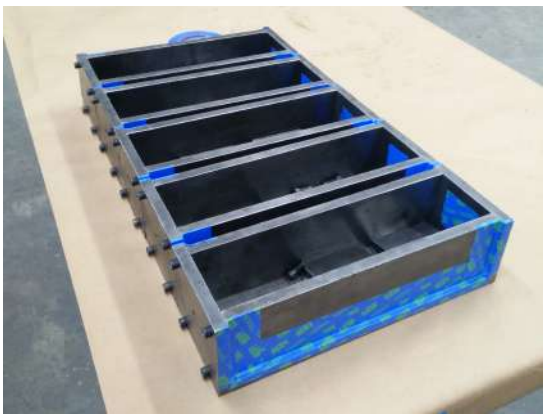
shorter compared to ASTM C666, it requires more complicated instrumentation.

Adding to the methods that have been listed here, there exist numerous other techniques developed for FT testing. A comparison of different test methods is difficult because each of them has been designed for specific purposes. Moreover, the criteria for durability is greatly dependent on environmental loading, specific application in practice, and the test methods used. Standardized test methods have been developed principally for the purpose of quality control. For research applications, the best understanding of concrete behavior may be obtained using multiple methods simultaneously.

2.4 Freeze and Thaw Resistance of Commercial Grouts

2.4.1 ASTM C666 Test Procedure

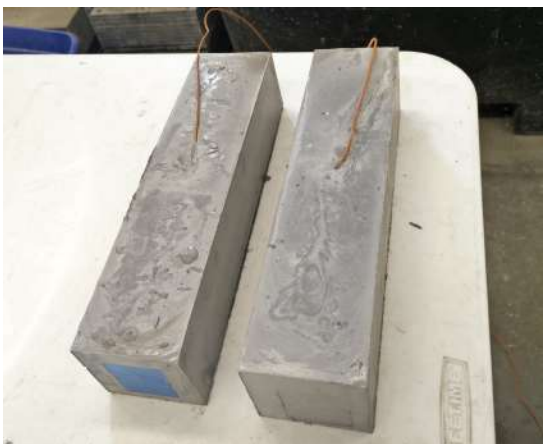
Four commonly available commercial grouts were tested according to ASTM C666. The specimens were 3"×3"×12" prismatic beams prepared in steel molds, as shown in Figures 2.5a and 2.5b. The specimens were cured under saturated lime water for 14 days after demolding. Identical specimens were required as controls to monitor the temperature inside the material during the testing because ASTM C666 specifies the control of the core temperature of the samples rather than the ambient temperature. Thermocouples were embedded within the control specimens (Figure 2.5c) for continuous acquisition of temperature data. A cycle period of 6 hours was used which enabled 4 cycles per day. The specimens were submerged in water throughout the testing and were kept in steel trays that were fabricated in-house meeting ASTM requirements. The specimens were subjected to FT cycles between 40 ± 3 °F (4 ± 2 °C) and 0 ± 3 °F (-18 ± 2 °C) in an environmental chamber (Figure



(a)



(b)



(c)



(d)



(e)



(f)

Figure 2.5 Photographs of various steps during the FT resistance testing procedure.

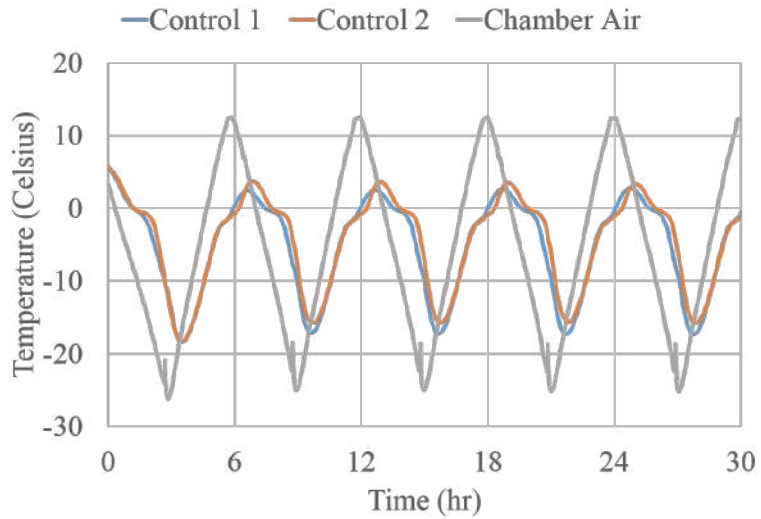


Figure 2.6 Typical cycles of the two control specimen temperatures and the environmental chamber air temperature.

2.5d and Figure 2.5e) that was capable of being programmed with a pre-defined temperature cycle. A typical temperature cycle for the control specimens and the chamber air is shown in Fig 2.6.

ASTM C666 specifies to assess material damage by monitoring the reduction in its relative dynamic elastic modulus. This was done in the following manner. The fundamental frequency of all specimens was measured at 40°F prior to subjecting them to testing. During testing, the specimens were removed from the chamber at intervals of no greater than 36 cycles to measure their fundamental frequency at that point. Since the dynamic elastic modulus of the material is directly proportional to the square of its fundamental frequency (Equation 2.2), the ratio of the squares of the frequencies is equal to the relative dynamic elastic modulus (RDME) as shown in Equation 2.3. The results are plotted in a graph with the number of cycles on the x-axis and RDME (E_N/E_0) on the y-axis. Specimen damage is

represented by a decrease in RDME as the number of cycles increase. Note that the term RDME and the ratio E_N/E_0 have been used interchangeably throughout this report.

$$E_D \propto f^2 \quad (2.2)$$

$$\frac{E_N}{E_0} = \frac{f_N^2}{f_0^2} \quad (2.3)$$

where,

E_D = Dynamic Elastic Modulus

E_N = Dynamic Elastic Modulus after N cycles

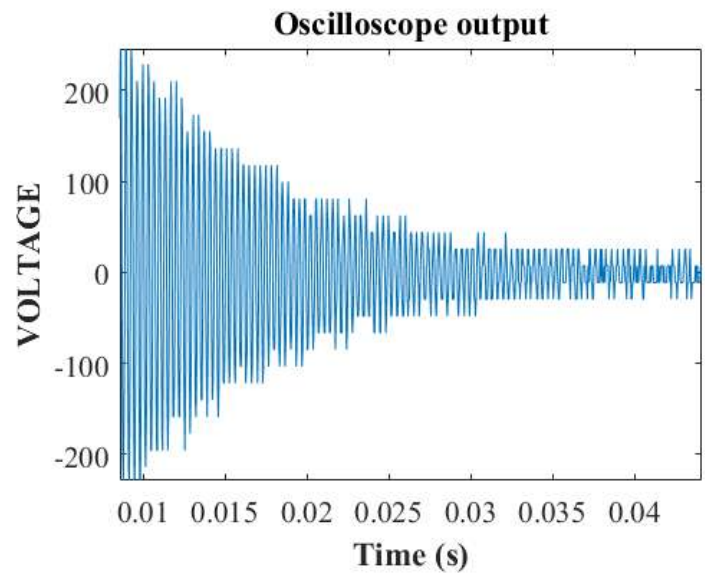
E_0 = Initial Dynamic Elastic Modulus

f_N = Fundamental frequency after N cycles

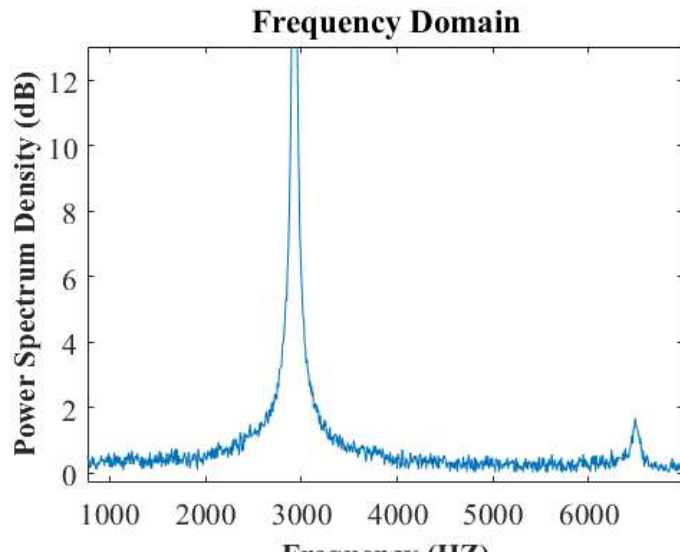
f_0 = Initial fundamental frequency

Measurement of the fundamental natural frequency of prismatic specimens was carried out according to ASTM C215 [Astd]. The setup is shown in Figure 2.5f. An accelerometer was attached to one of the ends of the specimen. The specimen was then placed on a damping mat and was impacted at the center with a hammer. The acceleration response of the specimen was recorded by an oscilloscope (Figure 2.7a). This time domain response is then converted computationally into the frequency domain (Figure 2.7b) to obtain the frequency corresponding to resonant peak, i.e., the fundamental natural frequency.

ASTM C666 defines a dimensionless number to be used as a parameter to compare different materials, called the durability factor. The durability factor (DF) according to ASTM C666 is defined as:



(a)



(b)

Figure 2.7 A typical time domain and frequency domain pair of specimen acceleration responses.

Table 2.5 Grout mixtures tested under ASTM C666.

Mixture Code	Water Content per bag (lbs.)	Durability Factor (DF)	Concluding Remarks
CG1	8.5	100%	Good Performance
CG1	9.0	100%	Good Performance
CG2	8.4	100%	Good Performance
CG3	6.6	100%	Good Performance
CG4	9.3	46%	Poor Performance
PG1	w/c=0.46	<10%	Extremely Poor Performance

$$DF = \frac{P \times N}{M} \quad (2.4)$$

where P is the relative dynamic modulus of elasticity at N cycles (E/E_0) in %, N is the number of cycles at which P reaches the specified minimum value for discontinuing the test or the specified number of cycles at which the exposure is to be terminated, whichever is less, and M is the specified number of cycles at which the exposure is to be terminated.

ASTM C666 Procedure A was performed on four different high-strength commercial cementitious grouts and one conventional concrete mix. Table 2.5 provides a summary of the results obtained for different materials. CG1-CG4 stand for cementitious grouts one to four, and PG1 stands for pea-gravel concrete.

2.4.2 Exploratory Investigation

To form some basis for detailed testing of different commercial grout materials, a series of specimens of the material labeled CG1 in this report was tested under FT cycling. Grout

CG1 was chosen since it was the same material used in the fabrication of large scale structural test specimens by Fulmer et al. [Ful15]. These CG1 specimens were divided into different batches depending on variables such as curing conditions and total water content per bag. Not all of these batches could be tested to completion due to unforeseen technical issues. Only those batches that were completed are discussed here.

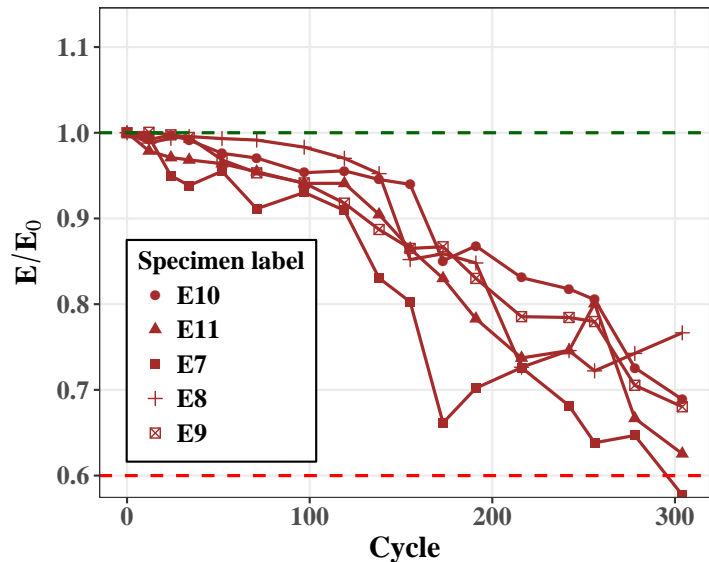
Since w/c ratio is an important parameter for FT resistance, an initial choice had to be made regarding the amount of water per bag of grout. Note that for commercial grouts, the mix proportion in a bag is proprietary. Therefore, it is impossible to ascertain the w/c ratio for a mixture. Accordingly, the water content per bag of grout was used as an indirect measure of the w/c ratio. The manufacturer specified range of water content per bag for CG1 was 9.0 lbs. to 10.5 lbs. Since FT resistance increases with reduction in total water content per bag, the minimum specified amount of 9.0 lbs. was chosen. The first batch of specimens E1 to E6 (not shown here) were terminated prematurely due to widely inconsistent behavior between specimens. These cured for more than the ASTM C666 specified 14 days. The inconsistency may have been due to poor quality of grout in that bag, or poor mixing quality. This was corroborated by subsequent results discussed later.

The second batch of specimens E7 to E11 was tested according to ASTM C666 and the results are shown in Figure 2.8a. The y-axis shows the E/E_0 ratio which is an indicator of damage. E is the elastic modulus of the specimen at the time (cycle number) of measurement and E_0 is the baseline elastic modulus of the same specimen before start of FT cycling. A higher reduction in elastic modulus is an indicator of a larger amount of damage due to cracking. The reduction in RDME was consistent among the specimens and all but one of the specimens completed 300 FT cycles above 60% RDME (ASTM C666 specified cut off).

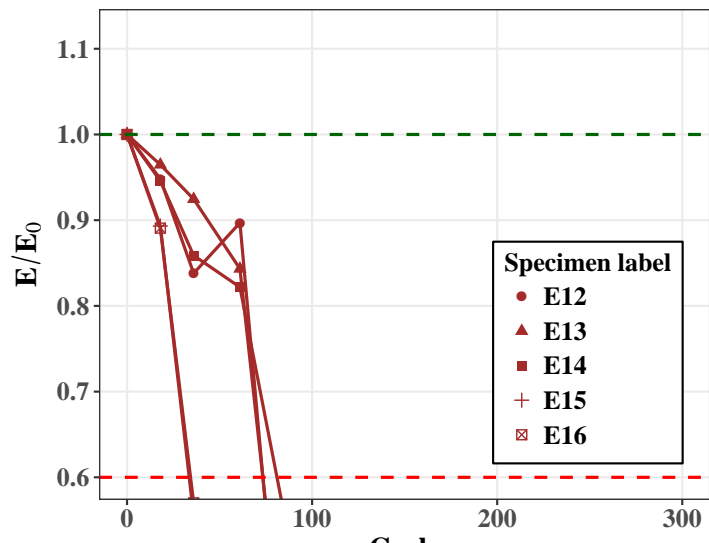
In hindsight, the drop in RDME is thought to be caused by another instance of poor bag of grout and mixing quality. Although, at the time, it was thought that the reason for material degradation could have been the severe nature of ASTM C666 Procedure A. To test this hypothesis, the next batch of specimens was cured in a sealed condition.

The third batch of specimens E12 to E16 was cured in sealed plastic bags after demolding. It was believed that curing in water may have been too severe of a condition. Curing in a sealed condition alleviates this issue by reducing the degree of saturation below the critical degree of saturation thereby improving the FT resistance. Sealed curing also more closely represents actual environmental conditions of the GSS connection since it is open only from one side and is rarely under water. Results of this batch are shown in Figure 2.8b. Clearly, they behaved contrary to expectations of better performance compared to the second batch. All specimens showed rapid deterioration within the first 100 cycles. Hence, the hypothesis that the second batch degraded due to the specimens being at a high degree of saturation due to curing under water before FT cycling, can be rejected. Consequently, new questions arose as to why the sealed cured specimens performed worse. One reason could have been a still high degree of saturation due to the high initial water content of 9.0 lbs. This was rejected upon obtaining more results that are discussed later in this report. Batches four and five were cast with a reduced 8.5 lbs. of water per bag. Note that this amount of water is slightly less than minimum amount of 9 lbs of water per bag, as recommended by the manufacturer. Due to an equipment malfunction, the testing of these specimens was terminated very early and hence are not discussed here.

Upon the conclusion of this exploratory investigation, the following observations were noted. The material behavior under FT cycling was highly inconsistent. Reasons for this



(a)



(b)

Figure 2.8 Results from exploratory investigation of FT resistance of grout material CG1: (a) with 9 lbs. water, and cured under water (b) with 8.5 lbs. water, and sealed cured.

were thought to have been poor quality of grout material and/or poor mixing resulting in poor air void distribution. Good air void distribution is essential for good resistance to freeze and thaw damage. Poor mixing could have been caused due to an old mixer or inexperienced labor. Results of sealed cured specimens performed significantly worse than water cured specimens which goes against general expectation. These issues were addressed in later tests and are discussed subsequently.

2.4.3 Freeze-Thaw Tests on Multiple Commercial Grouts

After the exploratory experiments on grout material CG1, additional grout materials were tested according to ASTM C666. These materials were labeled CG2, CG3, CG4 and PG1. A new batch of CG1 was also tested along with the other grout materials. PG stands for pea-gravel concrete which can be understood to represent the class of conventional flowable concrete ordered from a local ready-mix producer. The water content per bag used for each grout material (CG series) was chosen based on the amount specified by the manufacturers. These water contents are provided in Table 2.5, presented earlier. Note that the water content chosen for CG1 was 8.5 lbs. which is less than the 9.0 lbs. used in the exploratory study. All the specimens were cast using a concrete drum mixer of a larger capacity than that used earlier. This larger mixer was also more robust with regard to speed of rotation and drum tilt angle. Results from this series of tests is discussed next.

It is clear from Table 2.5 that most materials performed well and others performed poorly. Figures 2.9 to 2.11 show the results of all the materials that were tested. Five repeated specimens were cast for each material (CG1 to CG4, and PG1). For example, in CG1 results, these are labeled as CG101 to CG105. Figure 2.9 shows the result from specimens

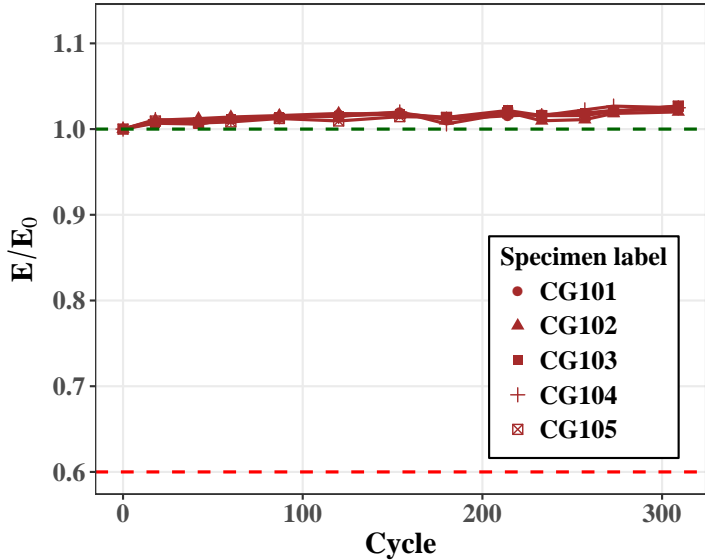
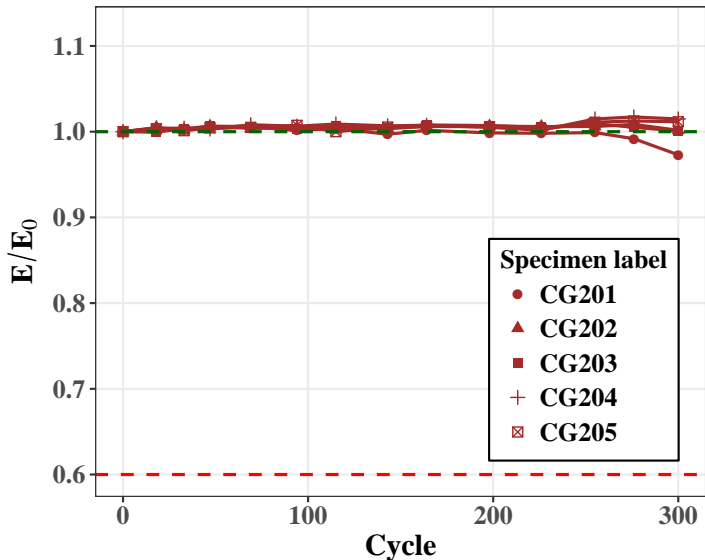


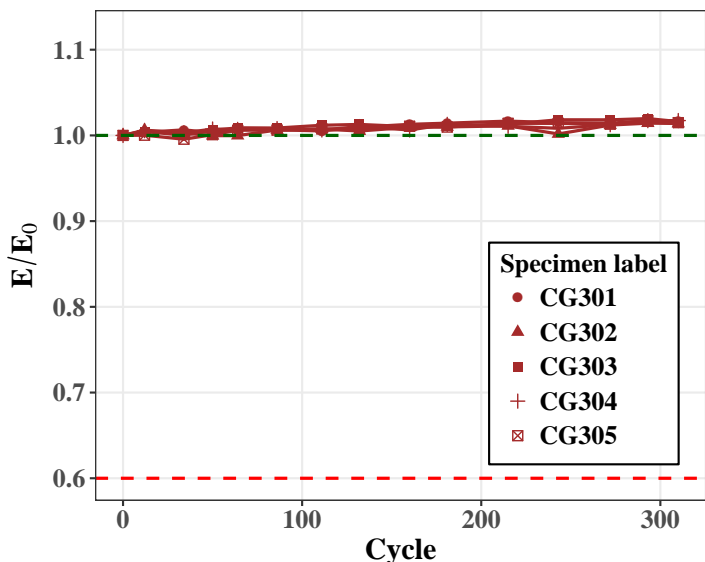
Figure 2.9 Results from ASTM C666 FT tests on multiple commercial grout (Good performance). Grout: CG1, Water per bag: 8.5 lbs.

of CG1 with 8.5 lbs. water per bag of grout. In Figure 2.9, as no reduction in E/E_0 is observed, there is minimal or no damage due to FT cycles. This is a different behavior from that observed during the exploratory study for the same material. The consistency of results in Figure 2.9 introduced the possibility that earlier poor results from tests of CG1 may have been an exception rather than the norm. Since a reduced water content was used for this new batch of CG1, another possibility for previous poor performance was the effect of excess water within the microstructure. In later tests discussed in the next section, it was observed that this is not the case.

CG2 and CG3 also showed similar resistance to freeze and thaw as that of CG1. Figures 2.10a and 2.10b show the results from tests of CG2 and CG3, respectively. Apart from a single specimen showing a slight dip in E/E_0 for CG2, all of the other specimens retained 100%

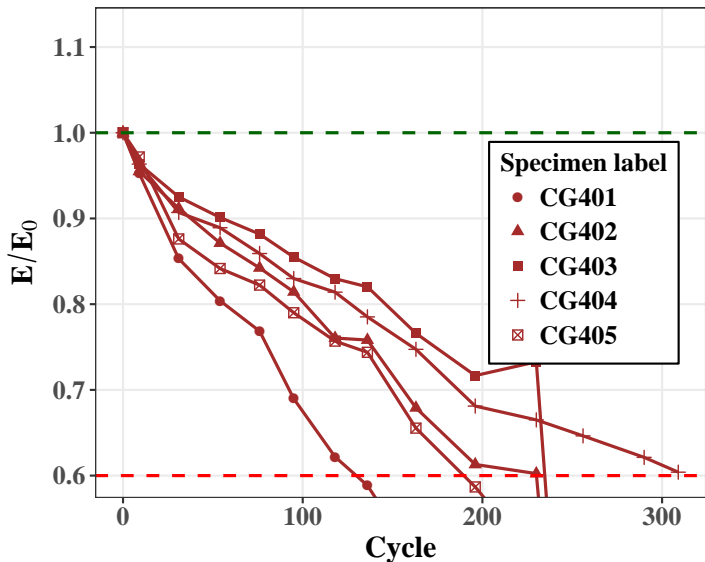


(a)

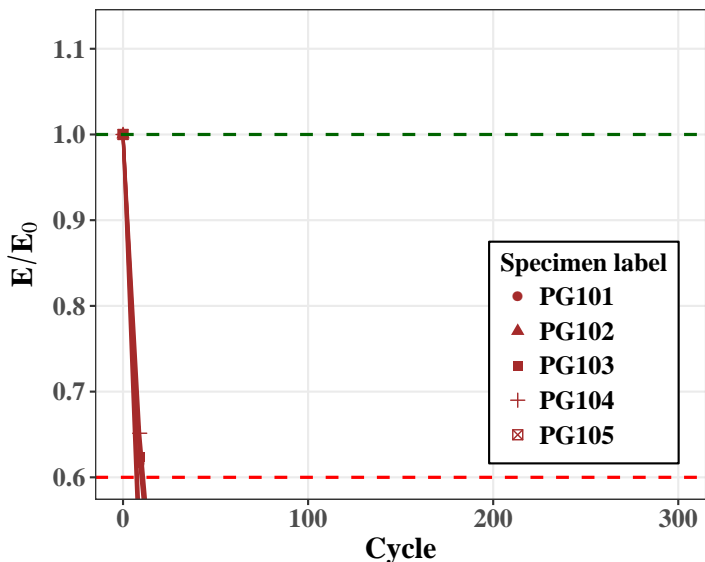


(b)

Figure 2.10 Results from ASTM C666 FT tests on multiple commercial grout materials (Good performance).: (a) Grout: CG2, Water per bag: 8.4 lbs., (b) Grout: CG3, Water per bag: 6.6 lbs.



(a)



(b)

Figure 2.11 Results from ASTM C666 FT tests on multiple commercial grout materials (Poor performance).: (a) Grout: CG4, Water per bag: 9.3 lbs., (b) Grout: PG1, w/c ratio: 0.46.

of their initial elastic modulus throughout the 300 cycles. It was concluded that grouts CG1, CG2 and CG3 show good FT resistance and were selected to proceed to the next phase of durability tests. Questions still remained concerning the poor results obtained for CG1 in the exploratory study which were addressed by two more FT tests that were performed on CG1. These are discussed in the next section.

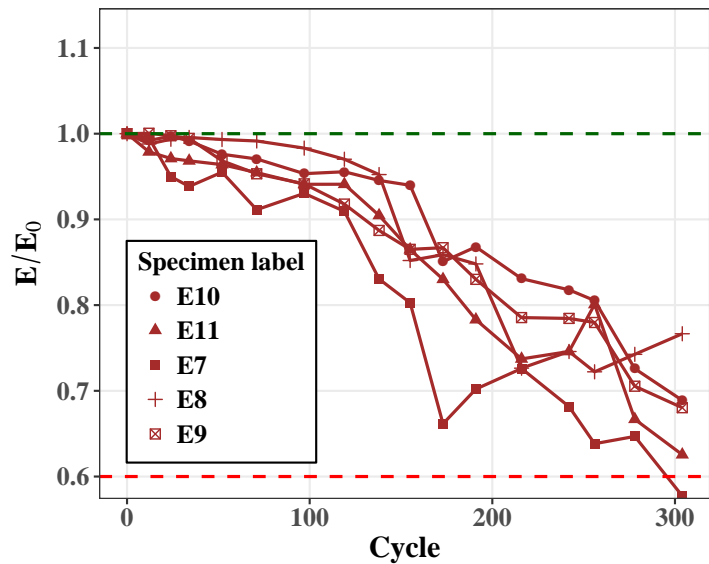
Not all the materials that were tested showed good performance. For example, in CG4 (Figure 2.11a), there is significant reduction in E/E_0 over time. CG4 is hence more prone to damage due to FT cycles. Figure 2.11b shows the results for PG1. All specimens of PG1 failed consistently within the first 10 cycles of freeze and thaw. Behavior of PG1, flowable pea-gravel concrete, merits some discussion. The water-cementitious ratio for this concrete was 0.46. According to the Powers' model [Pow60; PB46], a w/c ratio of 0.42 results in all the water being consumed for the hydration reaction. This implies that a w/c ratio of 0.46 would leave excess water within the microstructure forming capillary pores. In addition, the cementitious particles that contributed to the water-cementitious ratio included fly ash, which is pozzolanic in nature and only contributes to the strength of the microstructure in the long term. Hence, the effective early w/c ratio would have been some value higher than 0.46 resulting in larger a amount of water filled pores. This may have resulted in early attainment of the critical degree of saturation of the material. Although a 6% air content was specified within the mixture, the mixing may not have achieved good dispersion of air. A combination of all of the above could have caused the extremely poor results that were observed. Nevertheless, it was decided not to pursue further inquiry into pea-gravel concrete.

2.4.4 Closure to Freeze and Thaw testing

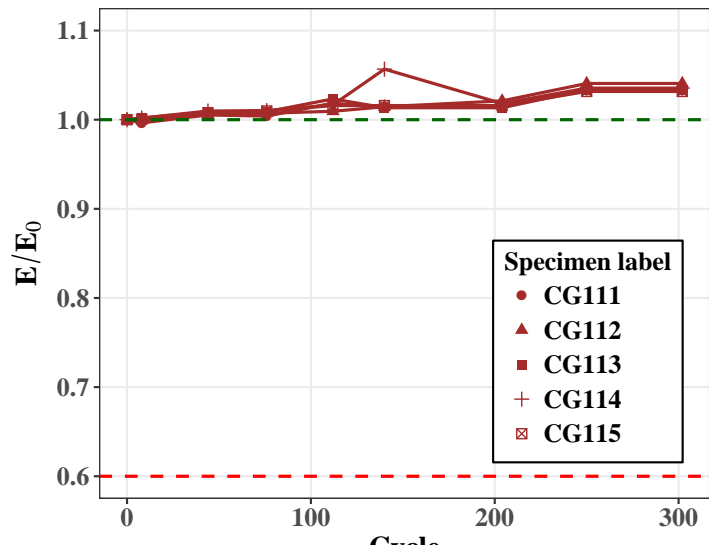
Insofar as the results of the ASTM C666 tests on multiple grout materials are concerned, CG1, CG2, and CG3 showed good FT resistance. However, results from exploratory investigations on CG1 had shown some poor results that still needed to be addressed. Two more FT tests on CG1 were planned to provide some closure on this issue. The two new batches of CG1 specimens were:

1. CG1 with 9 lbs. of water per bag mixed in the old mixer (the same mixer used in the exploratory study), cast, and cured under saturated lime water for 14 days. This batch was chosen to isolate the effect of mixing on the performance of FT specimens. Specimens in the exploratory study where mixed using the same mixer and had yielded poor results.
2. CG1 with 8.5 lbs. of water per bag mixed in a new mixer, cast, and cured in sealed plastic bags for 14 days. This batch was chosen to isolate the effect of sealed curing on the performance of FT specimens. In the exploratory study, sealed cured specimens had performed poorly.

Results of both tests are shown in Figures 2.12 and 2.13. For the first batch of CG1 (Figure 2.12b) with 9.0 lbs. of water mixed with the old mixer the specimens are consistently at a 100% or above the initial elastic modulus. This is different from the CG1 specimens tested in the exploratory study mixed with the same amount of water (Figure 2.12a). The results are exactly as the CG1 specimens with 8.5 lbs. water discussed in the previous section. An increase in the amount of water did not seem to affect the results in these specimens. Hence, it was concluded that the poor results obtained for CG1 during the exploratory

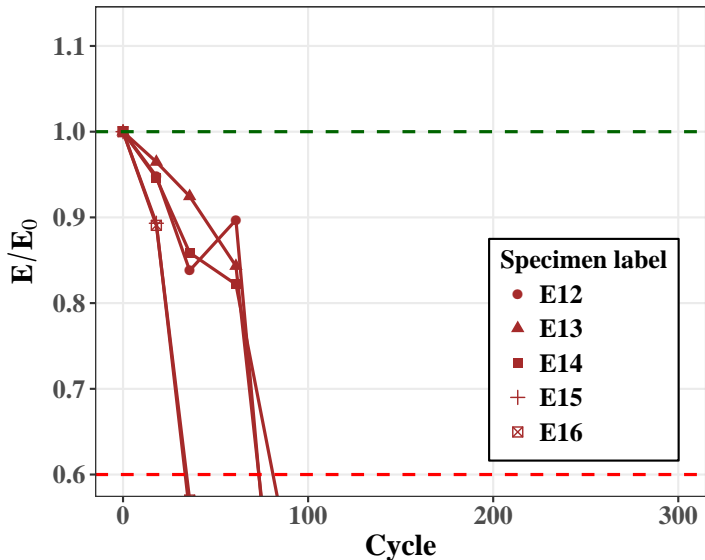


(a)

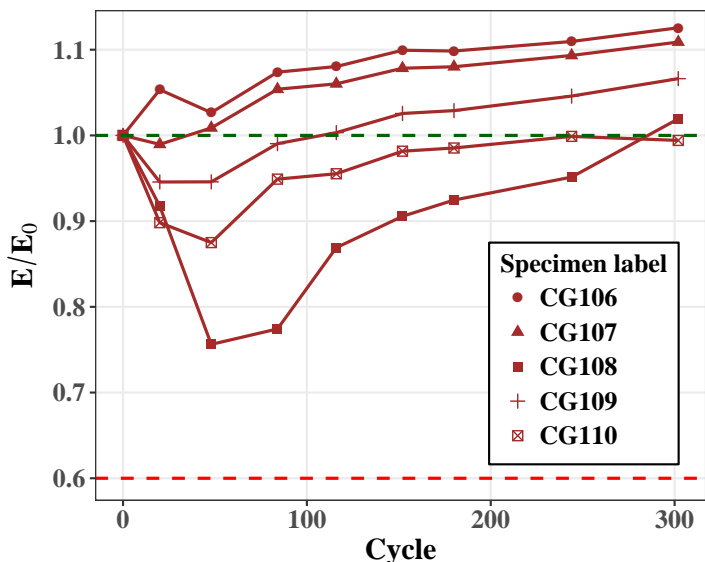


(b)

Figure 2.12 A comparison of results of the exploratory study performed on CG1 with 9 lbs. water per bag, and cured under water to the results of the same when repeated: (a) Exploratory (b) Repeat.



(a)



(b)

Figure 2.13 A comparison of results of the exploratory study performed on CG1 with 8.5 lbs. water per bag, and cured under sealed conditions to the results of the same when repeated:
 (a) Exploratory (b) Repeat.

study could have been either due to a poor quality batch of grout or due to inexperienced labor or both.

For the CG1 specimens that were sealed cured (Figure 2.13b), an initial drop in E/E_0 was observed. Note that the amount of water in these specimens was 8.5 lbs. per bag, the same as that for specimens which showed good FT resistance when cured under water. After the initial drop, the curves showed a reversal in direction. They reached the same value or even exceeded the initial elastic modulus before any FT cycling. Delayed hydration of the material could be one reason for such behavior. This hypothesis is strengthened by the curves exceeding the initial values of elastic moduli. Further studies are required to ascertain the true mechanism. For the purposes of GSS connection durability, this observation does not pose a serious issue because within the early period that the grout hydration progresses, a GSS connection in practice would see few FT cycles.

To summarize, as part of the study on FT resistance of cementitious grouts, multiple commercial grouts were tested according to ASTM C666 Procedure A. A comparison of results from these tests yields that some commercial grouts show good resistance to frost damage while others do not. Hence, it is important for engineers to choose the grout filler for the GSS connection with caution. Even a good choice of grout does not guarantee long service life with respect to FT resistance.

2.5 Shrinkage Cracking in Cementitious Grouts

2.5.1 Introduction

Portland cement-based materials undergo volume change as a result of the hydration process and consequent loss of moisture. This is called shrinkage. When allowed to shrink freely with no external restraint, no stresses develop within the material. However, concrete or grout materials are commonly restrained against free shrinkage. This restraint causes stress development in the material. If these stresses exceed the tensile strength of the material, cracking ensues. The potential for cracking depends on the magnitude of these stresses and the tensile strength of the material.

The shrinkage characteristics of the grout are important in the overall performance of the GSS connection because the force transfer occurs through multiple mechanisms dependent on the grout. The size and shape of the annular grouted zone, as well as the restraint provided by the inner steel pipe, play a role in the long-term performance of the GSS connection.

The standard test to determine the cracking age and the induced tensile stress under restrained shrinkage is ASTM C1581-18a [Astc] which is also known as the “restrained ring test” or simply the “ring test”. The core aim of the test is to determine the early age cracking tendency of concrete. The concrete material is cast as an annular ring around a circular steel ring. Due to shrinkage of the concrete ring, the imposed strain on the inside steel ring is measured as a function of time. When a crack forms, the tensile stress in the grout is released and a sudden reduction in the compressive strain in the steel ring is observed. The steel strain can be used as an indicator of the risk of cracking. When comparing different

materials, the earlier a material cracks, the higher is its cracking potential. Similarly, the higher the rate of strain development for a material, the sooner the material will crack. It should be noted that the ring test does not measure a fundamental material property. It rather measures the response of the material to a stimulus under a specific boundary condition. This means that if the boundary conditions (e.g., degree of restraint, drying rate, surface-to-volume ratio) change, the results of the test will also change.

2.5.2 A Literature Review of the Ring Test

In general, the ring test only provides the time to cracking and the steel strain at cracking. However, methods to obtain more information from the test results have been developed. Hossain & Weiss [HW04], obtained stresses in concrete from the measured steel strain and geometric properties of the ring. For this purpose, they used specimens with a sealed circumferential surface, allowing drying only from the top and bottom surface of the concrete ring. Top and bottom drying results in a simpler stress profile which simplifies the analytical calculations. Calculating the residual stress provides an estimate of the cracking potential for materials that do not crack during the test, by comparing the maximum residual stress developed to the tensile strength of the material. Hossain and Weiss also formulated an expression for the degree of restraint (Ψ) for a test specimen based on the elastic modulus, test geometry, and Poisson's ratio of the materials.

Hossain & Weiss [HW06] discussed the effects of specimen geometry and boundary conditions on stress development and cracking in the ring test. When allowed to shrink freely, specimens with larger drying surface to volume ratio had a higher shrinkage strain. Larger shrinkage strains arise because more water can leave the material during a certain

period of time.

In addition to top and bottom drying, a different exposure condition that has been studied is circumferential drying. In circumferential drying, the crack initiates from the outer circumference and propagates inward. This behavior is opposite to what is observed in specimens with top and bottom drying. The reason for the inward propagation of cracking in circumferential drying is the development of a complex stress profile as shown in Figure 2.14. Because of this complex stress profile, conventional stress analysis does not yield results for this boundary condition, and the need for a different approach was recognized. The degree of restraint also has a significant role on the cracking age. Rings with smaller degrees of restraint (thinner steel wall) cause concrete cracking at later times as compared to thicker steel rings.

Moon et al. [Moo06] quantified the influence of specimen geometry on the results of the ring test with the goal of tailoring the ring geometry for specific applications. They studied three different drying conditions:

1. Uniform shrinkage of the concrete ring (completely sealed specimens),
2. Shrinkage caused by top and bottom drying, and
3. Shrinkage caused by circumferential drying.

The role of moisture gradients, thickness of the concrete and the restraining rings, and the stiffness of concrete were considered in a series of numerical simulations. A direct result of this study was an expression in terms of the geometry of the test specimen, Equation 2.5, to check if it satisfied a given criterion which would yield good results for calculating the residual stress:

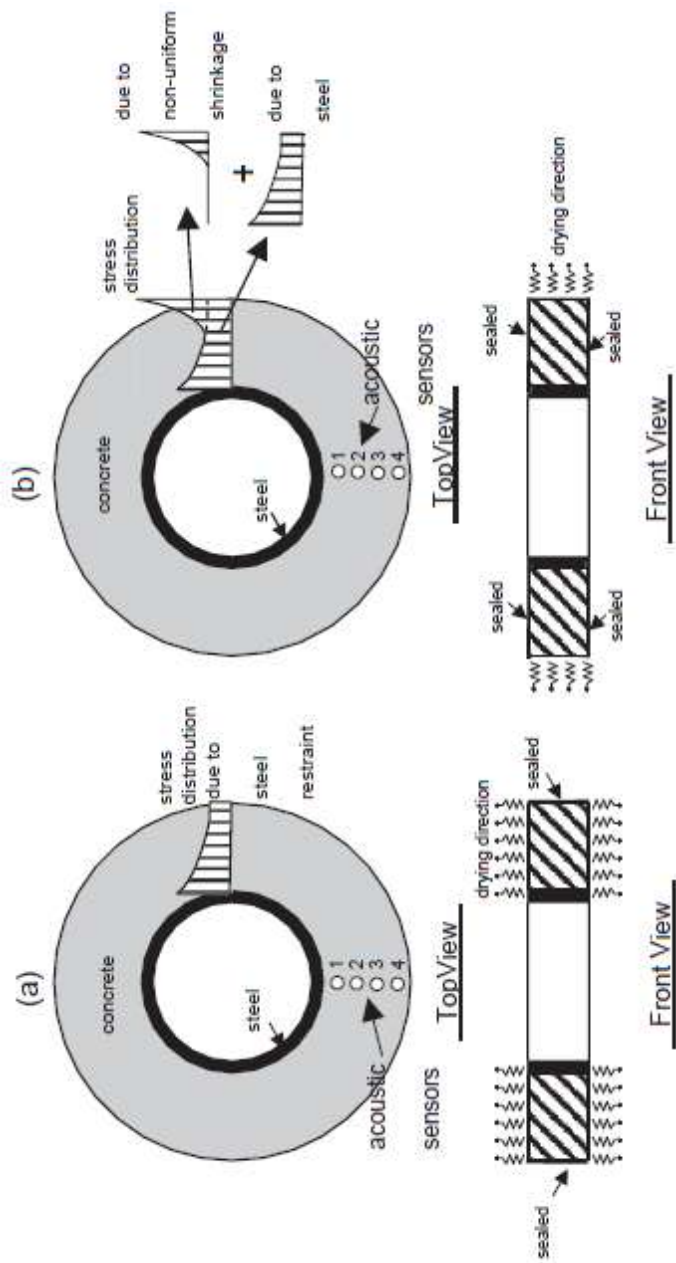


Figure 2.14 Restrained ring specimens: (a) top and bottom drying, and (b) circumferential drying, and their corresponding stress profiles as shown in Hossain & Weiss [HW06]

$$\frac{\epsilon_{st}(t)}{\epsilon_{SH}(t)} = \frac{E'_c}{E_s} \frac{2}{1 - \left(\frac{R_{IS}}{R_{OS}}\right)^2} \frac{1}{\frac{E'_c}{E_s} \left[(1 + \nu_s) \left(\frac{R_{IS}}{R_{OS}} \right)^2 + (1 - \nu_s) \right] - \left[(1 + \nu_c) \left(\frac{R_{OC}}{R_{OS}} \right)^2 + (1 - \nu_c) \right]} \quad (2.5)$$

where ϵ_{st} = measured steel strain on the inner surface,

ϵ_{SH} = free shrinkage strain of the concrete,

E'_c = effective elastic modulus of concrete (considering the creep effect),

E_s = elastic modulus of steel,

R_{IS} = inside radius of the steel ring,

R_{OS} = outside radius of the steel ring,

R_{OC} = outside radius of the concrete ring,

ν_s = Poisson's ratio of steel,

ν_c = Poisson's ratio of concrete.

The stipulated criterion was that $\frac{\epsilon_{st}}{\epsilon_{SH}}$ should be greater than 0.125 for a specific test set up to achieve good results. This result is followed by the expression for the degree of restraint (Ψ) shown in Equation 2.6.

$$\Psi = 1 - \frac{E'_c}{E_s} \frac{1}{\frac{E'_c}{E_s} - \frac{1 - \left(\frac{R_{IS}}{R_{OS}}\right)^2 \left[(1 + \nu_c) \left(\frac{R_{OC}}{R_{OS}} \right)^2 + (1 - \nu_c) \right]}{1 - \left(\frac{R_{OC}}{R_{OS}}\right)^2 \left[(1 + \nu_s) \left(\frac{R_{IS}}{R_{OS}} \right)^2 + (1 - \nu_s) \right]}} \quad (2.6)$$

Moon & Weiss [MW06] followed this study to try to analytically formulate an expression for the complex stress profile developed along the thickness of the concrete ring during circumferential drying. They superimposed the stress due to the external ring restraint ($\sigma_{\theta\theta,rest-ring}$) and the stress due to the self-restraint from differential shrinkage ($\sigma_{\theta\theta,diff-shr}$). These stress contributions were formulated separately and then superimposed to give the overall stress ($\sigma_{\theta\theta}$) at any point in the concrete ring,

$$\sigma_{\theta\theta}(r, \gamma) = \sigma_{\theta\theta,rest-ring} + \sigma_{\theta\theta,diff-shr} \quad (2.7)$$

$$\begin{aligned} \sigma_{\theta\theta}(r, \gamma) = & -\epsilon_{steel}(t) \cdot E_s \cdot \frac{R_{OS}^2 - R_{IS}^2}{2(R_{OC}^2 - R_{OS}^2)} \left(1 + \frac{R_{OC}^2}{r^2} \right) \\ & + \frac{\epsilon_{SH-const} E_c}{r^2} \left[\frac{r^2 + R_{IC}^2}{R_{OC}^2 - R_{IC}^2} \cdot (f(R_{OC}) - f(R_{IC})) + f(r) - f(R_{IC}) - erfc(A) \cdot r^2 \right] \end{aligned} \quad (2.8)$$

where

$$f(r) = \gamma^2 \cdot \left[\frac{1}{2} erfc(A) \cdot A^2 + erfc(A) \cdot \frac{R_{OC}}{\gamma} \cdot A + \frac{2}{\sqrt{\pi}} \left(\frac{-A}{4e^{A^2}} + \frac{\sqrt{\pi} \cdot erfc(A)}{8} + \frac{R_{OC}}{2e^{A^2}\gamma} \right) \right] \quad (2.9)$$

r = the radial distance of the point from outer surface, $erfc$ is the complementary error function, A and γ are constants defined as,

$$A = \frac{(R_{OC} - r)}{\gamma} \quad (2.10)$$

$$\gamma = 2\sqrt{Dt} \quad (2.11)$$

where D is the aging moisture diffusion coefficient of concrete and t is the drying time. This expression makes it possible to calculate the cracking potential of a material under non-uniform drying.

2.6 Restrained Ring Test on Cementitious Grouts

To investigate shrinkage cracking potential in this study, the same cross sectional geometry of the GSS connection was used rather than the size specified by ASTM C1581. The degree of restraint of the ASTM C1581 ring is 72.5% while that of the GSS connection is only 64%. It is important to model the degree of restraint in determining the shrinkage cracking potential. The complete test matrix for the restrained ring test is given in Table 2.6. Three grout materials that performed well in FT tests CG1, CG2, and CG3 were used in the first six ring tests. Each material was subjected to both circumferential drying and sealed (no drying) conditions. The schematic in Figure 2.15 shows the two different drying conditions that the specimens were subjected to. In circumferential drying, the grout ring 3.5" thick, is cast around a 6" tall steel ring of 16" diameter and 0.5" wall thickness, with the top and bottom sealed. To eliminate friction, the grout is separated from the steel ring by an acetate sheet oiled on both sides. The outside surface of the grout ring is exposed to the environment which is controlled at 23°C and 50% relative humidity (RH). Four strain gages are placed on the inside of the steel rings around 90°, apart. For specimens under sealed or no drying conditions, the only difference in the setup to that of circumferential

drying specimens is that their outer surface is no longer exposed. An outer steel ring covers the grout ring rendering the specimens fully sealed. Again, acetate sheet and oil layers separate the outer ring from the grout. Note that this outer ring does not influence any other characteristics of the test setup. Three specimens of each material (CG1, CG2 and CG3) were tested. The rings were placed inside an environmental chamber for temperature and humidity control. Figure 2.16 shows a photograph of a sample test setup. The rings in the figure are under circumferential drying conditions.

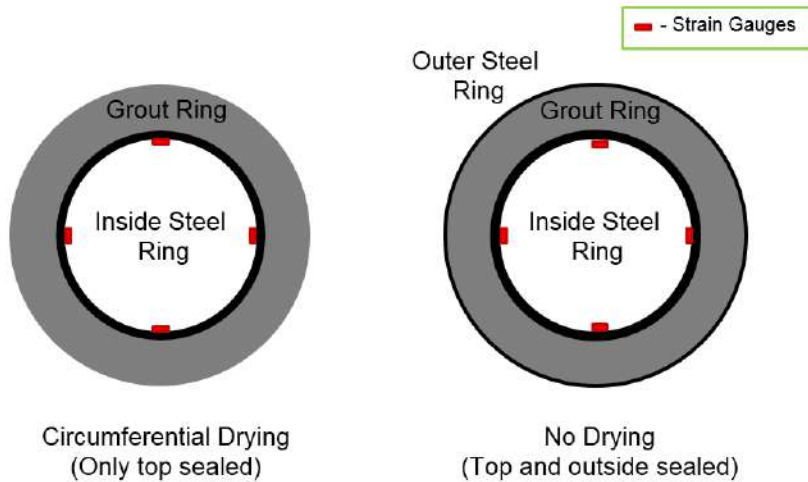


Figure 2.15 Restrained ring test specimen cross section schematic: Circumferential drying specimen (Left) and sealed specimen (Right).

Figures 2.17, 2.18, and 2.19 show the results for the first six ring tests. It is divided into two columns and three rows based on the two drying conditions and three grout materials. The sub-figures have time in days on the x-axis. This is the elapsed time from the moment of casting the material. Strain readings averaged over all of the strain gages on one specimen are given on the y-axis. The readings are in micro-strain ($\mu\epsilon$) units. The negative val-

Table 2.6 Test matrix and results for restrained shrinkage ring tests

Test No.	Material	Number of specimens	Drying Condition ¹	Shear Studs	Avg. age of cracking (days)	Avg. crack width (mm)	Avg. steel strain at cracking ($\mu\epsilon$)
1	CG1	3	CD	No	3.2	1.70	28
2	CG2	3	CD	No	6	1.00	23
3	CG3	3	CD	No	5.9	1.08	38
4	CG1	3	ND	No	9.5	0.40	68
5	CG2	3	ND	No	15.3	0.30	40
6	CG3	3	ND	No	N/A	N/A	N/A
7	CG1	2	ND	24-3/4" dia.	7.5	0.10	139
8	CG1	2	ND	8-1" dia.	9.9	0.10	134

¹ CD - Circumferential Drying; ND - Sealed (No Drying)



Figure 2.16 Restrained ring test specimens under circumferential drying conditions in the environmental chamber.

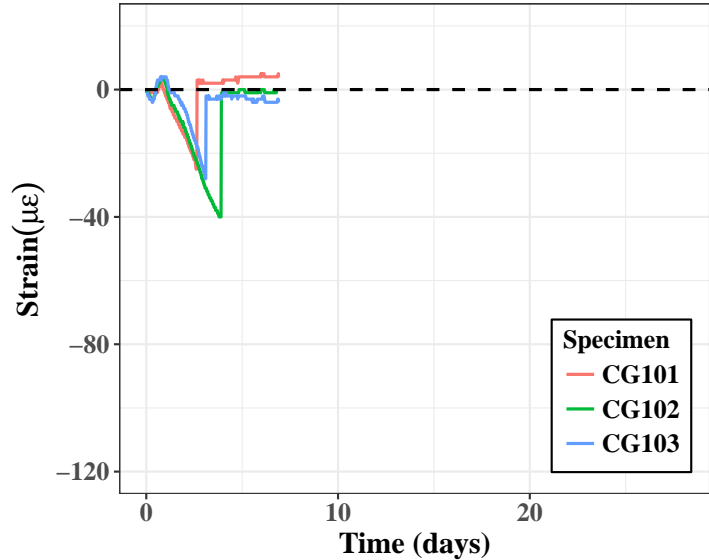
ues of strain indicate compression on the inside ring. As time progresses from casting, the strains increase until the point where the grout material cracks. The formation of a crack plane is accompanied by a release of stress which manifests itself in the figures as an instantaneous decrease in steel strain level. It is clear that the circumferential drying condition (left) is more severe than no drying (right). All the materials crack earlier under circumferential drying conditions compared to no drying. This matches expectations since the stress development inside the material due to restrained shrinkage is proportional to the amount of drying which in turn is proportional to the exposed surface-to-volume ratio of

the specimen. Since no surface is exposed for drying in the case of sealed conditions, the stress development is slower.

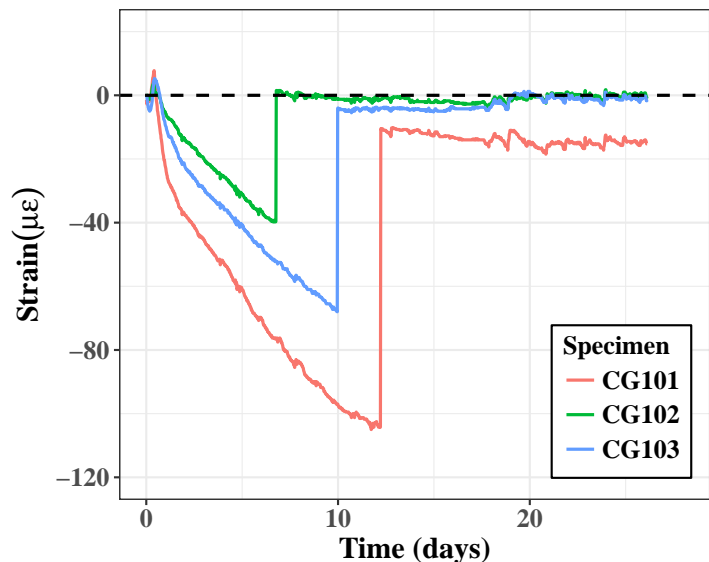
However, most of the specimens under no drying still crack, but at a later time. All specimens of CG1 and two specimens of CG2 cracked under no drying. None of the specimens of CG3 cracked. In comparison therefore, CG3 performed better than the other two, while CG1 had the highest potential for cracking. The strain at cracking is also an indicator of cracking potential. CG1 has a higher strain accumulation rate and also cracks at strains much higher than the other two. Since CG1 specimens accumulated high strains even under no drying conditions, it may be concluded that the autogenous shrinkage component is high for CG1. Autogenous shrinkage is the component of shrinkage that occurs without any exposure to the environment [MM17]. This happens within the grout microstructure as a result of the hydration reaction of cement. Autogenous shrinkage is comparatively lower for CG2 and CG3.

Along with age of cracking and the steel strain at cracking, the crack width of each specimen at 10 days post cracking was also measured. The crack widths are of interest since wider cracks facilitate more ingress of water and chemicals and can have more deleterious effects. For circumferential drying conditions, the crack widths were large for all three materials. CG1 had the highest crack width of 1.70 mm. When tested under no drying, the crack widths reduced drastically. This is reassuring since the connection geometry of the GSS connection results in conditions closer to no drying. Resulting data of average age of cracking, average crack width and average steel strain at cracking have been tabulated in Table 2.6.

It must be noted that the results obtained are only indicative of the cracking poten-

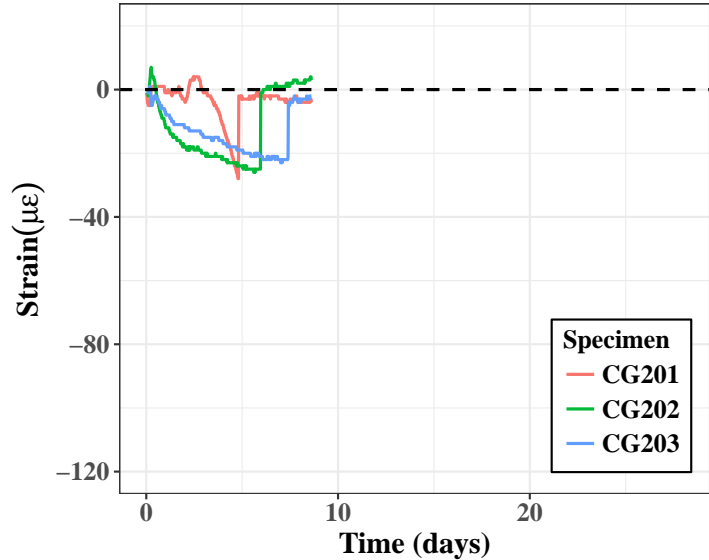


(a)

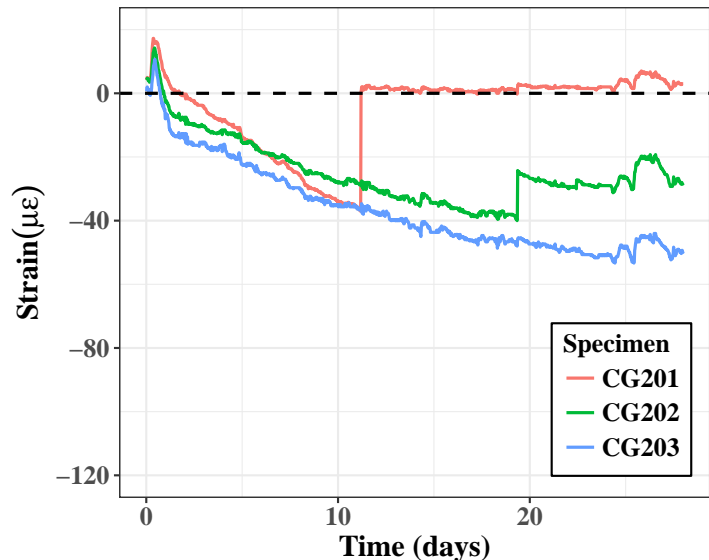


(b)

Figure 2.17 Results from restrained ring tests on CG1 under two different drying conditions: Circumferential drying (Left) and Sealed (Right) conditions.

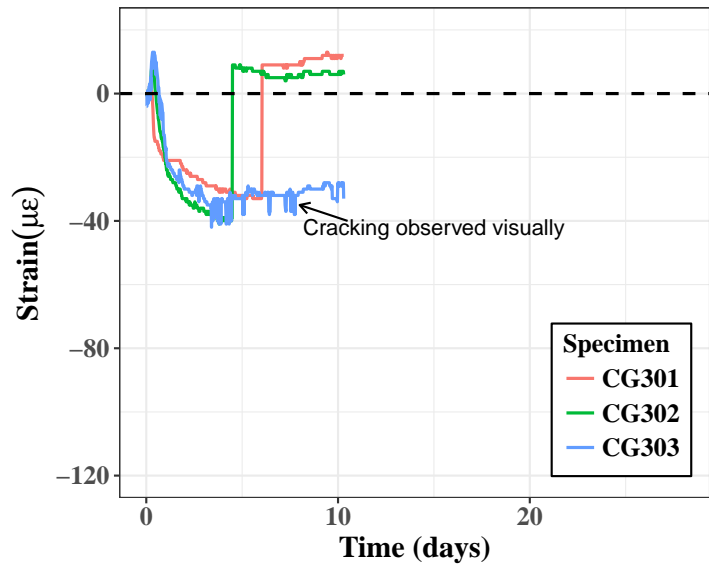


(a)

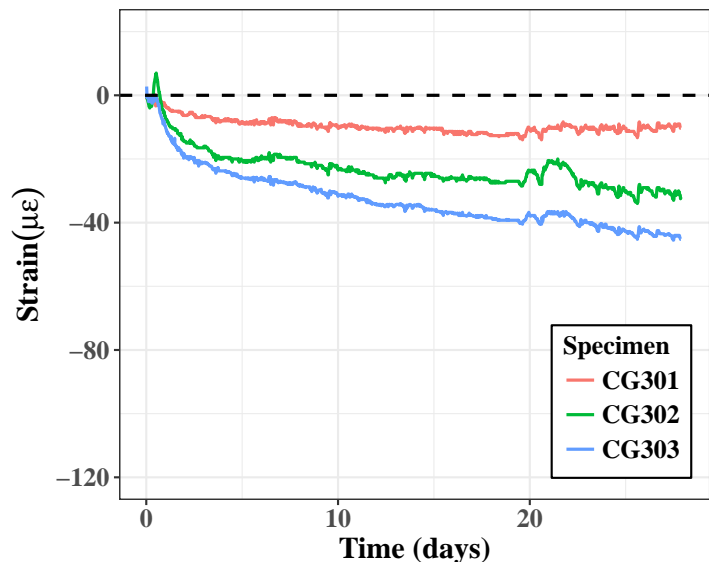


(b)

Figure 2.18 Results from restrained ring tests on CG2 under two different drying conditions: Circumferential drying (Left) and Sealed (Right) conditions.



(a)



(b)

Figure 2.19 Results from restrained ring tests tests on CG3 under two different drying conditions: Circumferential drying (Left) and Sealed (Right) conditions.

tial for the degree of restraint provided by the boundary conditions in the geometry used for these tests. This degree of restraint is 0.64 using Equation 2.6. In practice, the bridge columns making use of the GSS connection would have different degrees of restraint. One way to extrapolate results such as those obtained herein to practice is to use figures that plot degree of restraint versus the column radius, for given outer diameter to inner diameter ratios of the GSS connection. An example of such a figure is shown in Figure 2.20. The lines are calculated using Equation 2.6 for different input geometric parameters. Different lines indicate different column thicknesses. The dotted line shows the degree of restraint corresponding to the tests discussed here. Any degree of restraint below the dotted line can be understood to be less severe than that used for the ring tests in this study. This can be made use of when making decisions regarding the connection geometry for an actual bridge connection. For example, all the results obtained in this study are valid for a degree of restraint of 0.64 or higher. In practice therefore, any combination of column diameter and wall thickness that equals to a degree of restraint less than 0.64 will result in lesser grout cracking potential.

The next tests in the series of ring tests were done to identify the effect of shear studs on cracking potential. Grout material CG1 was chosen to perform these tests as it performed poorest among the three that were tested previously. Even under no drying condition, all specimens of CG1 cracked with an average crack width of 0.40 mm. Upon discussion with personnel from Alaska Department of Transportation and Public Facilities (AKDOT), it was learned that a crack width of 0.30 mm is an acceptable upper bound because it can be repaired by epoxy injection. The presence of shear studs within the grout produces two opposing effects with respect to cracking potential of the grout. Shear studs increase the

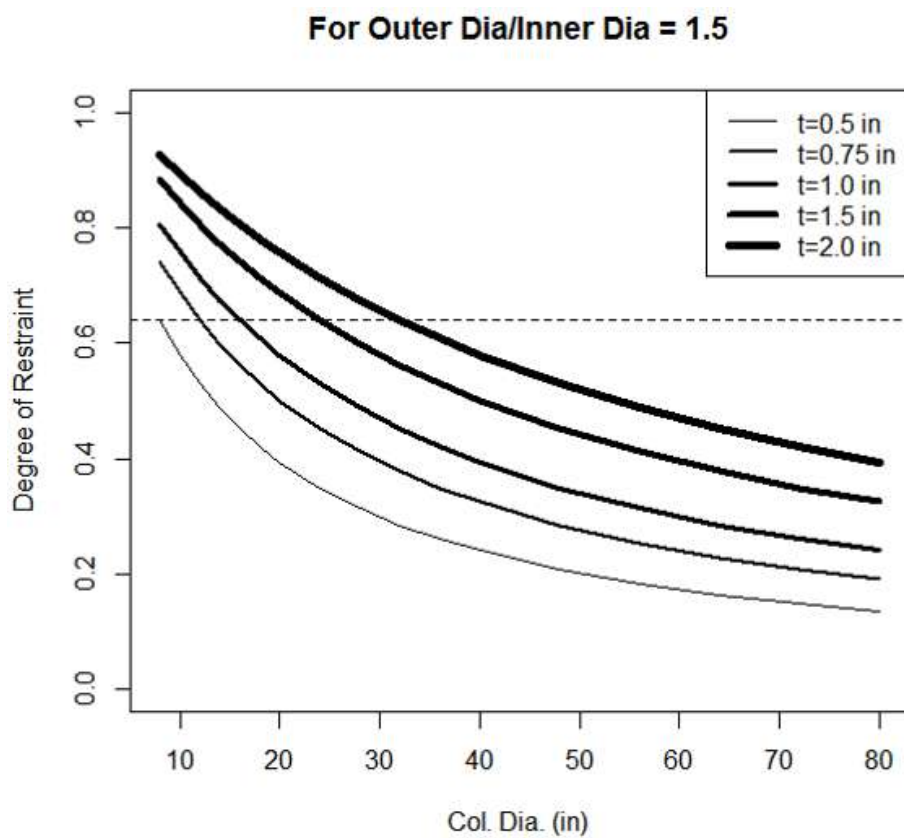


Figure 2.20 Degrees of restraint plotted against column diameter for a GSS connection outer-to-inner diameter ratio of 1.5.

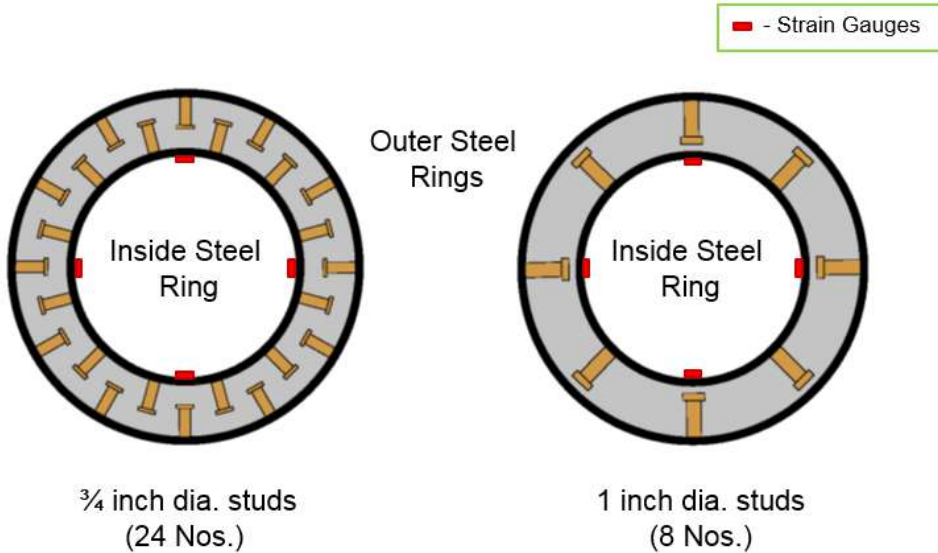
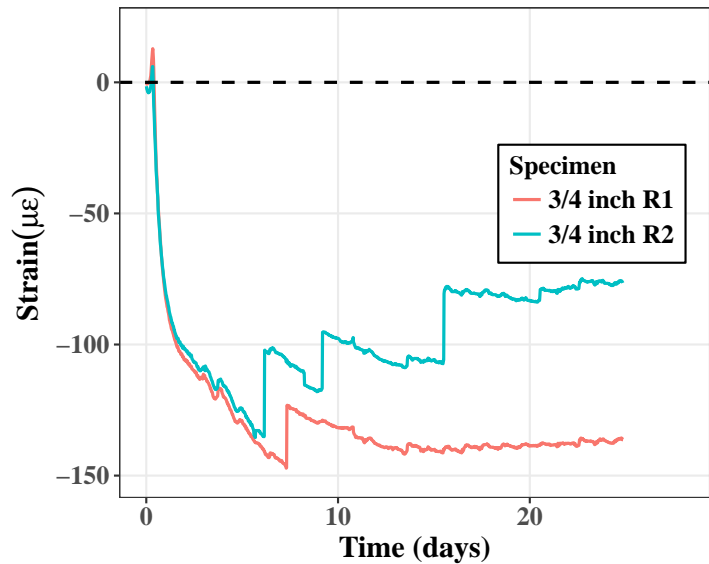


Figure 2.21 Restrained ring test specimen cross section schematic: 3/4" dia. shear studs (Left) and 1" dia. shear studs (Right).

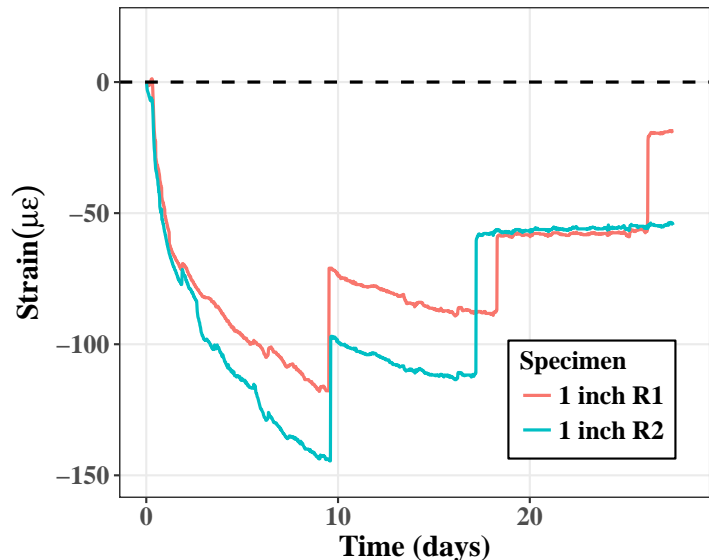
degree of restraint thereby hastening cracking, but simultaneously can create redundant load paths to distribute the cracking thereby reducing crack widths.

Two tests were planned to investigate the effect of shear studs. Each test was performed under no drying conditions with shear studs of different sizes. The first test (Test 7 in Table 2.6) had 24 shear studs of 3/4" diameter within the grout ring, while the second test (Test 8 in Table 2.6) had 8 shear studs of 1" diameter. The cross section schematic of both tests is shown in Figure 2.21. Strain gages were attached on the inside of the steel rings in the regions in between the welded studs. The presence of shear studs likely creates a non-uniform distribution of stress (and hence strain) in the steel ring, but it is thought that an average over all strain gages may still provide meaningful results.

Specimens with both 3/4" diameter and 1" diameter studs show a release of strain at an average of 7.5 days and 9.9 days, respectively. However, this observation did not corre-



(a)



(b)

Figure 2.22 Results from ring tests performed on specimens with shear studs: (a) 3/4" dia. shear studs (b) 1" dia. shear studs.

spond to visual cracking on the top surface. Since the release of strain was not to zero, it can be concluded that the shear studs contribute to resistance to cracking. Cracks started to appear on the surface not long after the first instance of stress drop. Instead of a single crack that was observed in earlier tests without shear studs, multiple cracks formed when shear studs were present. Moreover, these cracks were smaller compared to the wide single cracks observed earlier. This observation led to the conclusion that the shear studs play an important role in reducing crack widths. Further research is required to quantify the effect of shear studs on shrinkage cracking. A detailed investigation of this mechanism is beyond the scope of this study.

Among the tests that were conducted under sealed/no drying conditions, the results follow an expected trend. The ring specimens with the most number of shear studs (24) cracked the earliest. This result is due to the highest degree of restraint among the three different types of specimen. The rings with the second highest degree of restraint cracked later and those with the lowest degree of restraint among the three cracked last. A separate observation is that the rings with 24 shear studs cracked at relatively higher stresses in the grout. This can be an indication of the contribution of shear studs to the tensile strength of the ring. More tests are needed to confirm this hypothesis.

In summary, the ring tests to investigate early age cracking potential of multiple commercial grouts yielded the following results:

1. All tested grout materials cracked early under circumferential drying conditions.
2. Sealing the specimens delayed cracking in two materials (CG1 and CG2) and eliminated cracking in one (CG3). Sealing also reduced the crack widths.

3. Presence of shear studs (as in the GSS connection) helps reduce the cracking potential of grouts. Shear studs distribute the cracks and reduce crack widths by providing redundant paths for stress redistribution.

2.7 Chapter Summary, Recommendations, and Concluding Remarks

2.7.1 Chapter Summary

Previous studies have used cementitious grout to fill the annular space in the GSS connection. The grout serves an important function of force transfer for the satisfactory performance of the GSS connection. Our primary objective was to determine the long term durability of grout in the GSS connection. Cementitious grouts from four different manufacturers, all meeting AKDOT requirements, were chosen to assess their strength and durability characteristics. All four grouts developed high early age strength compared to normal concrete, some having much higher strength than the others.

Durability here means the potential of the grout material in the GSS connection, to provide a long service life in extreme cold climates. Two major durability concerns in this study were cracking due to freeze and thaw cycles, and cracking due to early age restrained shrinkage. Freeze and thaw cracking occurs due to cyclic expansion and accumulation of water in the grout microstructure causing internal stresses. Upon testing the freeze thaw resistance of the chosen grouts, some grouts are durable and some are not. Hence, one must choose grout for cold climate applications with caution. Early age shrinkage is an inherent

characteristic of cementitious materials. Under restrained conditions such as those in the GSS connection, tensile stresses are developed as a result of shrinkage and lead to cracking. All the grouts chosen for restrained ring tests cracked within the first few days after casting. This means that the geometry of the GSS connection provides a high enough restraint to crack high-strength grouts. However, when shear studs were added in the rings, the cracking was delayed and upon cracking, the grout rings formed multiple cracks of smaller widths. This result is, of course desirable. Hence, in addition to the structural requirement, shear studs serve a secondary function of distributing shrinkage cracks and reducing crack widths.

2.7.2 Recommendations

The following are suggestions for choosing and mixing cementitious grouts for applications in cold climates. Note that these recommendations are qualitative, based on observations during experimental testing of a set of different cementitious grouts.

2.7.2.1 Choosing a durable grout

Durability tests, especially those pertaining to cold climatic environmental conditions, are time consuming and require a significant amount of work. ASTM C666 Procedure A is a good testing standard to compare the freeze-thaw resistance of available grouts. It is recommended to choose grouts that meet a Durability Factor (DF) of at least 95% measured according to ASTM C666 Procedure A.

2.7.2.2 Mixing grout

It is worth re-emphasizing the importance of water in both strength and durability characteristics of cementitious grouts. The use of the minimum manufacturer specified water content per bag of grout for flowable consistency, is recommended. Good grout products generally have different specified water contents per bag for different consistencies such as plastic, flowable, or fluid. Note that each consistency label will give different strength and durability characteristics.

It was found that grout durability is largely independent of the mixing process. However, grout consistency (flowability) is dependent on the mixing process. For example, mixing a large amount of grout in a drum mixer provides better consistency than mixing smaller amounts in the same mixer, provided the time of mixing remains the same. This improved consistency results from larger amounts of grout revolving in a drum mixer, which provides more weight of grout to fall on top of itself, facilitating better mixing. Grout consistency can also vary based upon mixer type. When the same amount of grout was mixed in a drum mixer and with a screw mixer, the screw mixer took less time to reach the same level of consistency than the drum mixer. This result may be because of the higher shear rate of the screw mixer, compared the slow process of gravity aided mixing in a drum mixer. However, given enough time, both processes can achieve the same level of consistency. Therefore, it is important that the contractor is aware of this dependence so as to prevent the addition of excess water to increase flowability. It is recommended to be cautious of the setting times of the grout being used. Use grouts that have longer setting times is encouraged for better workability.

2.7.3 Concluding Remarks

Through a series of durability tests on commercially available cementitious grouts, it was found that some grouts are good while some are bad for use in the GSS connection in cold climates. A simple method to separate good ones from the bad ones does not exist. Developing such a method requires further studies. However, before proceeding in this direction, it is worth going back to the main objective of this project which is to answer the question: *Can the GSS connection be used in cold climates with no loss in the structural integrity of the lateral load resisting system?* Therefore, as the next step, it was necessary to consider the second part of the question: *How much impact does grout deterioration have on the consequent structural performance of the lateral load resisting system?* Phase 2 of the project, discussed in Chapter 4, answers this question.

CHAPTER

3

SIMULATING GROUT DETERIORATION FOR LARGE SCALE TESTS

3.1 Introduction

Years of exposure to a cold and wet climate tend to reduce the structural properties, such as compressive strength (f'_c) and elastic modulus (E) of cementitious grouts. Simulating this reduction in grout properties to effectively represent the long-term damage state of grout

was essential to define the levels of deterioration (LoD) for the large scale tests. Ideally, physical damage simulation must be achieved by subjecting the specimens to multiple accelerated freeze-thaw cycles. However, this is difficult to achieve for specimens that are of the scale to be tested.

Alternate methods of reproducing damaged states of grout were explored. Ravindrarahajah & Tuck [RT94] investigated properties of hardened concrete containing aggregates called expanded polystyrene (EPS). EPS is a stable low density foam and consists of discrete air voids in a polymer matrix [RT94]. They found that the water-cement (w/c) ratio is an important factor upon which the compressive strength of EPS concrete is dependent. They also provided an empirical expression (Equation 3.1) to calculate the static elastic modulus of EPS concrete, when the density (D), and cylinder strength (f'_c) are known.

$$E = 1.146D^{1.1} \sqrt{f'_c} \quad (3.1)$$

EPS has been used as ultra lightweight aggregate suitable for developing concretes for both structural and non-structural applications, by varying its volume percentage in mortar or concrete [BFY76; Per91]. Babu et al. [Bab05] and Babu et al. [Bab06] investigated the possibility of producing good quality lightweight concrete using volume replacement of aggregates by EPS aggregates. The mixtures they studied also included fly ash. During their study, Babu et al. [Bab05] observed that the compressive strength of EPS concrete reduced with increasing volume fraction of EPS, as shown in Figure 3.1 [Bab05]. They also observed the variation of the split tensile strength of EPS concrete with compressive strength (Figure 3.2) and provided the following expression:

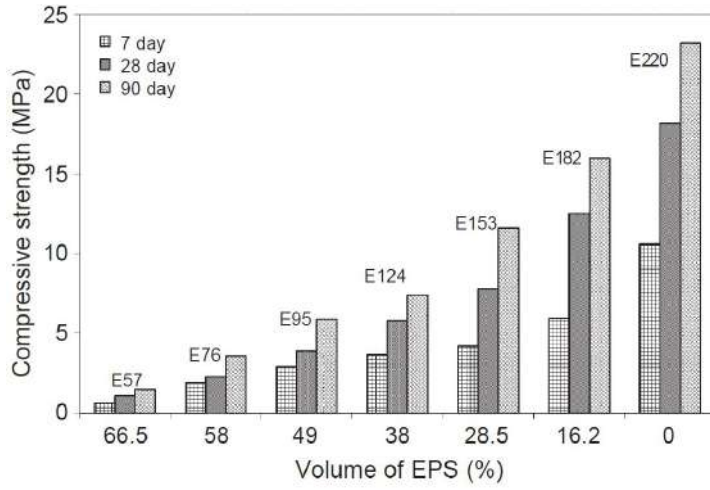


Figure 3.1 Variation of compressive strength with age and EPS volume for concrete added with fly ash [Bab05].

$$f_t = 0.358 f_{cu}^{0.675} \quad (3.2)$$

where f_t and f_{cu} is the split tensile strength and compressive strength in MPa, respectively. The study validated the expression for static elastic modulus (Equation 3.1) provided by Ravindrarajah & Tuck [RT94]. The authors also noted that the EPS mixes showed good flowability and no segregation was observed in any mix, although they did not explore the results beyond an EPS replacement volume of 40%.

Later, Bucher [Buc09] investigated the possibility of using what he called Lightweight Synthetic Particles (LSP) to reduce the potential for restrained shrinkage cracking in concrete. Aggregates in concrete and mortar provide restraint against deformations of the cement paste. The degree of restraint, discussed in Chapter 2, is not only a function of the

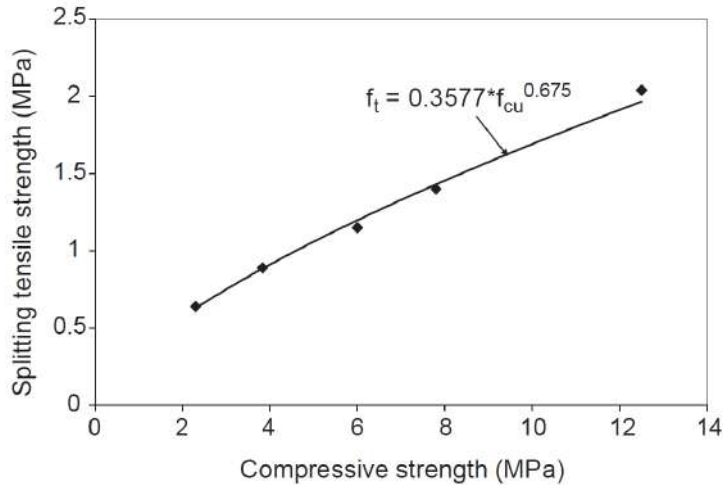


Figure 3.2 Variation of split tensile strength with compressive strength for EPS concrete added with fly ash [Bab05].

boundary conditions of concrete, but also of the aggregate content and distance of cement paste from aggregate. Bucher claims that LSPs can be used as low stiffness aggregates that lower stress concentrations at the aggregate, thereby decreasing the propensity for early-age cracking of mixtures.

In all of the studies above, the authors observed that adding EPS (synonymous to LSP) to a cementitious mixture can reduce its structural properties E and f'_c . In this study, these results are used for a different purpose, i.e., simulating the state of damaged grout, termed LoD herein. EPS beads of 0.15-0.20 inch diameter (Figure 3.3) with a density of 1.40-1.50 lbs/ft³ were used. Although this material achieves the required reduction in E and f'_c , some quantification was required to enable reproducible levels of deterioration (LoDs).

3.2 Physical Damage Simulation

3.2.1 Exploratory Study

Many trial grout mixtures were used to obtain a simple linear predictive model that relates the reduction in E to the percentage volume replacement of EPS in the grout mixture. Grout was mixed using a drum mixer. During mixing, EPS aggregates were added gradually, in parts. After mixing, prismatic grout samples of size 3"×3"×12" were taken. Relative Dynamic Modulus of Elasticity (RDME) discussed in Chapter 2 was used as a measure of reduction in the elastic modulus. However, the baseline E_0 in the now familiar E/E_0 , is the elastic modulus of the specimens with 0% EPS. RDME was measured on the 3rd day from the day of casting.

Table 3.1 shows the full matrix of the trial and error tests that were performed along with average values of measured RDME. Figure 3.4 shows the results of the trial and error tests. A negative trend can be seen in the normalized elastic modulus with increasing volume replacement of EPS. A simple linear model has been fit to be used as a guideline to control the LoD.

Since E and f'_c are positively correlated, reducing the former to predefined values also results in the latter being reduced. The modulus of elasticity, E , was chosen as the primary variable to be reduced for two reasons. One is that between the two, E is the parameter that is more difficult to reduce, i.e., a 40% reduction in E will result in a significantly higher percentage reduction in f'_c . Second, durability studies, especially those pertaining to freeze and thaw resistance, utilize E as the parameter that defines the failure limit states.

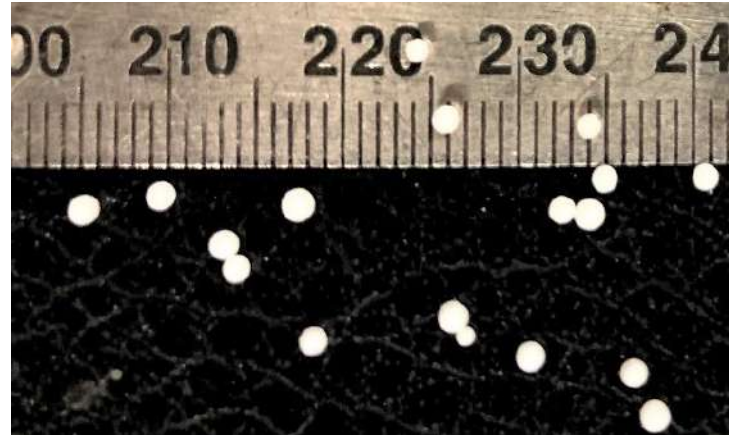


Figure 3.3 Expanded Polystyrene (EPS) beads.

Table 3.1 Trial and error test matrix to determine required EPS volume percentages.

Test No.	EPS by Volume	Number of Specimens	RDME (3 day)
1	0%	3	100%
2	5%	3	96%
3	10%	3	87%
4	15%	3	82%
5	20%	3	76%
6	25%	3	72%
7	30%	6	70%
8	35%	6	62%
9	40%	6	53%

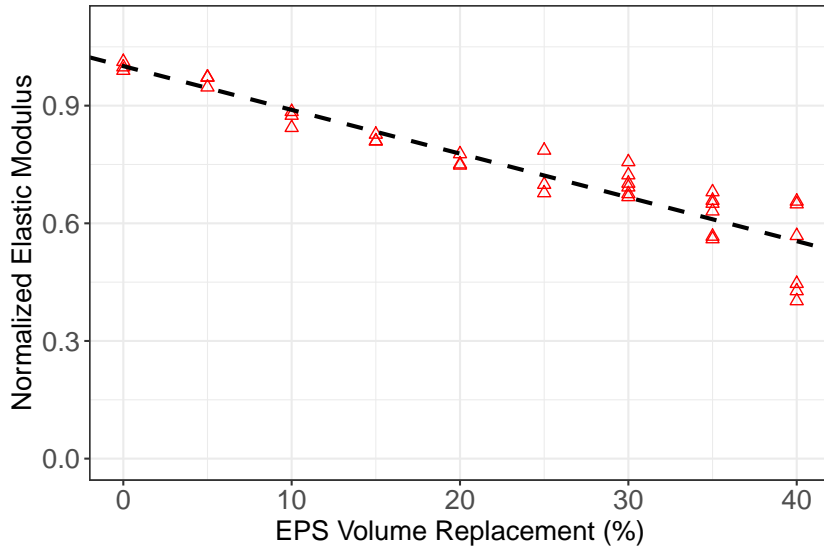


Figure 3.4 Elastic modulus normalized to value at 0% EPS plotted against EPS volume replacements for trial and error mixtures.

3.2.2 Preventing EPS migration

Although it was not observed in prismatic samples of grout with added EPS, the cylindrical samples after demolding showed signs of EPS aggregates migrating to the top. In Figure 3.5, this can be seen externally as a change in color between the top and bottom layers. Some samples have greater migration than others, indicated by the different levels at which this change in color is observed. This migration can be attributed to the extremely low density of the EPS beads in the wet grout mix. When such samples are tested under a compressive load, they display premature failure, a shown in Figure 3.6.

The migration of EPS aggregates was undesirable for the purpose of simulating reduced structural properties. In real bridges with the GSS connection, the deterioration, such as cracking, scaling etc., initiates at the bottom, since only the bottom surface is exposed, and



Figure 3.5 Migration of EPS aggregates observed in cylindrical grout samples.

progresses to the top. Hence, at all points of time, properties such as the elastic modulus and strength will be lower at the bottom compared to the top of the connection. EPS migration to the top would result in the opposite trend. Therefore, it was essential to solve this problem.

To solve the problem of EPS migration to the top of the cylindrical samples, new samples were cast in 2" thick layers. A 4"×8" cylindrical sample contained 4 layers of 2" thick pours. After each layer was cast, 30 minutes elapsed before casting the next layer. The assumption was that this strategy would provide enough time for each layer to achieve sufficient viscosity to prevent the beads from migrating upward. Figure 3.7 shows the samples after compressive strength testing. Although migration to the top of the samples were prevented, there was still migration of the aggregates within each layer. This migration created

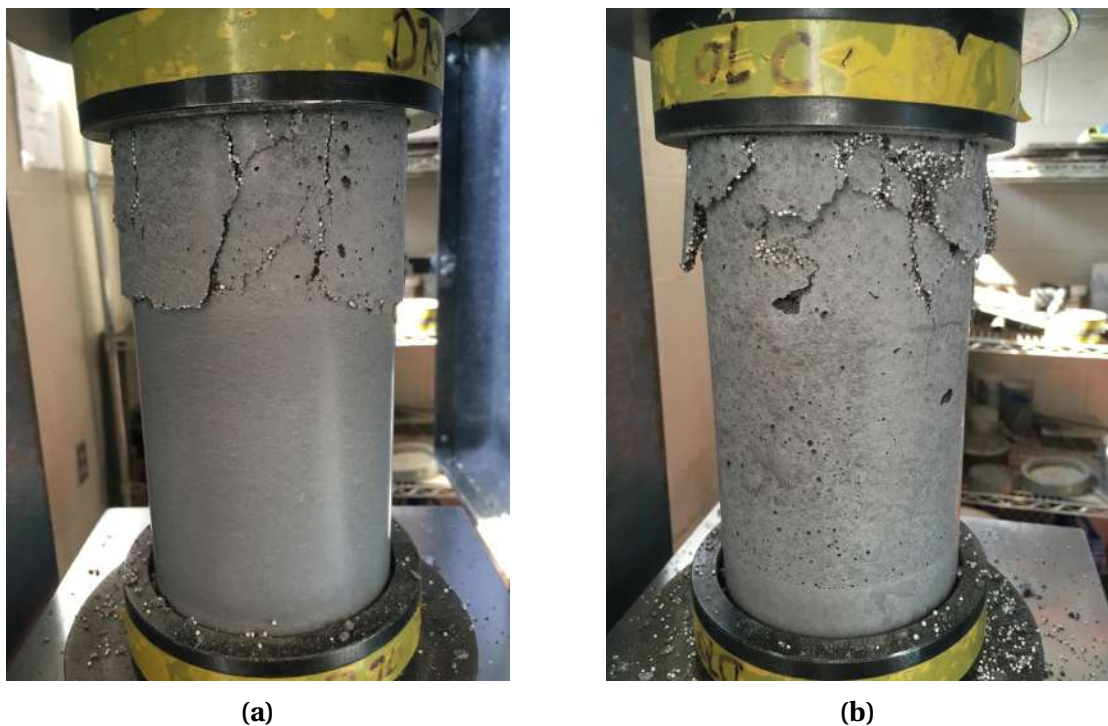


Figure 3.6 Premature failure observed in two different samples of grout mixed with 18% EPS. This corresponds to a 20% reduction of elastic modulus compared to standard grout.



(a)



(b)

Figure 3.7 Compressive strength cylindrical specimens cast in 2" layers with 18% EPS.

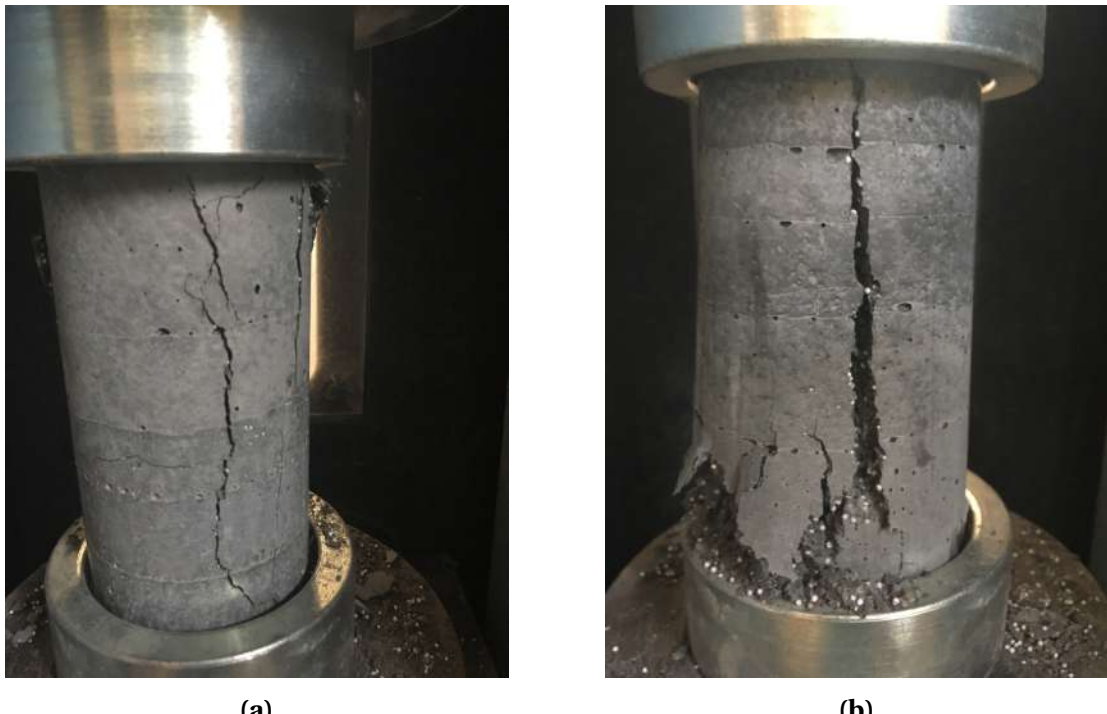


Figure 3.8 Compressive strength cylindrical specimens cast in 1" layers with 18% EPS.

weak planes along the height of the samples resulting once again in premature failure. This result was also deemed as a failure to effectively simulate grout deterioration.

Subsequently, the layer thickness in the cylindrical samples was reduced from 2" to 1". This resulted in eight 1" layers in a 4"×8" cylinder. Figure 3.8 shows the 1" layered samples after compression testing. The cylinders failed by cracking through the entire height, which was typical of normal concrete cylinders. No premature failure was observed, and the sample strengths were consistent. One half of a failed sample is shown in Figure 3.9. The EPS aggregates have a uniform distribution along the height of the sample. The layered casting scheme with 1" layers was therefore chosen as the method to physically simulate deterioration.



Figure 3.9 Uniform distribution of EPS aggregates observed in cylindrical grout samples under the 1"-layered casting scheme.



Figure 3.10 Formwork for the mock GSS connection.

3.2.3 Mock Connection

In addition to ensuring uniform distribution of EPS aggregates in the GSS connection, it was required to generate a reproducible level of deterioration for the large scale tests. To investigate reproducibility of elastic modulus and compressive strength measurements, a mock connection was cast. This mock connection was a replica of the grout ring in the GSS connection without the shear studs. The formwork for this connection was prepared using 24" dia. and 16" dia. sonotubes, as shown in Figure 3.10. The top was closed with a plywood sheet with two holes (one to pump in grout, the other to let air out) to replicate actual pumping conditions. The annulus between these concentric sonotubes was pumped with a grout mixture with 18% volume replacement of EPS to simulate the first LoD. The

grout mixture was cast in a layered scheme shown in Figure 3.11. The entire connection was 24 inches deep. For the first 9 inches from the bottom, 1" thick layers of grout were cast at intervals of 30 minutes. This wait-time allowed enough time for the fluid mixture to develop partial setting that prevented migration of EPS. The next 6 inches were cast in layers of 2" thickness with the same wait time. The last 9 inches were cast in layers of 3" thickness. This region will have some EPS migration. However, the forces during the test in this region are low and hence this region was less important than the lower half of the connection, from a damage simulation standpoint. Grout mixture samples were collected in round and square PVC pipes that were cut to 2' lengths. The sample collection followed the same layering scheme as the actual connection. Samples in round PVC pipes were later cut into discs to measure the elastic modulus (E) profile along the height of the connection [Lem98]. Samples in square PVC pipes were cut into cubes to measure the cube compressive strength (f_c).

After setting, the distribution of EPS was assessed qualitatively. Ultrasonic pulse velocity (UPV) measurements were made along the height of the mock connection to determine the time required for the ultrasonic wave to travel through the thickness. The locations of UPV measurements are shown in Figure 3.12. The elastic modulus is directly proportional to the square of the travel time; therefore a profile of elastic modulus along the height of the connection was obtained (Figure 3.13). In addition, samples were cast in round PVC pipes of the same height as the connection (Figure 3.11). These samples also followed the layered pouring scheme utilized in the mock connection. Cylinders and discs were cut from these samples to measure f'_c and E (Figure 3.14 and 3.15). The compressive strength was measured according to ASTM C39-18 [Asta] and the elastic modulus was measured utilizing

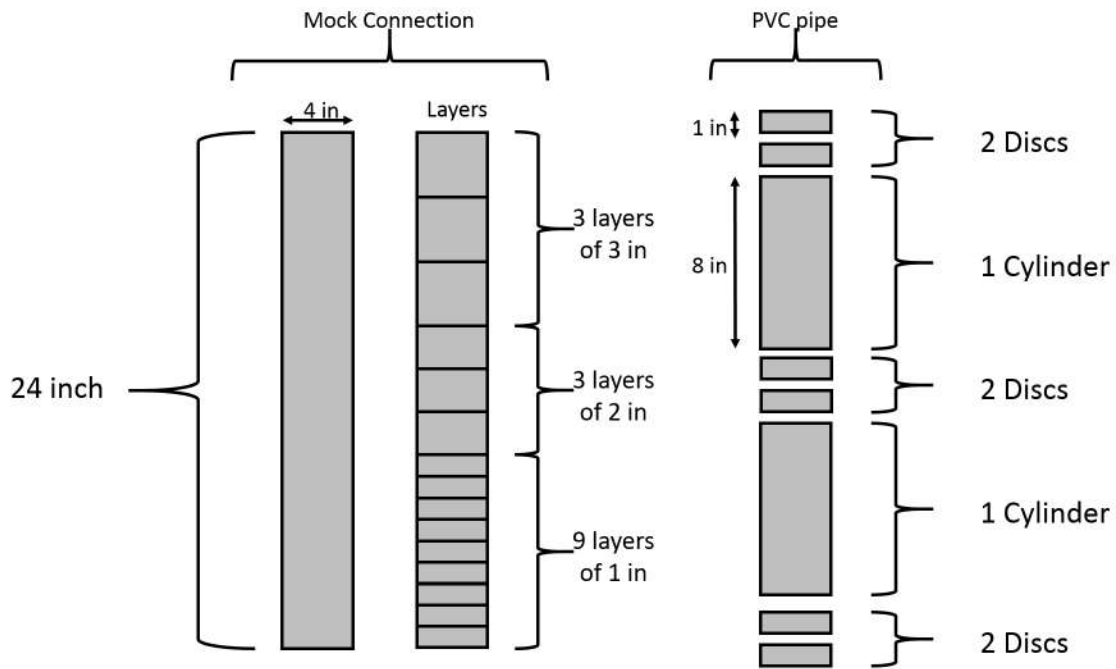


Figure 3.11 The layered scheme used to cast the mock connection and the corresponding 4"×24" PVC pipes.

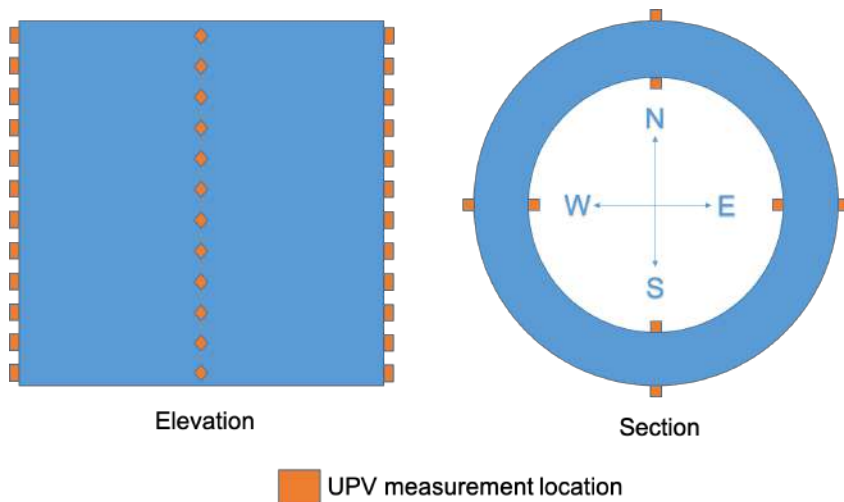


Figure 3.12 The locations of ultrasonic pulse velocity measurements along the height and around the section of the mock connection.

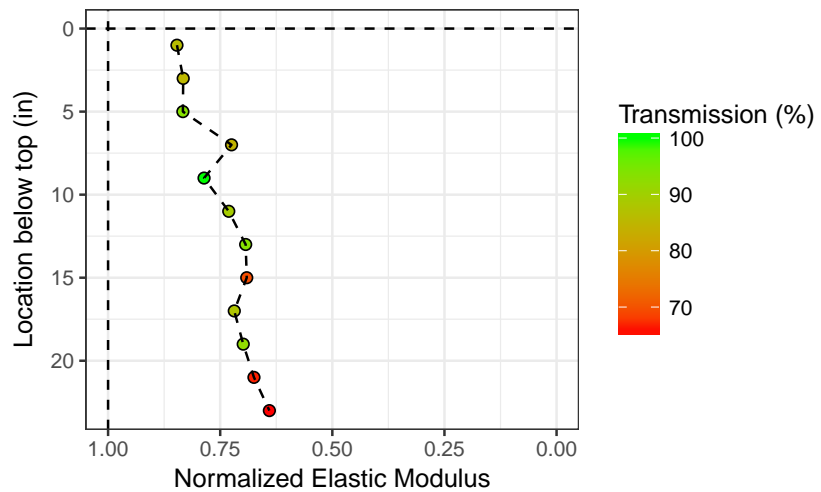


Figure 3.13 Results of the UPV test to measure relative elastic modulus along the height of the mock connection.

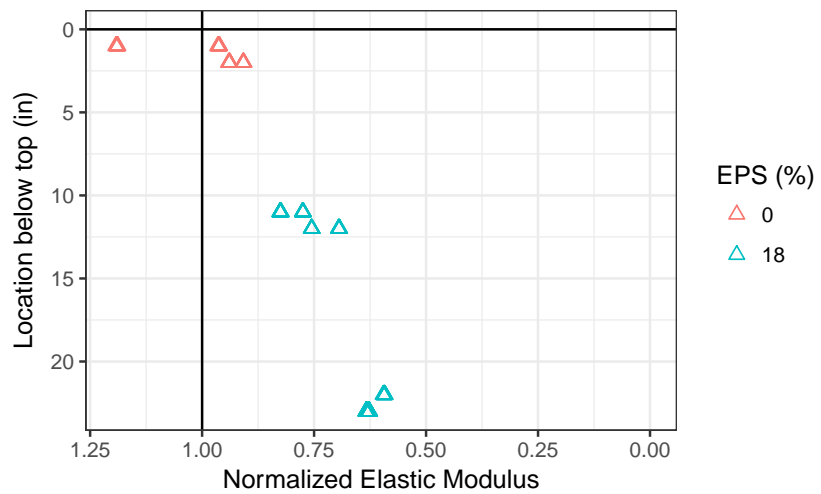


Figure 3.14 Results of elastic modulus measurements using disc samples along the height of the mock connection.

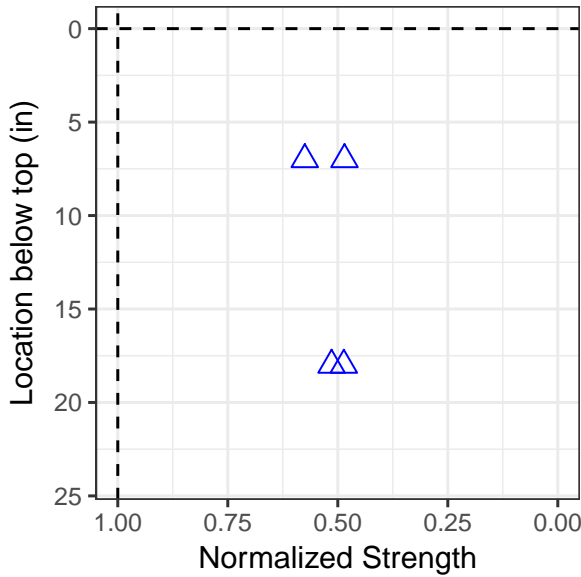


Figure 3.15 Results of compressive strength measurements using cylindrical samples along the height of the mock connection.

ing the method proposed by Leming et al. [Lem98]. Although obtained using two different non-destructive testing methods, Figures 3.13 and 3.14 show similar results.

3.2.4 Level of Deterioration for Large Scale Tests

The mock connection produced valuable information. The primary concern regarding the method of EPS addition for damage simulation was the upward migration of EPS beads because of their low density. This migration would have resulted in a reduced strength and elastic modulus closer to the top half of the connection rather than in the bottom. This distribution would have been unacceptable since in reality, the bottom half of the GSS connection will experience deterioration first, while the top remains essentially unaffected. Figure 3.14 shows the lowest values of elastic moduli at the bottom with an approximately

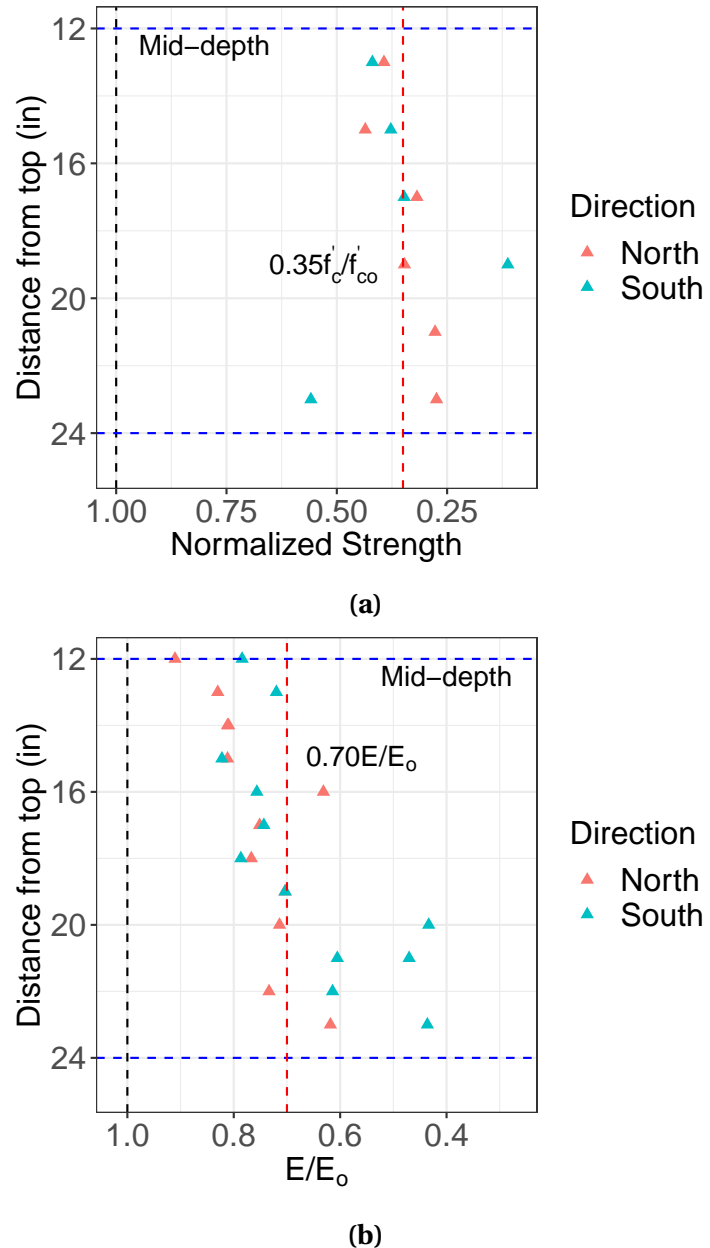
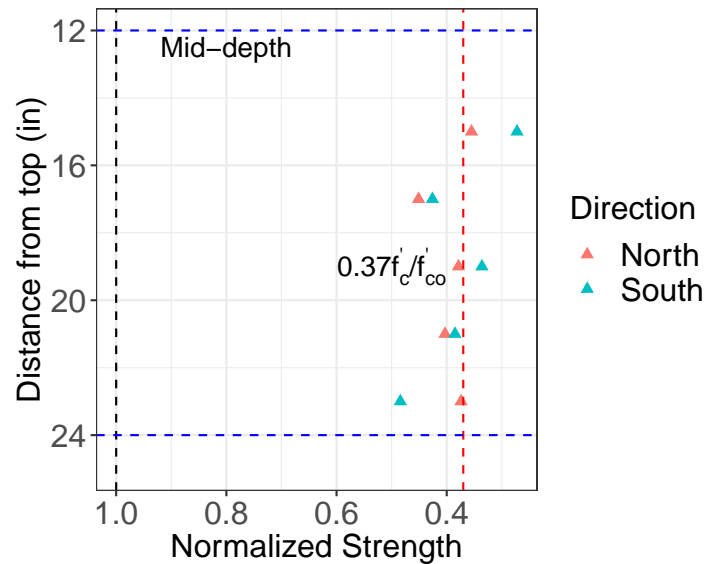
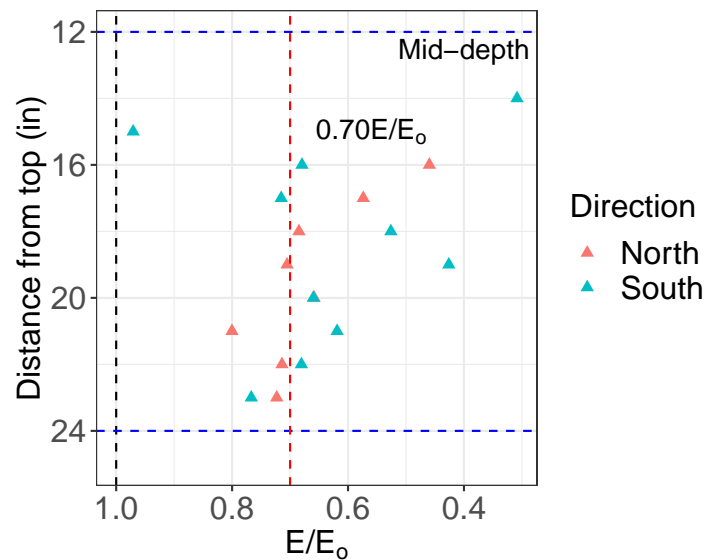


Figure 3.16 Results of grout properties from the GSS connection of **test 2** (a) Compressive strength profile obtained from cubic samples (b) Dynamic elastic modulus profile obtained from disc samples.



(a)



(b)

Figure 3.17 Results of grout properties from the GSS connection of **test 3** (a) Compressive strength profile obtained from cubic samples (b) Dynamic elastic modulus profile obtained from disc samples.

linear increase with height. This trend is what one would expect in a real GSS connection exposed to a few years of freeze-thaw cycles. The mock connection was able to achieve an LoD with average reduction in elastic modulus of approximately 30% and strength of about 50%.

The same process of grout casting was repeated for the construction of the specimens for large scale tests 2, 3, and 4. Grout samples were poured into round and square PVC pipes to obtain discs and cubes for E and f'_c measurements. Results from the testing of grout properties of the real specimens of tests 2 and 3 are shown in Figures 3.16 and 3.17, respectively. Results are shown separately for the two connections, North and South side of each specimen. Below the mid-depth of the connection, the elastic modulus profile shows the same trend as that shown in Figure 3.14 which indicate reproducibility. While there is some scatter, the GSS connections in tests 2 and 3 had, on average, a reduction in strength of 60% and in elastic modulus of 30% compared to those in test 1.

3.3 Chapter Summary

This chapter discussed the method that was followed to achieve a simulation of deteriorated GSS connections in the large scale tests. The objective of simulating deterioration was to be able to compare the structural performance of the deteriorated GSS connection to that of a standard undeteriorated connection. A literature search revealed that expanded polystyrene (EPS) aggregates when mixed with grout can reduce its compressive strength and elastic modulus. Therefore, EPS addition was chosen as the method through which damage simulation was achieved, since long term exposure to cold climates also results in reductions in the aforementioned structural properties.

EPS beads are extremely lightweight aggregates which tend to migrate upward in a grout mixture. This behavior was undesirable since a realistic simulation of damage must have a more uniform distribution of EPS near the bottom of the connection. A layered casting scheme was developed to overcome this problem. Practice casts were performed to ensure reproducibility of damage simulation. Finally, a grout mixture with enough EPS to simulate moderate-to-high levels of damage due to cold climate exposure was developed.

CHAPTER

4

CONSEQUENCES OF GROUT
DETERIORATION ON STRUCTURAL
PERFORMANCE OF THE GSS
CONNECTION

4.1 Introduction

This project began with the motivation of determining whether the GSS connection could be used in cold climates. Phase 1 of this project, discussed in Chapter 2, investigated the state of commonly available high-strength cementitious grout from the perspective of cold climate durability. This study was able to show that while all high-strength cementitious grouts do not possess good durability, some do, and testing samples of selected grouts for their durability can potentially separate the good ones from the bad. Before emphasizing the need for further study of cementitious grouts, it was worth determining the consequences of grout deterioration on the structural performance of the GSS connection. If grout deterioration does not significantly diminish the structural integrity of the lateral load resisting system, investigating additional commercial grouts may not yield significant further knowledge, from the GSS application standpoint. However, if grout deterioration does compromise the ability of the system to successfully function under lateral loading, further studies optimizing the grout material would likely be required.

The approach was to perform large scale structural tests on specimens having deteriorated GSS connections and compare the results to those of specimens having fresh non-deteriorated GSS connections. Theoretically, any effect of grout deterioration would be evident from the comparison of the results of these experiments. Each structural test utilized a certain level of deterioration (LoD) for the grout in its connections. A damage (or deteriorated) state for the GSS connections was simulated in each test specimen by using an additive known as expanded polystyrene (EPS) aggregates. Differences in their performance under cyclic quasi-static lateral loading were investigated. The GSS connections

in the first test specimen were initially “undamaged”. The subsequent tests had GSS connections that had reduced grout compressive strength (f_c) and elastic modulus (E), representative of a moderate-to-high level of damage due to freeze-thaw exposure. Despite a substantial reduction in grout strength of approximately 60%, and grout elastic modulus of about 30%, no significant differences were observed in the global system behavior, including hysteretic characteristics, maximum strength, and maximum ductility. This result suggests that grout durability is likely of little concern in the long term performance of the GSS connection in cold climates.

The remainder of this chapter elaborates on our experiments to determine the structural consequences of grout deterioration. To understand this part of the project, it is necessary to follow the chronological order of experiments. Each large scale test is discussed in detail. Important choices pertaining to several variables involved in each test were made at different points of time based on the most recent information. Decisions were made with due consideration of input from AKDOT engineers. To put these decisions into context, each test is described one after the other stating prior expectations and post implications of each.

4.2 Large Scale Experiments on Two-Column Bridge Piers -

Part 1

4.2.1 Research Approach

The objective of the large scale tests was to investigate the effect of GSS connection durability damage on the seismic behavior of the lateral load resisting system. An ideal procedure to determine the consequences of connection deterioration would be to cast multiple specimens with the GSS connection, test one of them as a control and subject the others to severe cold climate environment (real or simulated), and subsequently test them one by one at different points of their service life. Due to obvious constraints, this procedure was not adopted.

The approach taken was to artificially simulate different levels of deterioration (LoD) in the connection without environmental exposure. To elaborate, an LoD represents the effective state of the grout after years of service. As discussed in earlier chapters, the durability detriments, namely freeze and thaw, thermal gradients, and restrained shrinkage act on the GSS connection to produce cracking within the grout. The grout properties that are adversely affected by environmental exposure in cold climates are its compressive strength (f'_c) and elastic modulus (E). Incidentally, the grout properties that contribute to the integrity of the structural system are also its f'_c and E . By producing a grout mixture with the effective properties of deteriorated grout, an LoD could be achieved that would be an adequate substitute for a deteriorated connection.

The test specimens were large scale two-column bridge bents. These consist of two

steel columns connected to a steel cap-beam using the GSS connection. The procedure by which different LoDs were achieved was discussed in detail in Chapter 3. The idea was to introduce expanded polystyrene (EPS) beads to the grout mix by part replacement of grout. The EPS material is extremely lightweight and when distributed within the grout microstructure, it can take up space simulating air pockets. The larger the volume fraction of these beads in the hardened grout, the lesser will be the grout's compressive strength and elastic modulus. To achieve a controlled reduction of grout properties, many trials were carried out with different amounts of EPS mixed in grout.

Table 4.1 provides a summary of the results from all of the large scale experiments that were performed. Note that test 0 was not performed as part of this project. It was one of the tests performed by Fulmer et al. [Ful15], but is provided here because of its relevance to this project. In Table 4.1, tests 0 and 1 represent bridge bents that are new and hence have GSS connections that are undamaged. Tests 2 and 3 represent bridge bents exposed to multiple years of service in a cold climate. The connections in these bridge bents exhibit a moderate-to-high level of simulated grout deterioration. As seen in the table, all the tests from test 0 to test 3 show good structural behavior, i.e., ductile failure via plastic hinge formation in the columns just below the GSS connection. Soon after test 2, a meeting with AKDOT led to a change of scope of the project. Consequently, test 3 was adjusted to assess the impact of a reduced number of shear studs. This impact is discussed in Chapter 5. However in hindsight, it can also be used as another data point to determine the effect of grout deterioration, because the effect of shear studs on global response was later found to be insignificant. In this chapter therefore, test 3 results serve as a repeat of test 2. Each test and its implications are discussed later in detail.

Table 4.1 Test matrix used to determine consequences of grout deterioration on the structural performance of the GSS connection.

Test No.	Test ID	LoD (E and f'_{c0})	Number of Shear Studs	Result
0	SG-96	NA and $0.7f'_{c0}$	96	Good
1	SG-32	E_0 and f'_{c0}	32	Good
2	DG-32	$0.7E_0$ and $0.4f'_{c0}$	32	Good
3	DG-16	$0.7E_0$ and $0.4f'_{c0}$	16	Good

4.2.2 Large Scale Experimental Setup

Large scale experimental tests were conducted at North Carolina State University's Constructed Facilities Laboratory (CFL). In all cases, the test specimens were a large scale two-column steel bent as shown in Figure 4.1. The columns were 1/2" thick, 16" diameter round API 5L X52 PSL2 pipes while the short stub pipes were 1/2" thick, 24" diameter round sections of the same material. The cap-beam was a double-wide HP14x117 section. The height of the center of the cap-beam from the pin was 11'2", and the center-to-center distance between the two columns was 12'. The steel bent was supported by two base shoes through pinned connections. The steel pins were 5" in diameter. Such a boundary condition mimics the point of contraflexure that develops in the moment profile of an actual bridge system. The base shoes themselves were prestressed to the laboratory strong floor utilizing 1-3/8" diameter Dywidag bars, with a force of 150 kips per bar.

A 440-kip actuator mounted on the laboratory strong wall was used to apply cyclic quasi-stating lateral loading. A three-cycle set loading history, as shown in Figure 4.2, was used. The definition of this loading history consists of an initial elastic portion based on the anticipated yield force of the system, and a second section based on the experimen-

tally determined yield displacement of the system. The elastic portion consisted of double reverse cyclic load-controlled cycles of 1/4 first yield force increments until the full first yield force cycle was completed. The first yield force (F_y) for the two-column bent was determined as

$$F_y = \frac{2f_y S}{X} \quad (4.1)$$

where S represents the elastic section modulus of the pipe pile members, f_y represents the anticipated yield stress of the pipe material, and X represents the shear span from the pinned supports to the critical pile hinging section.

The second section of the load history was defined by displacement controlled incremental ductility levels where displacement ductility 1, or equivalent yield displacement, is defined by Equation 4.2 and subsequent displacement ductility levels are defined by Equation 4.3,

$$\mu_1 = \Delta_y = \Delta'_{y,exp} \frac{M_p}{M_y} \quad (4.2)$$

$$\mu_i = i\mu_1 \quad (4.3)$$

where $\Delta'_{y,exp}$ represents the experimentally determined first yield displacement, and M_p and M_y represent the full plastic moment capacity and the first yield moment capacity of the column section, respectively.

The instrumentation scheme for the test consisted of conventional electrical resistance strain gages and string potentiometers. Also utilized were NDI Certus OPTOTRAK sensors

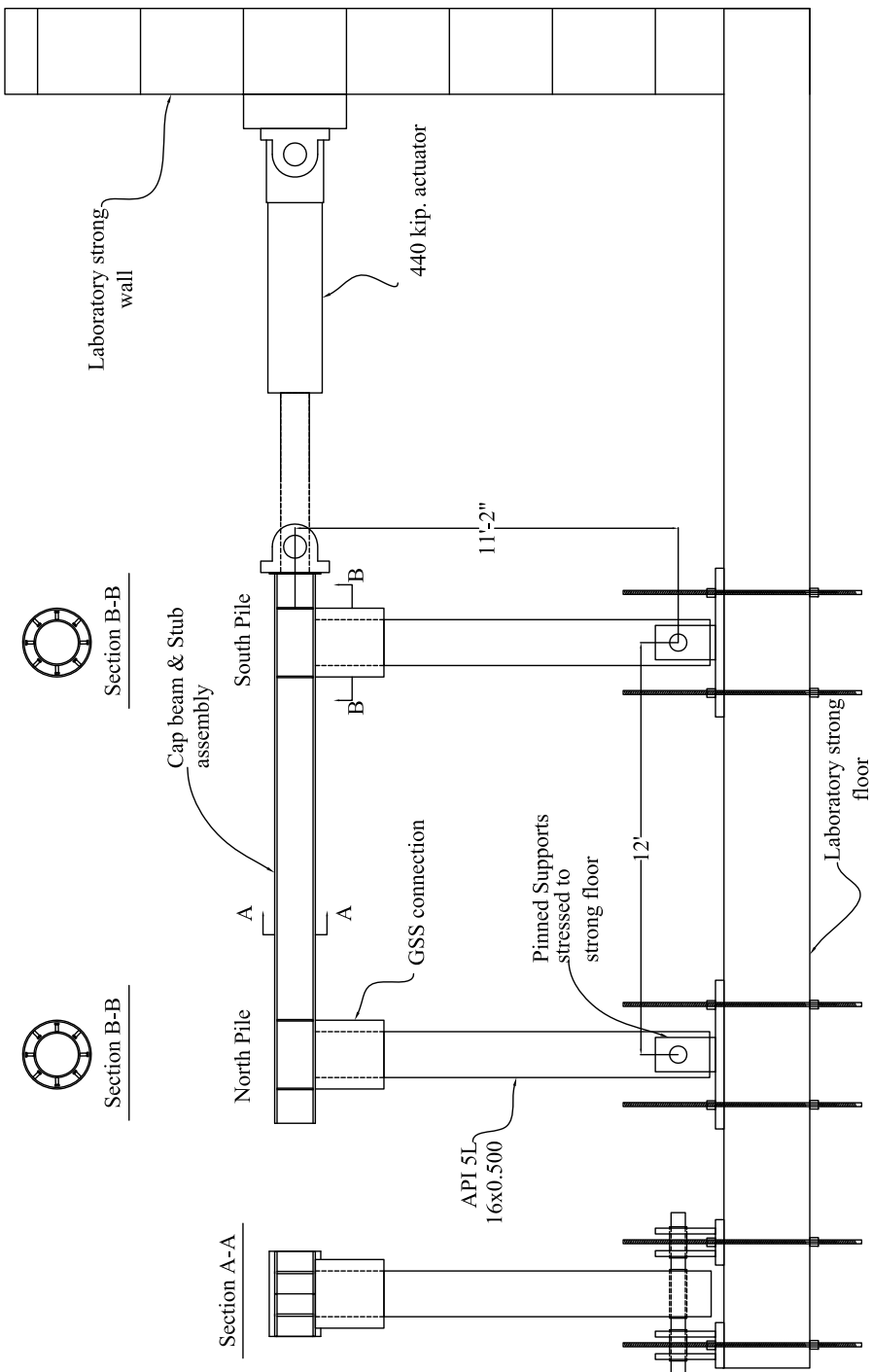


Figure 4.1 Laboratory large scale experiment setup

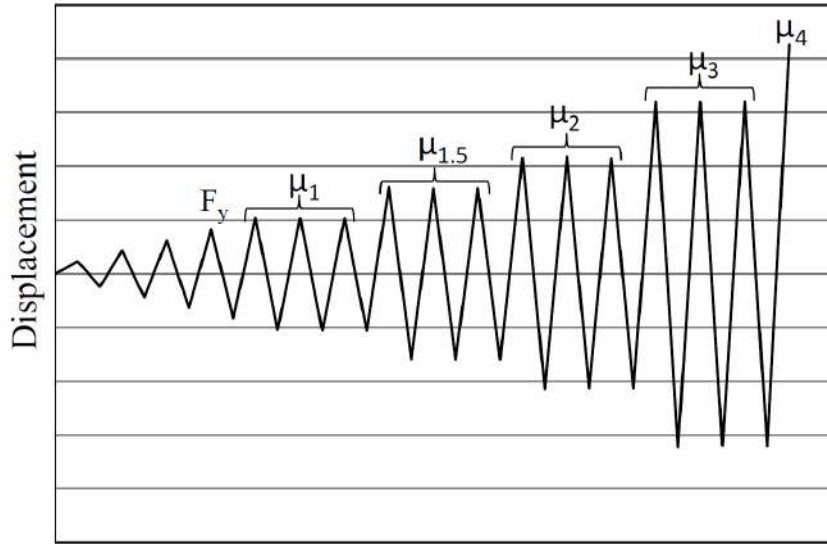


Figure 4.2 A typical three cycle set loading history.

that detect LED markers attached to the specimen. This system allowed the monitoring and recording of the three dimensional coordinates of each marker in real time. This coordinate data was post-processed to obtain displacement fields at locations of interest. Strains were then calculated from this data.

The construction process of the specimens in tests 1 through 4 was consistent. The process differed slightly from that of test 0 [Ful10b]. The differences are mentioned subsequently wherever relevant. Fabrication of the cap-beam/pipe-stub assembly was performed in the shop by a certified welder and inspected by a certified weld inspector. Figure 4.3 shows the fabrication details. The shear stud welding on the columns and stubs was also performed by the same welder. A lower number of larger sized shear studs was chosen for this test. These studs were cut (as they were too long), and hand welded. Shear studs were also welded to the top of the two pipe columns as shown in Figure 4.4.

The next step of the construction process was erecting the two pile columns on top of their pin supports. This was achieved by tying the erected piles to the floor using ratchet straps and D-rings (Figure 4.5). The cap-beam/stub assembly was then brought in and lowered onto the two columns (Figure 4.6a). The columns were inserted into the sockets created by the pipe stubs, and the cap-beam rested on top of the columns (Figure 4.6b). No additional welding was performed to connect the columns to the cap-beam.

Once the cap-beam was in place, the annular regions surrounding the column tops were filled with grout to complete the GSS connections. A manual grout pump was used to achieve this casting (Figure 4.7a). It is worth noting that the grout was pumped through an opening in the beam flange (bottom flange of the beam) at the top of the connection (Figure 4.7b). This casting process differed from that used in test 0 where the grout was pumped from the bottom.

4.2.3 Large Scale Test 1

4.2.3.1 Introduction

Recall that the motivation for Phase 2 of this project was to ascertain the consequences of deteriorated GSS connections on the global structural performance of bridge bents. Also, recall that the approach to achieve this objective was to compare structural response of bridge bents with deteriorated connections to those with undamaged connections. Test 1, discussed here, acted as a control test to provide a baseline for the comparison of the results of deteriorated connections (Tests 2, 3, and 4). Test 0 may also be considered to act as secondary control test. However, a one to one comparison of the results of tests 2, 3, and 4 to that of test 0 cannot be made because of some important changes made to the

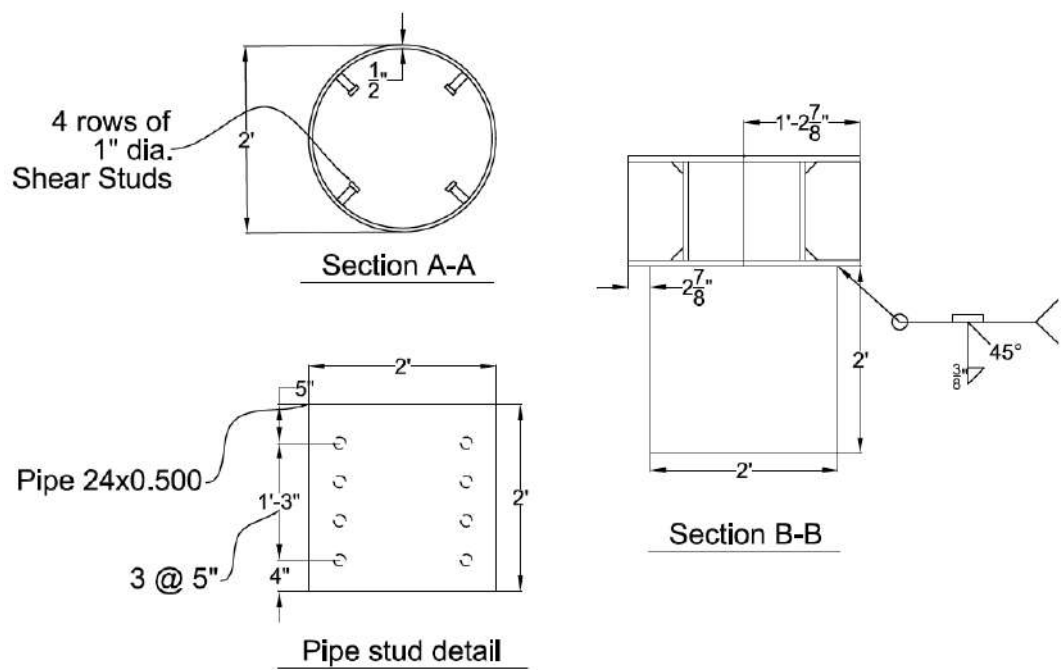
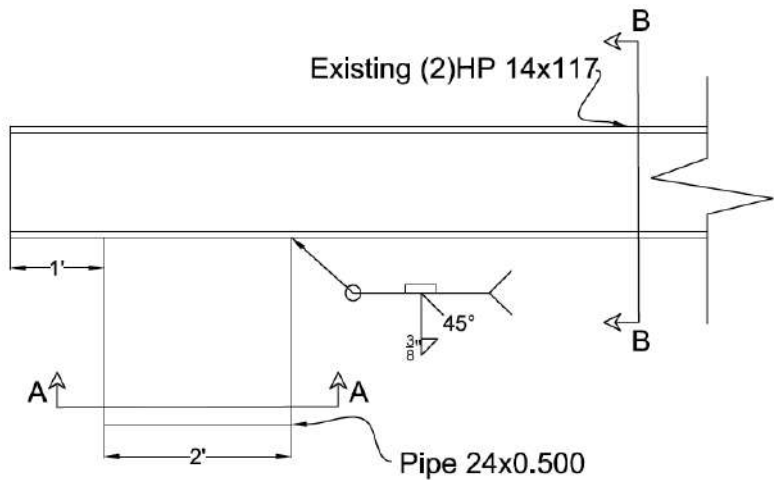


Figure 4.3 Fabrication details for the cap-beam stub assembly of Tests 1 through 4.

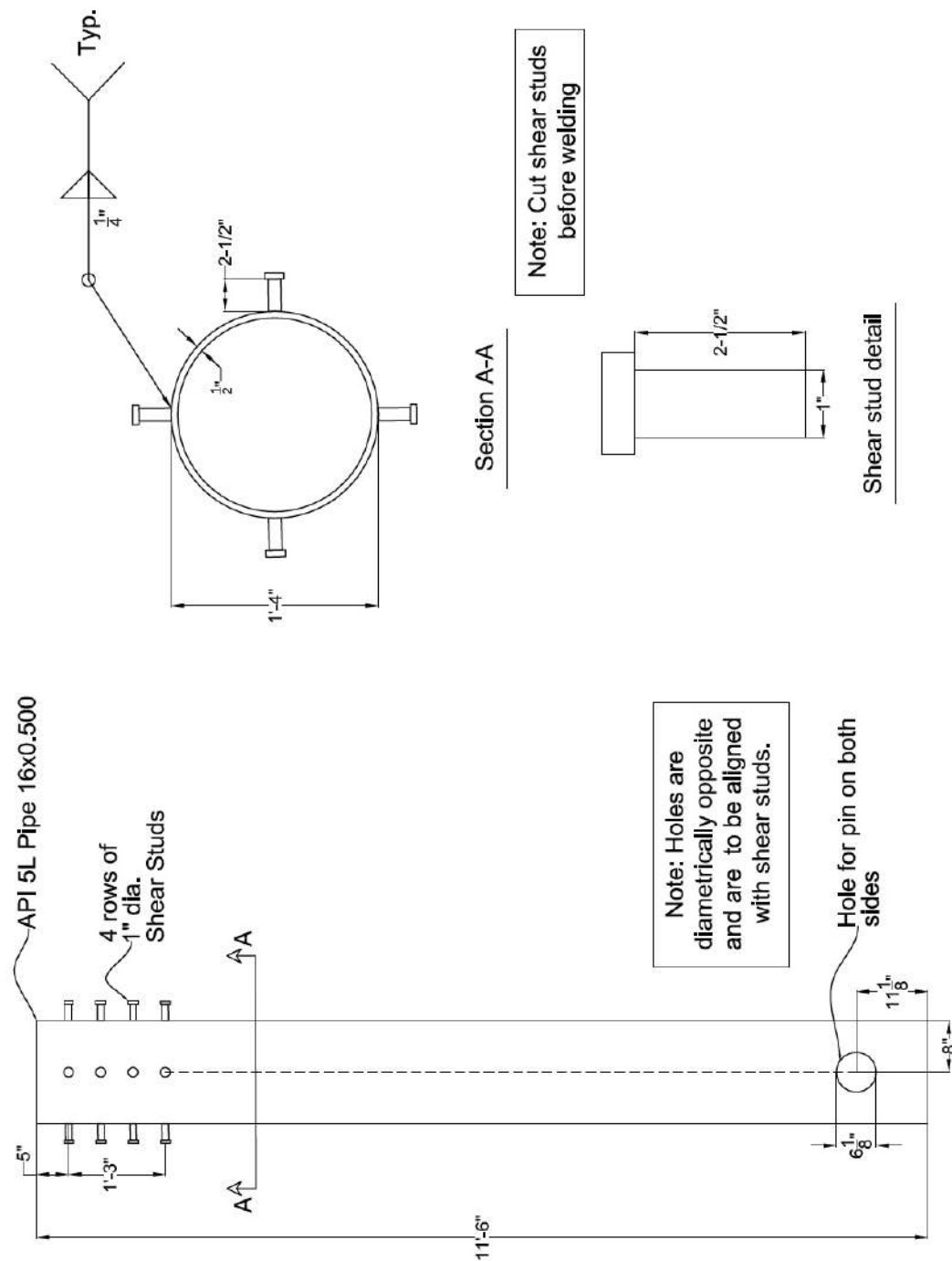


Figure 4.4 Fabrication details for the hollow circular columns used in Tests 1 through 4.



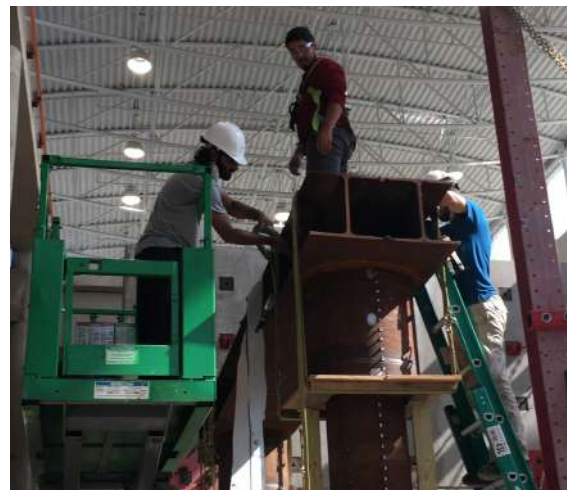
Figure 4.5 Columns erected and ready for cap-beam assembly.



Figure 4.6 Photographs showing (a) the cap-beam stub assembly being lowered onto the columns and (b) one of the columns afterwards.



(a)



(b)

Figure 4.7 Photographs showing (a) the grout pump and (b) the pumping process.

experimental setup of Tests 1 through 4, as discussed next.

4.2.3.2 Experimental Setup

AKDOT prefers to use steel pipe material API 5L X52 PSL2 for the construction of new bridges compared to conventional ASTM A500 Gr. B material. API 5L PSL2 is a steel material with better quality control. American Petroleum Institute (API) standards require this material to meet the following specifications. For pipe grade X52, a minimum and maximum material yield strength of 52.2 ksi and 76.9 ksi, respectively, must be met. This requirement is useful from a seismic design standpoint because material overstrength is better controlled and more importantly, defined. PSL2 rated material is required to be tested for its Charpy V-notch (CVN) energy absorption values. Typically, the CVN toughness of this material is above 200 ft-lb at 32°F (0°C). The high toughness provides the material with high ductility capacity even at low temperatures. Therefore, all columns and stub pipes used in tests 1 to 4 of this project were API 5L X52 PSL2 material. The geometry of the test setup remains the same as that in test 0.

Yet another difference from test 0 is that while it had a total of 96 shear studs of 3/4" diameter, per GSS connection, the specimens in tests 1 and 2 consisted of connections with a total of 32 shear studs of 1" diameter (16 on each column and 16 in each stub). Furthermore, Tests 3 and 4 consisted of a total of 16 shear studs of 1" diameter, per GSS connection. A detailed discussion of the reasons for this change is presented in Chapter 5. A shorter version is as follows. The design of the number of shear studs in test 0 was accomplished using an excessively high axial force demand versus what realistically develops. In addition, the capacity of shear studs embedded in confined grout may have been underestimated. AK-



Figure 4.8 Photographs showing the arrangement of shear studs in (a) the stub pipe on the cap-beam, and (b) the pile columns.

DOT wanted to explore the possibility of using a smaller number of larger diameter shear studs for economy and ease of construction. In test 1, a total of 32 (16 each on the column and stub pipe) 1" dia. shear studs were welded inside each GSS connection. A symmetrical condition was generated by 4 lines of 4 shear studs at 90 degrees center to center as shown in Figure 4.8.

4.2.3.3 Experimental Summary

The structural test was performed 30 days after casting the grout in the GSS connections. Cyclic quasi-static loading was applied to the two-column steel bent initially in the force control mode at a rate of 10 kips/min. The two columns of the test specimen were from different heats of manufacturing. The measured average yield strengths of the North and

South columns were 63.8 ksi and 69.6 ksi, respectively. The calculation of F_y used the lower yield strength of the two columns. Two cycles to each force level ($0.25F_y$, $0.50F_y$, $0.75F_y$ and F_y) were applied first. Within the first two cycles, there were audible sounds of grout cracking. These sounds continued until the force level of F_y . The force-displacement response of the system is provided in Figure 4.9.

After two cycles at yield force, the actuator control was changed from load control to displacement control. A load rate of 1 in/min was used for ductilities 1 and 2. The rate was changed to 2 in/min for subsequent ductilities. Three cycles at each ductility level (μ_1 , $\mu_{1.5}$, μ_2 , μ_3 and μ_4) were performed. The pipes showed minor slip and detachment from the surrounding grout rings during the first positive cycle of ductility 1.5. The maximum force at this stage was 143.7 kips. No strength drop was observed. Within the second negative cycle of ductility 1.5, large pieces of grout started spalling from the north GSS connection. The spalling continued for the next few cycles in the north GSS connection. The grout below the first row of shear studs spalled out in the north GSS connection after three cycles at ductility 1.5, as shown in Figure 4.10. This observation is a different behavior from that of test 0. Grout did not spall from the specimen in test 0 until ductility 4 cycles. A combination of factors could have contributed to this difference in test 1.

First, the number of shear studs in each GSS connection in test 1 is only one-third the number used in test 0. Therefore in test 0, a larger number of compression struts and tension ties are formed under loading. The larger number of these truss-like members help distribute the forces more efficiently, resulting in a reduced stress demand per unit volume of grout.

Second, under cyclic loading, a gap starts to open in the GSS connection between the

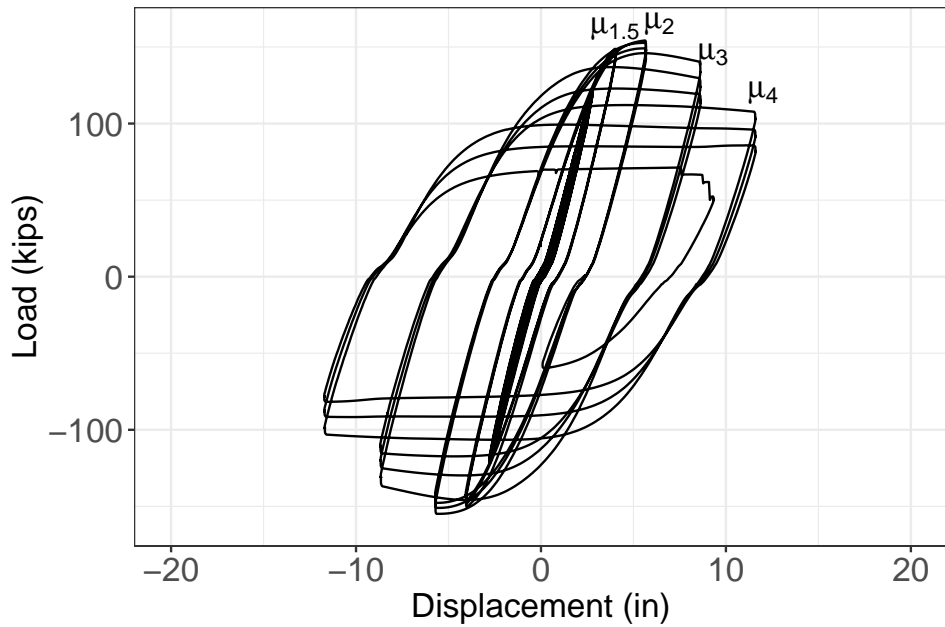


Figure 4.9 The force-displacement hysteretic response of Test 1.

outside surface of the grout ring and the inside surface of the stub pipe. The magnitude of this gap is dependent on the number of shear studs present near the bottom of the connection. When the grout ring tries to detach from the inside of the stub pipe, the shear studs prevent this detachment by mobilizing tensile stresses in them. The magnitude of the tensile stresses developed depends on the number of shear studs that help resist the demand. In test 1, the number of shear studs mobilizing this mechanism was much lower than that in test 0. The excessive tensile stresses thus developed, crack the grout near the bottom of the connection. Thus, the grout below this spalls out.

The mechanism of force transfer within the GSS connection, which is the topic of the next chapter, is complicated. In addition to the possible causes mentioned above, the location of the bottom row of studs in test 1 is much higher into the connection compared

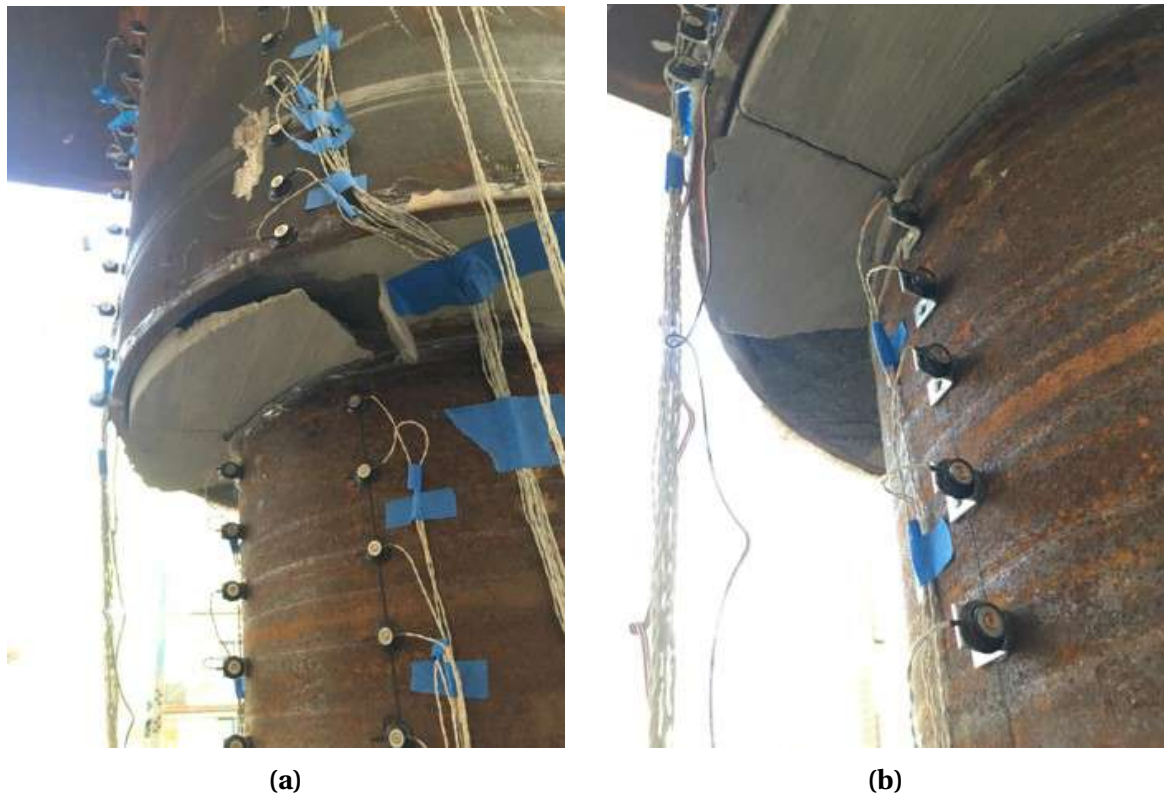


Figure 4.10 Grout spalling observed at (a) North column, South side, and (b) South column, South side (Ductility: 1.5, Cycle: -3, Force: 143.7 kips, Displacement: -4.1 in.).

to test 0. In other words, there is a much larger amount of plain grout cover in test 1 than in test 0. This large cover may also be unable to resist excessive tensile stresses developed as a result of the second mechanism mentioned above.

During the first positive cycle of ductility 2, minor local buckling was observed in the south face of the north pile section, just below the GSS connection. This is the same column and face where high grout spalling was observed earlier. The bottom row of shear studs was further visible. The GSS connection on the south pile started showing grout spalling during the third negative cycle of ductility 2. The bent showed slight drops in strength for each subsequent cycle of ductility 2. The maximum force during the ductility 2 cycles was 150.6 kips.

The first positive cycle of ductility 3 induced outward pile wall local buckling in the south face of the north pile, as shown in Figure 4.11a. On the subsequent negative cycle, similar local buckling was observed on the north face of the south pile (Figure 4.11b). Initially, the outward curvature of buckled pipe walls reduced and “straightened up” upon load reversals. The curvatures increased with each successive cycle and showed permanent buckling. The strength of the specimen continued to drop on each successive cycle. The maximum force during the ductility 3 cycles was 136.3 kips.

Three positive and three negative cycles of ductility 4 were completed successfully without rupture. Further grout spalled from both the connections. The plastic hinge length was observably small, with large curvatures evident in the buckled regions. Wall local buckling progressed around the circumference of the pile sections. The reductions in strength became larger. The maximum force during the ductility 4 cycles was 104.3 kips.

During the first positive cycle of ductility 5, the north face of the south pile experienced



(a)



(b)

Figure 4.11 Pile wall outward local buckling on the (a) south face of north pile (Ductility: 3, Cycle: +1, Force: 136.3 kips, Displacement: 8.62 in.) and, (b) north face of south pile during the first negative cycle of ductility 3 (Ductility: 3, Cycle: -1, Force: -132.2 kips, Displacement: -8.65 in.).



Figure 4.12 Pile wall rupture in the plastic hinge region on the north face of south pile during the first positive cycle of ductility 5 (Ductility: 5, Cycle: +1, Force: 51.0 kips, Displacement: 9.32 in.).

rupture in the plastic hinge region. This is shown in Figure 4.12. The specimen was deemed to have failed and the test was terminated. The specimen experienced a maximum displacement of 11.7 in before failure which corresponds to 9% drift (Figure 4.13).

4.2.3.4 Results and Discussion

Plastic hinge relocation was successfully achieved in test 1. A comparison of the force-displacement response of tests 0 and 1 is shown in Figure 4.14, in which the load on the y-axis is the normalized load. The load values were normalized to their respective peak loads for each test. This was to eliminate the effect of the difference in yield strengths of the steel used in each test. Note that the hysteretic behavior of the two specimens is similar. A reduction of the number of shear studs did not seem to significantly affect the response.



Figure 4.13 The test specimen experienced a maximum drift of 9% (Ductility: 4, Cycle: +3, Force: 82.2 kips, Displacement: 11.60 in.).

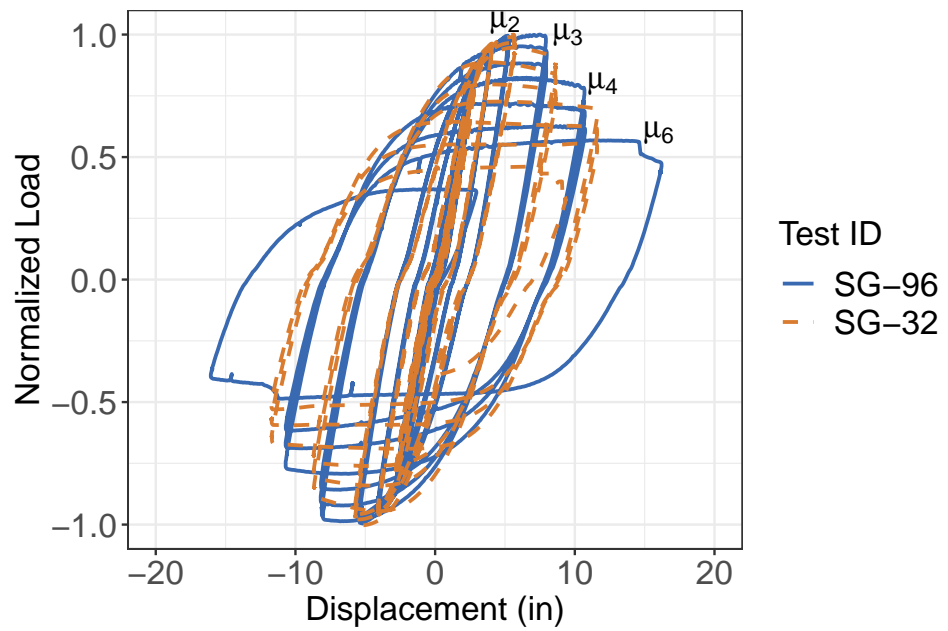


Figure 4.14 Comparison of the force-displacement response of Test 0 (SG-96) and Test 1 (SG-32).

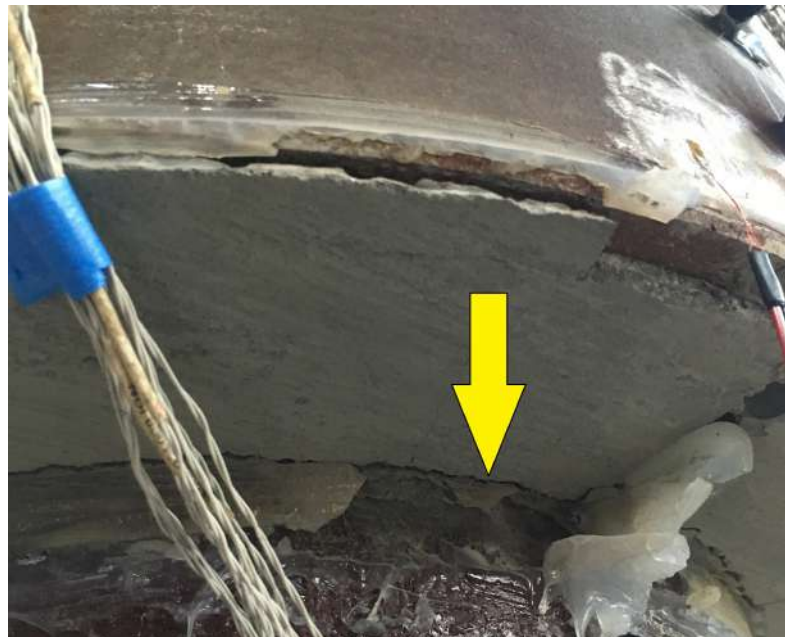


Figure 4.15 Detachment of the column from the surrounding grout ring on the tension side of the connection.

Close to zero load at all ductility levels, a slip was observed in test 1, indicated by a small kink in the force-displacement response. This slip is absent in test 0. This slip also seems to increase in magnitude at higher ductilities. From results of later tests, it was possible to conclude that this was caused by the opening of a gap between the pipe and the grout ring on the tension side of the connection, as shown in Figure 5.31a. When the column bears on the grout ring on the compression side, the round section deforms, and is no longer round. This behavior reduces the diameter of the column orthogonal to the neutral axis, pulling the tension side off of the grout ring. In test 0, however, the number of shear studs was larger compared to test 1. This large number of shear studs prevented the column from detaching from the grout ring, resulting in an insignificant gap. Therefore, the force-displacement response of test 0 does not exhibit slip. This slip in force-displacement response is of little concern.

4.2.4 Large Scale Test 2

4.2.4.1 Introduction

Test 1 results serve as a control to which the results of the tests with deteriorated GSS connection may be compared, to make inferences about the effects of grout deterioration on the structural performance of the connection. In test 2, EPS beads were added to the grout to reduce its elastic modulus and compressive strength to about 70% and 35% of that in test 1, respectively. The profile of the elastic modulus and compressive strength along the height of the connection below mid-depth is shown in Figure 4.16. The values have been normalized to the corresponding value of standard grout used in Test 1. It is assumed that these profiles are representative of GSS connections that have been exposed for many

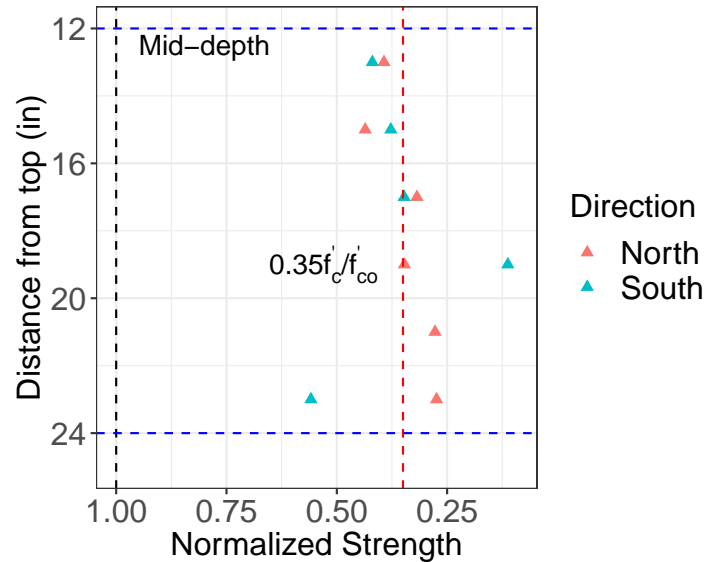
years in cold climates. The results of test 2, therefore, provided us information useful to determine the structural consequence of grout deterioration.

4.2.4.2 Experimental Setup

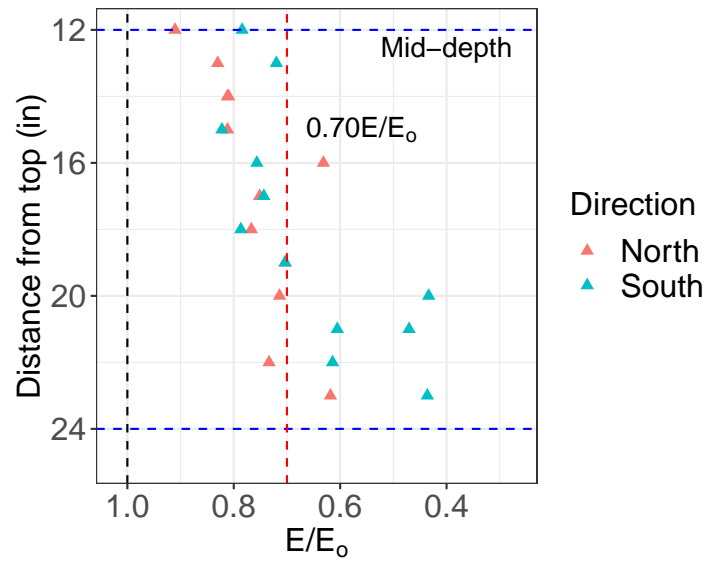
The test specimen was a large scale two-column steel bent similar to the one used in test 1. Test 2 followed the same displacement history as that of test 1. The entire test was performed in displacement control mode. After elastic cycles, three cycles at each ductility level were applied until test termination. The instrumentation scheme consisted of electrical resistance strain gages, string potentiometers, and OPTOTRAK sensors, the same as test 1.

A lower number of larger sized shear studs was used for this test. The only difference from test 1 was the position of these studs with respect to the connection. In test 1, there was 5" thick grout ring cover that was unreinforced with shear studs. In this test, this was reduced to 2.5" to mitigate early grout spalling. These studs were cut (as they were too long), and welded by hand rather than by a stud gun.

The GSS connections were filled with the grout mixture that was developed to simulate deterioration (Chapter 3). EPS beads were added to the grout mixture for this purpose. To prevent segregation and migration of the EPS beads, the connections were cast in layers as shown in Figure 4.17. For the first 9 inches from the bottom, 1" thick layers of grout were cast at intervals of 30 minutes. This wait-time allowed enough time for the fluid mixture to develop partial setting that prevented migration of EPS beads. The next 6 inches were cast in layers of 2" thicknesses with the same wait-time. The last 9 inches were cast in layers of 3" thickness. Grout mixture samples were collected in round and square PVC pipes



(a)



(b)

Figure 4.16 Results of grout properties from the GSS connection of **Test 2** (a) Compressive strength profile obtained from cubic samples (b) Dynamic elastic modulus profile obtained from disc samples.

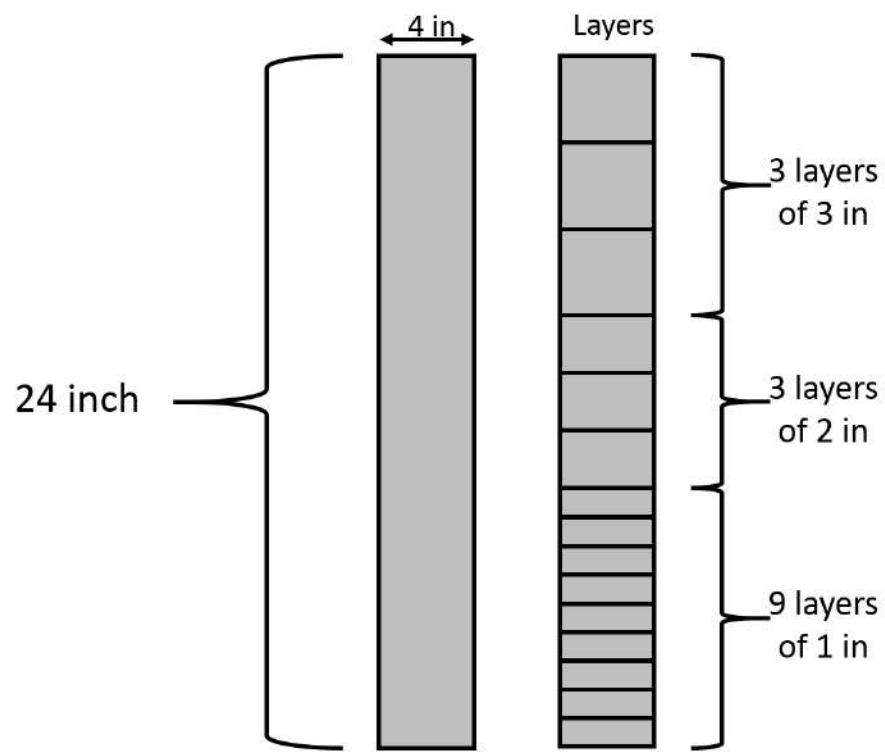


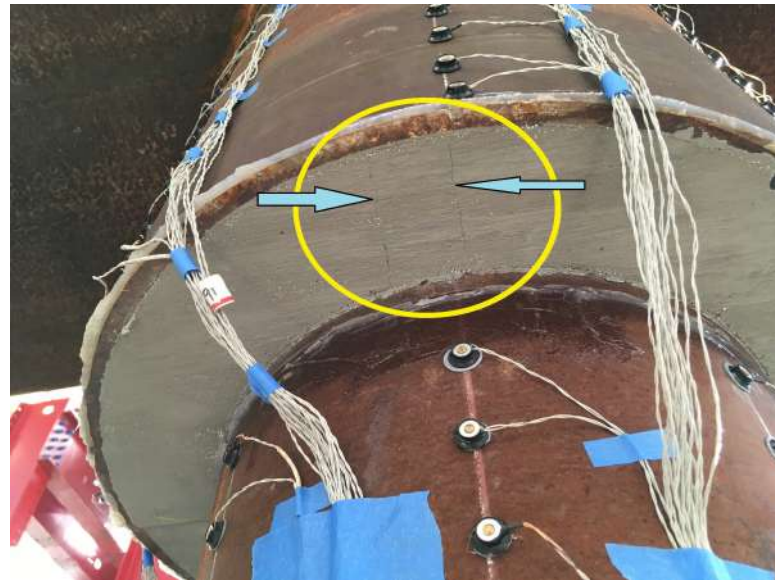
Figure 4.17 Layering scheme used to obtain uniform EPS distribution in GSS connections for physical damage simulation.

that were cut to 24" lengths. The sample casting followed the same layering scheme as the actual connection. Samples in round PVC pipes were later used to cut into discs to measure the elastic modulus profile along the height of the connection. Samples in square PVC pipes were cut into cubes to measure the cube compressive strength.

4.2.4.3 Experimental Summary

The structural test was performed 15 days after casting the grout in the GSS connections. Cyclic quasi-static loading was applied to the two-column steel bent in the displacement control mode. The initial load rate was 1.5 in/min which was later changed to 4 in/min in the inelastic cycles. Two cycles at each force level ($0.25F_y$, $0.50F_y$, $0.75F_y$, and F_y) were applied first. Within the first two cycles, there were sounds of grout cracking. These sounds continued to occur until the force level of F_y was reached. Visible separation of the grout ring from the pile wall was observed at about $0.75F_y$. Radial cracks near the neutral axis of the connection started to develop in both connections, as shown in Figure 4.18a. The cracks multiplied during the second cycle of F_y .

After three cycles at ductility 1, the gap between the grout ring and the pile column opened to nearly 0.1". The outer circumference of the grout ring also started to slip inside the stub pipe. At the second cycle of ductility 2, minor spalling was observed in the south column. Major spalling occurred in the same column on the first push cycle of ductility 3. The separation between the grout and the column increased to about 0.5" on the north column, as shown in Figure 5.32b. Pile wall local buckling was observed on the south side of the north column on the same cycle (Figure 5.34b). On the subsequent pull cycle, the north side of the south column also experienced pile wall local buckling. On the second



(a)



(b)

Figure 4.18 (a) Transverse cracking observed at the neutral axis of the GSS connection (Ductility: F_y , Cycle: +1, Force: 97.8 kips, Displacement: 2.53 in.), and (b) the observed gap between the column and surrounding grout ring (Ductility: 3, Cycle: +1, Force: 142.1 kips, Displacement: 8.64 in.).



Figure 4.19 Pile wall local buckling (Ductility: 3, Cycle: +1, Force: 142.1 kips, Displacement: 8.64 in.)

push cycle of ductility 3, there was further grout spalling on the north side of the south column and the first row of shear studs was visible. The separation between the pile and the grout ring on the south side during the same cycle increased to 0.7".

On every subsequent cycle, the load in the system dropped. During the first push of ductility 4, significant local buckling was observed in both columns, as shown in Figure 5.35b. All three cycles at ductility 4 were then completed without any sign of tear or rupture. After the first push cycle of ductility 5, some tear marks developed on the north column (Figure 5.37b). The specimen was then subjected to the first pull cycle at ductility 5. During this cycle, a loud popping sound was heard. Upon investigation, no pipe rupture had occurred yet. It is thought that the shear studs on the columns were bearing against the stub wall and consequently slipped with a sudden release of stored strain energy causing

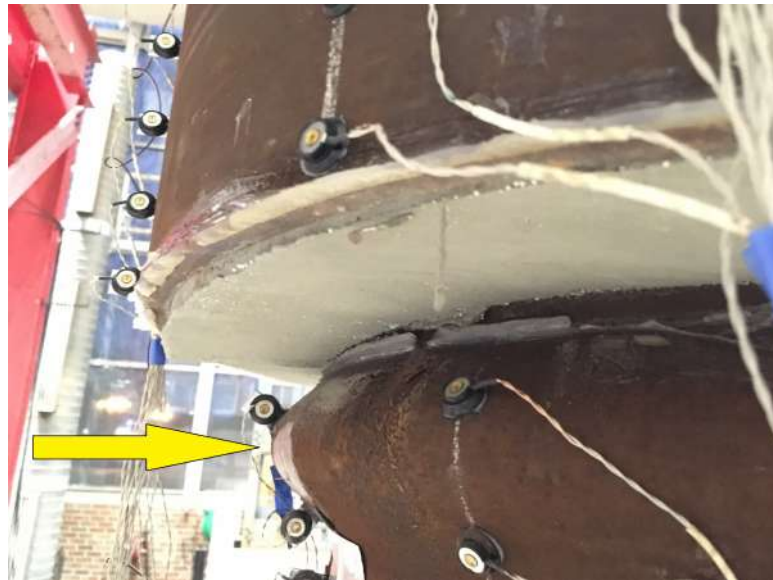


Figure 4.20 Pile wall local buckling (Ductility: 4, Cycle: +1, Force: 112.2 kips, Displacement: 11.50 in.)



Figure 4.21 Pile wall local buckling (Ductility: 5, Cycle: +1, Force: 84.1 kips, Displacement: 14.21 in.)



Figure 4.22 Structure drift of 11% (Ductility: 5, Cycle: +1, Force: 84.1 kips, Displacement: 14.21 in.)

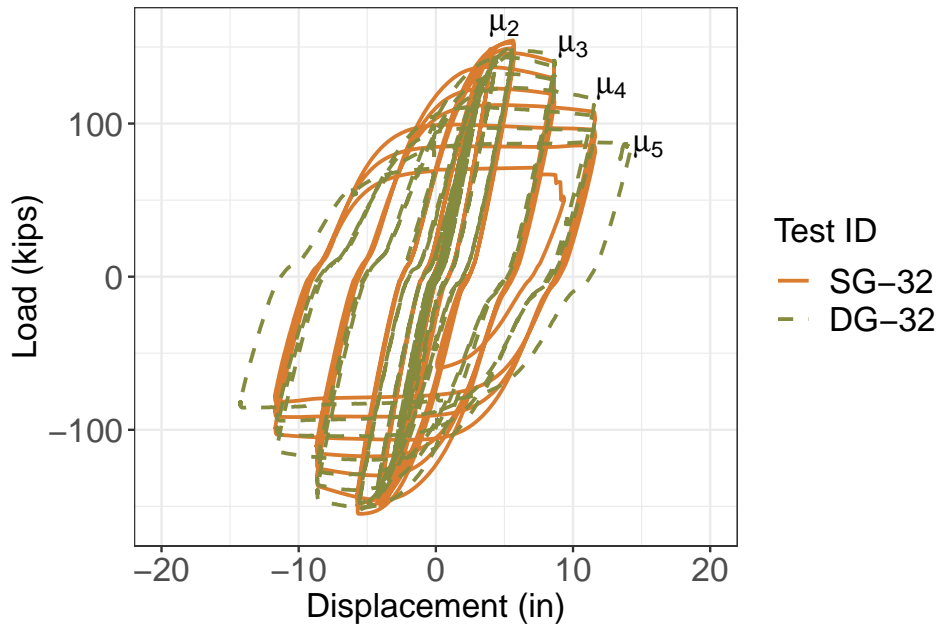


Figure 4.23 A comparison of the force-displacement hysteretic responses: Test 1 (SG-32) v Test 2 (DG-32)

the popping sound. The specimen was then brought back to zero force. By this point, the load had dropped by 60% and the specimen had attained a drift of 11% as shown in Figure 4.22. The test was terminated at this point because of stability concerns.

4.2.4.4 Results and Discussion

A comparison of the force-displacement responses of tests 1 and 2 is shown in Figure 4.23. In the figure, the notation SG-32 is the code for standard grout with 32 shear studs in the GSS connections of the corresponding test. Similarly, DG-32 is the code for deteriorated grout with 32 shear studs in the GSS connections of that test. Hence, Figure 4.23 shows the effect of deteriorated grout on overall structural response.

During the elastic cycles, test 2 specimen had a slightly reduced stiffness compared to Test 1 (Figure 4.24a). This was expected since the grout in test 2 had a reduced elastic modulus or stiffness. However, this reduction is barely noticeable on the complete force-displacement hysteresis curve. In ductility 1 and 2 cycles, the curvature demand in the plastic hinge region for test 1 columns was higher than that of test 2. This larger curvature resulted in a slightly larger energy dissipation by test 1 specimen compared to test 2 specimen (Figure 4.24b). The reduction in curvature demand in Test 2 specimen may be attributed to the higher flexibility of the grout as well as the gap that opens between the column and the grout ring.

During ductility 3 cycles, test 1 specimen had already started to lose its load carrying capacity as the plastic hinge was fully developed, and there was minor local buckling, as shown in Figure 4.25a. The section just below the plastic hinge pinched and thereby reduced the section modulus. test 2 specimen only started to lose strength at subsequent cycles, albeit at the same ductility. During ductility 4 cycles, both test 1 and test 2 started to show similar behavior once again (Figure 4.25b). Some differences here include a slightly higher load carrying capacity and a reduced reloading stiffness of test 2 specimen.

The observed differences between the global force-displacement response of the two specimens in tests 1 and 2 are minor from the perspective of satisfactory structural performance in an earthquake. Despite the grout properties being reduced considerably, the difference in the overall structural behavior of the two-column bent specimen is insignificant. These results suggest that a moderate to high level of durability damage is unlikely to compromise the structural integrity of the lateral load resisting system.

The force-displacement hysteretic curves of two tests (1 and 2) show a kink close zero

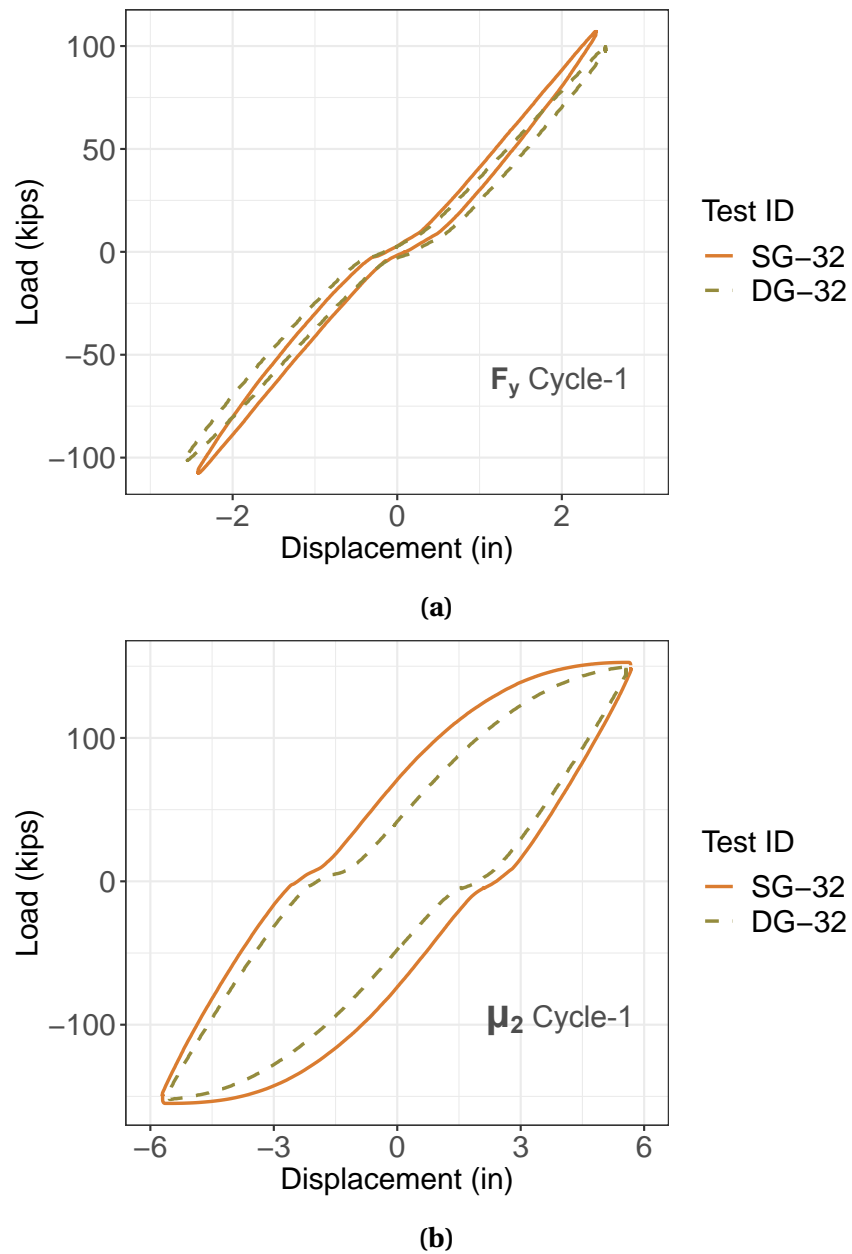


Figure 4.24 Comparison between hysteretic loops of Test 1 (SG-32) and Test 2 (DG-32) at different ductilities: (a) F_y (b) μ_2 .

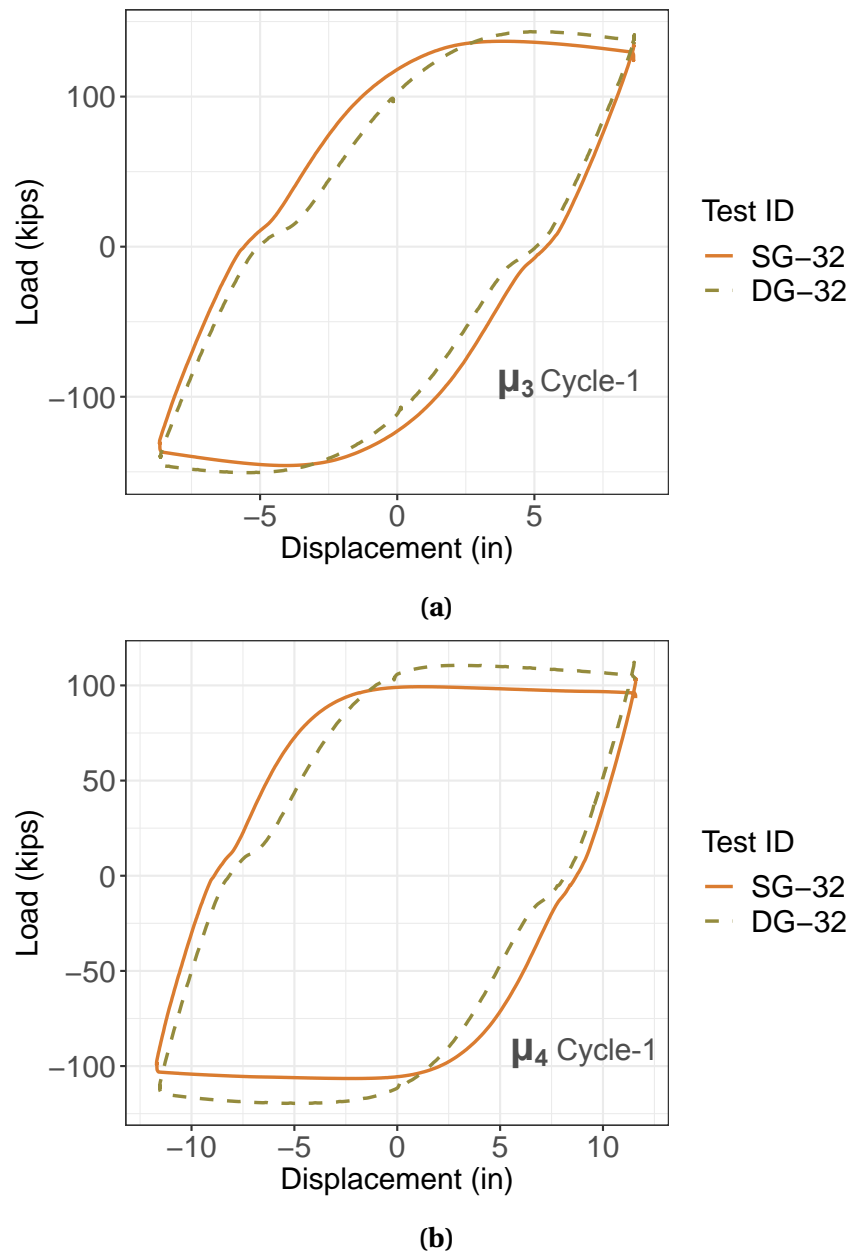


Figure 4.25 Comparison between hysteretic loops of Test 1 (SG-32) and Test 2 (DG-32) at different ductilities: (a) μ_3 (b) μ_4 .

force. Recall, that this kink or slip was not observed for test 0. The hypothesis of the gap opening between the column and the grout ring causing this “slip” in the hysteresis curve was corroborated in test 2. As discussed earlier, the gap that opened between the column and the grout in test 2 was much larger than that in test 1. This observation corresponds to the larger kink in the force-displacement response. Later (tests 3 and 4) produced further support for this hypothesis.

4.3 Chapter Summary and Conclusions

4.3.1 Summary

In this chapter, we discussed the large scale structural tests that were performed to determine whether grout deterioration in cold climates could cause significant problems for satisfactory performance of the GSS connection. Our approach was to test two large scale specimens that incorporated the GSS connection. While standard grout was used for the fabrication of the GSS connections in the first specimen, a grout mix designed to simulate representative conditions of cold climate deterioration was used in the fabrication of the connections in the second. The specimens used were two-column steel bridge bents connected to the floor by pin supports. The specimens were subjected to cyclic quasi-static lateral loading that simulated the demand on the real bridge bent from an earthquake. The global response of both specimens was measured and compared. The results suggest that a moderate to high level of grout damage due to cold climate exposure is unlikely to cause any significant deficiencies in the satisfactory structural performance of the GSS connection.

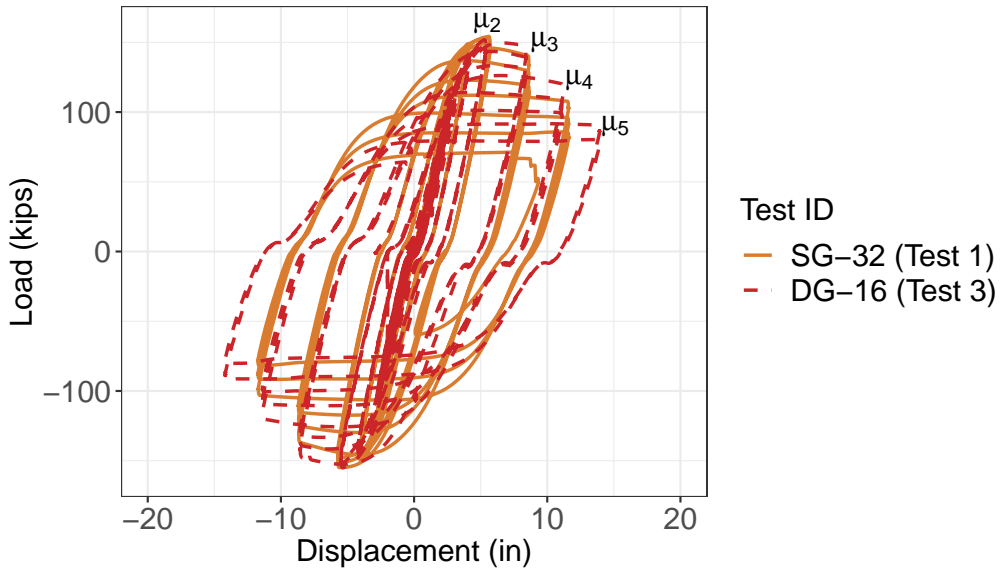


Figure 4.26 A comparison of the force-displacement hysteretic responses: Test 1 (SG-32) v Test 3 (DG-16)

4.3.2 Concluding remarks

After large scale tests 1 and 2, the research team met with AKDOT on February 1, 2019, to discuss project direction. In this meeting, it was decided to not pursue testing more specimens with further reduced grout properties in the connections. The subsequent tests would be used to determine the force transfer mechanism occurring within the GSS connection. This new path is discussed in detail in Chapter 5. However in hindsight, the results of the third large scale test (test 3) provide information relevant to this chapter. A short discussion follows.

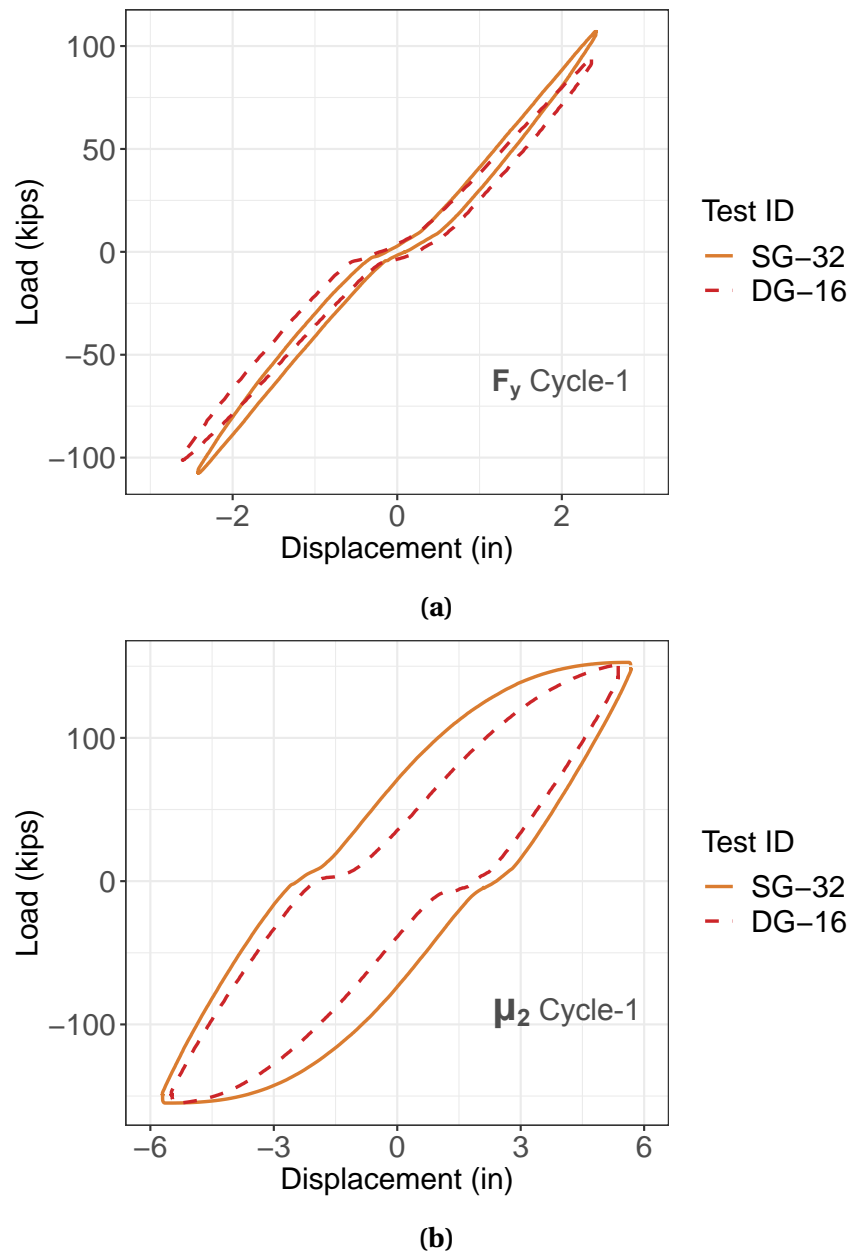


Figure 4.27 Comparison between hysteretic loops of Test 1 (SG-32) and Test 3 (DG-16) at different ductilities: (a) F_y (b) μ_2 .

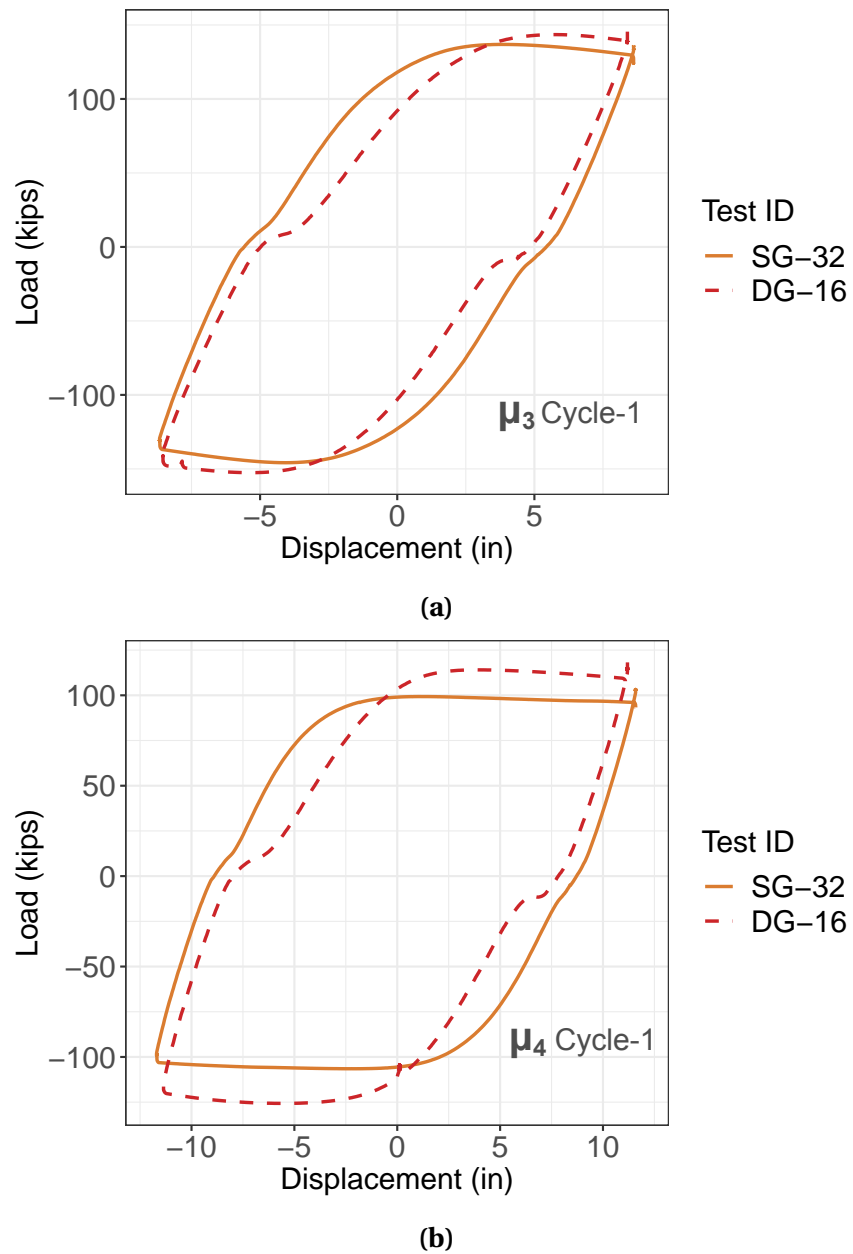


Figure 4.28 Comparison between hysteretic loops of Test 1 (SG-32) and Test 3 (DG-16) at different ductilities: (a) μ_3 (b) μ_4 .

4.3.3 Relevant results from Large Scale Test 3

Test 3, discussed in detail in Chapter 5, was performed on a two-column bent specimen that closely represented the test 2 specimen. The only difference between the specimens of tests 2 and 3 was the number of shear studs per GSS connection of each test. While the test 2 specimen had 32 shear studs in each of its connections, test 3 had only 16. However, this difference in the number of shear studs did little to affect the global structural behavior. A full description of the reasons for this behavior is provided in Chapter 5.

Since the difference in the number of shear studs was inconsequential, in hindsight, test 3 can be construed as a repeat of test 2. Comparing the results of test 3 to those of the control test (test 1) can either corroborate or invalidate the conclusions that were made based on the comparisons of test 1 and test 2. Figure 4.26 shows the comparison of the global force-displacement response of tests 1 and 3. The comparison looks strikingly similar to that of test 1 and test 2 in Figure 4.23. Force-displacement hysteretic loops at different ductility levels were also compared, as shown in Figure 4.27 and 4.28. The results show a similar trend as that seen in Figure 4.24 and 4.25, discussed earlier.

Test 3 did not invalidate any of the conclusions made after test 2. Therefore, it can be said with a higher certainty that grout deterioration within the GSS connection may be inconsequential from its structural performance standpoint.

CHAPTER

5

FORCE TRANSFER MECHANISM IN THE GSS CONNECTION

5.1 Introduction

The second large scale test which showed similar global behavior as the first, despite having weaker GSS connections, indicated that a moderate to high level of durability damage might not be a significant concern for design. According to the original plan for the large

scale tests, the third and fourth tests were to contain even weaker grout within their GSS connections. However, after a meeting with AKDOT, it was concluded that there was likely no new knowledge to be gained by following this plan. An alternative plan was suggested by AKDOT for carrying out the remaining two large scale tests.

Since tests 1 and 2 revealed that GSS connections with a much lower number of shear studs could satisfactorily protect the weld and relocate the plastic hinge to the column, AKDOT engineers were interested in determining the minimum number of shear studs required for a reliable design. AKDOT was also interested in investigating the repercussions of a lower socket depth (length of the stub pipe) on the structural performance. Information to help answer these questions, either wholly or partially, was important from a design perspective. Ideally, if the force transfer mechanism within the GSS connection can be described with a mechanics based mathematical model, this model can be used by engineers to better design steel bridge substructures through performance based and capacity design principles.

This chapter describes the approach that was taken to obtain more information regarding the force transfer mechanism within the GSS connection. Tests 3 and 4 were carried out to serve this purpose, and they provided valuable information regarding potential mechanisms involved within the connection during earthquakes. This information was used subsequently to develop a design model for the GSS connection, which is discussed in the following chapter.

5.2 Background

To better understand the approach, it is useful to discuss the background of large scale testing of the GSS connection, and how an understanding of the connection behavior has evolved over time.

In 2010, Fulmer et al. [Ful10b] investigated multiple design details for steel bridge column-to-cap-beam connections. The takeaway from this study was that among the connection details tested, the GSS connection was the most efficient in forcing the lateral load resisting system to predictably fail in a ductile manner. The study successfully showed the proof of concept of the GSS connection. The authors were only interested in achieving plastic hinge formation in the columns by capacity protecting the connection. Therefore, they followed a conservative design procedure for the GSS connection with available data on the capacity of shear stud connectors.

The mechanism of force transfer within the GSS connection was thought to be through a formation of complex compression struts between the shear studs on the column and the stub. The connection under tensile axial loading resulting from lateral loads in a two-column bent was considered as the critical connection. The column in such a connection is under the danger of being pulled out of the socket, if nothing resists the pull out. Given the capacity of a single shear stud, calculated according to Equation 5.1, they calculated the total number of shear studs required to resist the axial tension demand in the connection using Equation 5.2. The tensile axial demand in the connection was in turn calculated as the full axial yield force in the column section, per Equation 5.3.

$$Q_n = 0.5A_{sc} \sqrt{f'_c E_c} \leq A_{sc} F_u \quad (5.1)$$

$$N_{req} = \frac{T_y}{Q_n} \quad (5.2)$$

$$T_y = f_{y,exp} A_{g,col} \quad (5.3)$$

In Equations 5.1 to 5.3,

Q_n = Capacity of a single shear stud, kips

A_{sc} = Cross-section area of a shear connector, in²

f'_c = Compressive strength of surrounding grout, ksi

E_c = Elastic modulus of surrounding grout, ksi

F_u = Ultimate tensile strength of the shear connector, ksi

N_{req} = Required number of shear connectors

T_y = Axial tension demand on the GSS connection, kips

$f_{y,exp}$ = Expected yield strength of the column steel, ksi

$A_{g,col}$ = Gross cross-section area of the column, in²

This design procedure lead to a total of 96 shear studs of 3/4" diameter in a single GSS connection, 48 on the column and 48 on the stub pipe. All of the structural tests of two-

column bridge piers with this connection lead to successful outcomes. Plastic hinge relocation was achieved and the column section failed by rupture well after local buckling. One of the large scale tests performed by Fulmer et al. [Ful15] is discussed here. This test is referred to as Test 0 in this report and is relevant to the discussion of understanding the force transfer mechanism within the connection.

5.2.1 Large Scale Test 0

5.2.1.1 Introduction

As part of evaluating alternate steel column to cap-beam connections, Fulmer et al. [Ful15] performed four large scale tests on two-column bridge pier specimens incorporating the GSS connection. Out of all of the modified connection details, the GSS connection had previously stood out in its ability to aid and relocate the plastic hinge formation to the columns in a predictable, and reproducible manner. One of the four tests performed by Fulmer et al. [Ful15] is discussed in detail here because of its relevance to the problem at hand. It is referred to as test 0 (or SG-96) to differentiate it from the four new tests performed as part of this project. The new tests are referred to as Tests 1 through 4 (or SG-32, DG-32, DG-16, and DG-16-SS).

5.2.1.2 Experimental Setup

ASTM A500 Gr.B HSS 16×0.500 piles were chosen as the columns of the specimen. The cap-beam consisted of double ASTM A572 HP 14×117 sections to provide both a capacity protected cap element as well as adequate bearing seat width for single span girders, should a designer choose not to utilize continuous spans. Furthermore, in the case of the grouted

shear stud connection, a multi-wide HP cap beam was necessary to accommodate the size of the 24" diameter stub pipe sections. The 24"×0.500" pipe sections were manufactured to the material standards of ASTM A500 Gr. B specification. The diameter of the stub pipe was selected to provide an adequate gap for the placement of shear studs as well as to accommodate construction tolerances.

A total of 96, 3/4" dia., mild steel shear studs were welded inside each GSS connection. Forty eight were welded on the outside of the column and inside of the stub pipe. To generate a symmetrical condition, 12 vertical lines of 4 shear studs each, at 30 degrees on center, were used as shown in the photograph in Figure 5.1. To complete the connection, a high-strength cementitious grout material was then placed in the annular space formed by the pipe sections. This grout material was the same as that with the designation CG1 in the durability study discussed in Chapter 2. To assist in minimizing the possibility of air voids within the annular grout pocket, the grout was pumped vertically from the bottom of the connection to the top, where 1" diameter holes had been drilled in the cap beam flange to allow air to escape. A hand operated pumping system was utilized along with shut off valves that were attached onto the formwork and later removed to facilitated pumping of the grout. Note that this process was different from the one that was followed in the construction of specimens in tests 1 to 4. For tests 1 to 4, the grout was cast from the top of the connection through a larger hole on the cap-beam bottom flange.

5.2.1.3 Results and Discussion

The material yield stress was found to be 56.5 ksi for the A500 Gr. B columns. This yield stress resulted in a calculated first yield force of 93.3 kips, according to Equation 4.1. The



Figure 5.1 Shear stud detail and constituent elements of the specimen in Test 0.

experimentally determined yield displacement was 2.15 in and the equivalent yield or ductility 1 displacement was calculated to be 2.82 in, according to Equation 4.2. The measured average compressive strength of the grout material at 19 days (time after casting) was 6.85 ksi. Note that this is much lower than the strengths measured during the durability study as part of the current project. Measured 7-day strengths in excess of 8.8 ksi for the same grout material were obtained in this study. This reduced strength could be because the amount of water used by Fulmer et al. [Ful15] was much larger than bag labelled specifications. Therefore, it is recommended to be mindful of contractors not following manufacturer specifications. Specific directives can go a long way in controlling grout durability.

The force-displacement hysteretic response of test 0 is shown in Figure 5.2. Initiation of pile wall local buckling was observed as early as the third positive cycle of ductility 2 as shown in Figure 5.3. However, no strength loss was observed at this point. The second and

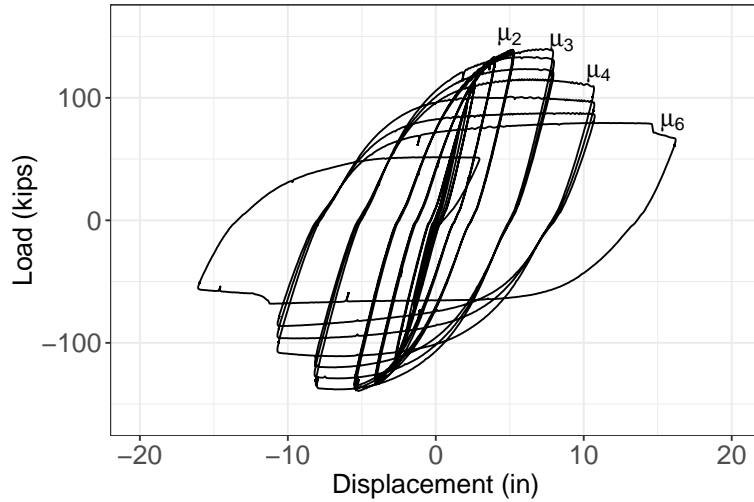


Figure 5.2 Force-displacement hysteresis of the two-column bridge bent specimen tested by Fulmer et al. [Ful10b], referred to as Test 0 in this report

third cycles of ductility 3 level produced propagation of the pile wall local buckling which consequently led to strength reductions of approximately 10% and 15%, respectively. It was during these cycles that significant grout spalling was observed, as shown in Figure 5.4. The grout located below the first row of shear studs began to spall out. Cycles at ductility 4 level started to produce tears in the buckled region of the pile walls. The test was terminated at the first negative cycle of ductility 6 when the pile wall finally ruptured at the buckled region (Figure 5.5). This mode of failure was the expected mode, i.e., the plastic hinge being relocated to the columns allowing high ductility cycles with gradual strength loss before failure. The specimen achieved a maximum drift of 12% as shown in Figure 5.6.

This test along with three other similar tests performed by Fulmer et al. [Ful15], conclusively showed that the GSS connection can successfully relocate the plastic hinge, thus protecting the weld connecting the stub pipe to the cap-beam.

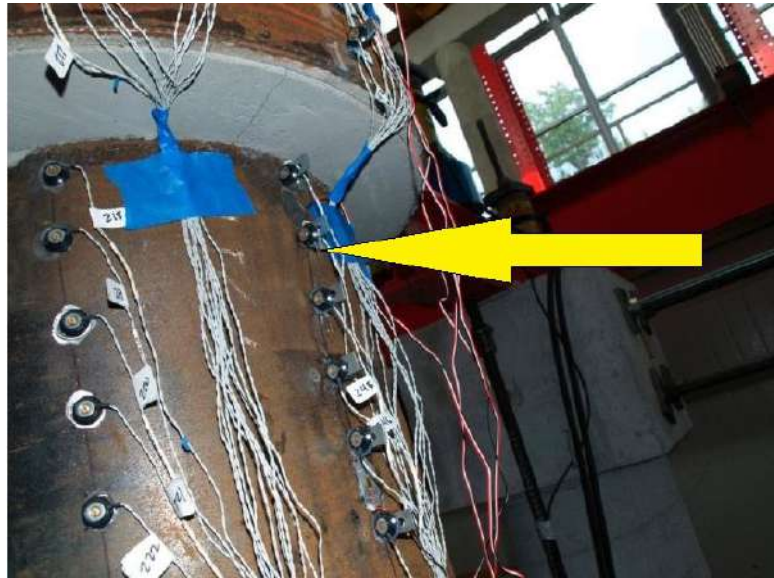


Figure 5.3 Observed local buckling initiation pile wall (Ductility: 2, Cycle: -3, Force: -132 kips, Displacement: -5.62").



Figure 5.4 Observed grout spalling and tear marks on the pile wall (Ductility: 4, Cycle: 3, Force: 85 kips, Displacement: 11.25").



Figure 5.5 Specimen failure mode of pile wall rupture (Ductility: 6, Cycle: -1, Force: -54 kips, Displacement: -16.88").



Figure 5.6 Drift of 12% was observed at termination of Test 0 [Ful10b] (Ductility: 6, Cycle: 1, Force: 75 kips, Displacement: 16.88")

5.3 Large Scale Experiments on Two-Column Bridge Piers - Part 2

5.3.1 Introduction

While planning the large scale tests for this project, 96 shear studs per GSS connection were deemed to be overly conservative. The full axial yield force of the column section in a two-column bent is seldom developed. Bending of the columns results in plastic hinging at the peak lateral load. Further cycles will result in reduced loads because of the pinching of the section. Therefore, the critical maximum axial load demand developed in the connection will be the tensile axial load corresponding to the peak lateral load in the system. This demand requires many fewer shear studs.

In tests 1 and 2, discussed in the previous chapter, only 32 shear studs per connection were used. Table 5.1 shows the large scale test matrix used to determine the force transfer mechanism of the GSS connection. The naming scheme for “Test ID” follows “SG” or “DG” for standard grout or deteriorated grout, respectively. The number that follows represents the total number of shear studs per connection. The abbreviation “SS” for Test 4 stands for the shorter stub length. The parameters that were varied in the tests were the number of shear studs per connection and the socket depth of the connection. The number of shear studs was varied in tests 0 through 3, while the socket depth was changed only for test 4. It was later determined that the socket depth is much more important than the number of shear studs to successfully achieve plastic hinge relocation.

Tests 0, 1, and 2 have already been discussed in detail, elsewhere in this report. The

Table 5.1 Test matrix used to determine the force transfer mechanism of the GSS connection.

Test No.	Test ID	Shear Studs	Stud Area	Socket Depth	Performance
0	SG-96	96	42.4 in ²	24"	Adequate
1	SG-32	32	25.1 in ²	24"	Adequate
2	DG-32	32	25.1 in ²	24"	Adequate
3	DG-16	16	12.6 in ²	24"	Adequate
4	DG-16-SS	16	12.6 in ²	16"	Inadequate

next section discusses tests 3 and 4. Following that, this chapter is concluded with results and discussion.

5.3.2 Large Scale Test 3

5.3.2.1 Introduction

Tests 0, 1, and 2 showed similar results despite the number of shear studs per connection was reduced from 96 to 32. This result suggested that the number of shear studs may not be as important in force transfer as previously thought. However, the plastic bending moment developed at the column-to-connection interface was somehow resisted successfully in all the three tests. An alternate load path must have developed to explain this behavior. To be fully certain of the impact of shear studs, the number of shear studs was further reduced to 16, 8 on the column and 8 on the stub pipe, for the third large scale test.

5.3.2.2 Experimental Setup

The test specimen was a large scale two-column steel pier similar to the one used in tests 1, and 2. Test 3 followed the same displacement history as that of Test 1. The entire test was

performed in displacement control mode. After elastic cycles, three cycles at each ductility level were applied until test termination. The instrumentation scheme consisted of electrical resistance strain gages, string potentiometers, and OPTOTRAK sensors, the same as in test 1.

Fabrication of the cap-beam pipe-stub assembly was performed in the shop by a certified welder. The shear stud welding on the columns and stubs was also performed by the same welder. Because each stud was welded manually, one sample was subjected to a bend test to ensure the integrity of the welding. The weld did not fracture after the shear stud attained a large plastic deformation, as shown in Figure 5.7. The number of shear studs per connection was reduced to 16 in this test. As a consequence, a choice regarding the locations for each row of shear studs was required. Figure 5.8 shows a schematic of how the rows of shear studs were arranged with relative to each other among the three tests. In test 3, the second and fourth rows of shear studs from the top, were cut off to obtain the desired number of 16 shear studs. The clear grout cover in the connections of the test 3 specimen was 8".

The next step of the construction process was erecting the two pile columns on pin supports. This was achieved by tying the erected piles to the floor using ratchet straps and D-rings. The cap-beam stub assemble was then brought in and lowered onto the two columns. The columns were inserted into the sockets created by the pipe stubs until the cap-beam rested on top of the columns. No additional welding was performed to connect the columns to the cap-beam.

Once the cap-beam was in place, the annular regions surrounding the column tops were filled with grout to complete the GSS connections. The grout was pumped with a



Figure 5.7 Result of the bend test on a sample 1" diameter shear stud.

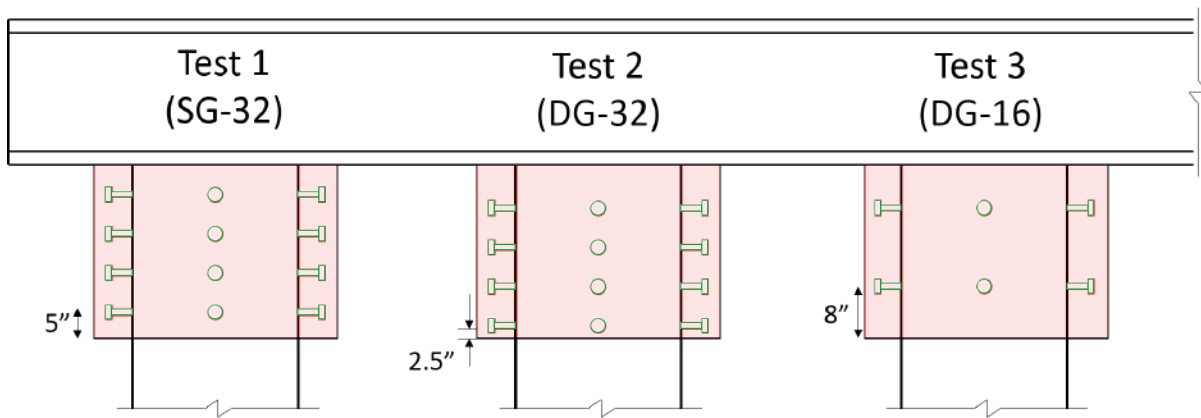


Figure 5.8 Comparison of the locations of shear studs in each of the first three large scale tests
(Not to scale).

pump through an opening on the bottom beam flange at the top of the connection. EPS beads were added to the grout mixture to simulate deterioration. To prevent segregation and migration of EPS beads, the connections were cast in layers as discussed in Chapter 4.

5.3.2.3 Experimental Summary

The structural test was performed 7 days after casting the grout in the GSS connections. Cyclic quasi-static loading was applied to the two-column steel pier in the displacement control mode. The initial load rate was 1.5 in/min which was later changed to 4 in/min in the inelastic cycles. Two cycles at each force level ($0.25F_y$, $0.50F_y$, $0.75F_y$, and F_y) were applied first. Visible separation of the grout ring from the pile wall was observed around $0.75F_y$. Radial cracks near the neutral axis of the connection started to develop in both connections, as shown in Figure 5.9. The cracks multiplied during the first cycle of ductility 1.

After three cycles at ductility 1, the gap between the grout ring and the pile column opened to about 0.1". This gap increased with each successive ductility level until it reached its widest at ductility 3, around 1.5", as shown in Figure 5.10. Unlike the previous tests, no grout spalling was observed at the bottom of the grout ring on the extreme fibers during bending. Figure 5.11 shows the state of the grout at ductility 3 during this test. By ductility 3, tests 1 and 2 had already started to show signs of grout spalling.

Pile wall local buckling was observed on the south side of the north column on the first push cycle of ductility 3 (Figure 5.12). On the subsequent pull cycle, the north side of the south column also experienced pile wall local buckling. On every subsequent cycle, the load in the system dropped. During the first push of ductility 4, significant local buckling



Figure 5.9 Cracks observed at the neutral axis of the GSS connection (Ductility: 1, Cycle: 1, Force: 111 kips, Displacement: 2.79")



Figure 5.10 The gap between the column wall and the grout ring. (Ductility: 3, Cycle: 1, Force: 145.1 kips, Displacement: 8.39")



Figure 5.11 GSS connection at ductility 3; No grout spalling was observed in Test 3. (Ductility: 3, Cycle: 1, Force: 145.1 kips, Displacement: 8.39")



Figure 5.12 Minor buckling observed on the north column. (Ductility: 3, Cycle: 1, Force: 145.1 kips, Displacement: 8.39")

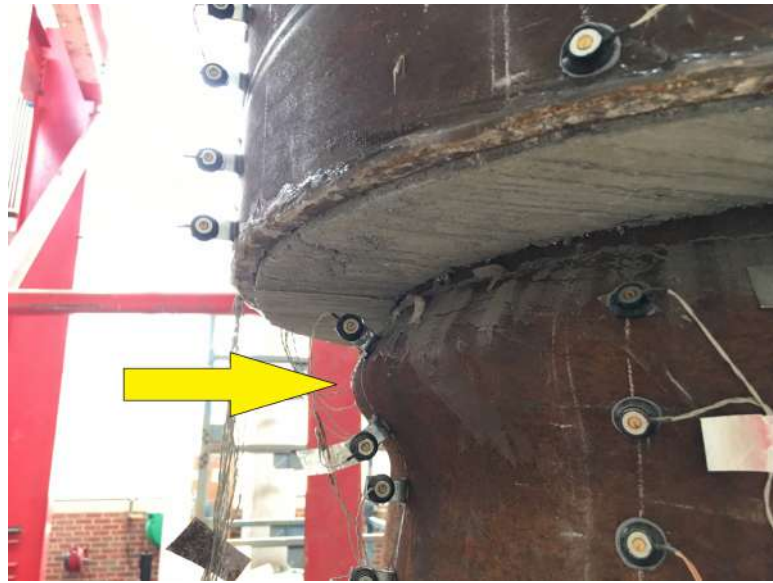


Figure 5.13 Minor buckling observed on the north column. (Ductility: 4, Cycle: 1, Force: 119.1 kips, Displacement: 11.19")

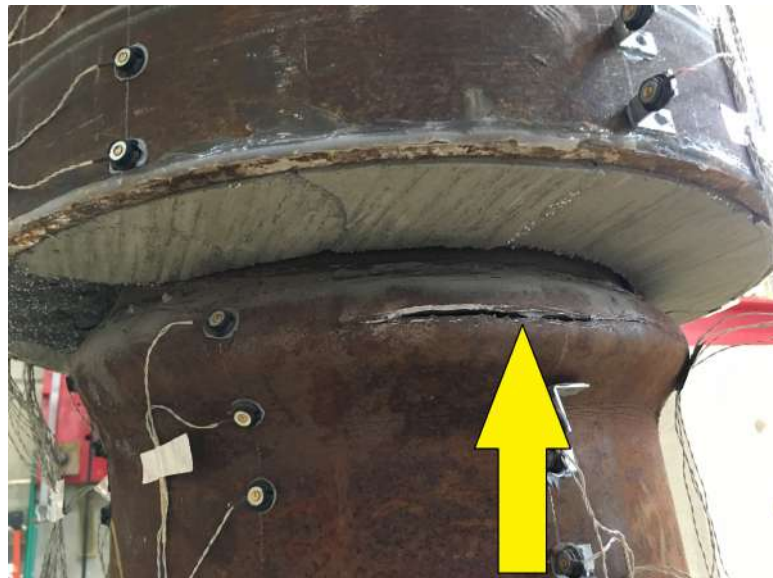


Figure 5.14 Minor buckling observed on the north column. (Ductility: 5, Cycle: 3, Force: -77.5, Displacement: -14.18")



Figure 5.15 Final drift of 11% achieved by the test 3 specimen.

was observed in both columns, as shown in Figure 5.13. All three cycles at ductility 4 were then completed without any sign of tearing or rupture. After the first push cycle of ductility 5, some tear marks developed in the north column. Pile wall rupture was observed during the third cycle of ductility 5, as shown in Figure 5.14. During ductility 5 cycles, two popping sounds were heard similar to that in Test 2. This could have been the shear studs rubbing against the wall of the stub pipe. At the end of Test 3, the load had dropped by 60% and the specimen had attained a drift of 11% as shown in Figure 5.15.

5.3.2.4 Results and Discussion

A comparison of the force-displacement responses of tests 1 and 2 is shown in Figure 5.16. Overall, the global behavior of both the tests is almost identical. Similarly, the force-displacement response of tests 0 and 1 is compared in Figure 5.17. In both of these compar-

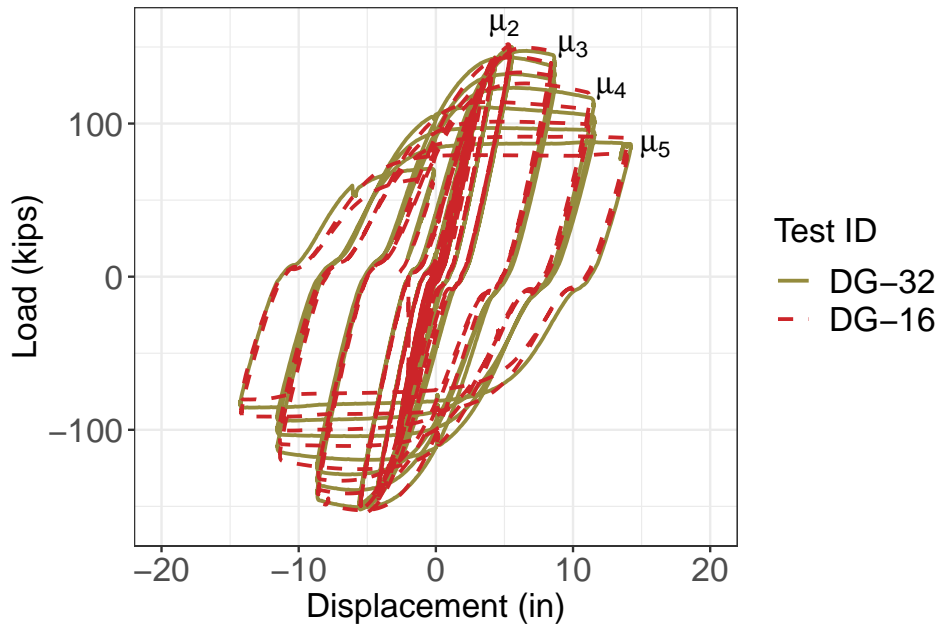


Figure 5.16 A comparison of the force-displacement hysteretic responses: Test 2 (DG-32) and Test 3 (DG-16)

isons, the only parameter that changed is the number of shear studs per GSS connection. The similarity in their global responses, despite the reduction in the number of shear studs per connection, suggests that the contribution of the shear studs to resisting the bending moment demand on the connection, is likely minor.

A closer look at the individual loops of tests 0, 1, 2, and 3 does show some effect of the number of shear studs in a connection. For example, in Figures 5.18 through 5.21, all four aforementioned tests are compared at each ductility level. In each figure, a zoomed in version of the plot on the left, near the zero force region, is shown on the right. In this region, one can observe a “slip” in the force displacement response of tests 1, 2, and 3, that have 32, 32, and 16 shear studs, respectively. This behavior is not present in the response of test

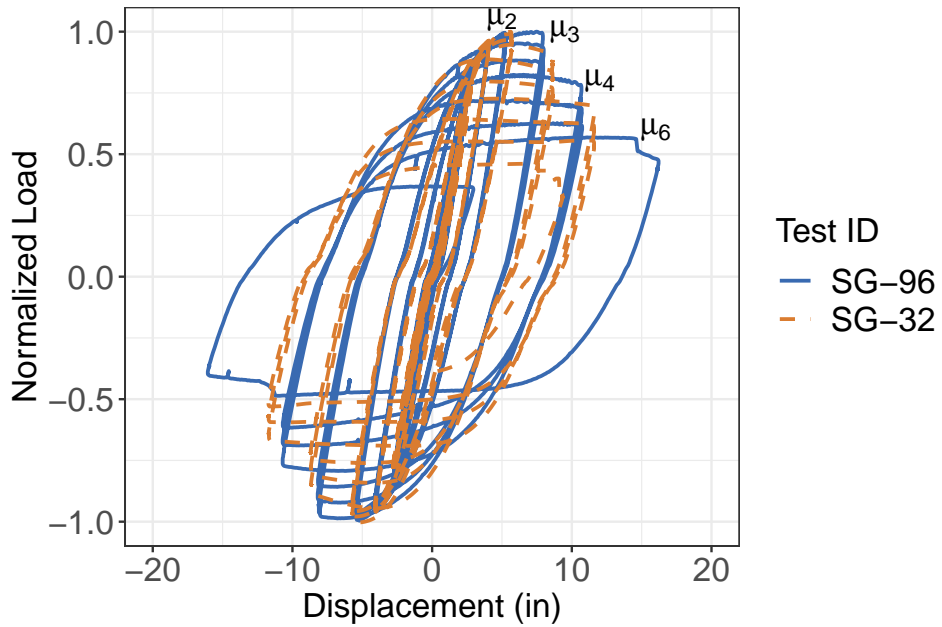


Figure 5.17 A comparison of the force-displacement hysteretic responses: Test 0 (SG-96) and Test 1 (SG-32)

0, that has 96 shear studs per connection. The magnitude of the slip in displacement is higher for each successive ductility level. It is also clear that the slip increases as the number of shear studs per connection decreases. Although grout deterioration also contributes to this phenomenon, the contribution of shear studs is also as significant, if not more so.

One hypothesis to explain this behavior is the contribution of the shear studs to the size of the gap that opens between the column wall and the inside of the grout ring. The shear studs close to the bottom of the connection are engaged in tension providing resistance to the opening of the gap. Since test 0 had the highest number of shear studs close to the bottom, the gap size may have been significantly reduced. As the number of shear studs reduced in subsequent tests, the resistance to gap opening reduced, resulting in larger gaps.

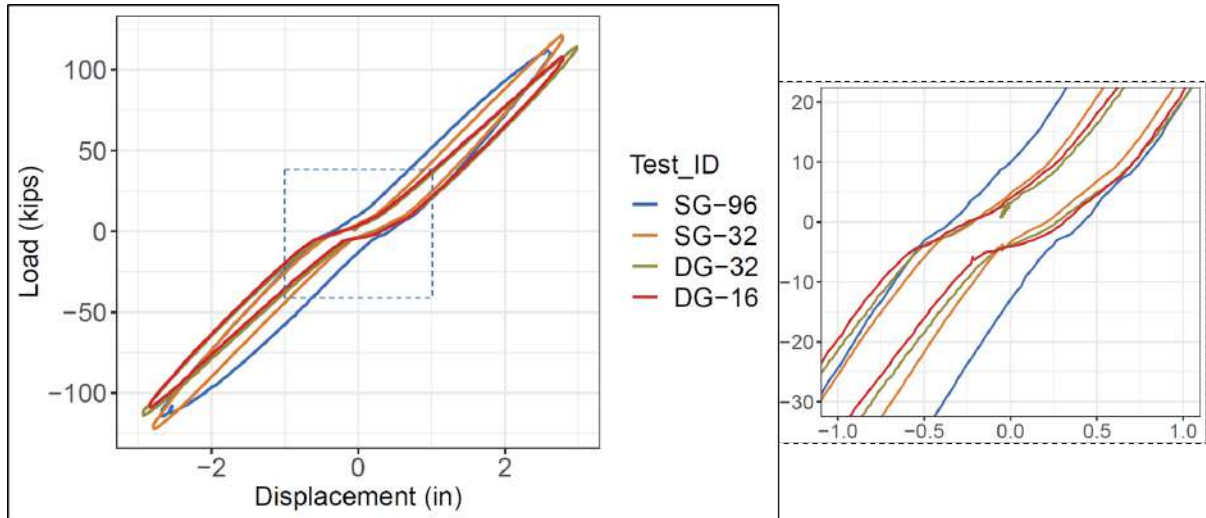


Figure 5.18 Comparison of the slip in the force-displacement response in ductility 1 cycle.

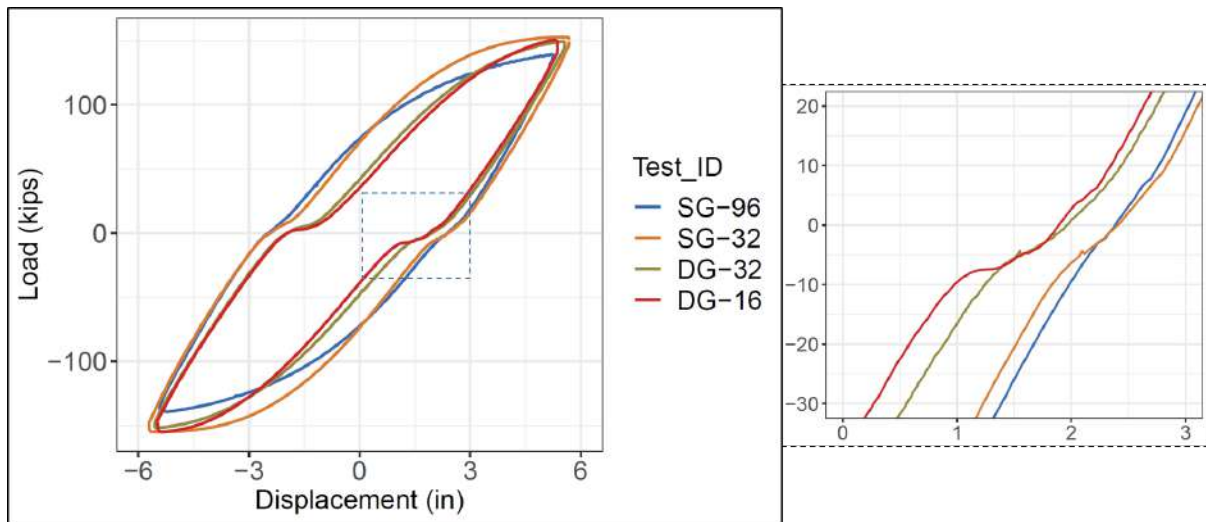


Figure 5.19 Comparison of the slip in the force-displacement response in ductility 2 cycle.

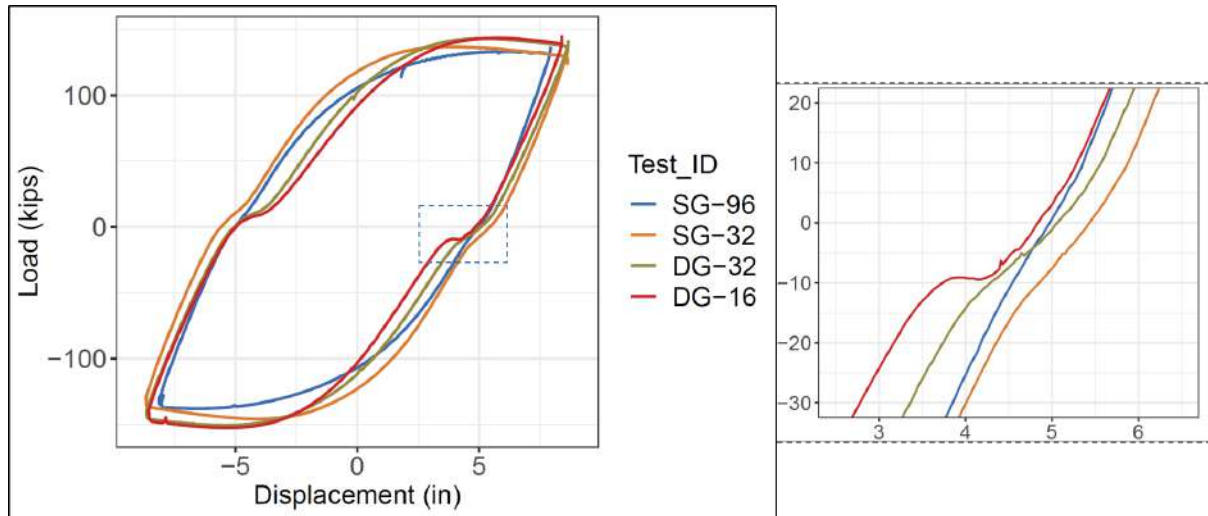


Figure 5.20 Comparison of the slip in the force-displacement response in ductility 3 cycle.

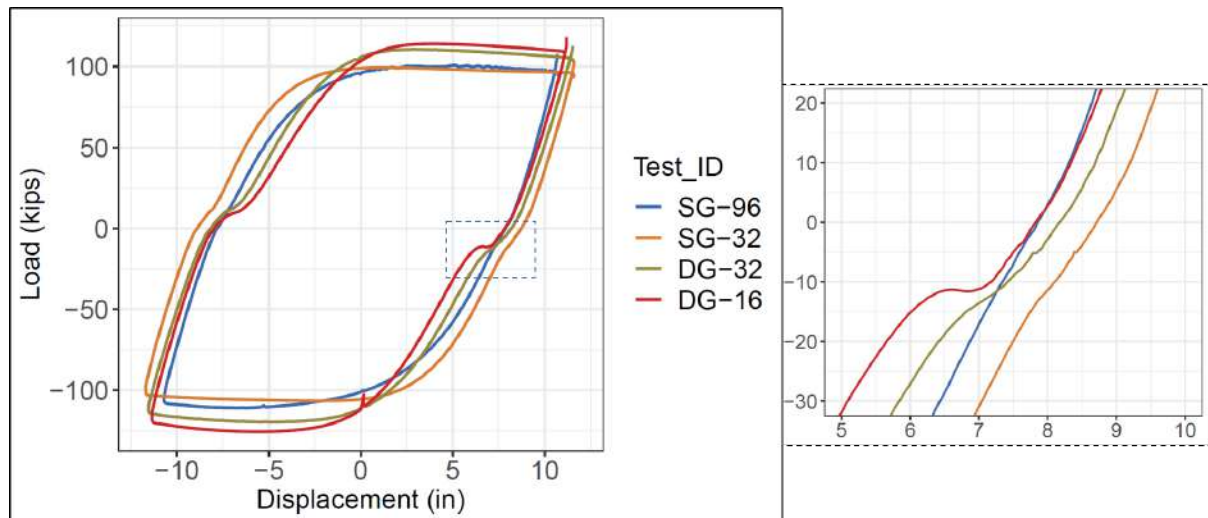


Figure 5.21 Comparison of the slip in the force-displacement response in ductility 4 cycle.

These gaps allow the columns to rock within the connection. When the gap shifts from one side to the other as the tension and compression sides reverse, the size of the gap dictates the amount of displacement observed with little additional force input, which is reflected as the slip in the hysteretic response. This phenomenon, however, is but a minor observation from the perspective of successful structural performance under lateral loading. The difference in energy dissipation characteristics, as well as the failure limit state achievement is negligible among the four tests. Hence, it is concluded that the number of shear studs may have a relatively minor impact on the structural performance of the GSS connection. A discussion of the role of shear studs is provided in last section of this chapter.

5.3.3 Large Scale Test 4

5.3.3.1 Introduction

Test 3 results suggested the possibility of alternate load paths to resist the bending moment demand on the GSS connection. A plausible load path that was considered next was a pair of normal forces at the top and bottom of the connection producing a force couple that resists the bending moment.

Figure 5.22 shows a schematic of the dominant force transfer mechanism within the GSS connection. The maximum bending moment demand (M_p) is equal to the plastic moment of the column section. The tensile axial load demand (T_a) is equal to the axial load developed in the tension column of the two-column bent under lateral loading. To equilibrate the bending moment, a pair of normal forces, N_c and N_t , are developed due to the column bearing on the bottom and top of the GSS connection, respectively, under lateral loading. In addition, surface forces are developed parallel to the longitudinal axis of the

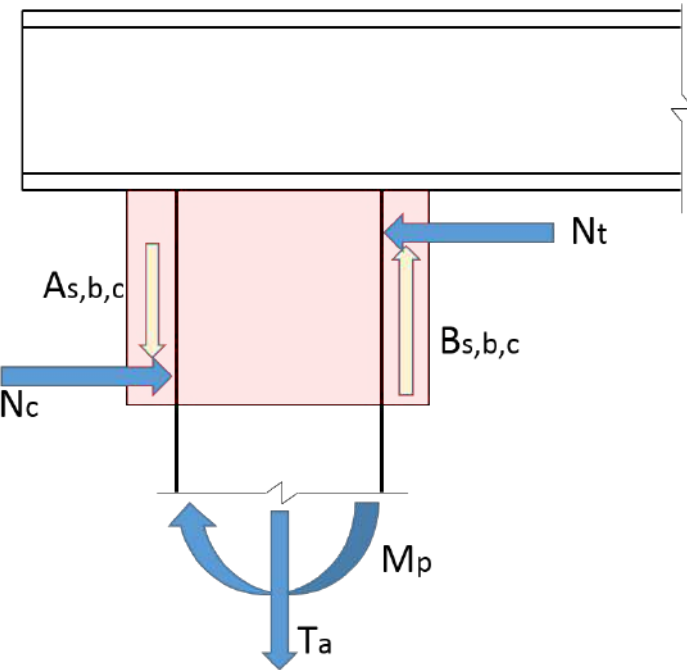


Figure 5.22 Hypothesized force transfer mechanism within the GSS connection.

column. These forces are named $A_{s,b,c}$ and $B_{s,b,c}$. The subscripts represent the potential contribution from multiple mechanisms such as shear strength of the studs (s), bond or friction between the steel and grout (b), and compression struts formed between the shear studs (c). These surface forces are opposite to each other but are not equal. These act in the same direction as the axial force demand in the connection and develop so as to resist pullout of the column.

To evaluate this model, the test 4 specimen was designed so that the GSS connections would have a reduced socket depth. This reduction in turn reduces the lever arm between the two normal forces thereby increasing the magnitude of forces to equilibrate the bending moment. In all of the previous tests, the ratio of the socket depth to the column diam-

eter was 1.5, which meant a 24" deep socket. For test 4, this ratio was reduced to 1, which meant a 16" deep socket. Figure 5.23 shows a visual comparison of the test specimens with 24" and 16" deep sockets.

5.3.3.2 Experimental Setup

Test 4 followed the same experimental setup as the previous three large scale tests. However, the socket depth of each connection was reduced to 16". This increased the shear span or clear height of the columns. Due to this increase, a choice regarding the loading protocol for this test was required. The increased clear height meant additional flexibility of the two-column bent system. If the loading protocol was based on system ductility, one would observe higher displacements in test 4 at the same ductility level, than in the previous tests. To be able to compare the force-displacement responses of all tests at equal displacements, it was decided to base the loading protocol on displacement rather than ductility. As a result, the same displacement corresponds to a smaller force in test 4 compared to the other three tests. It is important to note however, that in the following discussion, the term "ductility", is still used to refer to different levels of displacements. This reference to ductility is used for convenience in discussion, and is not the true ductility of the system.

5.3.3.3 Experimental Summary

During the test, grout cracking and spalling initiated early in the initial cycles at ductility 1, as shown in 5.24. The force in the system was also observed to drop in each successive cycle at ductility 1. A peak load of 108 kips was observed during the first cycle of ductility 2.



(a)



(b)

Figure 5.23 Specimens for large scale tests: (a) Test 3 (b) Test 4.

Grout spalling continued to excessive levels throughout the cycles at ductilities 1.5, and 2. During the first cycle of ductility 2, the gap between the column and the grout ring became visible, as shown in Figure 5.25. The grout above the first row of shear studs started pushing the stud down resulting in permanent bending of the stud on the north side of the north column (Figure 5.26).

The grout material did not mobilize the strength required to resist the bending moment. Once excessive grout spalling was observed, the column remained straight and rocked inside the connection under lateral load, as shown in Figure 5.27. It was clear at this point that the system did not possess enough capacity to form a plastic hinge in the columns. Hence, the test was terminated after the first cycle at ductility 3.

5.3.3.4 Results and Discussion

Figure 6.11 shows the comparison of force-displacement response of tests 3 and 4. Both of these tests had the same grout strength and number of shear studs per connection. The only variable was the socket depth. Figure 6.11 shows a striking difference between their responses. A shorter socketed depth completely changed the behavior of the lateral load resisting system. The columns did not dissipate energy and were at or below yield. The grout was unable to mobilize enough compressive strength to form the normal force pair.

The results indicate that the mechanism hypothesized earlier in this section may be correct. A deep enough socket depth or a long lever arm is necessary for the GSS connection to be able to relocate the plastic hinge to the column without premature failure.



(a)



(b)

Figure 5.24 (a) Grout spalling initiated (Ductility: 1, Cycle: 1, Force: 80.4 kips, Displacement: 2.87") (b) The first row of shear studs visible (Ductility: 1, Cycle: 3, Force: 74.4 kips, Displacement: 2.88").



Figure 5.25 Gap opening up between the pile and grout ring (Ductility: 2, Cycle: 1, Force: 107.9 kips, Displacement: 5.46").



Figure 5.26 Bent shear stud (Ductility: 2, Cycle: 3, Force: 85.5 kips, Displacement: 5.49").



Figure 5.27 Column remaining straight under lateral loading (Ductility: 3, Cycle: 1, Force: 96.1 kips, Displacement: 8.48").

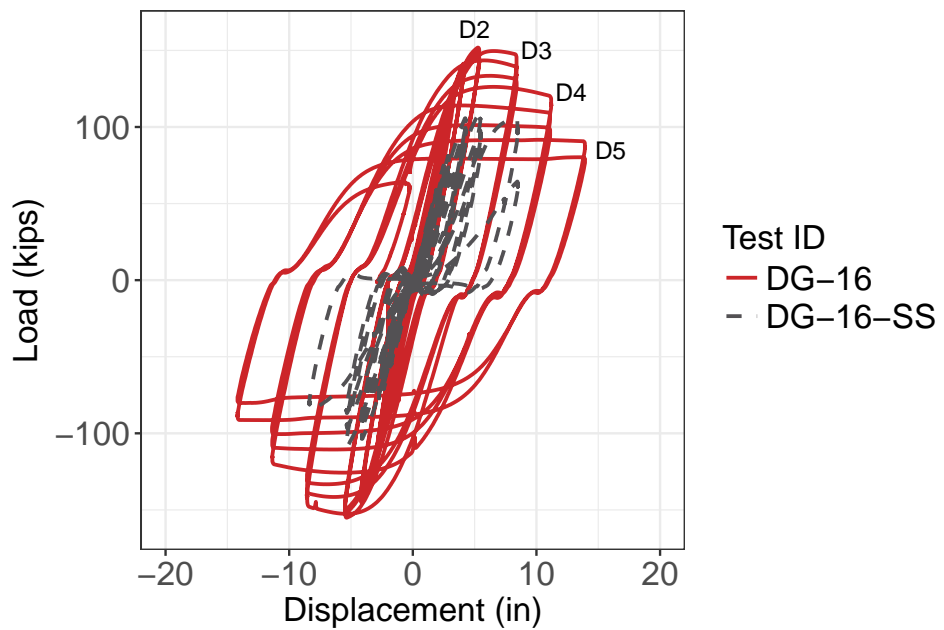


Figure 5.28 A comparison of the force-displacement hysteretic responses: Test 3 (DG-16) v Test 4 (DG-16-SS)

5.4 Limit States from Experimental Observations

Through observations during the large scale tests, we were able to identify five different limit states in the behavior of the GSS connection in a lateral load resisting system. These are discussed in this section. Note that these limit states occurred only for the GSS connections that were able to successfully relocate the plastic hinge to the columns. Experimental photographs from tests 1, 2, and 3 are compiled to discuss how each limit state was attained in each of the three tests.

5.4.1 Cracking at the Neutral Axis

At or above ductility 1, the grout rings in all three tests cracked radially at the neutral axis of the connection. The cracks were aligned transverse to the direction of loading, as shown in Figure 5.29. This cracking likely develops due to the following. Under lateral loading, the columns bear against the grout rings on the compression side, as shown in Figure 5.30. The bearing pressure on the inside of the grout ring on the compression side induces tensile hoop stresses. When this tensile stress exceeds the tensile strength of the grout material, cracking ensues. Note that this is a simplification, and the hoop stress profile along the grout ring circumference is likely more complicated as the internal pressure is not uniform. Subsequently, the reaction of the grout ring on the column section results ovalization of the section. While the extreme ends are pushed inwards, the section is pushed outwards at the neutral axis. This causes compressive stresses to develop around the neutral axis region of the grout ring which has already cracked. Previous cracking in this region allows the grout to spall.

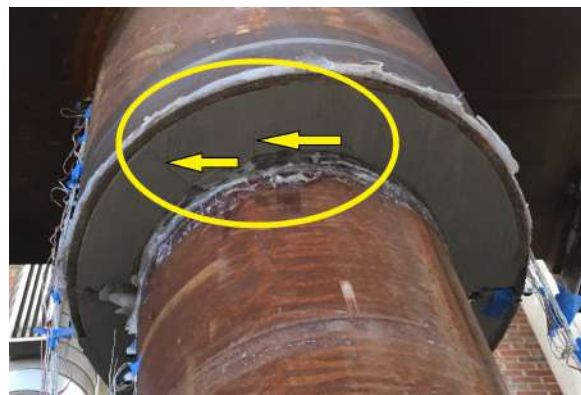
In test 1, this cracking was observed later (ductility 1.5) than in both tests 2, and 3 (ductility 1). One explanation could be that since the grout material in test 1 was much stronger than in tests 2 and 3, the grout ring could sustain higher stresses before cracking.

5.4.2 Socket Detachment

As the tests progressed past ductility 1, a gap between the outside surface of the column and the inside surface of the grout ring opened. This is termed socket detachment. Due to the ovalization of the column section under lateral loading, the extreme ends get pushed inwards. This causes the tension side of the section to detach from the grout ring resulting in a gap.

The gap became visible at ductility 1.5 in all the three tests, as shown in Figure 5.31. A larger gap was observed in test 3 compared to tests 1 and 2. Test 1 had the smallest gap. Figure 5.32 shows the state of this gap at ductility 3. The gaps at ductility 3 were wider than the corresponding ones at ductility 1. Similar to ductility 1, a comparatively smaller gap was observed for test 1, still larger in Test 2, and the largest in test 3. In short, fewer studs led to larger gaps.

The difference in the size of the gap for each test may be attributed to both the strength of the grout and the amount of clear cover in the GSS connections. The compressive strength of the grout and the presence of shear studs close to the bottom of the connection prevent socket detachment by acting in compression and tension, respectively. Test 1 had the strongest grout. The first row of shear studs in test 1 was 5" from the bottom of the connection. Test 3 meanwhile, had a deteriorated grout as well as a large cover of 8". Test 2 also had deteriorated grout; however, the small cover of 2.5" reduced the size of the gap



(a)



(b)



(c)

Figure 5.29 Grout cracking observed in the GSS connection transverse to the direction of loading in (a) Test 1 at $\mu_{1.5}$, (b) Test 2 at μ_1 , and (c) Test 3 at μ_1 .

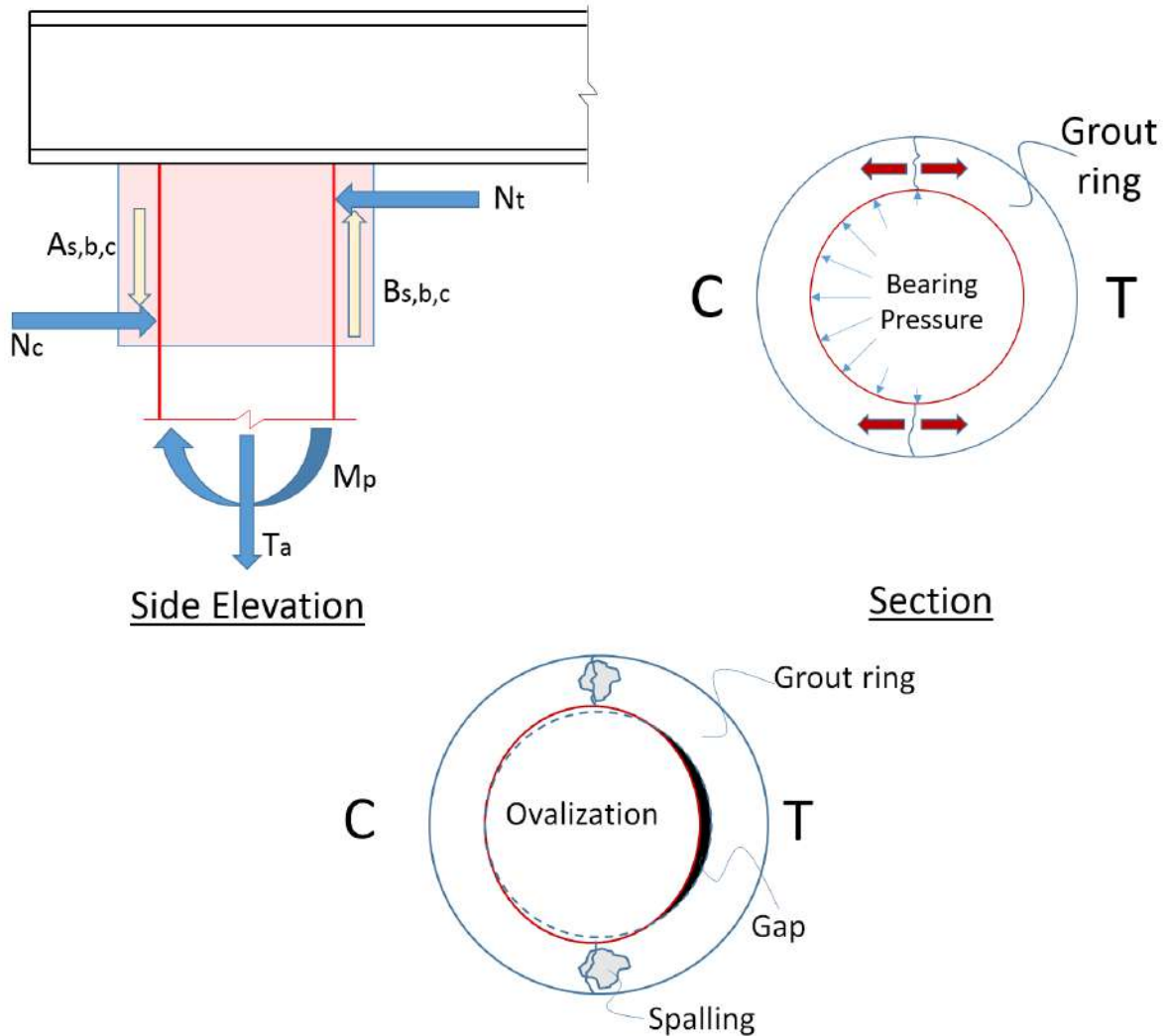
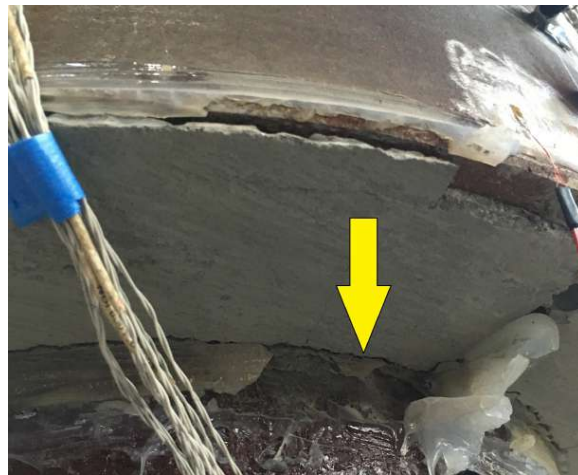


Figure 5.30 A schematic to explain cracking observed at the neutral axis, and the socket detachment limit state of the GSS connection.



(a)



(b)



(c)

Figure 5.31 Socket detachment observed in the GSS connection on the tension side of the column under bending (a) Test 1 at $\mu_{1.5}$, (b) Test 2 at $\mu_{1.5}$, and (c) Test 3 at $\mu_{1.5}$.



(a)



(b)



(c)

Figure 5.32 Socket detachment observed in the GSS connection on the tension side of the column under bending (a) Test 1 at μ_3 , (b) Test 2 at μ_3 , and (c) Test 3 at μ_3 .

compared to that in Test 3.

5.4.3 Grout Spalling

The grout on the extreme ends (regions farthest from the neutral axis under bending) of the GSS connection spalled off after ductility 2 cycles. However, in test 3, no spalling was observed even past ductility 4. This may be attributed to the absence of a row shear studs close to the bottom of the connection. Figure 5.33 shows the occurrence of this limit state in the first two tests. As has been discussed earlier, the presence of shear studs closer to the bottom of the connection help resisting the widening of the gap between the column and the grout ring. The shear studs are engaged in tension to achieve this resistance. As the shear studs are loaded axially in tension, the grout immediately around them is also subjected to tensile stresses. When this stress exceeds the tensile capacity of the surrounding grout, the grout cracks and spalls out of the connection.

In test 3, there was a large enough grout cover of 8" from the bottom, that the gap at the level of first row of shear studs was smaller compared to the other two tests. This increased cover resulted in a reduced tensile stress demand on the grout surrounding these shear studs. This may explain the observation of no spalling in test 3.

5.4.4 Pile Wall Buckling

Under cyclic loading, the column section reverses its compression and tension sides. Beyond a certain critical inelastic tensile strain, the pile wall has a propensity to buckle on the subsequent compression cycle. Pile wall buckling followed by plastic hinge formation just beneath the GSS connection is the desirable mode of failure for the bridge bent systems



(a)



(b)



(c)

Figure 5.33 Grout spalling observed in a GSS connection in (a) Test 1 at μ_2 , and (b) Test 2 at μ_3 (c)
No spalling was observed in Test 3.

discussed in this report.

Figure 5.34 shows the first instance of visible pile wall buckling in tests 1, 2, and 3. Buckling initiated earlier in test 1 compared to the other two tests. This level of buckling typically straightens itself during the subsequent opposite cycle. Figure 5.35 shows buckling which was permanent. Similar to buckling initiation, this level of buckling also occurs earlier in test 1. And finally, Figure 5.36 shows excessive levels of buckling in the columns before rupture. Once again, test 1 attained the same level of buckling earlier at ductility 4 compared to the other two tests, that attained this at ductility 5.

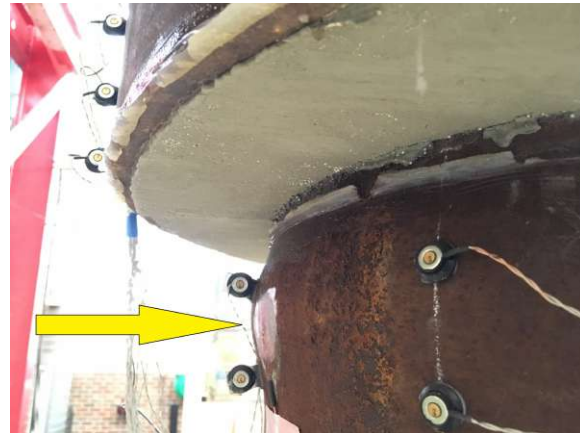
The grout in test 1 had almost 150% more compressive strength and 40% more elastic modulus than that in tests 2 and 3. These differences resulted in 1) lower penetration of inelastic strains into the GSS connection, and 2) smaller socket detachment and in turn a smaller effective column height, and hence a higher strain demand for the same system displacement. Both of these factors contributed to the critical column section in test 1 attaining a higher curvature demand at every ductility level. This increased curvature demand may have led to the specimen in test 1 to initiate and propagate pile wall buckling sooner than that in tests 2 and 3.

5.4.5 Pile Wall Rupture

The ultimate limit state in the columns in a bridge bent incorporating the GSS connection is pile wall rupture. Figure 5.37 shows pile wall rupture in tests 1 and 3. Although not ruptured, the pile wall in test 2 showed tear marks. Tear marks were also observed in tests 1 and 3 before rupture during subsequent cycles. This limit state occurs after a large number of inelastic cycles. In test 1, the pile ruptured during the first push to ductility 5. In tests 2



(a)



(b)

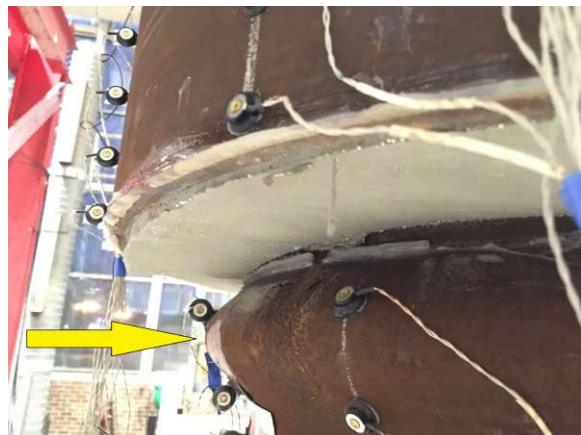


(c)

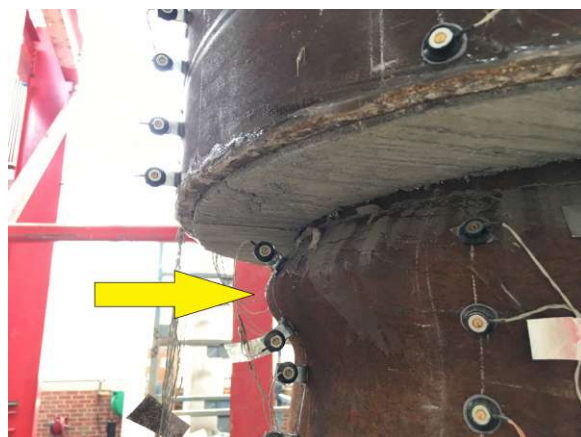
Figure 5.34 Visible pile wall buckling in (a) Test 1 at μ_2 , and (b) Test 2 at μ_3 (c) Test 3 at μ_3 .



(a)

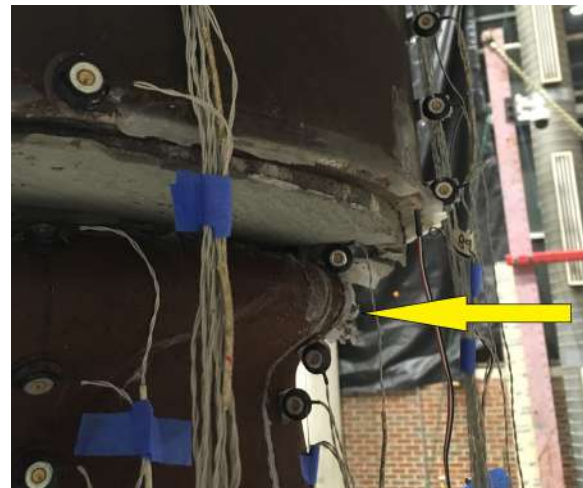


(b)



(c)

Figure 5.35 Permanent pile wall buckling in (a) Test 1 at μ_3 , and (b) Test 2 at μ_4 (c) Test 3 at μ_4 .



(a)



(b)



(c)

Figure 5.36 Excessive pile wall buckling in (a) Test 1 at μ_4 , and (b) Test 2 at μ_5 (c) Test 3 at μ_5 .

and 3, this occurred during the final cycle at ductility 5.

5.5 Chapter Summary and Conclusions

The need to better understand the force transfer mechanism within the GSS connection was described, and the background of large scale tests performed on steel bridge bents incorporating the GSS connection was discussed. One of the large scale tests from Fulmer et al. [Ful10b], referred to as test 0, was then discussed in detail.

The design procedure used by Fulmer et al. [Ful15] to determine the number of required shear studs in a GSS connection was judged to be overly conservative. Two large scale tests (test 3 and test 4), one with GSS connections having a significantly reduced number of shear studs and the other with a reduced socket depth, were performed to investigate the force transfer mechanism.

Test 3 results suggest that the number of shear studs does not have much impact on the global structural performance of the steel bent, provided there is a deep enough socket. Test 4 results suggest that sufficient depth of socket is the most important requirement to successfully transmit the demands in the column to the cap-beam. A qualitative mechanics based model was proposed showing a pair of normal forces which develops to maintain equilibrium of the connection. When the connection fails to mobilize a moment through the normal force pair large enough to resist the bending moment demand, premature failure of the connection ensues, i.e., the column remains straight and rocks within the grout annulus.

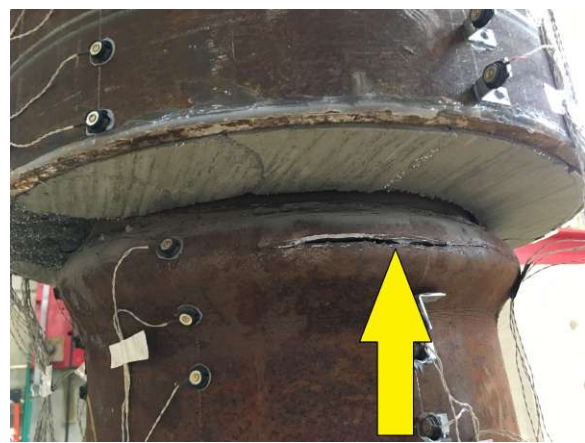
Five different limit states were identified for the GSS connection when it successfully relocates the plastic hinge into the column. Because of hoop stress induced by bearing of



(a)



(b)



(c)

Figure 5.37 Pile wall rupture in (a) Test 1 at μ_4 , and (b) Test 2 at μ_5 (c) Test 3 at μ_5 .

the column on the inside the of the grout ring, cracking initiates at the neutral axis. Subsequently, ovalization of the column section causes the detachment of the grout ring from the column on the tension side. Further loading causes the grout material on the extreme ends of the connection to spall. After progressing well into the inelastic range, the pile wall undergoes buckling below the connection. This local buckling is followed by plastic hinge formation and subsequent rupture of the pile wall.

CHAPTER

6

ANALYTICAL MODEL FOR DESIGN OF THE GSS CONNECTION

6.1 Introduction

Large scale structural tests of steel bridge piers were discussed in the previous chapters. To date, there have been seven such tests which implemented the GSS connection. Conclusions regarding the GSS connection so far, can be summarized as follows. The GSS con-

nection can successfully relocate the plastic hinge to the columns, thereby mobilizing the full strength and ductility capacity of the lateral load resisting system. The connection itself is capacity protected, which in turn, protects the weld present at the interface of the stub pipe and cap beam. And last, despite the grout being an integral component of the connection, the structural performance of the connection is not sensitive to variations in the strength and elastic modulus of the grout.

The next logical step in the progression of the GSS connection into engineering practice is the development of structural design criteria. Earlier, Fulmer et al. [Ful10a] had proposed design equations for the GSS connection. However, the mechanism of force transfer that these equations are based on is likely misplaced, as described in the previous chapter. The objective of this chapter is to discuss a revised model of force transfer derived using classical mechanics and some simplifying assumptions. First, the logic for the model and preceding assumptions are described, which are based on empirical evidence gathered from a review of existing literature and observations from the large scale tests. This description is followed by details of the proposed model and how it can be used to estimate the capacity of the GSS connection. This model was then used to perform a parametric study to ascertain the sensitivity of the model to different variables contained in it.

6.2 Literature Review

While there are no past studies that have addressed the force-transfer mechanism in the GSS connection, there exists a vast amount of literature that has focused on some of the underlying mechanisms. The use of pile-to-cap connections, wherein piles are embedded into reinforced concrete cap-beams, has been widespread for bridges, piers, and wharves.

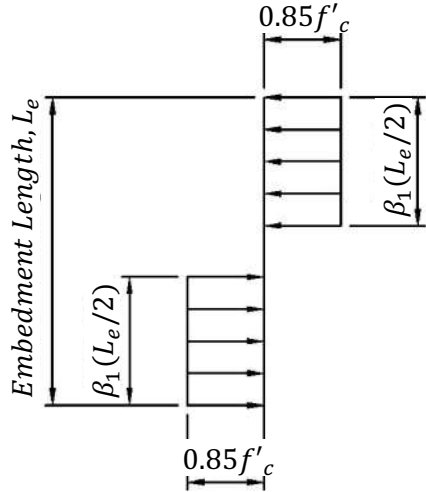


Figure 6.1 Embedment stress block as per PCI handbook [Han99]

These piles can be made of any material including steel, reinforced concrete, or concrete-filled steel composites. Typically, after the piles are erected, the cap-beams are cast-in-place around the pile tops creating the required embedment of piles. These connections are considered as fully fixed at the cap-beam pile interface.

The PCI Handbook [Han99] gives equations for the moment capacity of the steel pile-to-cap connection by embedment in concrete. This capacity is calculated by assuming a resistive couple formed due to stress blocks developed inside the grout ring, as shown in Figure 6.1. Xiao et al. [Xia06] improved the moment capacity equation by accounting for the reduction in capacity because of a large accompanying shear force. In their model, the connection capacity is also a function of the shear span of the pile, as shown in Equation 6.1. In Equation 6.1, f_{co} is the concrete compressive strength, b is the effective pile width, L_e is the embedment depth, a is the shear span and e is the shear span plus one-half the embedment depth, as shown in Figure 6.2.

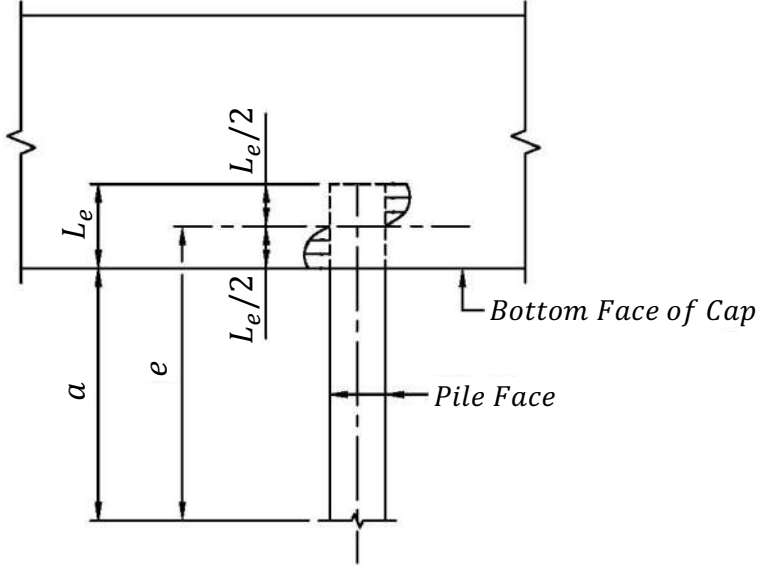


Figure 6.2 Illustration of Moment Capacity Calculation by Xiao et al. [Xia06].

$$M_{ue} = \left[\frac{0.85 f_{co} b L_e}{1 + 3.6 \left(\frac{e}{L_e} \right)} \right] a \quad (6.1)$$

Until recently, there has been some reluctance in using piles embedded plainly into cap-beams because this type of connection, as was practiced, did not have sufficient embedment length [Lar13]. Larosche et al. [Lar13] further studied these connections and determined that the cyclic behavior of the connection improves as the embedment length increases, thereby making it a feasible design detail. They proposed a value of $1.3D$ for the embedment depth, where D is the pile diameter.

Shama et al. [Sha02a] studied similar connections with steel wide-flange pile sections in both strong and weak axis bending under cyclic loading. In their study, pile bent connections oriented in bending about their strong axes, embedded into the reinforced concrete

cap beam failed in a nonductile manner within the cap beam. While the adhesive bond between the steel pile and concrete remained intact and the connection strength (M_j) exceeded the strength of the pile (M_p), the majority of overall deformation arose primarily through ductile deformation of the steel. However, once the adhesive bond was lost, such that $M_j < M_p$, the rocking motion of the steel pile rapidly degraded the concrete, forming cracks, which eventually failed the connection. This observation is similar to the failure observed in this study for the specimen in large-scale test 4. Furthermore, Shama et al. [Sha02a] noted that due to their lower strength, piles bending about their weak axes showed ductile performance where the plastic hinge occurred within the steel pile.

Hammett [Ham17] investigated the rotation of the embedment itself which contributed to the total displacement. Earlier models were unable to predict the total displacement because they assumed that the connection was rigid. Hammett [Ham17] concluded that the behavior of these embedded steel pile connections depends on pile embedment depth, concrete compressive strength and pile section properties. They added that the embedment depth and concrete compressive strength also have a large impact on the rotational stiffness. Grilli et al. [Gri17] made similar conclusions when they studied embedded columns for building moment frame base connections.

In summary, for embedded pile-to-cap or pile-to-footing connections, the moment capacity is generally determined by the lower value between the plastic section moment of the pile and the moment due to the two forces developed as a result of columns bearing on surrounding concrete. Therefore, the concrete strength and the embedment length are the two most important parameters that control the design of such a connection.

6.3 GSS Force Transfer Mechanism

The geometry of the GSS connection and the presence of shear studs within, likely lead to a complex force transfer mechanism, as discussed in the previous chapter. Plausible force components that contribute to the force transfer in the GSS connection are shown in Figure 6.3. Among these, the dominant mechanism is the moment resistance provided by the two bearing normal forces F_B and F_T . In addition to these two forces, some small resistance will also be provided by two force components, $A_{s,b,c}$ and $B_{s,b,c}$, acting parallel to the column longitudinal axis. Each of these two forces will be a summation of contributions from different transfer mechanisms such as the shear resistance of the studs (s), bond or friction between the outer steel circumference and the grout material (b), and compression struts which likely form between rows of shear studs (c). All of the aforementioned contributions are directly or indirectly related to the number of shear studs in the connection.

The GSS connection is capacity protected, i.e., it is designed to remain elastic or almost undamaged beyond the point of plastic hinging in the columns. Therefore, a conservative design assumption that can be made is that the moment resistance is exclusively provided by the normal forces F_B and F_T . This simplification is made to avoid the complexity of calculating the individual contributions of various mechanisms to the forces $A_{s,b,c}$ and $B_{s,b,c}$. Furthermore, the large-scale tests showed that the contribution of shear studs to the overall structural performance of the bridge bents was significantly smaller compared to that of the socket action of the column.

From large-scale test 0 to test 3, the number of shear studs in the GSS connection var-

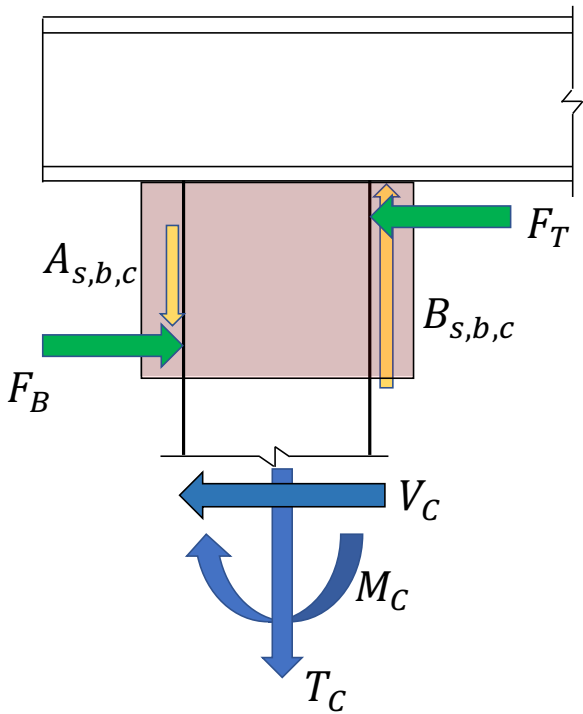


Figure 6.3 Hypothesized force transfer mechanism within the GSS connection.

ied from 96 to 16. Despite such a drastic reduction, the overall structural performance of the bridge pier specimens remained the same. However, when the embedment length of the column was reduced in test 4 to 16" from the longer 24" in test 3, there was a drastic shift in the structural behavior of the bridge bent specimen. The maximum strength of the system reduced by 33%, no plastic hinge formation was observed, and the energy dissipation capacity dropped significantly. The grout material reached its failure limit state first, resulting in progressive loss of an increasing amount of grout on each cycle. This observation was an indication that the embedment length is a much more critical parameter in the design of the GSS connection compared to the number of shear studs. The analytical model proposed next emphasizes this dependence of the system on the embedment length.

6.4 Analytical Model

Under lateral loading, the columns in a typical bridge pier are in double bending because of the fixity condition that arises due to the piles being embedded deeply into the ground. Figure 6.4 shows the typical profile of bending moments in the columns of a bridge pier in this condition. After formation of the plastic hinge, the magnitude of the bending moment below the connection, M_p , is the plastic moment capacity of the column. The bending moment at the cap-beam centerline, M_{cap} , can be calculated by extrapolating the linear bending moment diagram. The large-scale test specimens mimicked the portion above the point of contraflexure.

The proposed analytical model for force transfer is discussed using a free body diagram of one of the columns above the point of contraflexure, as shown in Figure 6.5. In

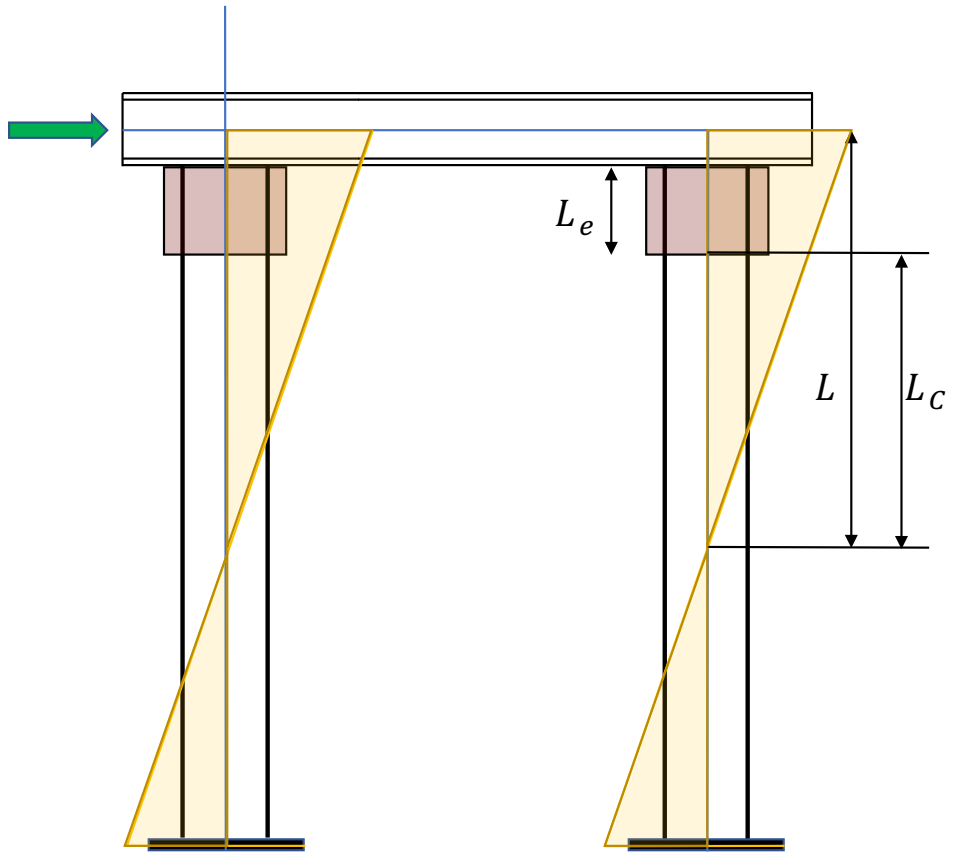


Figure 6.4 A typical profile of bending moment on a bridge pier under lateral loading.

this free body diagram, V_c is the shear force in the column at the point of contraflexure. The maximum value of this shear force can be calculated from the plastic moment (M_p) of the column section and the clear cantilever length (L_c), as shown in Equation 6.2. A two-dimensional (2D) truss mechanism is assumed to transmit this shear force into the GSS connection. This 2D model is a simplification of a more complex three-dimensional (3D) arrangement, as shown in Figure 6.6. Under the load V_c , the column bears on the top and bottom of the inside grout surface of the GSS socket, resulting in the mobilization of force reactions F_T and F_B , respectively.

$$V_c = \frac{M_p}{L_c} \quad (6.2)$$

The real distribution of stresses inside the connection is quite complex, especially with the presence of shear studs. A simplification of this distribution is shown in Figure 6.5, as the oval-shaped black-colored arrows, where f'_{cm} is the maximum amplitude of this stress distribution. One can simplify further by assuming a uniform distribution of bearing stresses around the semi-circumference of the column, as shown by the light-red arrows in Figure 6.5. The magnitude of this distribution can be considered as an “equivalent average” value of stress, if the total force resultants in both of the aforementioned stress distributions are the same. If the value of this average stress is f'_{ca} , the total reaction force can be calculated from the typical ACI:318-19 stress block using Equation 6.3, where L_e is the embedment length of the column inside the connection and β_1 is a factor between 0.65 and 0.85, as given in ACI:318-19 [ACI19].

The allowable maximum stress (f'_{cm}) will depend on the degree of confinement and hence can be equated to the confined grout compressive strength (f'_{cc}). The confined grout

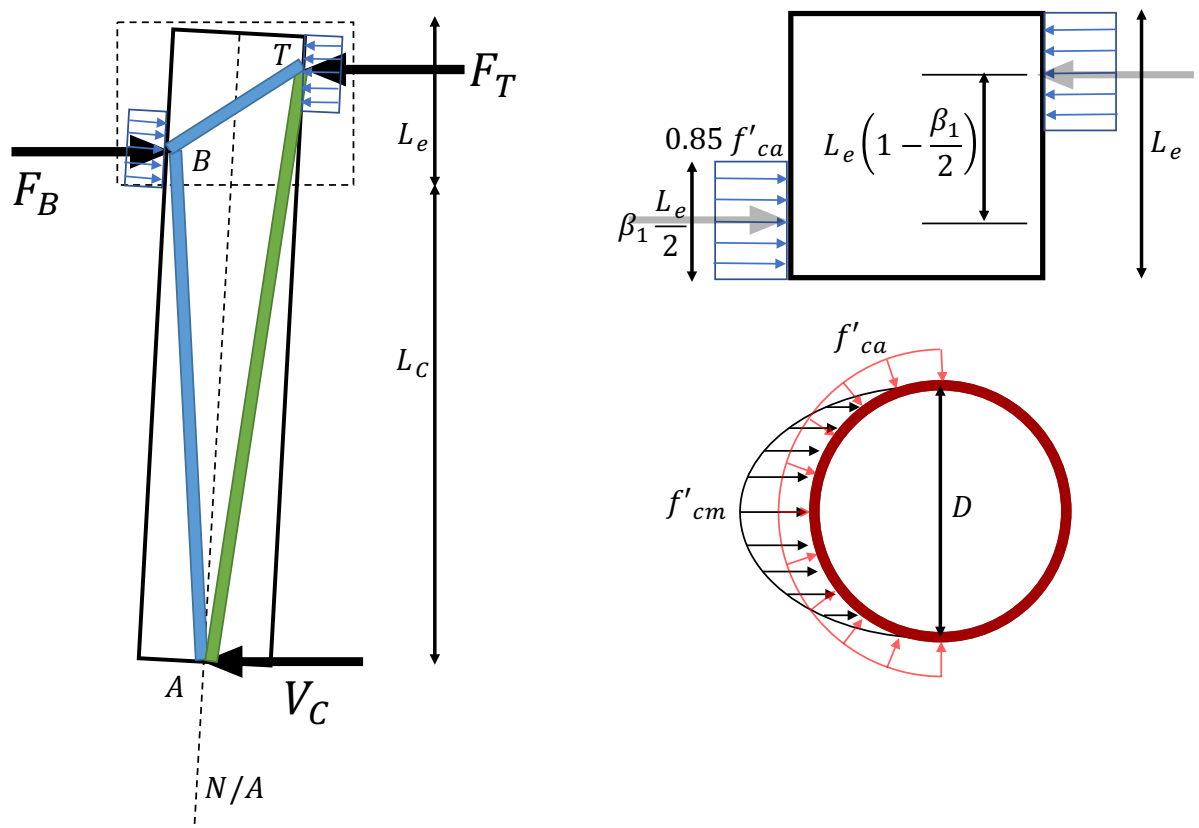


Figure 6.5 A schematic showing the strut-and-tie mechanism of force transfer in a single column.

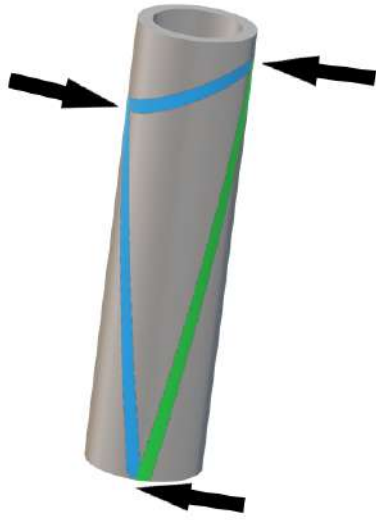


Figure 6.6 A 3-D representation of the assumed 2-D strut formation around the hollow column.

compressive strength (f'_{cc}) can be estimated using Equation 6.4, which was proposed by Richart et al. [Ric28]. In Equation 6.4, f_l is the lateral confining pressure, as estimated using Equation 6.5. f_l can be derived by solving for force equilibrium of the free body diagram of half of the stub pipe, as shown in Figure 6.7. The average uniform stress (f'_{ca}) will be less than the true maximum stress experienced by the grout in the connection. With no information regarding the relationship between f'_{cm} and f'_{ca} , it is recommended to be conservative and assume that the maximum stress is double the average stress, as shown in Equation 6.6.

$$F = 0.85 f'_{ca} \beta_1 \frac{L_e}{2} D \quad (6.3)$$

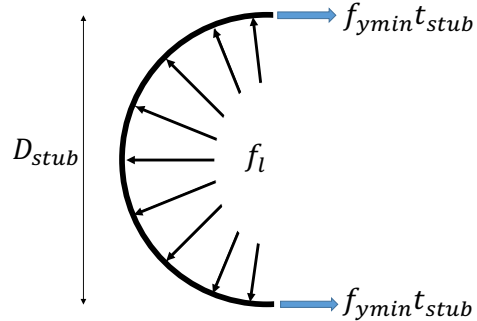


Figure 6.7 Free body diagram of half of the outer ring of the GSS connection providing confinement to the grout contained within.

$$f'_{cc} = f'_c + 4.1f_l \quad (6.4)$$

$$f_l = \frac{2f_{ymin}t_{stub}}{D_{stub}} \quad (6.5)$$

$$f'_{ca} \leq \frac{f'_{cc}}{2} \quad (6.6)$$

A relationship between the mobilized force F_B , in Figure 6.5 and the column shear force (V_{Cmax}) can be established from the geometry of the column and the connection. In the free body diagram of point A (Figure 6.8a), it can be shown that F_{AB} is approximately equal to F_{AT} for typical column L/D ratios. The value of F_{AB} can, in-turn, be calculated as

$$F_{AB} = \frac{V_c \left(L_c + L_e \left(1 - \frac{\beta_1}{4} \right) \right)}{D} \quad (6.7)$$

Subsequently, in the free body diagram of point B (Figure 6.8b), F_{BT} can be evaluated as

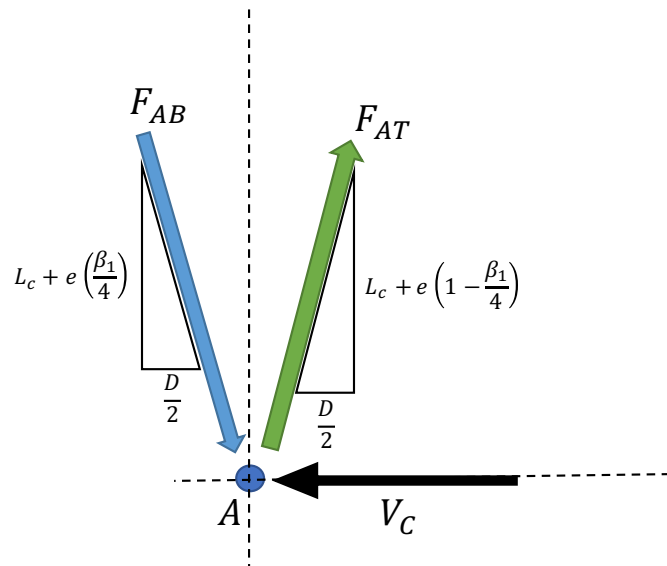
$$F_{BT} = F_{AB} \frac{\sqrt{D^2 + L_e^2 \left(1 - \frac{\beta_1}{2} \right)^2}}{L_e \left(1 - \frac{\beta_1}{2} \right)} \quad (6.8)$$

The bearing force F_B can then be calculated by adding the components of F_{AB} and F_{BT} in the same direction.

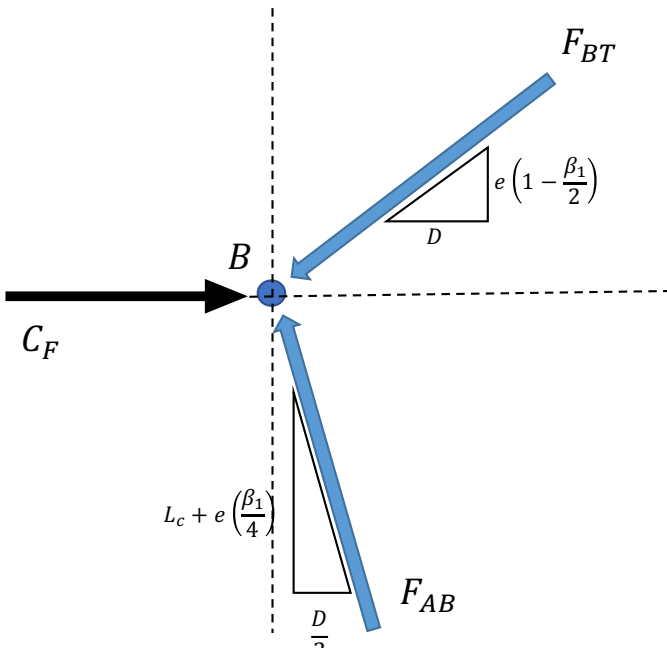
$$F_B = F_{AB} \frac{D/2}{L_c + L_e \left(1 - \frac{\beta_1}{4} \right)} + F_{BT} \frac{D}{\sqrt{D^2 + L_e^2 \left(1 - \frac{\beta_1}{2} \right)^2}} \quad (6.9)$$

Simplifying further, the bearing force can be written as a function of the column shear force,

$$F_B = V_c \left(\frac{1}{2} + \frac{L_c + L_e \left(1 - \frac{\beta_1}{4} \right)}{L_e \left(1 - \frac{\beta_1}{2} \right)} \right) \quad (6.10)$$



(a)



(b)

Figure 6.8 Free body diagrams of points in the strut-and-tie model shown in Figure 6.5: (a) Point A; and (b) Point B.

When designing the connection, this bearing force must be kept below the bearing capacity calculated using Equation 6.3.

$$F_B \leq F \quad (6.11)$$

To design the GSS connection using capacity design principles, it is therefore sufficient to limit the maximum allowable column shear force, V_C , that satisfies the foregoing inequality. Consequently, Equation 6.12 can be used to estimate the maximum capacity of the GSS connection.

$$V_C \leq \frac{0.85f'_{ca}\beta_1 D \left(\frac{L_e}{2} \right)}{\left(\frac{1}{2} + \frac{L_c + L_e \left(1 - \frac{\beta_1}{4} \right)}{L_e \left(1 - \frac{\beta_1}{2} \right)} \right)} \quad (6.12)$$

For typical values, $\beta_1 = 0.8$ and $L_e = 0.2L_{tc}$, the above equation reduces to Equation 6.13.

$$V_C \leq 0.008f'_{ca}D L_{tc} \quad (6.13)$$

It must be noted that the axial force present in the column is ignored in this model. This assumption is justifiable because of two reasons. First, this model attempts to estimate

the resistance of the GSS connection to the flexural demand under lateral loading. The axial force is resisted by the grout-to-steel bond and the shear studs present inside the connection. The number of shear studs in the connection is chosen to provide a positive load path to resist the axial tension force, assuming no contribution from the bond. This is to account for the unlikely event of losing all of the bond capacity over time or during a seismic event. This means that there is sufficient capacity in mechanisms not considered in this model to fully resist the mobilized axial force. Second, the type of axial force critical to the integrity of GSS connection is the tension force that causes pullout. The magnitude of this tension force is often reduced because of the superstructure dead load. Therefore, it can be argued that the impact of axial force on the design of embedment length is much smaller than that of the bending moment input due to column flexure.

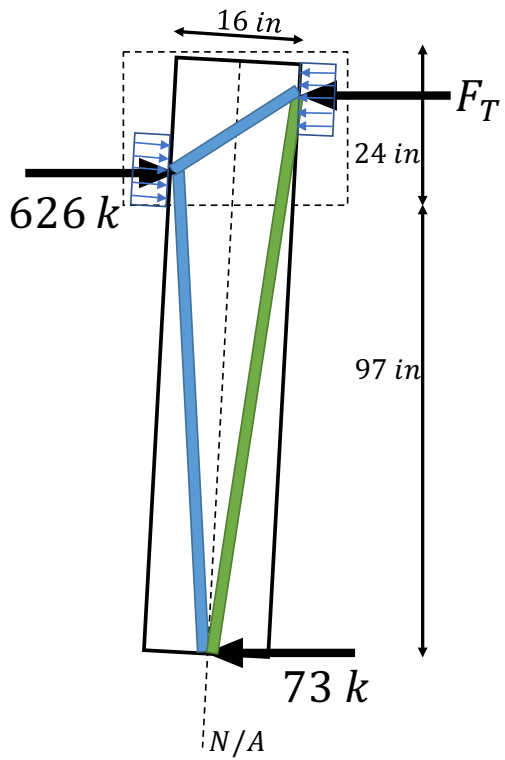
6.5 Application of the Analytical Model to Large-Scale Experiments

The proposed analytical model was developed using mechanics by making simplifying assumptions regarding force transfer in the GSS connection. Tests 3 and 4 provided empirical data to test the sufficiency of this model. Table 6.1 shows the step-by-step calculations performed to determine the capacity of the GSS connections in tests 3 and 4. The material properties f_y and f'_c were obtained by independent measurements of the steel coupons and grout samples, respectively, for each test. The remaining input variables are based on the geometry of the test setup. Figure 6.9 shows the comparison of these dimensions for the two tests.

Table 6.1 Step-wise calculation of the capacity and demand in the GSS connections in tests 3 and 4.

Step No.	Quantity (units)	Test 3	Test 4
1	f_l (ksi)	2.71	2.71
2	f'_c (ksi)	3.7	4.1
3	f'_{cc} (ksi)	14.5	14.9
4	f'_{ca} (ksi)	7.3	7.5
5	L_e (in)	24	16
6	F (kips)	953	650
7	f_y (ksi)	63	68
8	L_c (in)	97	105
9	V_C (kips)	73	79
10	F_{AB} (kips)	530	582
11	F_{BT} (kips)	792	1131
12	F_B (kips)	626	1010
13	D/C	0.66	1.5

Test 3 (DG - 16)



Test 4 (DG - 16SS)

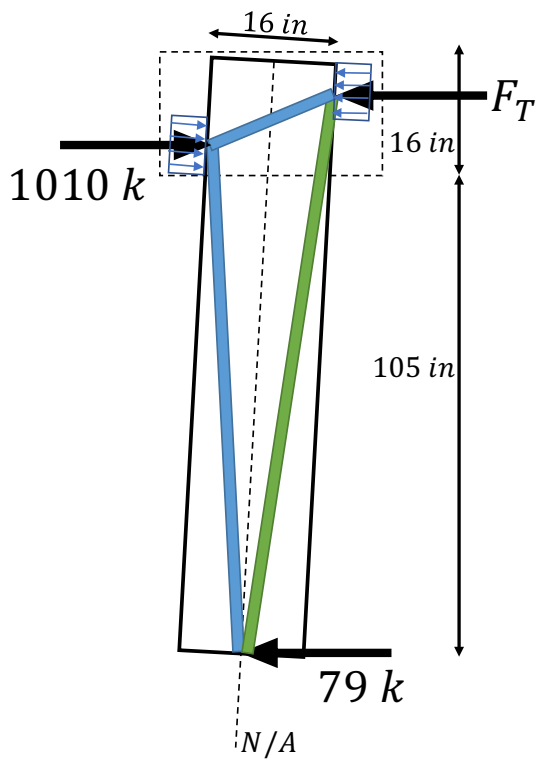


Figure 6.9 Comparison of the strut-and-tie model for tests 3 and 4.

The last row of Table 6.1 provides the ratio of the demand to capacity (D/C) of the grout material to sustain the bearing forces induced by socket action. A D/C value of less than one means that the connection can withstand the maximum possible demand which will be mobilized when the plastic hinge develops below the connection. If D/C is greater than one, the failure limit state of the grout material is achieved first and therefore no plastic hinge can be developed. In this case, the strength capacity of the bridge pier is determined by the grout compressive strength.

The value of D/C for test 3 which had a longer embedment length of 24" was 0.66, while that of test 4, with a shorter embedment length of 16", was 1.5. It is therefore not surprising that the mode of failure for both tests were different. While test 3 failed in the desirable manner through plastic hinge formation, test 4 failed by grout spalling and the ensuing column rocking behavior with no plastic hinge formation.

The analytical model also can be used to determine the maximum strength of the system. The shear force demand in a column is one of the input variables of the model. The D/C ratio for different values of shear force demand can therefore be calculated and plotted. Figure 6.10 shows the result of such a calculation for both test 3 and test 4. The D/C ratio varies linearly with the applied shear force. The intersection of the two lines with the dashed line at the D/C ratio equal to 1.0 can be used to read the shear force capacity of the columns in tests 3 and 4, which are equal to 106 kips and 52 kips, respectively. The total system lateral force capacity can then be calculated by multiplying the column capacities by the number of individual columns. Therefore the calculated system force capacity for tests 3 and 4 become 212 kips and 104 kips, respectively. The force-displacement backbone response of tests 3 and 4 are reproduced here in Figure 6.11. It can be seen that the

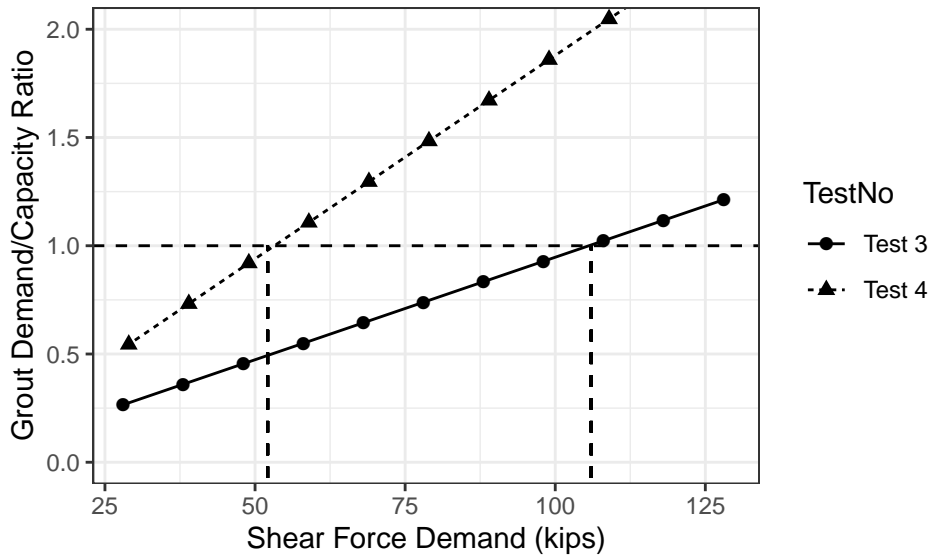


Figure 6.10 D/C ratio versus the shear force demand in each column of tests 3 and 4.

maximum strength of the test 4 specimen is close the value predicted by the model. On the other hand, full plasticity in the columns was mobilized in test 3 before reaching the predicted connection capacity.

Equation 6.1 proposed by Xiao et al. [Xia06] can also be used to calculate the moment capacity or the shear force capacity. However, to match the values so estimated to the results of tests 3 and 4, the average grout confined compressive strength f'_{ca} must be used in place of f_{co} in Equation 6.1. For tests 3 and 4, the shear force capacities calculated using this equation are 139 kips and 62 kips, respectively.

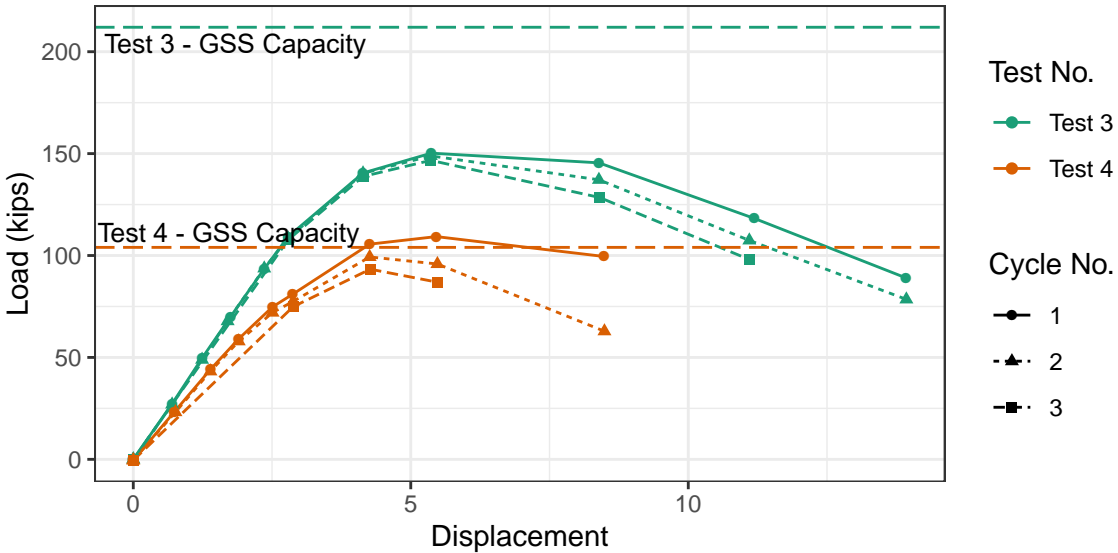
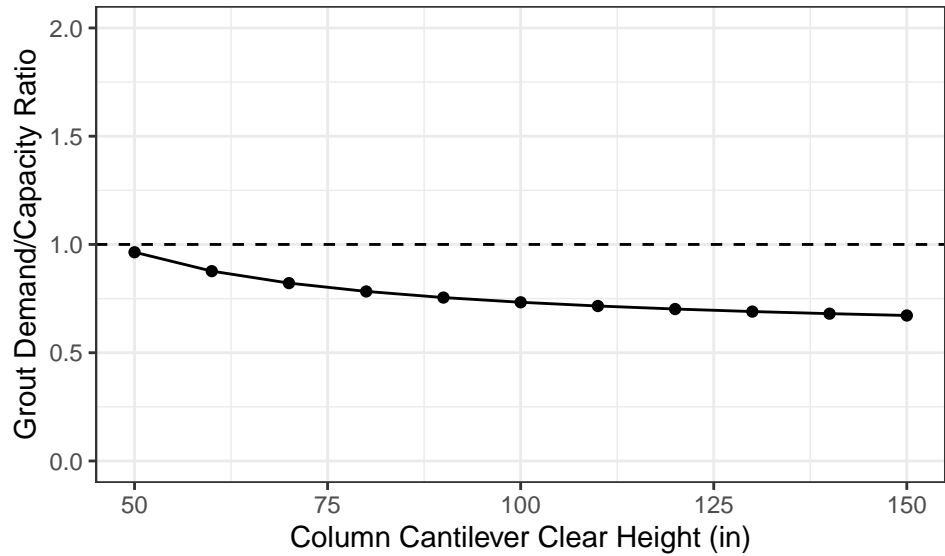


Figure 6.11 Comparison of the force-displacement backbone response of tests 3 and 4.

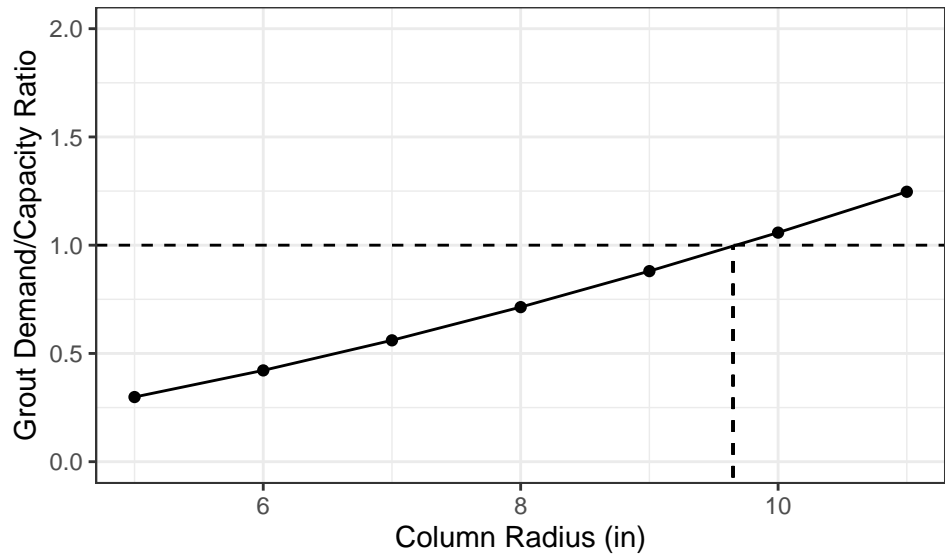
6.6 Parametric Study and Design Equations

The proposed analytical model was used to perform a parametric study to ascertain the applicability and range of predictions of the model. This study was performed by varying the input variables in the model. Typical values were chosen for each variable in the study. Table 6.2 shows all of the input variables and their values used in the parametric study. First, the sensitivity of the demand over capacity ratio to each of the variables was ascertained. Figure 6.12 shows the typical variation in D/C ratio with respect to each variable while keeping all of the other variables constant.

While keeping everything other than themselves constant, the embedment length and the column radius seemingly have a much larger impact on the D/C ratio. Therefore, while designing the GSS connection, it is recommended that these two variables be given the

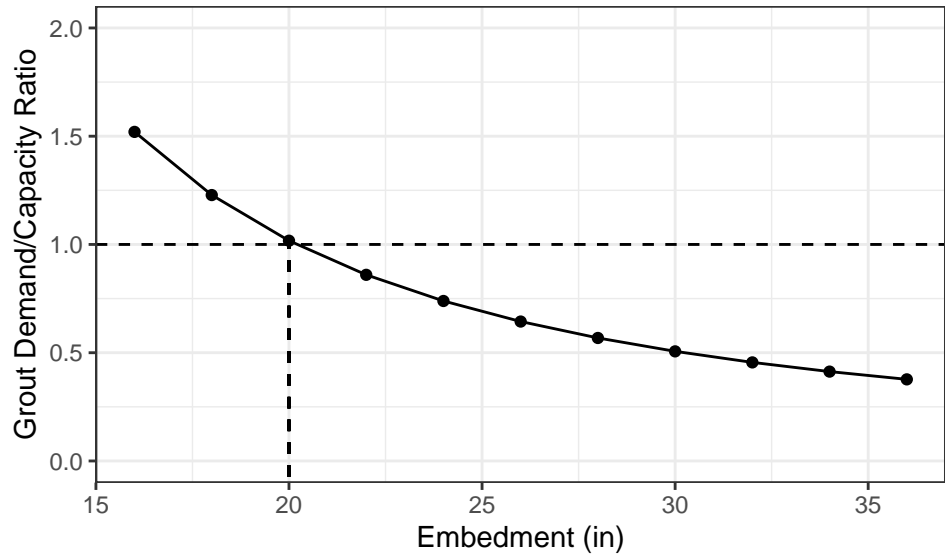


(a)

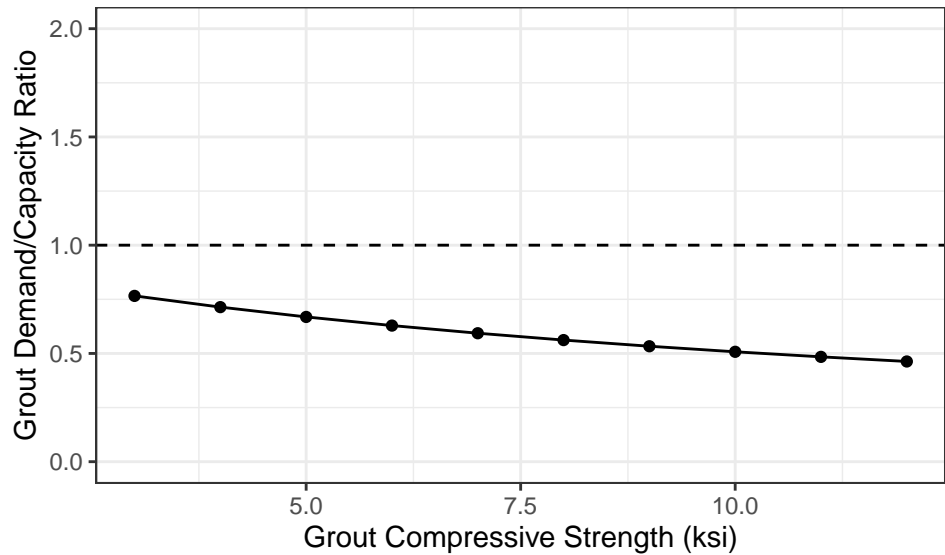


(b)

Figure 6.12 Sensitivity of D/C ratio with respect to the variables in the parametric study.

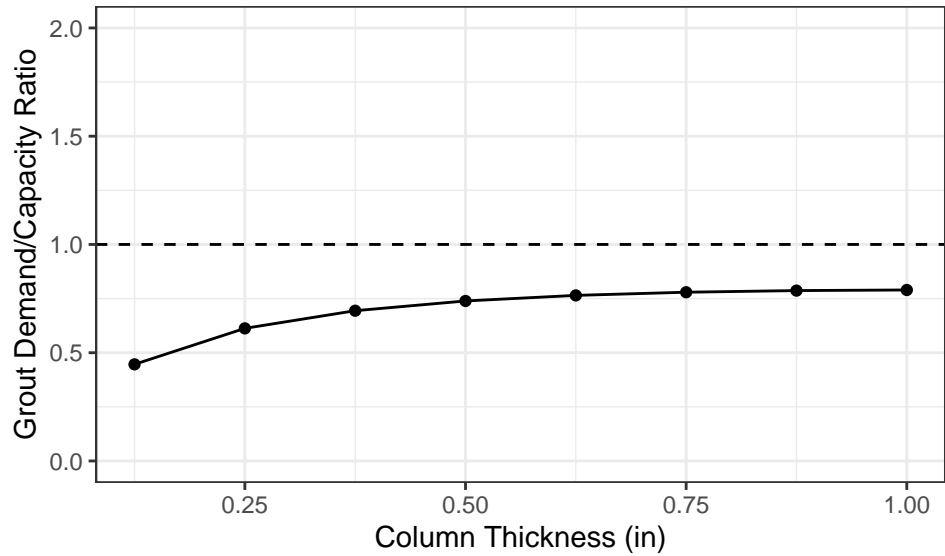


(c)

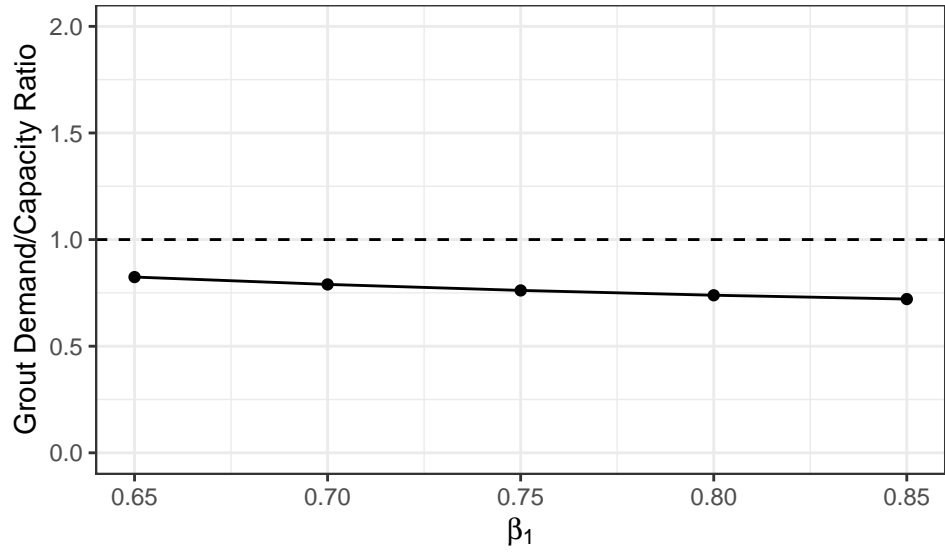


(d)

Figure 6.12 Sensitivity of D/C ratio with respect to the variables in the parametric study (cont.)



(e)



(f)

Figure 6.12 Sensitivity of D/C ratio with respect to the variables in the parametric study (cont.)

Table 6.2 Input variables and their values used in the parametric study.

Input Variable (units)	Values
Column pipe radius (in)	6, 8, 10, 12, 14, 16
Column pipe thickness (in)	0.25, 0.50, 0.75, 1.00, 1.25
Stub pipe thickness (in)	0.25, 0.50, 0.75, 1.00, 1.25
Column clear cantilever height (in)	60, 70, 80, 90, 100, 110, 120, 130, 140, 150
Embedment length (in)	16, 18, 20, 22, 24, 26, 28, 30, 32, 34, 36, 38, 40
Steel yield strength (ksi)	50, 60, 70
Grout compressive strength (ksi)	4, 5, 6, 7, 8, 9, 10, 11
β_1	0.65, 0.70, 0.75, 0.80, 0.85

most consideration.

Equation 6.12, derived previously, can be used to ensure that the GSS connection remains capacity protected under a seismic event. However, input variables to this equation, such as the column embedmend length (L_e), column cantilever length (L_c), and column diameter (D), remain undetermined at the start of the design process. Results from the parametric study were therefore used to determine approximate geometric proportions of the bridge pier to start with. Equation 6.12 can then used as a capacity check. If necessary, an iterative procedure can be applied to converge to an adequate design.

Two important geometric ratios, when correctly proportioned, which would lead to a satisfactory design, are the embedment length to total cantilever length (L_e/L_t) ratio and the embedment length to column diameter (L_e/D) ratio. Among more than 2 million different cases realized in the parametric study, a large sample consisting of 200,000 observations was chosen to perform simple statistical analysis to reveal trends in the variation of the aforementioned ratios.

$$L_t = L_e + L_c \quad (6.14)$$

First, the D/C ratio was plotted against the L_e/L_t ratio. Note that L_t is the sum of the embedment length (L_e) and the column cantilever length (L_c), as shown in Equation 6.14. On average, when the L_e/L_t ratio increases, the D/C ratio decreases because longer embedment results in a longer lever arm for the resistive force couple developed in the GSS socket. Figure 6.13a shows the D/C ratio plotted against the L_e/L_t ratio from the random sample obtained from the parametric study, which illustrates this conclusion. The shaded area in the figure corresponds to the region where the D/C ratio is between 0.6 and 0.9. It is recommended that for design, the D/C ratio falls inside this range. Observations in the parametric study that fell within the range were plotted as a histogram, as shown in Figure 6.13b. The L_e/L_t ratio between 0.2 and 0.3 had the most likelihood of achieving this desirable design condition. Note that the experimental specimens discussed in this study possessed a L_e/L_t ratio of 0.18.

Next, the D/C ratio was plotted against the L_e/D ratio. On average, when the L_e/D ratio increases, D/C ratio decreases for the same reason as increasing embedment length. This is illustrated by Figure 6.14a, that was obtained by plotting the D/C ratio against the L_e/D ratio of the random sample obtained from the parametric study. Again, the shaded area corresponds to the region where the D/C ratio is between 0.6 and 0.9. Observations in the parametric study that fell within the range were plotted as a histogram, as shown in Figure 6.14b. The L_e/D ratio between 1.2 and 1.6 had the most likelihood of achieving this desirable design condition. Note that the experimental specimens discussed in this study possessed a L_e/D ratio of 1.5. Also note that the foregoing recommended range of L_e/D

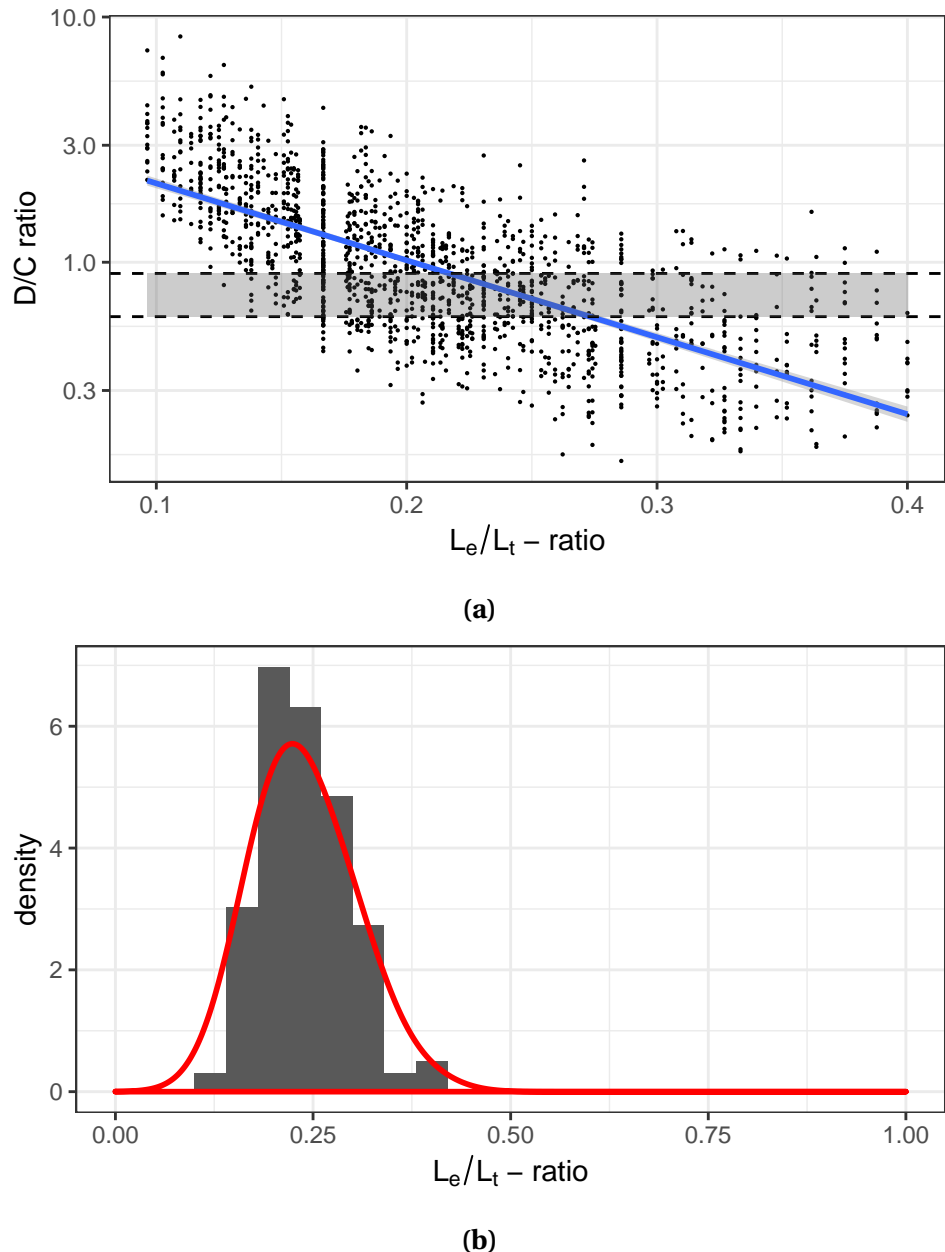
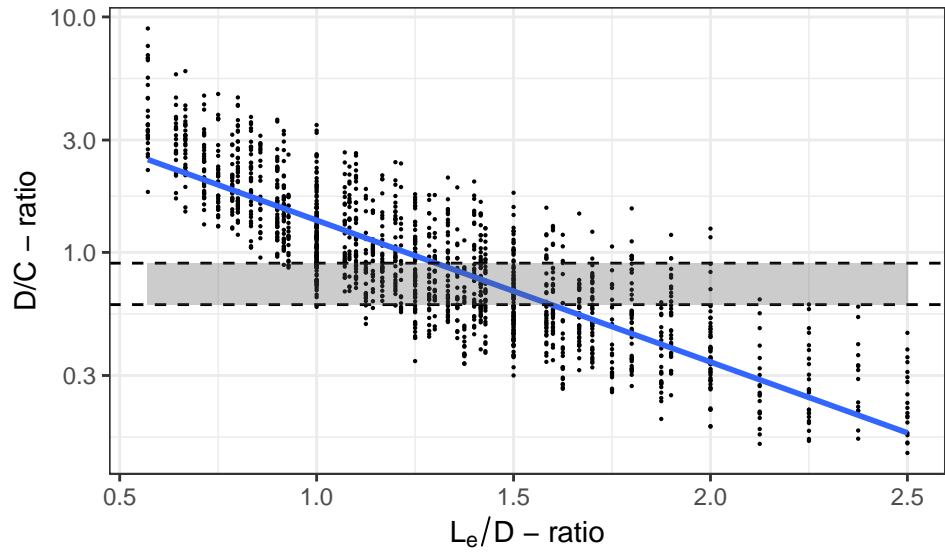
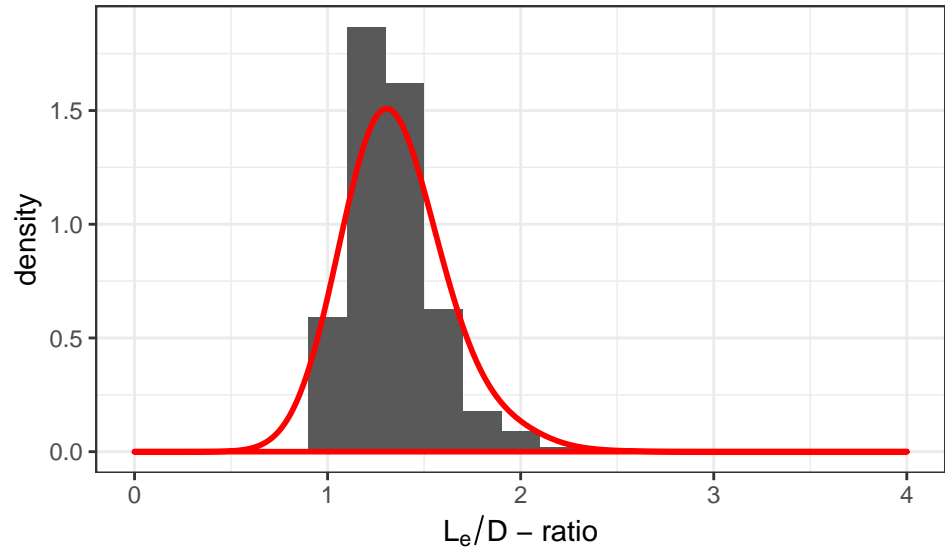


Figure 6.13 (a) D/C ratio versus L_e/L_t ratio from the parametric study. (b) Probability density of L_e/L_t ratios that led to optimum GSS connection design.



(a)



(b)

Figure 6.14 (a) D/C ratio versus L_e/D ratio from the parametric study. (b) Probability density of L_e/D ratios that led to optimum GSS connection design.

also contains the value of 1.3, that was recommended by Larosche et al. [Lar13].

6.7 Chapter Summary

The objective of this chapter was to develop a mechanics based model for the structural design of the GSS connection. This model must be in agreement with the force transfer mechanism discovered during the experimental phase of this study. This force transfer mechanism, first described in the previous chapter, involves the resistance offered by the forces developed due to the column wall bearing on the inside wall of the GSS socket because of the socket action. This mechanism was approximated as a strut and tie formulation that enabled the derivation of an equation to estimate the force capacity of the GSS connection. This model, when applied to the last two large scale tests, yielded predictions which matched empirical observations. Next, a parametric study was performed using this model to 1) ascertain the sensitivity of this model to input variables and 2) determine approximate geometric proportions of bridge piers that can lead to optimum design. It was determined that the embedment length to total cantilever length (L_e/L_t) ratio between 0.2 and 0.3, and the embedment length to column diameter (L_e/D) ratio between 1.2 and 1.6 can lead to an optimum GSS connection design.

CHAPTER

7

LIMIT STATE DISPLACEMENTS OF STEEL SUBSTRUCTURES WITH THE GSS CONNECTION

In recent years, there has been an increasing number of efforts to make use of the direct displacement-based design procedure for the seismic design of hollow cross-section steel pile supported structures [Har19]. The design procedure known as Direct Displacement-

Based Design (DDBD) was developed during the early 2000s with to mitigate the deficiencies in force-based design (FBD). The fundamental difference of the DDBD procedure from that of FBD is that it characterizes a structure through equivalent single-degree-of-freedom (SDOF) representations of its performance at various limit states. This is in contrast to FBD, which makes use of the structure's initial elastic characteristics [Pri07].

For nonlinear structural response, local damage can be directly correlated to demand parameters such as strains or curvatures, which in turn are functions of system displacements. Therefore, DDBD emphasizes on displacement as the primary design variable because it is a better indicator of structural damage than force. Consequently, in the DDBD procedure, it is imperative to be able to estimate inelastic displacements of a structure at various limit states.

For bridges, piers, or wharves, the use of socket-type connections, such as the GSS connection, for construction of substructure systems introduces significant error in the conventional approach to predict of limit state displacements. The objective of this chapter is to identify these limitations and to establish a set of equations that can be used to predict inelastic structural displacements at key limit states. These limit states are column yielding, wall local buckling, and different levels of strength degradation.

In this chapter, a summary of the fundamentals of DDBD is provided first. A description of the material and section behavior of steel columns follows. Then, the conventional approach to estimation of limit state displacements is discussed. This approach is extended to systems with hollow steel columns and in the process, deriving a few essential parameters. Subsequently, attention is drawn to issues regarding why simply considering column limit states may lead to an underestimation of pier displacements. A fiber-based numerical

model was developed to overcome these issues related to prediction of inelastic displacements. The development of this model is also discussed here. Using this numerical model, a parametric study was performed to derive two different correction factors, which when multiplied by the previously estimated target displacement, provide accurate predictions. Lastly, strength degradation in these types of systems is discussed, and a model is developed to capture this phenomenon. The chapter is then concluded with a summary.

7.1 Direct Displacement-Based Design

The fundamental steps of the DDBD procedure have been presented in many prior publications [Pri00; Pri03; Pri07]. However, a brief description of these steps is presented here. It is convenient to illustrate the DDBD procedure using an SDOF structure. For MDOF structures, the usual practice is to represent them as equivalent SDOF structures using the substitute structure method proposed by Shibata & Sozen [SS76]. In Figure 7.1a, a regular frame building and its equivalent SDOF structure is conceptualized. It must be noted that this approach can be extended to any structural type. The bilinear envelope of the lateral force-displacement response of the equivalent SDOF representation is shown in Figure 7.1b.

The first step in this procedure is to characterize the limit states of the structure. Generally, these limit states are based either on structural damage or functional limitations of the structure. For example, in steel pile supported bridges, buckling of the pile cross-section is an important limit state because it precedes a drastic reduction in the strength of the system. Alternatively, if these bridges are simply supported at the abutments, the seat width of girders at the abutments may determine a functional limit state, i.e., the gird-

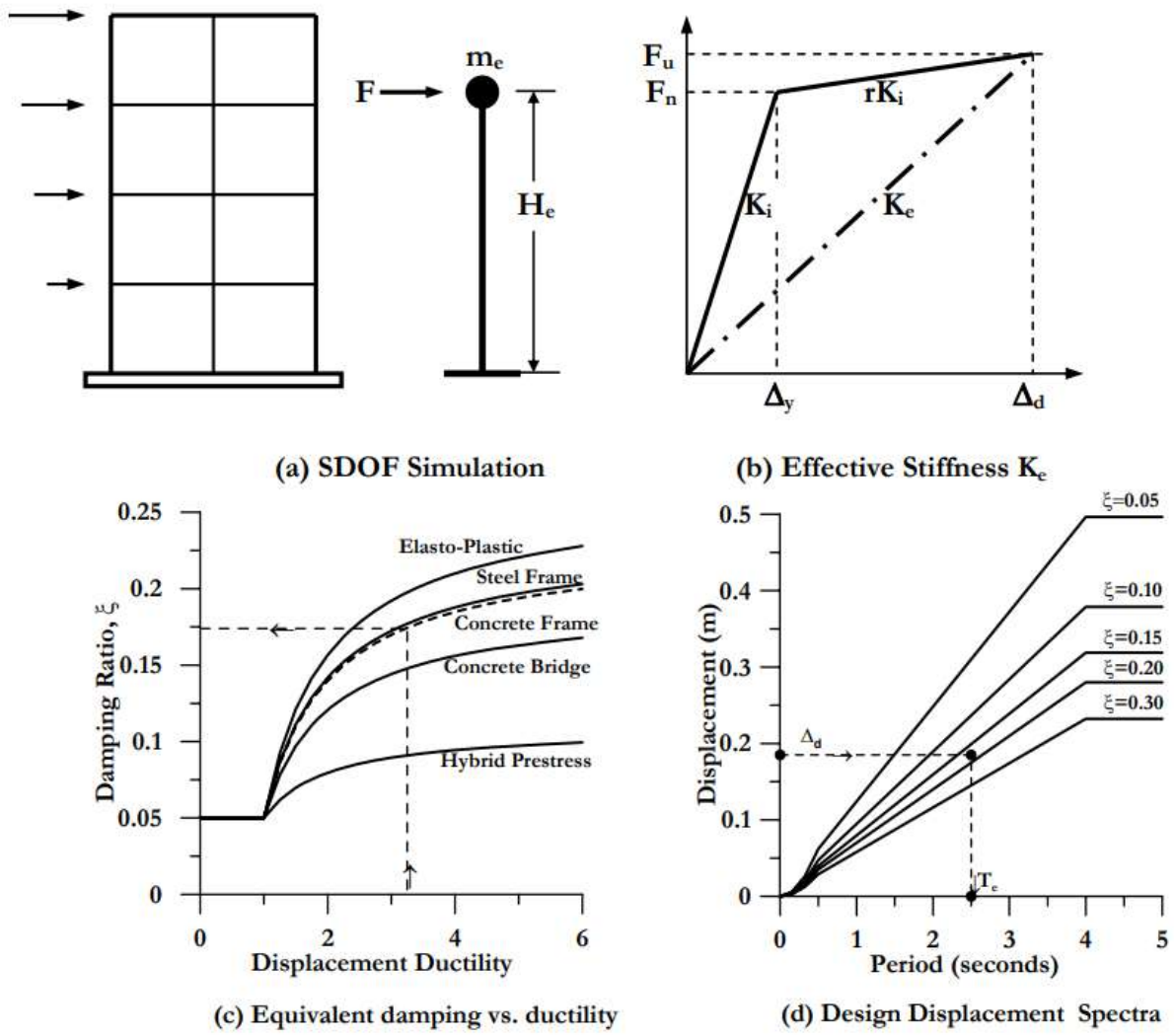


Figure 7.1 Fundamentals of DDBD [Pri07].

ers must not slide off their supports. In either case, these limiting events can be translated into a level of structural displacement of these bridges. In DDBD, these displacements that correspond to a given limit state are called the *Target Displacements* for design. The goal of the DDBD procedure is to force the structure to respond desirably, in the sense that the structure undergoes a peak displacement (Δ_d) equal to the target displacement (Δ_t) under the design level seismic event.

Once the target displacement is determined, the next step is to use the design displacement response spectra to determine the effective period of the structure. The effective period (T_e) of a structure is the period of its most significant mode shape at peak response. T_e can be calculated using the secant stiffness (K_e) of the structure at any given limit state, as shown in Figure 7.1b. Naturally, T_e depends on the corresponding limit state under consideration and must be differentiated from the initial elastic period T_i , which is a parameter commonly used in force-based design. T_e can be determined for a given hazard by entering the design displacement spectrum on its y-axis at the value given by Δ_d , as shown in Figure 7.1d. T_e can be read from the x-axis of the response spectrum curve corresponding to the appropriate level of damping in the system.

The damping in a structure is characterized by what is known as the equivalent viscous damping ratio (ξ_{eq}) [Pri07]. ξ_{eq} of a structure is evaluated as a linear combination of its inherent viscous component and the hysteretic component. Viscous damping is a catch-all quantity to represent contributions from many different mechanisms that contribute to structural damping. On the other hand, hysteretic damping is exhibited by the structure under an earthquake because of its nonlinear excursions that dissipate strain energy. ξ_{eq} can also be understood as the damping ratio of the equivalent elastic SDOF struc-

ture, that upon excitation by the same ground motion, results in the same peak response as the inelastic MDOF structure. There exist relationships [Pri07] between equivalent viscous damping and system ductility for various classes of structures, represented graphically in Figure 7.1c. For any given level of displacement ductility, which can be evaluated using the target, and yield displacement limits, ξ_{eq} can be read from Figure 7.1c. This information is then used to determine the response spectrum curve that must be used to obtain the effective period.

The next step is to calculate the total base shear of the structure, which can then be used to obtain design forces for structural members. After evaluating T_e , Equation 7.1 can be used to obtain the effective or secant stiffness (K_e) of the equivalent SDOF structure, where M is the total participating mass of the structure. Subsequently, Equation 7.2 can be used to determine the base shear (V_B).

$$K_e = 4\pi^2 \frac{M}{T_e^2} \quad (7.1)$$

$$V_B = K_e \Delta_t \quad (7.2)$$

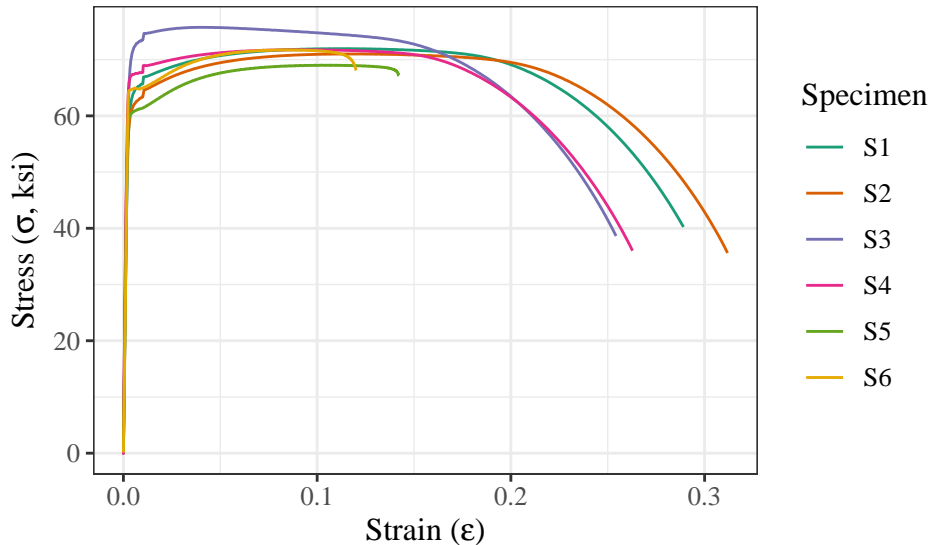
Under a few minimal assumptions, the base shear (V_B) can also be evaluated directly using a single equation [Pri07], as shown in Equation 7.3. In this equation, Δ_c and T_c are corner point displacement and period as given by the design response spectrum.

$$V_B = \frac{4\pi^2 M}{\Delta_t} \left(\frac{\Delta_c}{T_c} \right)^2 \frac{7}{2 + \xi_{eq}} \quad (7.3)$$

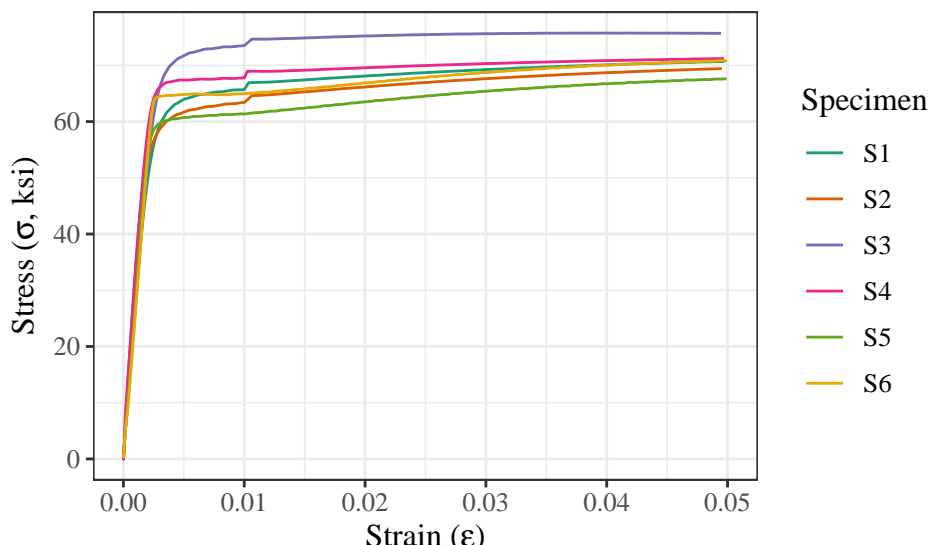
In summary, to perform the DDBD procedure for seismic design of systems that incorporate socket-type connections, such as the GSS connection, two important aspects have to be considered and accounted for in the form of simple models. First is the estimation of target displacements corresponding to the important limit states of such systems. And second is the estimation of an accurate level of equivalent viscous damping in these systems. The remainder of this chapter explores the former issue of predicting target displacements in detail and provides recommendations for carrying out the design procedure efficiently and accurately.

7.2 Material and Section Behavior of Hollow Steel Sections

For the fabrication of steel piles or pile-columns, preferred grades are ASTM A500 Gr. B, ASTM A53 Gr. B, and API 5L XNN, where XNN denotes the grade, e.g., X52. Recall that the large-scale test columns used in this study were API 5L X52 PSL2, whereas those used by Fulmer et al. [Ful15] were ASTM A500 Gr. B. While both of these materials are ductile, API 5L steel possesses a much higher Charpy V-Notch toughness which makes it suitable for seismic applications, especially in cold climates. During the studies performed on the GSS connection, both ASTM A500 and API 5L materials were tested according to ASTM:A370-19e1 [Ae19]. Figures 7.2 and 7.3 show the stress-strain curves obtained from these tests. API 5L material shows much less variation in yield strength compared to ASTM A500. Both

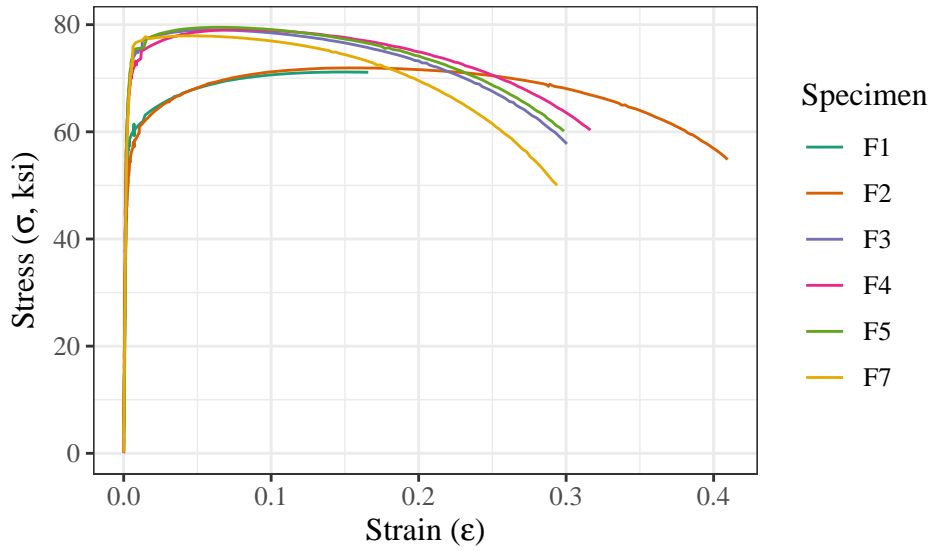


(a)

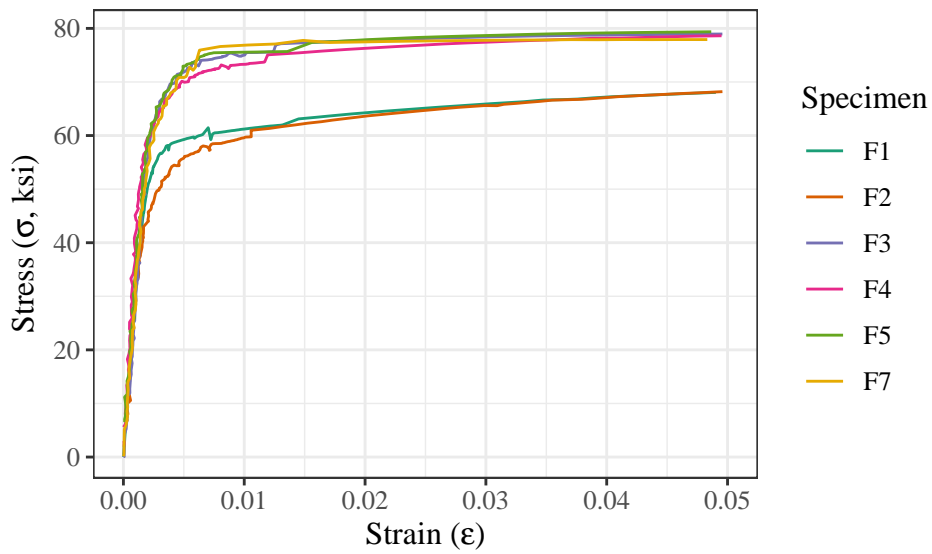


(b)

Figure 7.2 Stress-strain diagrams of API 5L X52 PSL2 steel material: (a) Full (b) Zoomed-in.



(a)



(b)

Figure 7.3 Stress-strain diagrams of ASTM A500 Gr. B steel material: (a) Full (b) Zoomed-in.

materials show some strain hardening, which however is more pronounced in ASTM A500. It must be noted that these curves were obtained from tension tests and therefore do not represent the real behavior of steel in beam-column cross sections at large strains because of the local buckling phenomenon, discussed next, observed on the compression face of the columns.

Depending on the diameter-to-thickness (D/t ratio) ratio of their cross sections, hollow circular steel members exhibit differences in their propensity to undergo local buckling. While non-compact sections exhibit local buckling at smaller strains, compact sections manifest the same only at large plastic strains. Harn et al. [Har19] summarized prior work performed to identify the compressive strain of steel columns at the onset of local buckling. They state that while more work is needed to conclusively establish reliable relationships between buckling strain limits and column D/t ratios, currently available models can provide reasonably good estimates. Harn et al. [Har19] propose a conservative expression for design (Equation 7.4). This expression provides a lower bound value for strain at buckling (ϵ_b) where D and t are the column diameter and wall thickness, respectively. Two alternate models, identified by Harn et al. [Har19], that estimate mean values from past experimental data are the Gresnigt [Gre14] model and British Standards [BS93] model. These models are shown in Equations 7.5 and 7.7, respectively. It must be noted that a prevalent model currently in usage, provided in Priestley et al. [Pri07], recommends a constant value of $\epsilon_b = 0.02$ as the strain limit for damage control in steel members.

Harn et al. model:

$$\epsilon_b = 10 \left(\frac{D}{t} \right)^{-2} \quad (7.4)$$

Gresnigt model:

$$\epsilon_b = 0.5 \frac{t}{D} - 0.0025 + 3000 \left(\frac{(p_i - p_e)D}{2tE_s} \right)^2 \quad (7.5)$$

where p_i and p_e are the internal and external pipe pressure, E_s is the elastic modulus of steel. Note that this equation was developed for underground pipes. For bridge piers, this equation reduces to

$$\epsilon_b = 0.5 \frac{t}{D} - 0.0025 \quad (7.6)$$

British Standards model:

$$\epsilon_b = 15 \left(\frac{D}{t} \right)^{-2} \quad (7.7)$$

The large-scale tests discussed earlier in this dissertation, provided an opportunity to extract more information regarding the strains in the columns at the instance of local buckling. Instrumentation of these test specimens with arrays of LED sensors permitted identification of local strains in critical sections of the steel columns. Each marker could provide its 3-D coordinates which was recorded by the Optotrak system in the form of time-series data. From their 3-D coordinates, the distance between two markers could be calculated at each point in time. Consequently, the strain could be calculated by simply dividing the instantaneous distance by the initial distance. Figure 7.4 shows a schematic of the instrumentation employed for the measurement of strains at pile wall local buckling. Strains on

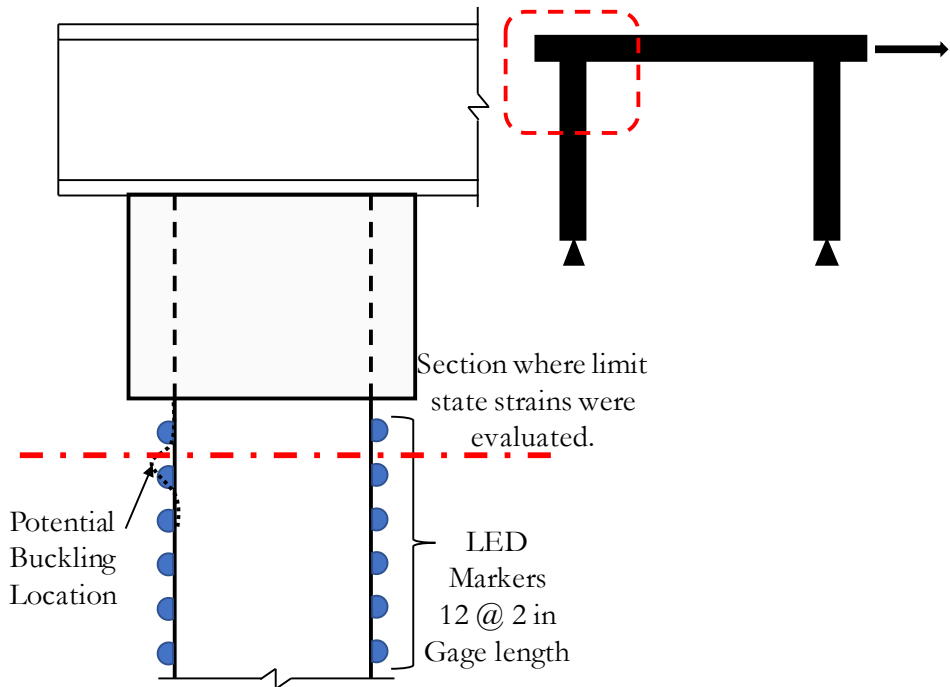


Figure 7.4 Optotruk instrumentation schematic for measurement of strain at buckling.

the extreme fibers were obtained by post-processing LED sensor data for the section in between the top two rows of markers. This section is henceforth referred to as the critical section.

Identification of the onset of local buckling in experimental studies has been a subjective exercise in the past. Currently, there is no standardized research procedure for the same. Conventionally, during a cyclic loading experiment, the actuator that loads the specimen is paused at zero and peak displacements of each cycle to note observations. As a result, the strain limit for local buckling is generally established by the strain corresponding to the peak displacement preceding visually identified buckling. In this study, an effort was made to implement an objective approach to identify this limit state. This approach

Table 7.1 Large-scale experiments performed on hollow circular steel columns connected to the GSS connection.

S No.	No. of Shear Studs	Steel Gr.	L_e	Failure Mode	Comments
1	96	ASTM A500 Gr.B	24"	PH,LB	Fulmer et al. Test 2
2	96	ASTM A500 Gr.B	24"	PH,LB	Fulmer et al. Test 4
3	96	ASTM A500 Gr.B	24"	PH,LB	Fulmer et al. Test 6
4	32	API 5L X52 PSL2	24"	PH,LB	This Study Test 1
5	16	API 5L X52 PSL2	24"	PH,LB	This Study Test 2
6	16	API 5L X52 PSL2	24"	PH,LB	This Study Test 3
7	16	API 5L X52 PSL2	16"	PC	This Study Test 4

¹ L_e = Embedment length into the connection

² PH: Plastic Hinging; LB: Local Buckling; PC: Premature Connection Failure

is discussed next.

To date, there have been seven large-scale tests on bridge piers that use hollow circular steel columns with the GSS connection. Table 7.1 provides the complete test matrix. Three of these tests were performed by Fulmer et al. [Ful15], and four were completed as part of this study. In all of these tests, when the strain history of critical sections is plotted against the applied force, irregularities indicative of local buckling could be observed. Figure 7.5 shows two examples where irregularities can be seen in the force-strain hysteretic curve. In all of the tests, this behavior was observed during loading cycles of ductility 2, which was commensurate with the instance associated with the onset of strength reduction in the global system. Hence, the peak compressive strain prior to such displays of irregularities was chosen as the limit state strain.

The compressive strain limit for local buckling was evaluated for all but two of the available large scale tests that exhibited this phenomenon. Test 6 in Fulmer et al. [Ful15] differed

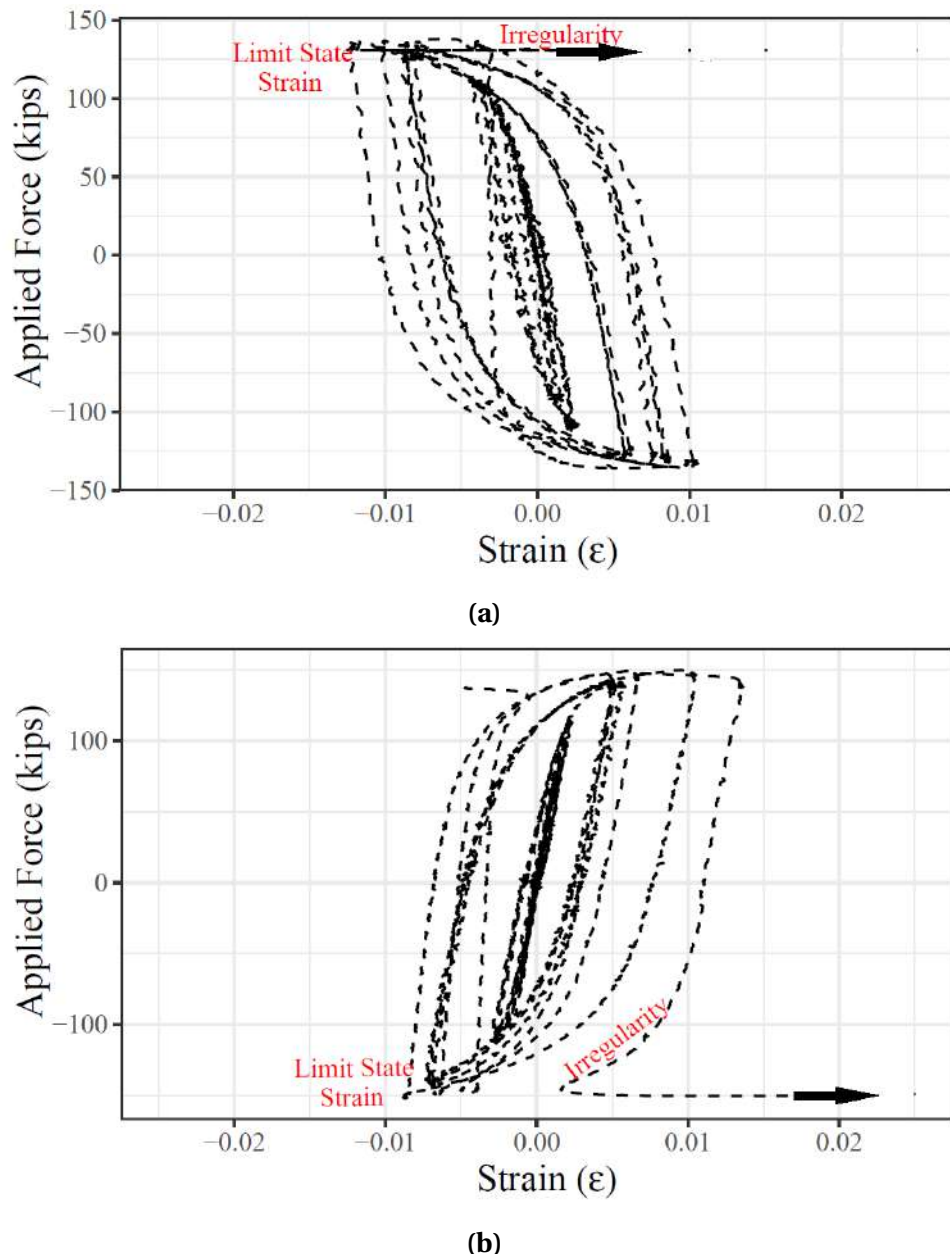


Figure 7.5 Applied force versus strain at critical sections during cyclic loading: (a) Fulmer et al. Test 2 Column 1 South face and (b) This Study Test 2 Column 1 North Face.

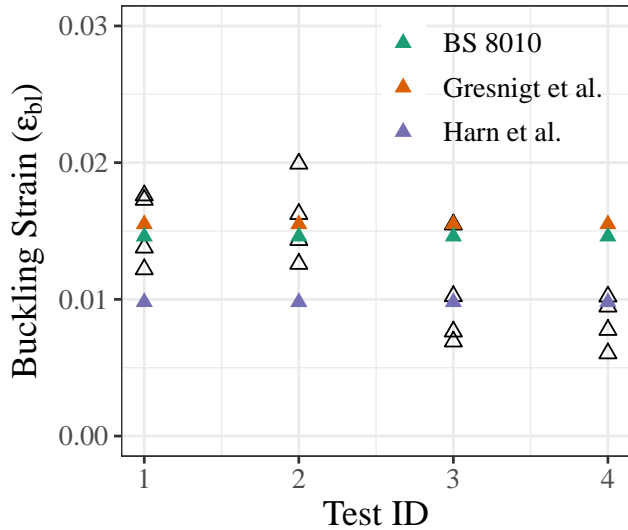


Figure 7.6 Empirical compressive strains prior to local buckling.

from the rest in the application of an external axial load on the test specimen. Since the axial load impacts strain measurements, this test was not considered for evaluation. Furthermore, results from test 1 of this study also had to be excluded because there was an excessive amount of noise in the strain measurements that rendered real data unrecoverable. Strain limits evaluated from the rest of the tests are shown in Figure 7.6. Results observed from the experiments are also compared to existing models that prescribe strain limits. It can be observed that for a D/t ratio of 32, the models provide reasonable approximations. Harn et al. [Har19] model is a conservative limit, as intended by the authors. The Gresnigt [Gre14] and British Standards [BS93] models provide an average fit.

The limit strains measured in this study can be observed to be collectively lower than those of Fulmer et al. [Ful10b]. It is thought that this may be because of the “weaker” connection used in this study, as discussed in previous chapters. In the GSS connections of

this study, a fewer number of shear studs and weaker grout were used. This caused the critical section to propagate upwards along the column. In effect, the strains measured using the top two rows of LED sensors might not resemble accurate limits. In addition, the possibility of this variation caused by the difference in steel grade also cannot be ruled out without further studies. Regardless, it was concluded that the existing models provide adequate estimates of the limit state strain for local buckling of hollow circular pile/columns.

7.3 Displacement Limits of Cantilever Columns

Structural displacements at various limit states are imperative for DDBD because they dictate the choice of target displacement for the design level hazard. For hollow steel columns, important limit states are yielding of the column, wall local buckling, and appropriate levels of percentage strength reduction. In DDBD, the capacity of a structural component is defined using simplified representations of their force-displacement response, as shown in Figure 7.7. Therefore, to carry out seismic design or assessment, it is sufficient to have a fully defined force-displacement response numerically characterized by the ordered pairs of displacement and force (Δ, F) for each limit state.

If fully defined, Figure 7.7 contains useful pieces of information. First, it provides the values for target displacement necessary to design for each limit state. Second, the member ductility at any given limit state can be calculated, which is used to establish the level of equivalent viscous damping. And third, the secant stiffness at any limit state can be determined which is useful for equivalent linearization.

The objective of the remainder of this chapter is to calibrate a simplified force-displacement response for systems with hollow steel columns as members forming plastic hinges. This

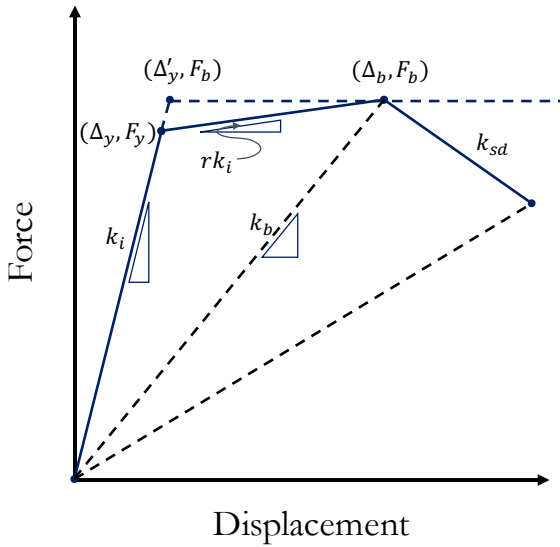


Figure 7.7 Simplified force-displacement response.

was achieved by using experimental data in combination with computational modeling. First, limit states for a single hollow steel column have to be considered before extending the discussion to systems with multiple columns.

7.3.1 Yield Limit State

Yielding of steel members with doubly symmetric sections, by definition, occur at the first instance where column-section extreme fibers are subjected to yield strain (ϵ_y), as given by Equation 7.8, where f_y is the minimum yield strength and E_s is the elastic modulus. The section curvature that corresponds to this point is known as the yield curvature (ϕ_y). A Moment-curvature analysis or simple section analysis can be used to obtain the yield curvature and the yield moment (M_y). For symmetric sections, the neutral axis can be reasonably assumed to be at the section mid-height. Consequently, Equation 7.9 can be

used to determine ϕ_y , where D is the section depth/diameter.

$$\epsilon_y = \frac{f_y}{E_s} \quad (7.8)$$

$$\phi_y = \frac{2\epsilon_y}{D} \quad (7.9)$$

The yield curvature can then be used to determine the yield displacement (Δ_y) using the 2nd moment-area theorem. The displacement at the free end of a cantilever can be calculated by finding the first moment of the area under the curvature diagram, as shown in Figure 7.8. For the yield limit state, this area will be that of a triangle, and Δ_y can be calculated using Equation 7.10, where L_c is the clear cantilever length of a column. Note that this evaluation of displacement does not account for shear deformations. However, the contribution of shear deformation to the overall displacement of the type of columns considered here is negligible because of the low shear stress developed due to their slenderness.

$$\Delta_y = \frac{\phi_y L_c^2}{3} \quad (7.10)$$

The yield force can be calculated from the yield strength (f_y) of the material and the elastic section modulus (S) of the column section using Equation 7.11. The numerator in

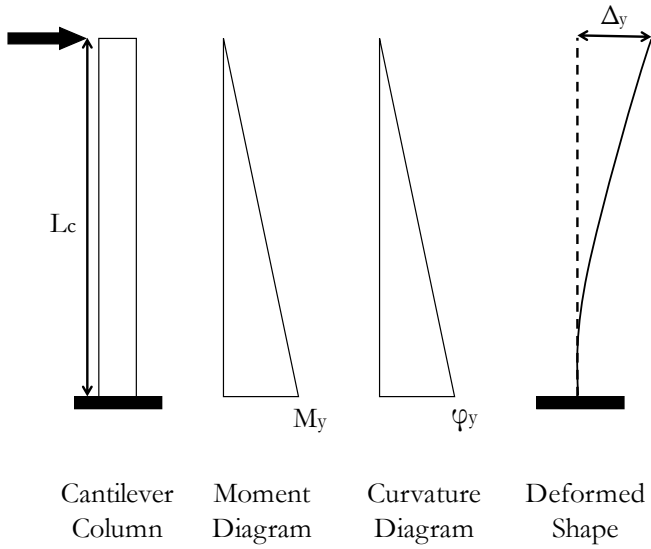


Figure 7.8 Moment area method for the calculation of yield displacement.

this equation is the yield moment (M_y).

$$F_y = \frac{f_y S}{L_c} \quad (7.11)$$

7.3.2 Local Buckling Limit State

Column wall local buckling is considered as an important limit state for hollow steel sections because of the accompanied onset of system strength reduction. Usually, this limit state occurs as a precursor to plastic hinging, but the order of occurrence can occasionally be reversed for sections with small D/t ratios. For design, this limit state can be assumed to occur when the compressive strain in extreme fibers reaches the limit prescribed by empirical models discussed in the previous section. Since the Gresnigt and British Standards

Table 7.2 Section details and their strain limits for local buckling as determined using British Standards model.

S No.	D/t ratio	Strain Limit (ϵ_b)
1	21.3	0.033
2	25.6	0.023
3	26.7	0.021
4	32.0	0.017
5	37.3	0.011
6	38.4	0.010
7	40.0	0.009
8	44.8	0.007
9	48.0	0.006
10	56.0	0.004

models more closely matched the experiments in this study, these were chosen as the models that defined buckling for the remainder of this chapter. For a circular column with D/t ratio of 32, the strain limit for buckling was thus evaluated to be about 0.017. Strain limits for other D/t ratios that were used for numerical studies, discussed later, are provided in Table 7.2.

The ideal method to determine the section curvature at buckling (ϕ_b) is to perform a moment-curvature analysis of the section and extract the curvature corresponding to the point when strain in extreme fibers becomes equal to the prescribed strain limit. However, a simpler method was also sought to enable a quick, but approximate calculation. An expression of the same format as that used to obtain yield curvature was developed, which is given by Equation 7.12. Note that the coefficient b_c is analogous to the number “2” in Equation 7.9, but is a function of the section D/t ratio. This coefficient was calibrated by linear regression of data obtained by performing hundreds of moment-curvature analyses

on hollow steel sections with varying D/t ratios and axial loads. The D/t ratios that were used are provided in Table 7.2 and the axial load ratios varied from 0% to 10%.

$$\phi_b = \frac{b_c \epsilon_b}{D} \quad (7.12)$$

$$b_c = 2.81 - 0.019 \left(\frac{D}{t} \right) \quad (7.13)$$

Note that the columns will be well into their nonlinear range at the time of local buckling. The moment-area method may still be applied to obtain the limit state displacement. However, it is not as straightforward as it was to calculate the yield displacement. The plastic hinge method [Pri07] can be implemented to simplify this calculation.

The plastic hinge method assumes that the total displacement at the top of a cantilever column is composed of two independent displacement components: elastic (Δ_e) and plastic (Δ_p). This concept is illustrated in Figure 7.9. At the local buckling limit state, say, the maximum bending moment at the critical section is denoted by M_b , the bending moment diagram is shown in Figure 7.9. Adjacent to the bending moment diagram, shown in black, is the nonlinear curvature diagram. Recall that the first moment of the area under this curvature diagram about the column top gives the top displacement. This curvature profile can also be idealized to be composed of a triangular and a rectangular area, shown in red. It is easier to calculate the first moments of the area of these regular shapes, which in turn provides two separate values. These two values can be added together to get the top displacement (Equation 7.14). These displacement components are termed as the elastic (Δ_e) and the plastic (Δ_p) components.

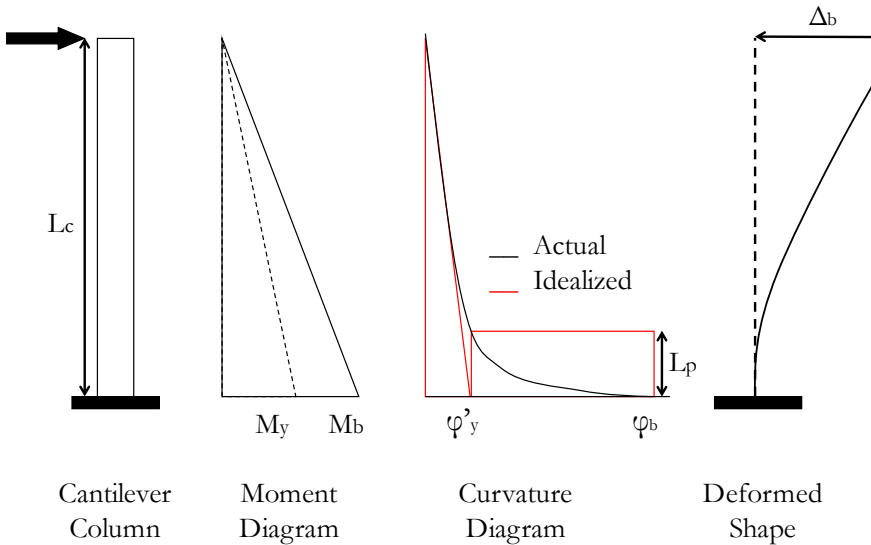


Figure 7.9 Plastic hinge method for the calculation of displacement at local buckling.

The elastic component (Δ_e) of displacement can be calculated in the same way as the yield displacement, albeit with a minor difference, as shown in Equation 7.15. The curvature term (ϕ'_y) in this equation is an equivalent curvature, which may be calculated using Equation 7.16, where M_y and M_b are the bending moments at yield and buckling limit states, respectively. The calculation of buckling moment (M_b) is discussed later. Such an adjustment to the curvature is a mathematical convenience to facilitate the division of the nonlinear curvature diagram into two regular areas as accurately as possible.

$$\Delta_b = \Delta_e + \Delta_p \quad (7.14)$$

$$\Delta_e = \frac{\phi'_y L_c^2}{3} \quad (7.15)$$

$$\phi'_y = \phi_y \left(\frac{M_b}{M_y} \right) \quad (7.16)$$

$$\Delta_p = L_p (\phi_b - \phi'_y) \left(L_c - \frac{L_p}{2} \right) \quad (7.17)$$

$$L_p = k_p L_c \quad (7.18)$$

$$k_p \approx 0.035 \quad (7.19)$$

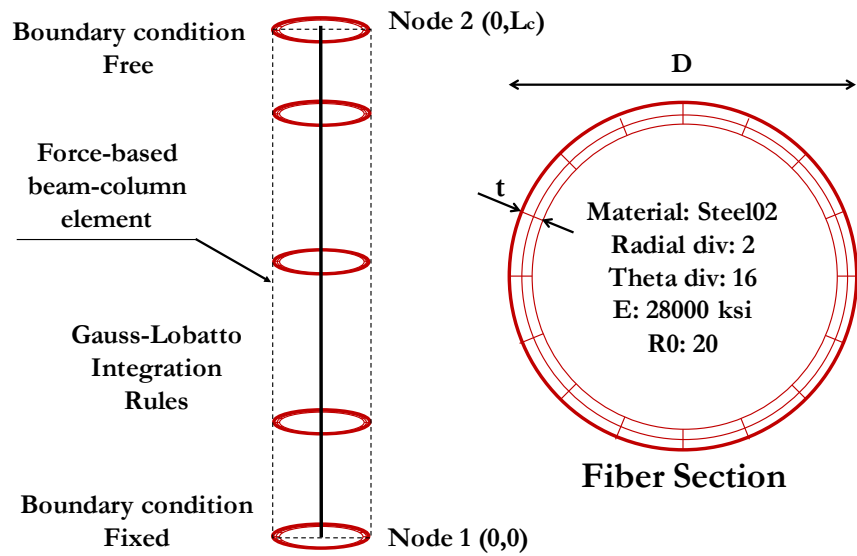
The plastic component (Δ_p) may be obtained by calculating the first moment of the rectangular area about the top, as shown in Equation 7.17. The height of this rectangle is called the plastic hinge length (L_p), which is a mathematical construct calibrated so that the plastic hinge method provides accurate results. To calibrate L_p , a parametric study was performed. In this study, fiber-based models of cantilever hollow steel columns were subjected to monotonic pushover analyses. There were 540 models in total, which were obtained by varying the cantilever length (L_c), column diameter (D), column wall thickness (t), steel yield strength (f_y), and steel strain hardening ratio (b_{sh}). The range of each variable used in the experimental study matrix is shown in Table 7.3. Pushover analyses were performed in OpenSees [McK10]. A generalized schematic of these models is shown in Figure 7.10. A single force-based element was used with discretized sections, as shown. OpenSees's *Steel02* material model was utilized. Gauss-Lobatto integration rule was employed to obtain section responses parameters, such as stress, strain, moment, and curva-

Table 7.3 Independent variables in the numerical experimental study matrix.

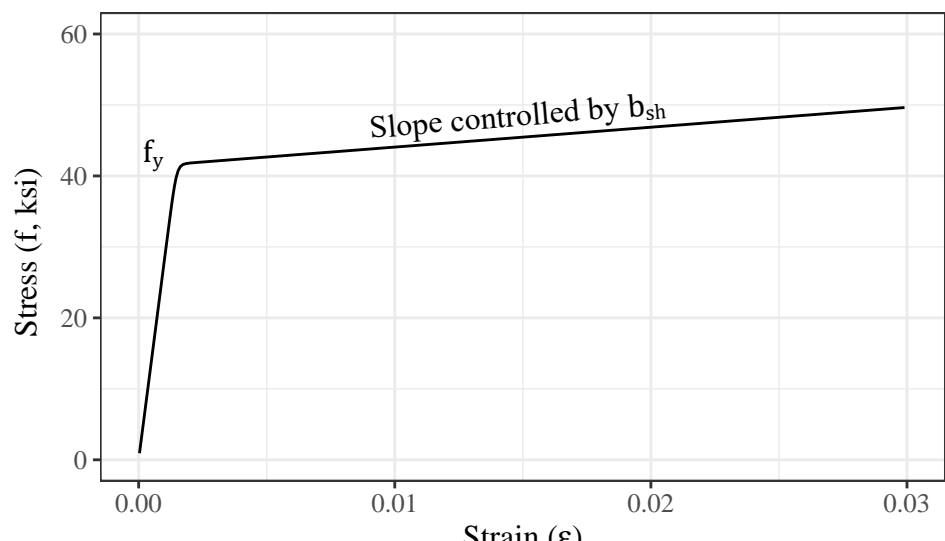
Variables	Values
Cantilever Length, L_c (in)	80, 100, 120, 140, 160
Column Diameter, D (in)	16, 20, 24, 28
Column Wall Thickness, t (in)	0.500, 0.625, 0.750
Steel Yield Strength, f_y (ksi)	42.0, 52.0, 62.0
Strain Hardening Ratio, r	0.001, 0.005, 0.010

ture, at the fixed support.

Each separate analysis could provide the section curvature and the column top displacement corresponding to the local buckling limit state, which was identified by the strain limits provided by the British Standards [BS93] model. A typical result from a single analysis is shown in Figure 7.11. For all of the 540 analyses, the top displacement at local buckling was equated to Δ_b from Equation 7.14. This equality allowed solving for the lone unknown variable, L_p . It was found that L_p is directly proportional to the cantilever length (L_c) with k_p as the constant of proportionality, as shown in Equation 7.18. The coefficient k_p was largely insensitive to most of the other independent variables. The only variable to which k_p was somewhat sensitive to was the strain hardening ratio (b_{sh}) of the material model. Figure 7.12 shows k_p , plot against the column cantilever length (L_c). It can be seen that k_p remains unchanged for all column lengths. The impact of different strain hardening ratios on k_p are also shown in Figure 7.12. An average value of k_p was calculated for each b_{sh} , as shown in the figure. These values are also tabulated in Table 7.4. However, a constant k_p value of 0.035 produces results with reasonable accuracy.



(a)



(b)

Figure 7.10 (a) Implemented fiber-based model of cantilever column and (b) stress-strain response of steel material employed in the model.

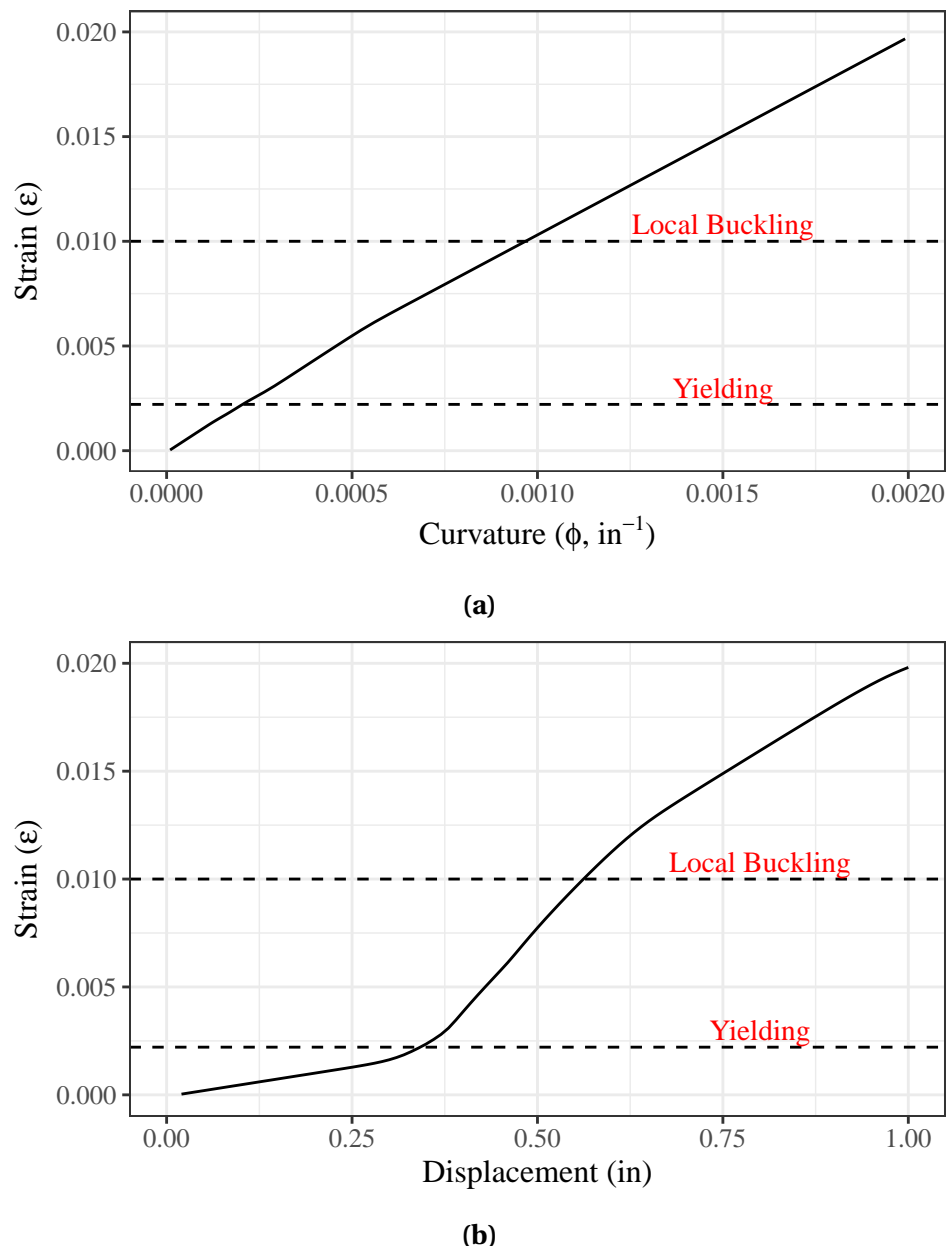


Figure 7.11 Typical results from pushover analysis of a cantilever column: (a) Strain versus Curvature and (b) Strain versus Displacement.

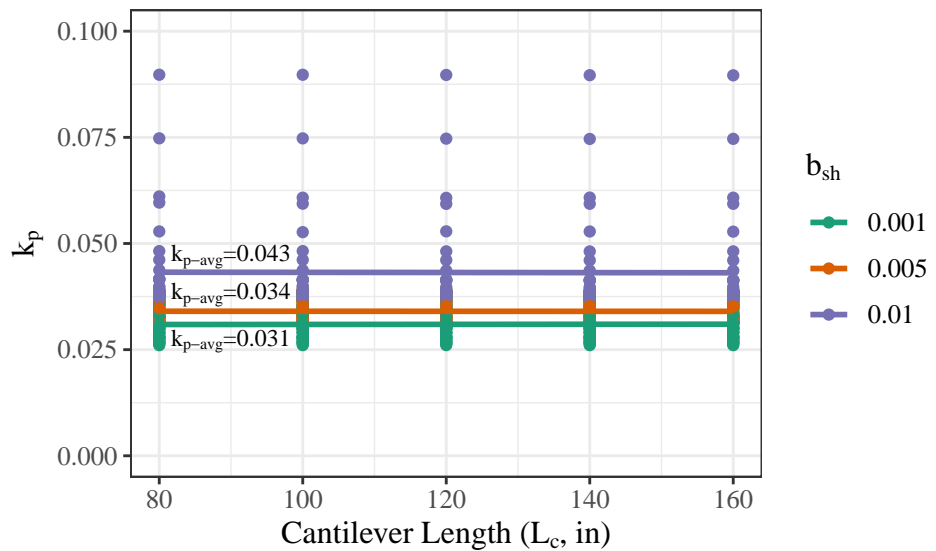


Figure 7.12 Coefficient (k_p) to estimate the plastic hinge length.

Table 7.4 Average values of k_p to calculate the plastic hinge length.

Strain Hardening Ratio (b_{sh})	k_p
0.001	0.031
0.005	0.034
0.01	0.043

7.3.3 Buckling Moment and Force

To fully define a simplified multilinear force displacement response, the system strength at the local buckling limit state must also be derived. The strength at local buckling is also likely to be the maximum strength capacity of the system because hollow steel columns experience a reduction in strength post-buckling. In Figure 7.7, r is the ratio between the second slope stiffness and the initial stiffness (k_i). If the bi-linear factor (r) is known up-front, then the force at local buckling can be calculated using Equation 7.20. Correspondingly, the moment capacity of the column section can also be obtained by multiplying both sides of this equation by the column cantilever length (L_c). Here, the capacity is capped by the plastic moment capacity (M_p) of the section. The results from the parametric study, discussed earlier, were used to obtain an approximate value of r , that can be used if the section geometry of the columns is known. While this may not be possible at the start of the design process, further refinement can be performed by iteration. Equation 7.21 provides a simple relationship between r , D/t ratio, and the steel yield strength. This relationship is visualized in Figure 7.13a. Empirical data is superposed with the model obtained by linear regression. A clear linear trend can be identified from this figure. Equations 7.20 and 7.21 were then used to estimate the force at the local buckling limit state in all of the cases considered in the parametric study. The results were compared to those obtained by numerical pushover analyses of fiber models. This comparison is shown in Figure 7.13b. The proposed equations estimated F_b with reasonable accuracy.

$$F_b = F_y \left[1 + r \left(\frac{\Delta'_b}{\Delta'_y} - 1 \right) \right] \leq \frac{M_p}{L_c} \quad (7.20)$$

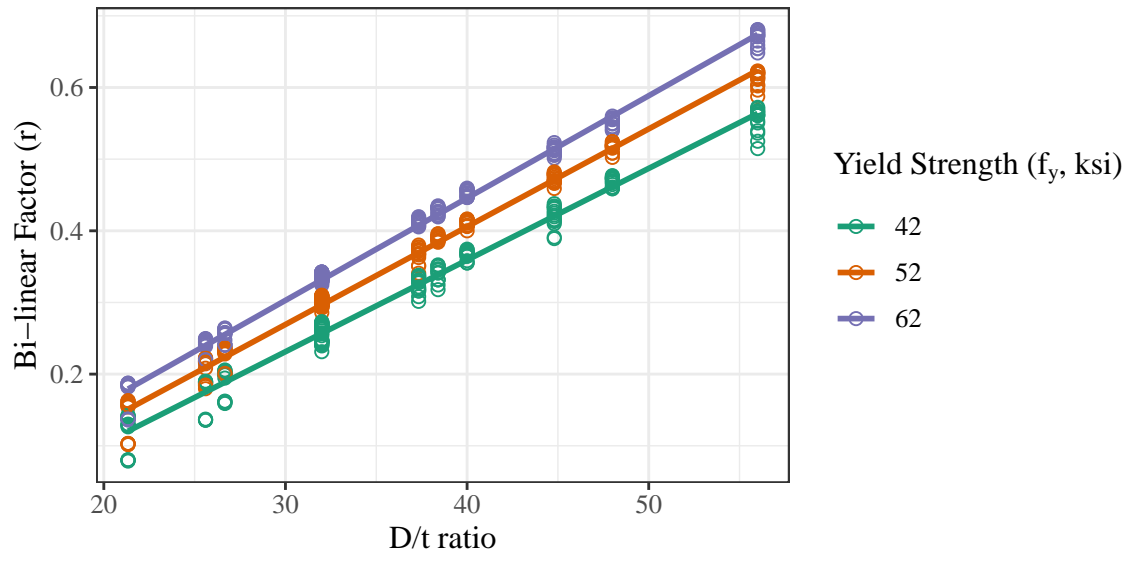
$$r = 0.0136 \left(\frac{D}{t} \right) + 0.004 f_y - 0.35 \quad (7.21)$$

7.3.4 Post-buckling Limits and Strength Degradation

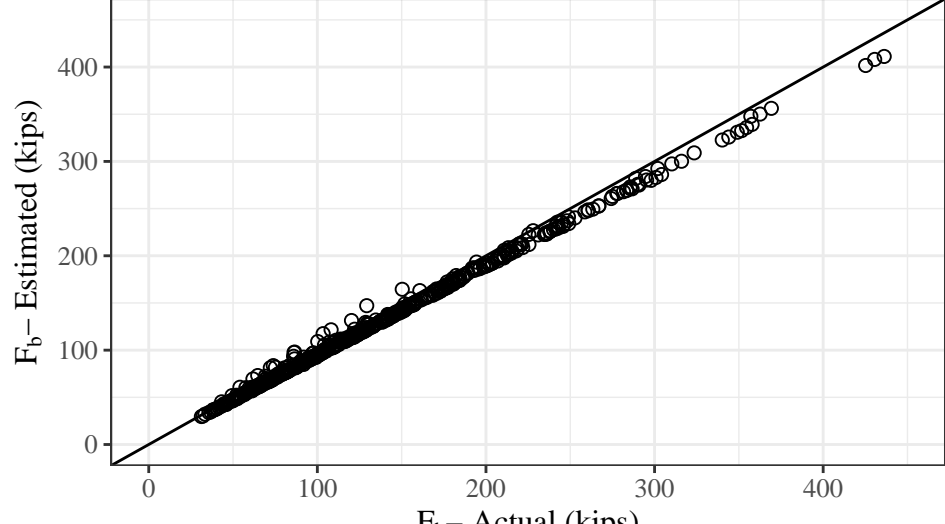
Equations 7.8 through 7.21 can be employed in a design process to form the multilinear force-displacement diagram for hollow steel piles/columns until the limit-state of column wall local buckling. In the large-scale experiments performed as part of this study and those in Fulmer et al. [Ful15], it has been observed that these structural systems are capable of reliably deforming past the point of wall local buckling and plastic hinging. Therefore, it may be more efficient to consider some level of strength degradation as the ultimate limit state. However, before describing the post-buckling behavior and associated limit states of hollow steel columns, a few more details regarding experimental data and a more refined numerical model merit discussion. These are discussed in the next section before proceeding to propose relationships to establish post-buckling limit states.

7.4 Fiber-based Computational Model for Limit-state Prediction

Predominant use of hollow steel piles/columns as substructures for bridges, piers, or wharves does not just involve a single column. Generally, these systems consist of two or more



(a)



(b)

Figure 7.13 (a) Bi-linear factor (r) versus D/t ratio and (b) Comparison between the value of force at local buckling (F_b) obtained from pushover analysis and that calculated using proposed equations.

piles/columns connected by a cap element. The simplified procedure for obtaining limit state displacements described in the preceding section does not account for the added flexibility afforded to these systems by the connections and/or cap elements. To be able to capture these effects, a simple computational model and associated calibration factors are presented, which can be made use of to get accurate estimates of limit state displacements through pushover analysis. This model is based on fiber elements and therefore requires software that allow for such modeling practice. In this study, OpenSees [McK10] was chosen to perform the required analyses.

7.4.1 Total Displacement of a Bridge Pier System

In a lateral load resisting bridge pier system, flexural stiffness of the piles/columns are not the only source of global stiffness. Consequently, to estimate the target displacement of a bridge pier, one must consider the contribution from all of the additional flexibility in the system. It is convenient to differentiate all of the major contributors to the total displacement using Figure 7.14.

A typical bridge pier consisting of two pile columns and a cap-beam is shown in Figure 7.14a. Also shown is the typical bending moment diagram under a lateral force, F_T . All of the specimens in the large-scale tests discussed in this document mimicked the portion above the point of contraflexure by using pinned supports. If only column flexure is considered first, the bridge pier will undergo a lateral displacement, Δ_T , when subjected to F_T . This condition can be modeled numerically by using a rigid element for the cap-beam, as denoted by condition 1 in Figure 7.14b. Here, the GSS connection is also modeled as a rigid element, which resembles common practice for connections of this kind. Note that

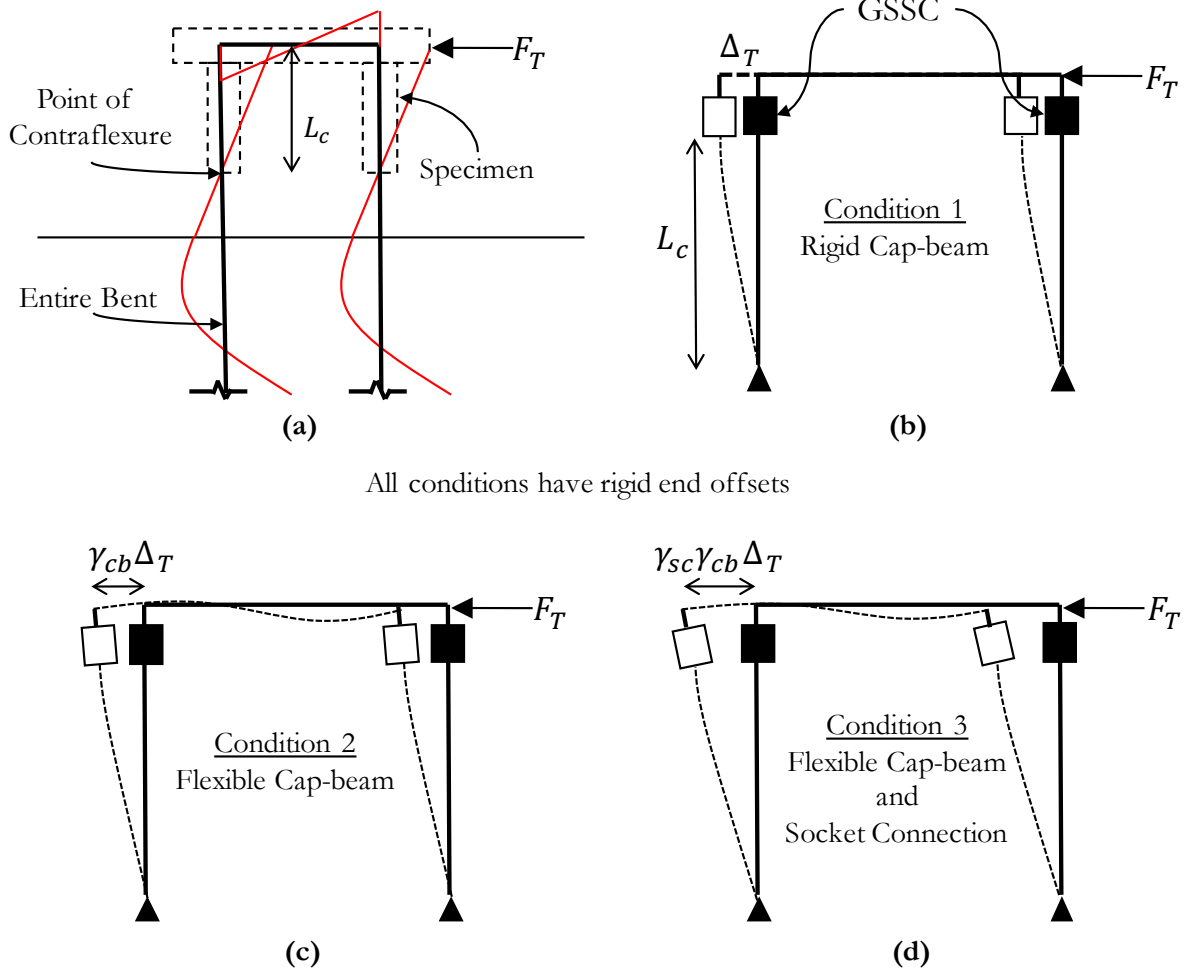


Figure 7.14 Illustration of displacement components in a bridge pier: (a) A typical bridge pier under lateral loading; (b) System displacement due to column flexure; (c) Modified displacement due to cap-beam flexibility; (d) Modified displacement due to socket action.

the subscript T stands for *Target* and represents any limit state of importance. The target displacement for a given limit state under this condition is exactly equal to the displacement limit evaluated for a single column, discussed earlier.

In reality, however, the cap-beam may not behave as a rigid element in bridge piers. Note that there are cases where the cap-element can be considered rigid, e.g., in a wharf. In bridges, the cap-beam is a flexible capacity protected member and therefore behaves elastically. Cap-beam flexibility increases the global displacement of the system under the same force, F_T , as shown in Figure 7.14c referred to as condition 2. Here, this displacement is represented as Δ_T modified by a cap-beam flexibility coefficient (γ_{cb}).

Socket connections such as the GSS connection introduces even more flexibility in the system, mainly because of two reasons. There is a minor contribution from the flexure of the socket itself, which in reality is not a rigid element. This additional flexibility increases with increasing embedment length (L_e), discussed in Chapter 5. There is a much larger contribution from the socket action mechanism, also discussed in Chapter 5. For the same force, F_T , an additional global displacement will be observed because of column rocking behavior inside the socket. This condition is visualized as condition 3 in Figure 7.14d. A socket connection flexibility coefficient, γ_{sc} is used to capture the additional displacement produced as a result.

In a numerical model representing bridge piers that use GSS connections, all of the above flexibility mechanisms will need to be accounted for. A comparison between the force displacement responses of a two-column bridge pier when modeled according to the three previous conditions is shown in Figure 7.15a. There is a significant difference in the initial stiffness between the three different model types. When the monotonic re-

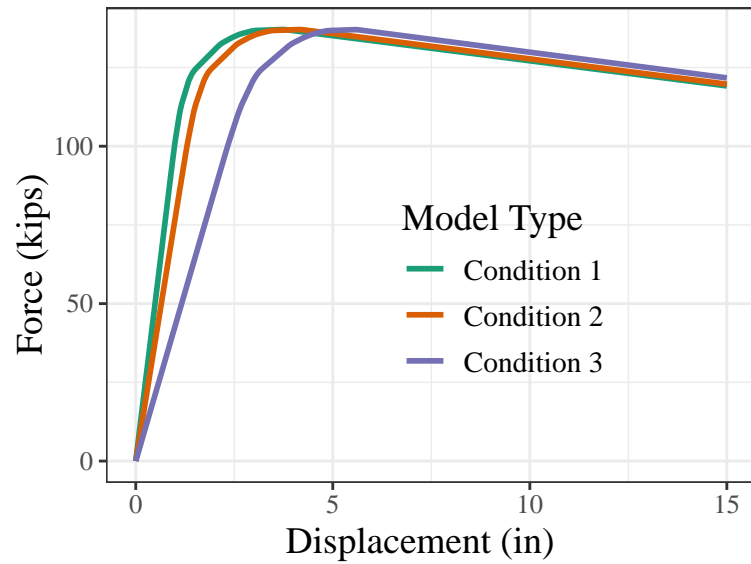
Table 7.5 Comparison of estimated limit state displacements of the experimental specimen calculated using different models.

Model	Yield Displacement (in)	Buckling Displacement (in)
Plastic Hinge Method (Eq. 7.8 - 7.21)	0.95	1.89
Condition 1 - Fiber model (Δ_T)	0.93	1.97
Condition 2 - Fiber model ($\gamma_{cb}\Delta_T$)	1.23	2.54
Condition 3 - Fiber model ($\gamma_{sc}\gamma_{cb}\Delta_T$)	2.09	5.31
Experimental Observation	2.04	5.39

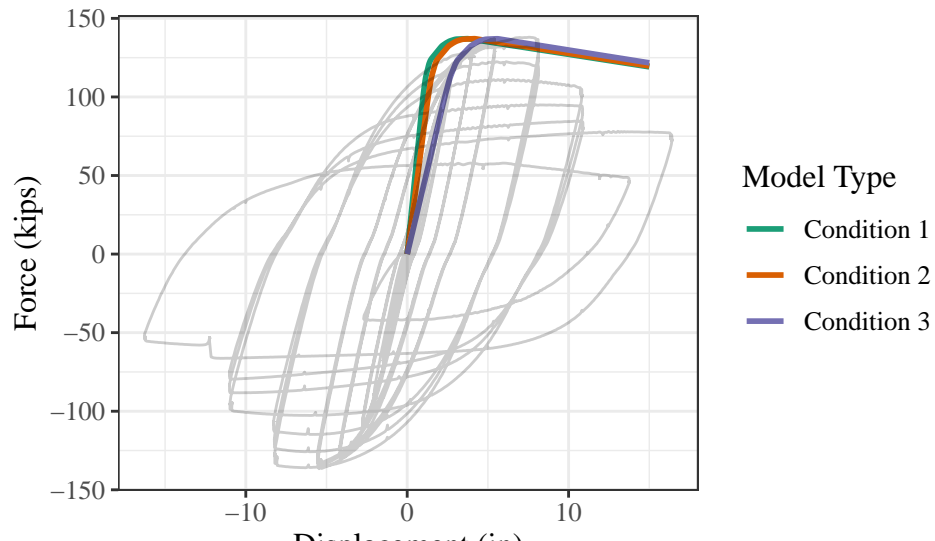
spose curves are superimposed upon the cyclic response of the bridge pier obtained from experimental data, it can be seen that condition 3 accurately resembles the flexibility in the system. Table 7.5 shows the comparison of values of system displacement at yield and buckling limit states obtained from different methods. It can be observed that results from condition 1 numerical model are close to those obtained for a cantilever column using the plastic hinge method, discussed earlier. Similarly, results from condition 3 numerical model more closely match observations from the large scale experiment. Details of the numerical model used to obtain these results follow subsequently.

7.4.2 Development of the Numerical Model

The primary objective of the numerical model was to estimate accurately the global displacements of a two-column bridge pier under lateral forces. Accuracy in this scenario refers to the capability of mapping local strains at the plastic hinge section to global displacement, as observed in the structural tests. It must be noted that such a mapping is only valid until the limit state of local buckling is achieved because afterwards conventional



(a)



(b)

Figure 7.15 Comparison of force-displacements responses of numerical models: (a) Three conditions 1, 2, and 3 shown in Figure 7.14 and (b) same curves superimposed on the corresponding experimental cyclic response.

strain measurements are rendered meaningless due to permanent pinching of the section. The secondary objective was to capture the rate of post-buckling strength degradation accurately so that at the global level, it is possible to define a degrading force-displacement curve until an ultimate limit is reached. The model that was developed to achieve these objectives is outlined in Figure 7.16.

This model is in 2-D and consists of two nonlinear force-based (FB) beam-column elements representing columns. They have multiple integration points at which the hollow circular cross-section is discretized into fibers. These column elements are pin supported on one end and connected to zero-length rotational springs on the other. These springs replicate the additional flexibility afforded to the system due to socket action. These springs are, in turn connected to the GSS connections, which are also modeled as beam-column elements. Albeit, these are capacity protected. However, their elastic flexibility needed to be accounted for and hence are modeled with discretized fiber sections with steel and grout material, as shown in the figure. The pier cap-beam is modeled as an elastic element along its centerline to account for cap-beam flexibility. Its section properties mirrored those of the cap-beams in the experiments. This cap-beam is connected to the GSS connection elements using a rigid links, emulating half the depth of the beam.

The material model implemented for structural steel was the *Hysteretic Material* model available in OpenSees. This model was chosen because of its ability to allow a user-defined backbone and potential for capturing post-buckling strength degradation. The grout material in the connection was modeled using the *Concrete01* material in OpenSees. The Mander et al. [Man88] model was used to calculate the confined strength of grout inside the connection, which was used as input for the material model. Gauss-Lobatto integration

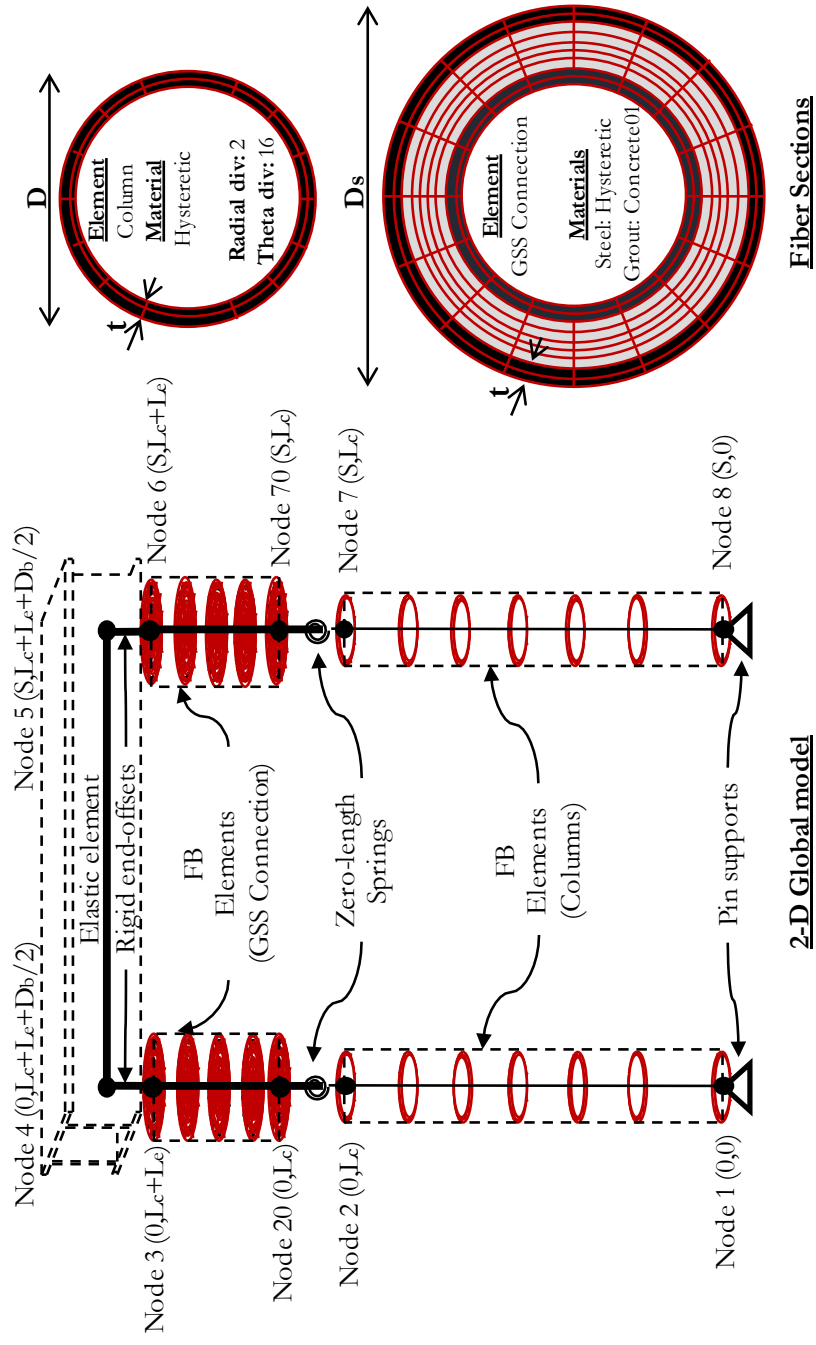


Figure 7.16 Fiber element model summary.

rule was used for the analyses because it includes both endpoints in the set of integration points. This was necessary because the section response variables such as strain and curvature at the interface between the column and the GSS connection was required to identify limit states based on strain. In total, there were 7 integration points in the columns and 5 in the connection elements.

Many different modeling approaches were tried before converging to the model presented here. During model development, there was a set of rules/criteria that had to be met for the final model to be useful. These are enumerated below:

1. At a minimum, the model must be able to predict yield displacement and the displacement at pipe wall local buckling, given the respective strain limits are established previously.
2. The model must be scalable, i.e., it should be able to provide reliable results for varying bridge geometries and column section properties, including D/t ratios.
3. The model must be able to provide an approximate backbone estimate of post-buckling strength degradation behavior.
4. The model must be reproducible with a small number of calibration constants.

7.4.2.1 Behavior Prior to Local Buckling

To accurately capture system yield displacement, it is critical to account for the full flexibility of the system. This can be achieved by creating a numerical model that resembles flexibility condition 3 in Figure 7.14. To this end, rotational springs were introduced at the interface between column and connection elements. The moment-rotation property for

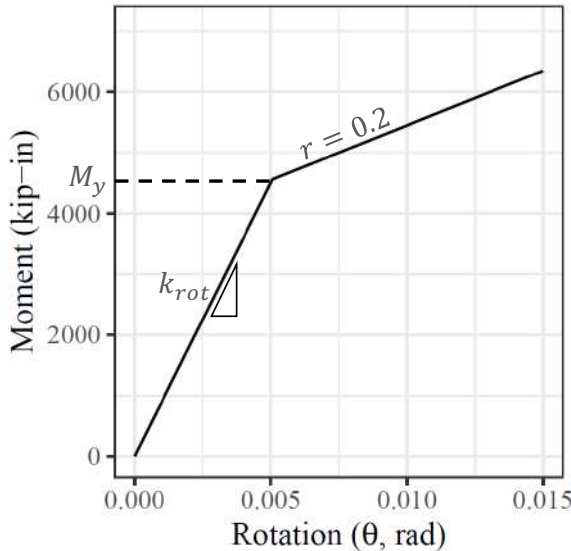


Figure 7.17 Moment-rotation rule for rotational spring.

the rotational spring followed a bilinear curve, as shown in Figure 7.17. The elastic stiffness (k_{rot}) of this spring dictates the overall initial flexibility of the connection. In their experiments, Fulmer et al. [Ful15] employed a stiff connection with high strength grout and 96 number of 3/4" shear studs. In comparison, the test specimens in this study, which contained between 16 and 32 shear studs and an engineered reduction in grout compressive strength, exhibited increased socket action and a more flexible connection. Figure 7.18 illustrates the variation in initial stiffness between different experiments. The value of k_{rot} was calibrated for each experiment.

Similarly, the yield point of the rotational spring determines the total displacement at local buckling. It was found that reasonably accurate values of total displacement at local buckling could be achieved if the yield point of the spring matches the yield point of the column. For example, the yield moment (M_y) of the columns tested by Fulmer et al. was

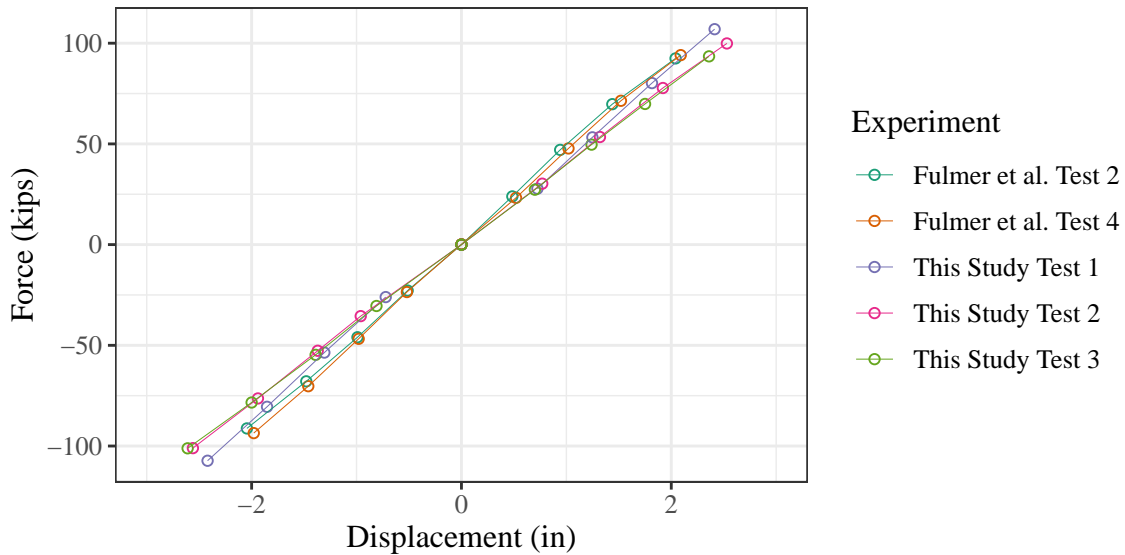


Figure 7.18 Comparison of initial stiffness between five different large scale tests.

less than those tested in this study because of the difference in their yield strength. The total displacements at buckling for each experiment reflected the observed value more closely when their respective M_y was used as the yield moment for the rotational springs. The responses of the numerical model, thus calibrated, is compared to the response of the experimental specimens in Figure 7.19 and Table 7.6.

Note that these results were obtained by modeling the two-column bent and its components according to their physical and geometric properties. The calibration parameters that control the variation in the model responses in Figures 7.19 and 7.20 are k_{rot} and M_y . M_y is the column yield moment. However, to determine an accurate value of k_{rot} , further experiments to study socket action are warranted. An interesting observation regarding k_{rot} is the following. Drastically varying connection stiffnesses between the experiments of Fulmer et al. do not result in an equivalent degree of variation in system stiffness. Further-

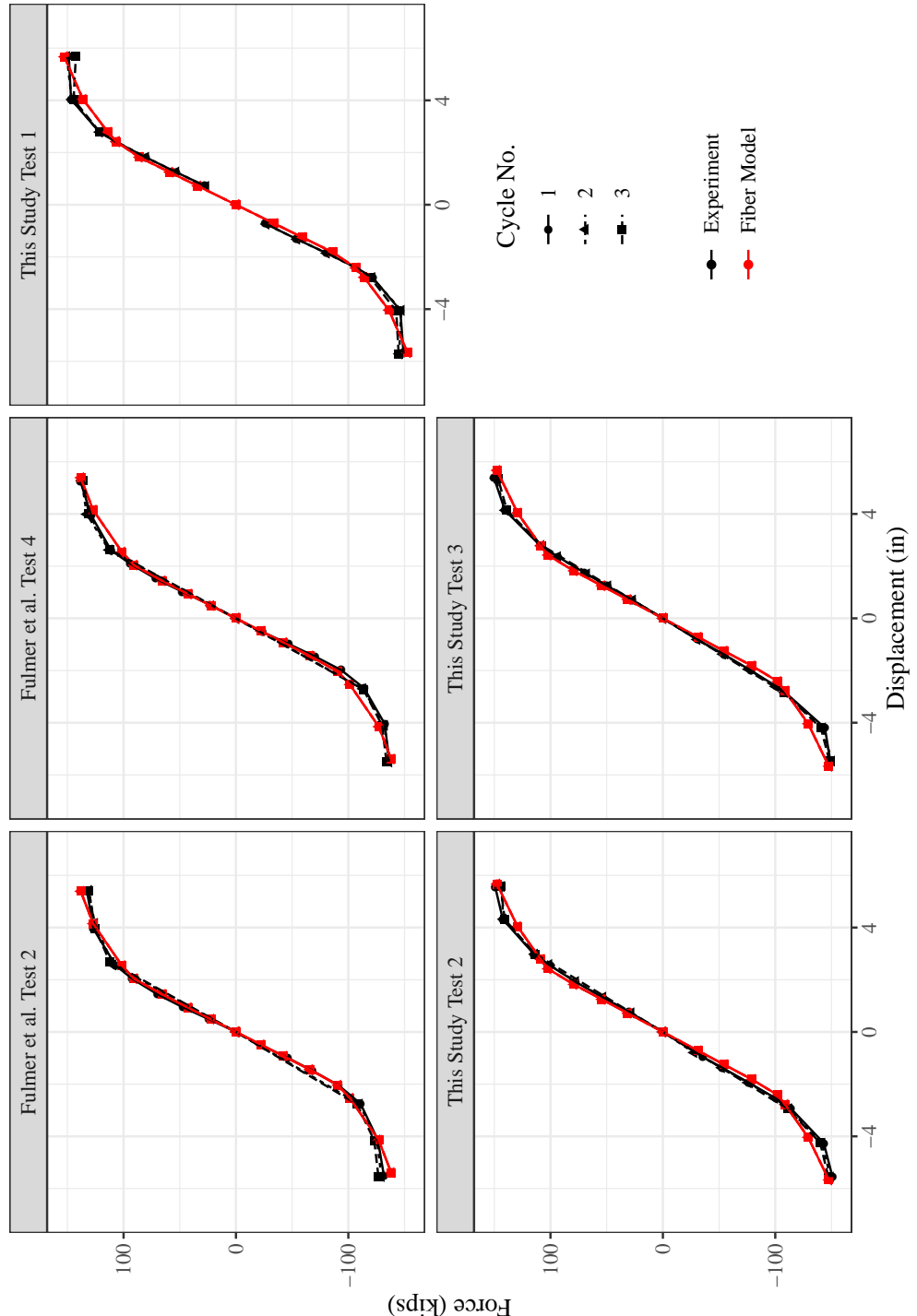


Figure 7.19 Comparison between experimental and simulated force-displacement backbone response until buckling.

Table 7.6 Comparison of yield displacement, buckling displacement, and rate of strength degradation between experiments and numerical models.

Test ID	Source	Yield Displacement (in)	Buckling Displacement (in)	Strength Degradation Rate (kip/in)
Fulmer et al. Test 2	Experiment	2.01	5.51	-7.41
	Fiber model	1.93	5.26	-7.16
Fulmer et al. Test 4	Experiment	2.09	5.28	-7.05
	Fiber model	1.93	5.09	-7.16
This Study Test 1	Experiment	NA ¹	NA ¹	-9.05
	Fiber model	2.07	5.66	-9.54
This Study Test 2	Experiment	2.53	5.56	-7.20
	Fiber model	2.24	5.89	7.62
This Study Test 3	Experiment	2.36	5.37	-7.72
	Fiber model	2.24	5.3	- 7.62

¹ NA: Missing Data

more, to emulate these system stiffnesses, the value of k_{rot} that was used ranged between $6.5 \times 10^5 - 8.0 \times 10^5$ kip-in/rad. It is reasoned that the actual stiffness of a well designed GSS connection will be somewhere in between the two extremes considered here. Therefore, until further information becomes available, it is recommended that k_{rot} be taken anywhere between $7.0 \times 10^5 - 7.5 \times 10^5$ kip-in/rad.

7.4.2.2 Post Local Buckling Behavior

Column wall local buckling is generally followed by system strength degradation. The *Hysteretic* material model available in OpenSees enables the modeling of this degradation. Post local buckling strength degradation can be achieved by defining a multilinear stress-strain response in which the third branch has a declining slope, as shown in Figure 7.21a.

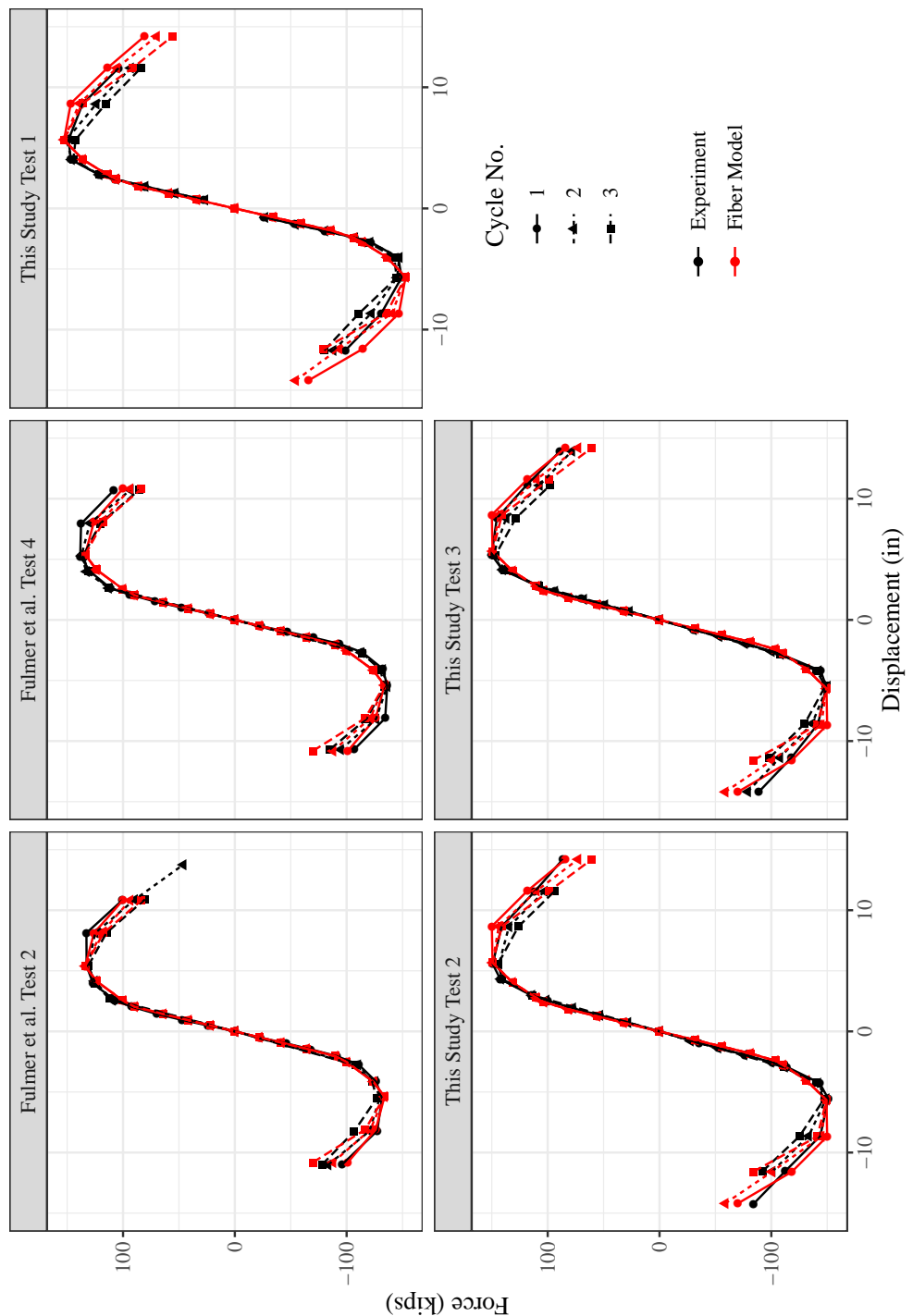


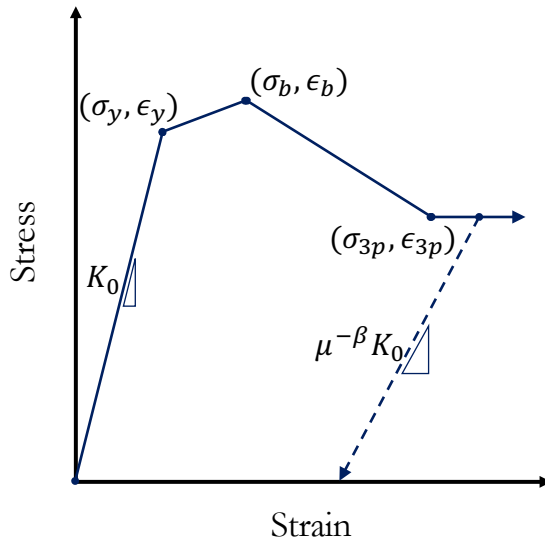
Figure 7.20 Comparison between experimental and simulated force-displacement backbone response from full cyclic pushover analyses.

In the figure, the initial stiffness K_0 is the elastic modulus of the material, and the ordered pairs of stress and strain (σ, ϵ) with subscripts y and b represent yielding and buckling, respectively. Parameters σ_{3p} and ϵ_{3p} control the strength degradation rate and therefore were calibrated using experimental data. Likewise, parameter β determines the rate of stiffness degradation based on ductility μ . Parameter β also required to be calibrated. Figure 7.21b shows the stress-strain response of the extreme fiber of one of the columns during a pushover analysis.

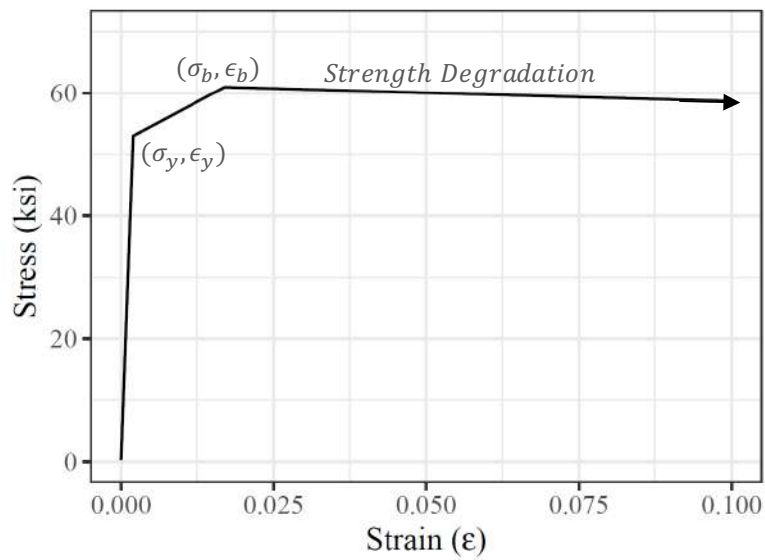
Calibration of post-buckling behavior was performed separately for each large scale test by trial and error. The objective of the trial and error procedure was to obtain the correct combination of parameters σ_{3p} , ϵ_{3p} , and β that will produce the same rate of strength degradation observed during the experiments. In all cases, ϵ_{3p} was kept constant at 0.6, while the other two parameters were varied. The rate of strength degradation under cyclic pushover analyses is compared to the corresponding experimental degradation in Table 7.6. The backbone curve obtained from cyclic pushover analyses is shown in Figure 7.20 accompanied by the results from experiments. A comparison of the full force-displacement hysteretic response curves between the fiber model and experimental data is shown in Figure 7.22. It can be seen that the model was able to produce a good match.

7.4.2.3 Extension to other D/t Ratios

All of the large scale experiments performed on the GSS connection consisted of columns with section D/t ratio of 32. This value of the D/t ratio is at the limit of what are classified as compact sections. To extrapolate results from these experiments to a model for estimating the behavior of columns with other D/t ratios, one must account for the accompanying



(a)



(b)

Figure 7.21 Hysteretic Material model from OpenSees: (a) Idealized; (b) From pushover analysis.

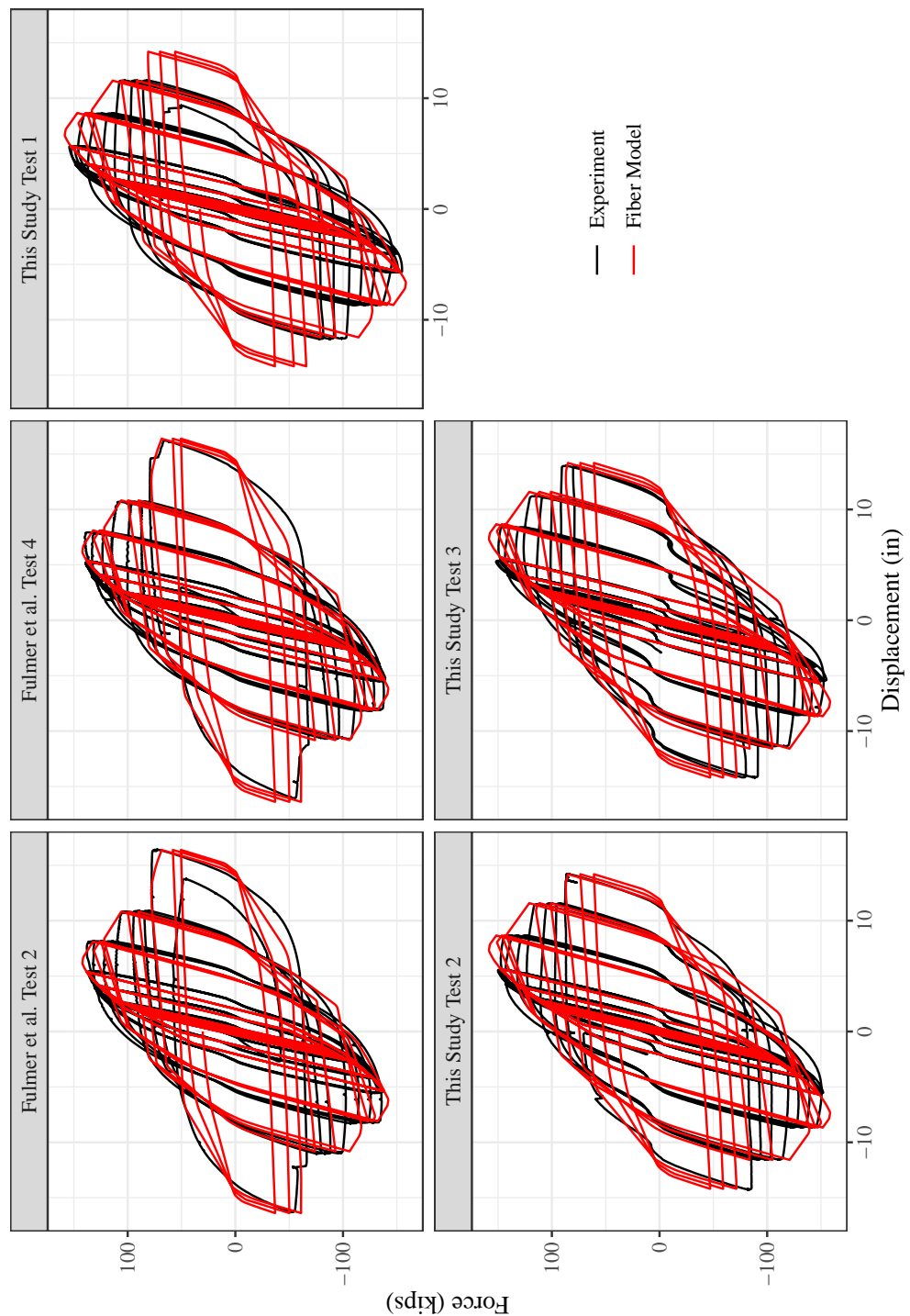


Figure 7.22 Comparison between experimental and simulated cyclic force-displacement response.

changes in structural response caused by changing D/t ratios. The ideal approach will be to perform further experiments on specimens with a variety of D/t ratios. However, such an effort will be expensive and time-intensive. As such, it is useful to implement numerical studies in combination with an intuitive understanding of the impact of D/t ratios from past studies to obtain a working model, that can be updated as experimental data becomes available.

The impact of D/t ratio on the behavior of hollow steel cross-sections has been extensively studied in the past. A large proportion of these studies focus on thin-walled cross sections. In the existing literature, generally, hollow steel pipes are classified based on their radius to thickness (R_t) ratio and slenderness ratio (λ_r), which are given by Equations 7.22 and 7.23, respectively. In these equations, r is the radius of gyration, ν and E are the Poisson's ratio and elastic modulus of the material, D and t are the column diameter and wall thickness, and h is the column height. R_t and λ_r originated from analytical solutions to the problem of buckling, both local and global, and have been in use since. The impact of λ_r on the behavior of columns pertain to their global stability and is outside the scope of this work. Dimensionless parameter R_t and its impact is discussed herein using the alternate definition of the diameter-to-thickness (D/t) ratio.

$$R_t = \frac{\sigma_y}{E} \frac{D}{2t} \sqrt{3(1 - \nu^2)} \quad (7.22)$$

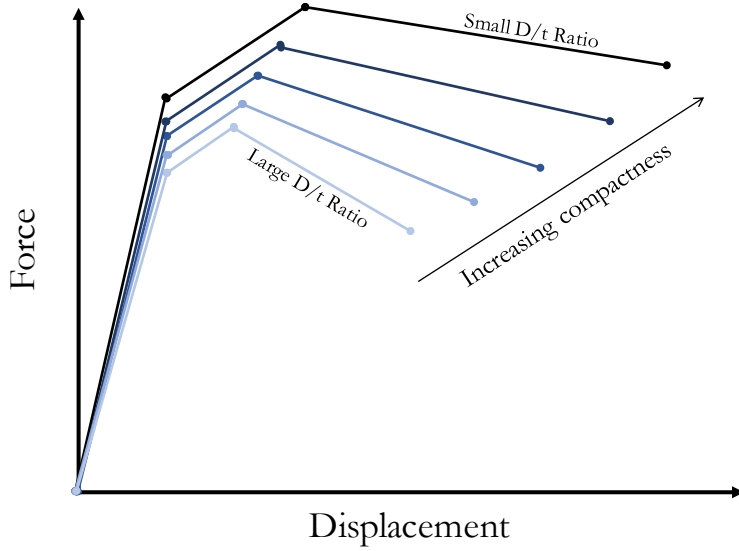


Figure 7.23 Idealized force displacement envelopes of hollow columns illustrating the impact of D/t ratio.

$$\lambda_r = \frac{2h}{r} \frac{1}{\pi} \sqrt{\frac{\sigma_y}{E}} \quad (7.23)$$

The impact of D/t ratio on the force-displacement behavior of single steel columns is illustrated in Figure 7.23. The figure shows idealized force-displacement curves of columns with the same height and diameter, but different D/t ratios. The yield displacement of the columns remains the same because it is a function of the diameter. The major behavioral changes pertain to the point of wall local buckling and the rate of strength degradation. Nominally, columns with larger D/t ratios exhibit local buckling at smaller strains, and consequently, displacements. Furthermore, the rate of post-buckling strength degradation is also higher for larger D/t ratios.

Researchers in the past have implemented both experimental and numerical approaches to study the local buckling behavior of hollow steel circular columns, both under monotonic and cyclic loading. Usami & Ge [UG98], Goto et al. [Got06], Kulkarni et al. [Kul09], and Al-Kaseasbeh & Mamaghani [AKM18] have proposed various models to calculate three parameters that are often used to characterize the ductility of these columns. H_m/H_0 , a strength factor that provides the ratio of maximum strength to yield strength; δ_m/δ_0 and δ_{95}/δ_0 , ductility factors that provide the ductility at maximum strength and at the point of 5% reduction in maximum strength. Al-Kaseasbeh & Mamaghani [AKM18] implemented a purely numerical approach and used finite element models to show that the strength and ductility capacity of hollow thin walled steel columns are affected by the D/t ratio, slenderness ratio, and axial load ratio. While the number of cycles does not impact the force-displacement response prior to local buckling, a larger number of cycles increases the post-buckling rate of strength degradation. Furthermore, Al-Kaseasbeh & Mamaghani [AKM18] also propose an expression for displacement at 10% strength reduction. It must be noted that all of the aforementioned studies cover a range of D/t ratios that fall within the classification of non-compact and slender cross-sections.

Experimental data for cyclic behavior of hollow circular steel columns with small D/t ratios (compact sections) remain scarce. Fulmer et al. [Ful10b] also used a numerical approach to ascertain the impact of the variation in D/t ratios on column behavior. They developed finite element models of two column bridge piers with hollow circular columns and GSS connections, similar to their experiments. These models, which employed 3D shell and solid elements, were able to capture wall local buckling in accordance with experimental observations. Subsequently, they performed a parametric study by varying the

D/t ratio of columns and the axial load ratio (ALR) of the piers. D/t ratios that were chosen varied between 20 and 48, while ALR ranged from 5% to 10%. The outcome of this parametric study was a theoretical understanding of the impact of the independent variables on the strength degradation characteristics of these bridge piers. The current study builds on these outcomes to achieve the chapter objective of fully defining force-displacement envelopes to estimate inelastic limit state displacements of bridge pier systems incorporating the GSS connection.

It must be noted that the models in Fulmer et al. [Ful10b] used to perform the parametric study were developed with the motivation of capturing strength degradation of hollow circular columns. As such, the GSS connections were modeled in a way that did not fully account for the phenomenon of socket detachment. Nonetheless, the rate of strength degradation, which is solely a function of the column critical section, can be assumed to be well captured by these models. The results obtained from the parametric study by Fulmer et al. [Ful10b] were used as the basis to calibrate the fiber models developed in this study, to emulate the strength degradation characteristics of columns with varying D/t ratios.

In total, five different D/t ratios and three ALR were utilized by Fulmer et al. [Ful10b] in their parametric study. These are provided in the first two columns of Table 7.7. Calibration of all fifteen fiber models was performed individually by trial and error to match the backbone envelope of strength degradation under cyclic loading. Recall that a single parameter, σ_{3p} , of the *Hysteretic Material* model controls the rate of strength degradation in the fiber models. The results of calibration by varying this parameter is shown in Figure 7.24. Each row of plots in Figure 7.24 represents a different D/t ratio, while each column represents a different value of ALR. It can be observed that the fiber models can reasonably

approximate the strength degradation behavior, albeit missing some features that a more detailed FEM model can produce. E.g., for larger D/t ratios, a higher ALR causes a slight nonlinear sagging behavior of the degrading curve, which was not captured by the fiber models. However, during calibration, an attempt was made to achieve a reasonable linear representation of the degrading curve, that can be useful for design.

It is important to point out that the fiber models did not include the rotational spring that accounts for connection flexibility. This exclusion was necessary to in order to match the global stiffness of the FEM models that did not account for socket action of the GSS connections. The impact of this detail on the results of model calibration aimed at capturing strength degradation was assumed to be negligible.

Strength degradation characteristics of the numerical models can be captured using a parameter termed as the rate of strength degradation (k_{sd}). In this study, it is defined as the slope of the degrading portion of an idealized trilinear force-displacement backbone response. The models were subjected to a three-cycle set loading protocol. As such, k_{sd} for each model was obtained by equating it to the slope of a linear regression line for the set of data points formed by the peak responses. An example of this evaluation of k_{sd} is shown in Figure 7.25. A comparison of strength degradation rates for all of the calibrated models is provided in Table 7.7. For small D/t ratios, the both numerical approaches produce similar results. However, as the D/t ratio increases, the values of strength degradation rate diverge between the two. This divergence may be attributed to the aforementioned sagging behavior of the backbone curve observed for results from FEM models. Recollect that the strength degradation is a linear fit to the peak points under cyclic pushover analysis. This linear curve is more suitable to fitting results from fiber models that do not exhibit the

Table 7.7 Comparison of rate of strength degradation between numerical models in Fulmer et al. [Ful10b] and this study.

D/t Ratio	ALR (%)	Source	Strength Degradation Rate (kip/in)	Strength Degradation Rate (%/in)
20	5 7.66	FEM	-4.82	-2.41
		Fiber model	-4.54	-2.32
		FEM	-5.54	-2.84
	10 7.66	Fiber model	-5.57	-2.89
		FEM	-5.95	-3.13
		Fiber model	-5.99	-3.19
25.6	5 7.66	FEM	-3.54	-2.29
		Fiber model	-4.83	-3.04
		FEM	-3.75	-2.50
	10 7.66	Fiber model	-5.30	-3.33
		FEM	-4.11	-2.88
		Fiber model	-5.96	-3.92
32	5 7.66	FEM	3.17	-2.87
		Fiber model	-6.75	-5.33
		FEM	-3.95	-3.62
	10 7.66	Fiber model	-6.39	-5.18
		FEM	-4.72	-4.53
		Fiber model	-7.78	-6.39
42.7	5 7.66	FEM	-2.80	-3.82
		Fiber model	-5.80	-6.61
		FEM	-3.41	-5.29
	10 7.66	Fiber model	-6.18	-7.19
		FEM	-3.95	-6.65
		Fiber model	-7.29	-8.78
48	5 7.66	FEM	-2.51	-4.17
		Fiber model	-6.10	-8.45
		FEM	-3.02	-5.81
	10 7.66	Fiber model	-6.49	-9.19
		FEM	-3.45	-6.83
		Fiber model	-6.17	-9.39

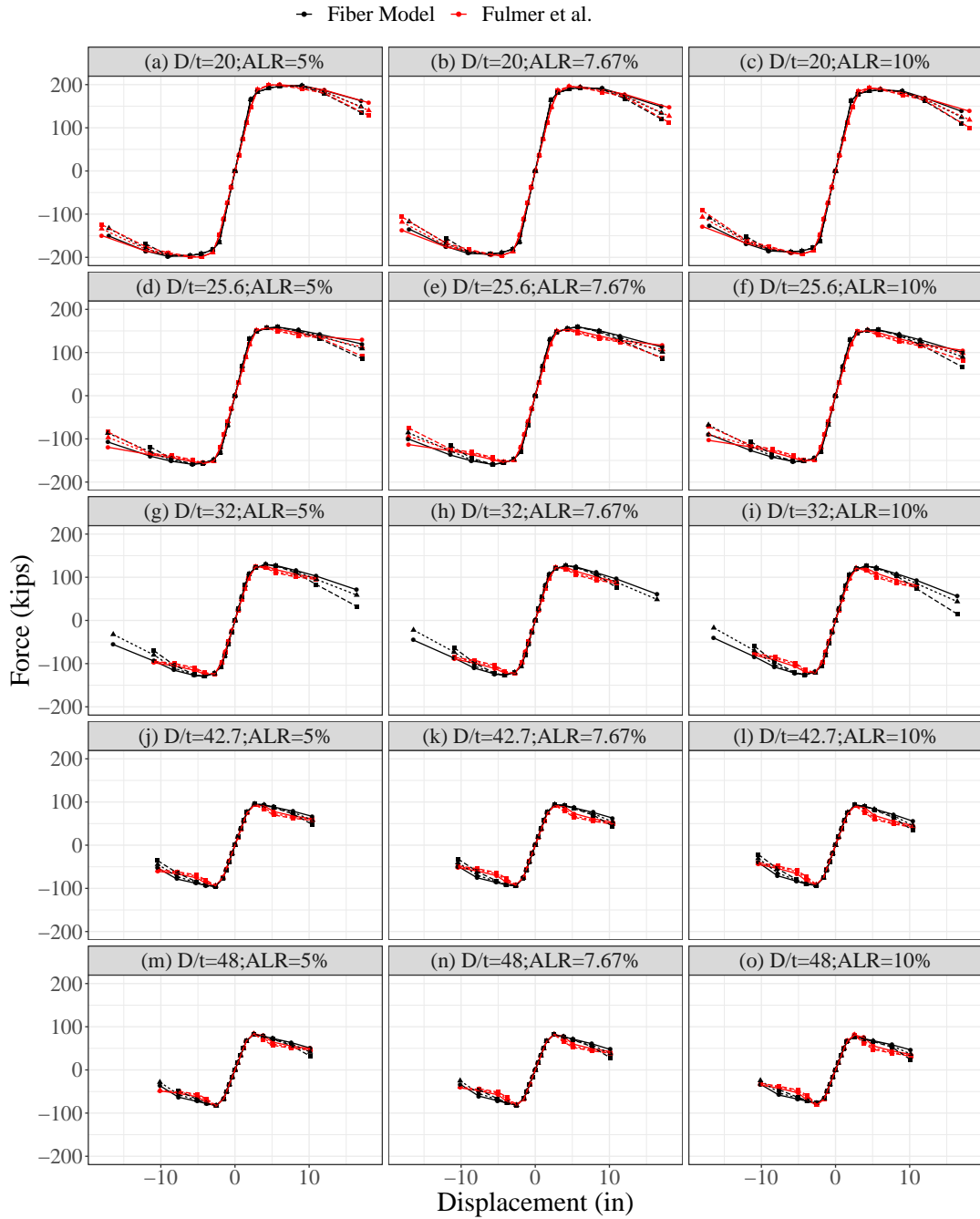
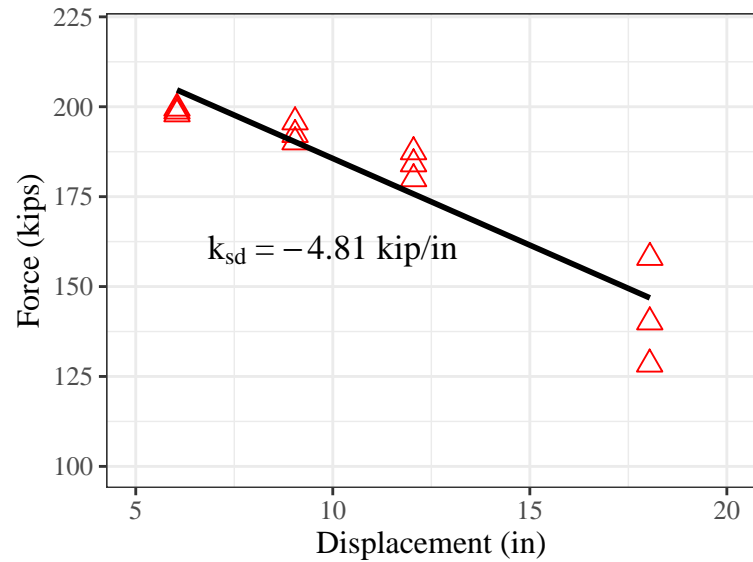
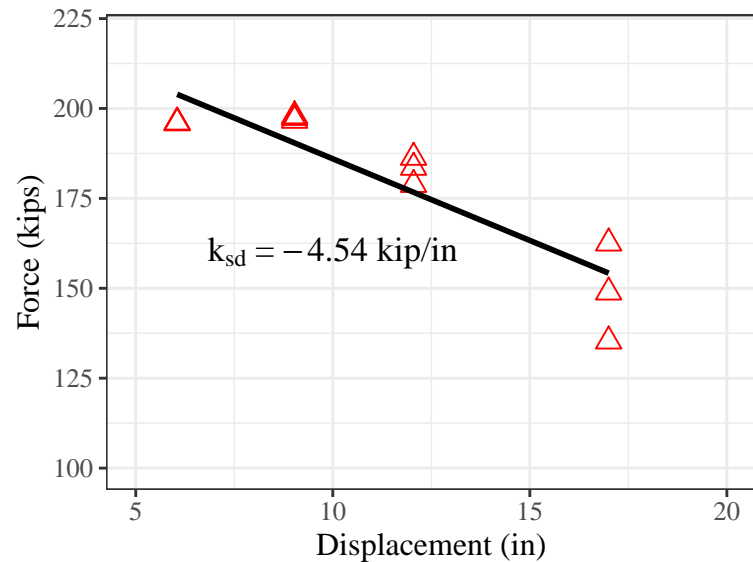


Figure 7.24 Comparison between backbone envelopes of bridge piers modeled by Fulmer et al. and this study.



(a)



(b)

Figure 7.25 Evaluation of the strength degradation rate for numerical models with D/t ratio = 20 and axial load ratio = 5%: (a) FEM and (b) Fiber model

sagging trend. However, in all cases, fiber models produce a more conservative (i.e., higher) rate of strength degradation, which may be used until more data becomes available.

7.5 Displacement Limits of Two-column Bridge Piers

The overall objective of this chapter was to develop the capability to estimate target displacements for important limit states of bridge piers that use hollow steel pile/columns in conjunction with the GSS connection. The numerical model discussed in the previous section can provide estimation of target displacements. However, this approach demands the ability to build fiber-based computational models, that may not be available in some commercial software. Therefore, an easier, more intuitive, and less computationally intensive approach was developed. The fundamental idea of this approach is to first calculate the respective limit state displacements for a single column, as discussed earlier, and then adjust these values by scalar coefficients to account for the additional flexibility arising because these columns are part of a pier system.

As has been discussed previously with the aid of Figure 7.14, the total displacement of a two-column bridge pier can be thought of as consisting of three major components. These are contributions to total displacement arising from the (1) flexural behavior of columns, (2) cap-beam flexibility, and (3) connection flexibility. A nomenclature consisting of three conditions was discussed earlier, shown in Figure 7.14. Having developed a computational model that can emulate bridge pier behavior accurately, it could subsequently be used to implement each of these conditions numerically.

The idea of deriving adjustment factors was simple. If the system displacement under a lateral load F_T in condition 1 can be termed Δ_T , this value can be calculated for any geom-

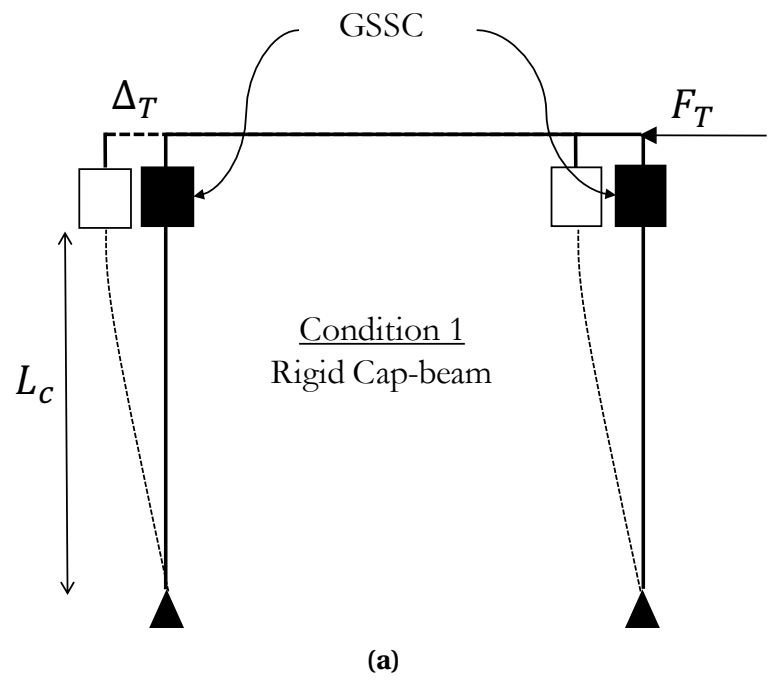
etry using a fiber model of condition 1. Similarly, conditions 2 and 3 can also be modeled. By calculating the total displacement in condition 2 under the same lateral load and then dividing it by Δ_T from condition 1, coefficient γ_{cb} can be evaluated. If the same procedure is carried out for condition 3, coefficient γ_{sc} can also be determined. Thus, if a parametric study is designed to capture the variation in coefficients γ_{cb} and γ_{sc} , these coefficients can be expressed in terms of empirical equations. Consequently, the limit state displacement of the two-column pier system can be estimated by using Equation 7.24.

$$\Delta_{sys} = \gamma_{sc} \gamma_{cb} \Delta_T \quad (7.24)$$

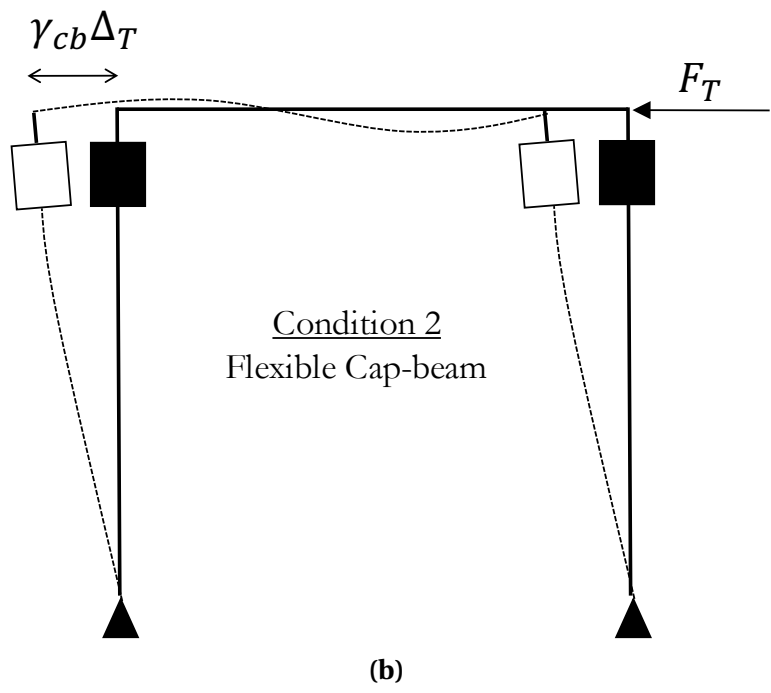
7.5.1 Cap beam flexibility: Condition 2 versus Condition 1

Additional displacement of the two-column bridge pier attributable to cap-beam flexibility can be identified by considering the two conditions 1 and 2, as reproduced in Figure 7.26. In Figure 7.26a, the pier is shown to possess a rigid cap-beam. The displacement (Δ_T) of this pier at any given limit state will be equal to that of a single cantilever column at the same limit state. In Figure 7.26b, because of the flexible cap beam, the stiffness in the joints will reduce, which leads to an increased joint rotation under the same force. Therefore, the displacement of the pier in condition 2 at any given limit state will be larger than that of condition 1 (Figure 7.26a). In other words, the displacement under condition 2 can be evaluated by adjusting the condition 1 displacement (Δ_T) by a scalar coefficient, γ_{cb} , henceforth referred to as the cap-beam flexibility coefficient.

Fundamentally, the value of this coefficient must be a function of the stiffness of the joints, which in-turn is dependent on the relative stiffness of the cap-beam with respect to



(a)



(b)

Figure 7.26 Schematic comparison: Condition 1 versus Condition 2.

the columns. It is possible to evaluate the relative stiffness of the cap-beam with respect to the columns using equations used in classical structural analysis known as the moment-distribution method. This relative stiffness is a function of the lengths, moments of inertia, and support conditions of members coinciding at each joint in the structure. In the case of the two-column bridge piers discussed here, there are two joints. At each joint, the cap-beam and one of the columns are the members that come together. The relative bending stiffnesses of the members at a joint is given by Equation 7.25. Thus, if the relative bending stiffnesses of the cap-beam (K_{cb}) and the columns (K_{col}) are evaluated using Equation 7.25, the total bending stiffness at one of the joints can be calculated by Equation 7.26. In elastic analysis, the additional joint rotation as a result of cap-beam flexibility must be a function of the relative stiffness of the cap-beam (K_{rcb}) with respect to the total stiffness of the joints, which is given by Equation 7.27.

$$K = \begin{cases} \left(\frac{I}{L}\right) & \text{If the far-end is fixed} \\ \left(\frac{3}{4}\right)\left(\frac{I}{L}\right) & \text{If the far-end is hinged} \end{cases} \quad (7.25)$$

$$K_j = K_{cb} + K_{col} \quad (7.26)$$

$$K_{rcb} = \frac{K_{cb}}{K_{cb} + K_{col}} \quad (7.27)$$

A parametric study was performed to ascertain the relationship between the relative stiffness of the cap-beam (K_{rcb}) and the cap-beam flexibility coefficient (γ_{cb}). The numerical model developed previously was used. In the model, the cap-beam span and moment

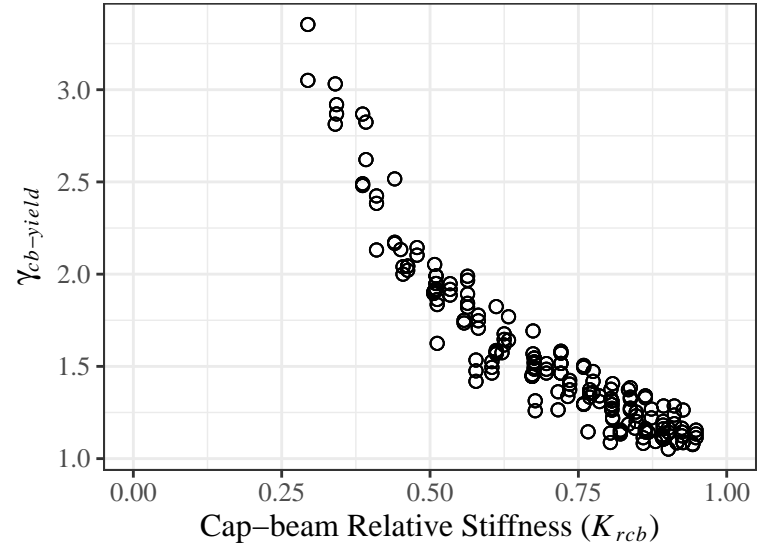
Table 7.8 Independent variables in the parametric study to evaluate γ_{cb} .

Variables	Values
Cap-beam span, L_{cb} (ft)	6, 9, 12, 15
Cap-beam moment of inertia, I_{cb} (in ⁴)	610, 1220, 2440, 4880

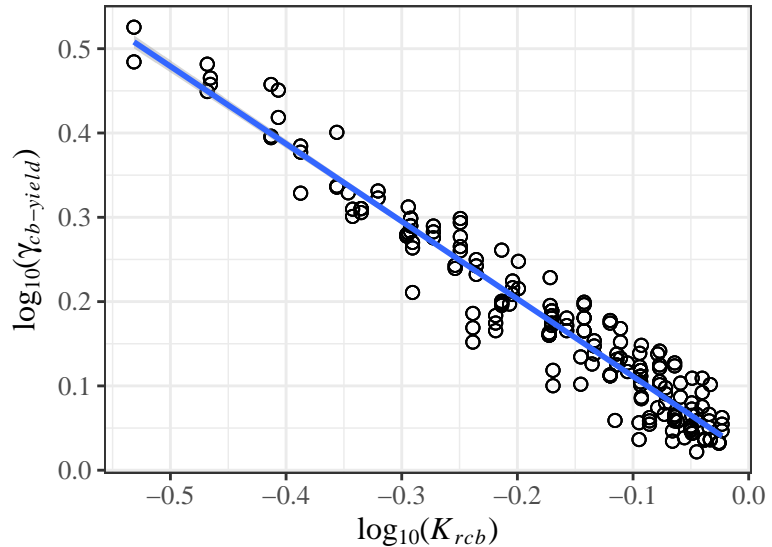
of inertia were varied to generate many possible values of K_{rcb} . All combinations of the numerical values of these independent variables, given in Table 7.8 were realized and implemented in cyclic pushover analyses. γ_{cb} was calculated for each analysis using the procedure described earlier. Evaluation of γ_{cb} was done separately for both yield ($\gamma_{cb-yield}$) and buckling ($\gamma_{cb-buckling}$) limit states. Figure 7.27a shows $\gamma_{cb-yield}$ versus K_{rcb} . A nonlinear correlation can be observed. To obtain a simple linear expression, a logarithmic transformation was applied to $\gamma_{cb-yield}$ and K_{rcb} , which is shown in Figure 7.27b. A linear regression line was fit to this data, producing an empirical equation for calculating $\gamma_{cb-yield}$, given by Equation 7.28. The linear regression showed an R-squared value of 0.94.

$$\gamma_{cb-yield} = 1.05 \left(\frac{1}{K_{rcb}} \right)^{0.92} \quad (7.28)$$

A strong relationship between $\gamma_{cb-yield}$ and K_{rcb} exists because, at this point in time in its response, the structure is still close to elastic behavior, wherein the initial relative stiffnesses of component members play an important role in determining the distribution of forces. Further along the response curve, in the plastic region, the columns exhibit a reduction in stiffness due to plasticity. Therefore, estimates of $\gamma_{cb-buckling}$ did not show a strict relationship to K_{rcb} . Furthermore, $\gamma_{cb-buckling}$ is also a function of the column D/t-ratio and the axial load ratio (ALR). Figure 7.28 illustrates the relationship between the



(a)



(b)

Figure 7.27 Cap-beam flexibility coefficient ($\gamma_{cb-yield}$) for yield displacement calculation as a function the relative stiffness of cap-beam, K_{rcb} .

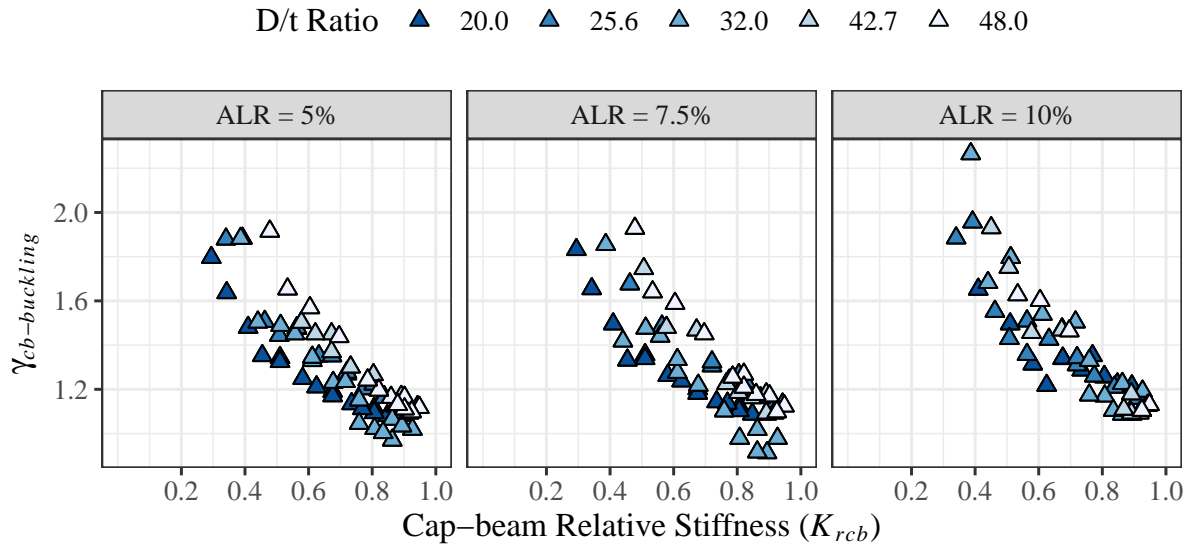


Figure 7.28 Cap-beam flexibility coefficient ($\gamma_{cb-buckling}$) for displacement at local buckling as a function of K_{rcb} , D/t-ratio, and ALR.

aforementioned variables. Multiple linear regression after a logarithmic transformation yielded an expression for estimating $\gamma_{cb-buckling}$, as shown in Equation 7.29. The multiple linear regression showed an R-squared value of 0.83. Although this relationship is not as strong as that for the yield limit state, it is still significant and can be used to achieve a good estimate. The strength of this relationship could be increased if the effective stiffness of columns are used in the calculation of K_{rcb} .

$$\gamma_{cb-buckling} = 0.65 \left(\frac{1}{K_{rcb}} \right)^{0.58} \left(\frac{D}{t} \right)^{0.14} \quad (7.29)$$

It must be noted that the strength degradation rate is not a function of the cap-beam stiffness. Therefore, the expression for calculating the rate of strength degradation is assumed to remain the same regardless of the pier geometry. This expression is discussed

later.

7.5.2 Connection flexibility: Condition 3 versus Condition 2

Similar to how the cap-beam flexibility coefficient (γ_{cb}) was determined, the connection flexibility coefficient (γ_{sc}) was investigated by comparing condition 3 and condition 2. A similar parametric study to that discussed earlier, was performed by modeling both conditions numerically and subjecting them to cyclic pushover analyses. The total displacement, as shown in Figure 7.29, at yield and buckling limit states were extracted for both conditions. For all models, dividing the displacement obtained using the condition 3 model by that obtained using a corresponding condition 2 model provided many observations of the connection flexibility coefficient (γ_{sc}).

The additional displacement observed for condition 3 models is as a result of the extra flexibility provided by the rotational spring. Recall that the properties of this spring were calibrated based on the available experimental data. Two independent variables that influence the spring properties are the GSS connection stiffness, which is a function of the number of shear studs and grout compressive strength, and the yield moment of the column. The GSS connection stiffness can largely remain unaffected during the service life of the structure, if the recommendations regarding construction and maintenance provided in the final chapter are followed. Therefore, the connection flexibility coefficient (γ_{sc}) is likely only a function of the column yield moments. For the same pier geometry, the yield moment is a function of the D/t ratio of the column section. Thus, γ_{sc} was plotted as a function of D/t ratio to ascertain the strength of the relationship. Figures 7.30a and 7.30b show these plots for limit states of yield and local buckling. While there is an indication of a linear

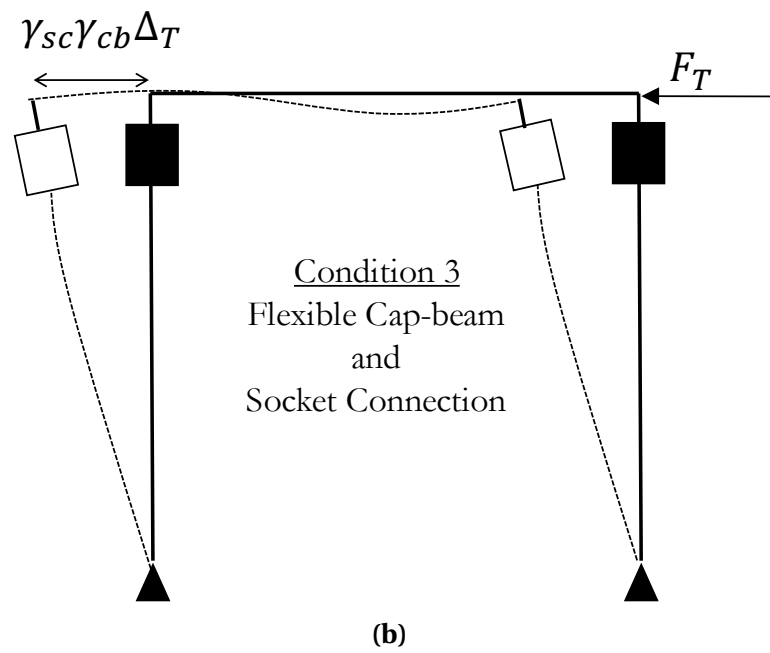
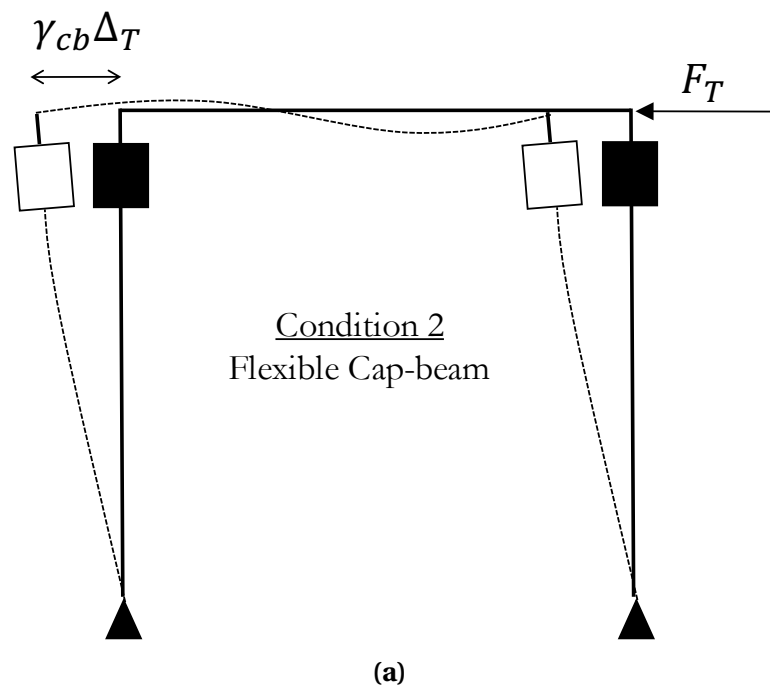


Figure 7.29 Schematic comparison: Condition 2 versus Condition 3.

relationship between the mean values of $\gamma_{sc-yield}$ and the D/t ratio, $\gamma_{sc-buckling}$ remains fairly stable across the range of D/t ratios. It must also be noted that there is considerable, but consistent scatter around the mean values. It is recommended that the expressions for mean values, as given by Equations 7.30 and 7.31, be used for design. However, the standard deviation ($\sigma_{\gamma_{sc}}$) is also provided in Equation 7.32, for completeness. This standard deviation is low and therefore conveys good confidence.

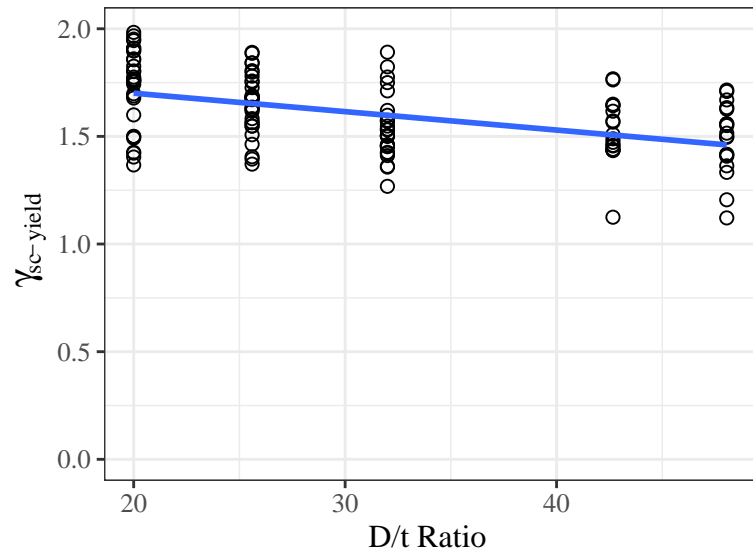
$$\gamma_{sc-yield} = 1.88 - 0.01 \left(\frac{D}{t} \right) \quad (7.30)$$

$$\gamma_{sc-buckling} = 1.73 \quad (7.31)$$

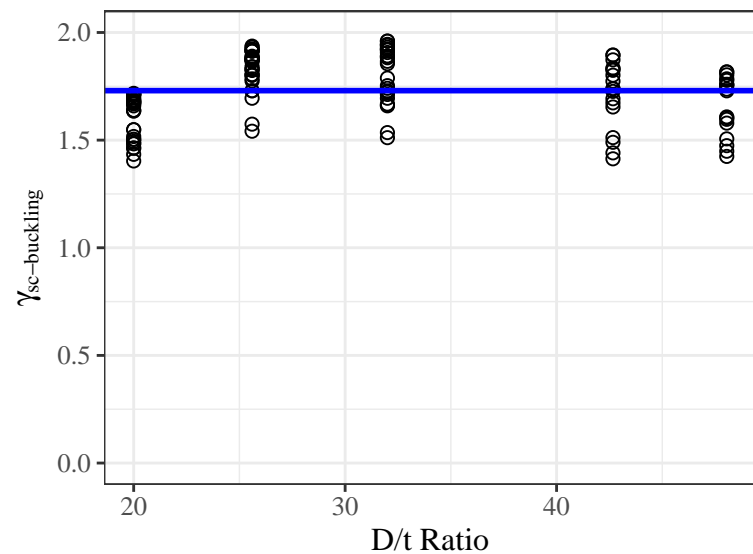
$$\sigma_{\gamma_{sc}} = 0.16 \quad (7.32)$$

7.6 Strength Degradation Rate

To be able to fully define an idealized multi-linear backbone response of pier-systems using steel columns, a reliable estimation of the force and displacement at various levels of strength degradation is necessary. The strength degradation rate (k_{sd}) was introduced earlier in this chapter as a metric to capture the post-buckling behavior of hollow circular steel columns. The parameter k_{sd} is simply a degrading linear fit to post-buckling peaks that emerges from a cyclic pushover analysis. This parameter was introduced previously in terms of *strength reduction per unit displacement*. The unit for k_{sd} requires a minor modification to be able to extrapolate results to bridge piers of varying heights. To this end, specifying k_{sd} as *percentage strength reduction per unit drift ratio* instead of displacement



(a)



(b)

Figure 7.30 Cap-beam flexibility coefficient for (a) yield displacement ($\gamma_{sc-yield}$) and (b) displacement at local buckling ($\gamma_{sc-buckling}$) as a function the column D/t ratio.

provides a better measure.

For all of the pushover analyses on numerical models representing condition 3, performed as part of the parametric study discussed in the previous section, k_{sd} was also evaluated. It was found that k_{sd} is dependent on the column D/t ratio and the axial load ratio. These observations were expected because the only source of degrading strength is from the column critical section. The cap-beam and GSS connections are capacity protected and therefore are expected to remain elastic throughout. Figure 7.31 shows the plot of observed values of k_{sd} against the column D/t ratio. The variation in axial load ratio is displayed by the different colors. The values of k_{sd} are negative to denote degradation, and the unit is *percentage of maximum strength per percent drift*. A nonlinear trend can be seen between k_{sd} and D/t ratio. Polynomial regression was used to obtain the best model to estimate k_{sd} as a function of D/t ratio and axial load ratio (P/P_u), which is provided in Equation 7.33. This regression model is also shown in Figure 7.31.

$$k_{sd} = 540 \left(\frac{D}{t} \right)^{-1.3} - 0.18 \left(\frac{P}{P_u} \right) - 11.3 \quad (7.33)$$

To estimate the total displacement at a given level of strength degradation, it is sufficient to follow these two steps:

1. Estimate the maximum force (F_N) and the displacement (Δ_N) corresponding to this force using Equations 7.20 and 7.24, respectively.
2. Estimate the displacement (Δ_{sd-n}) corresponding to a strength reduction of $n\%$ of F_N using the following equation, where L_e is an effective column length from the

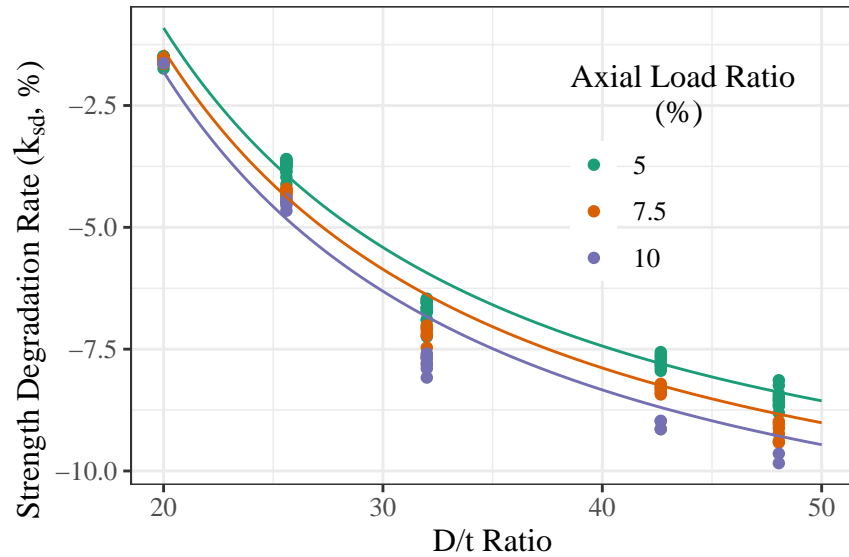


Figure 7.31 Strength degradation rate of hollow circular columns as a function of D/t ratio and axial load ratio.

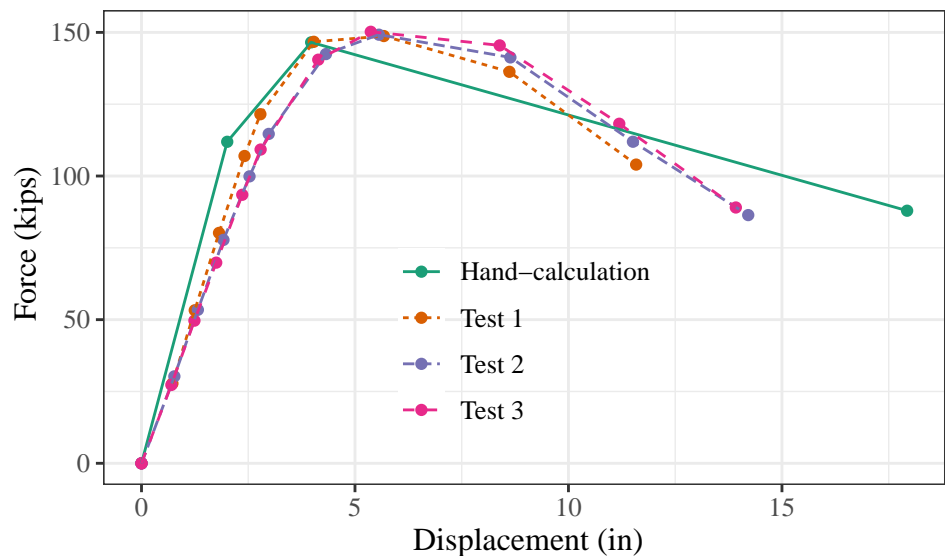
point of contraflexure to cap-beam centerline:

$$\Delta_{sd-n} = \Delta_b - \frac{F_b L_e (1 - 0.01n)}{100 k_{sd}} \quad (7.34)$$

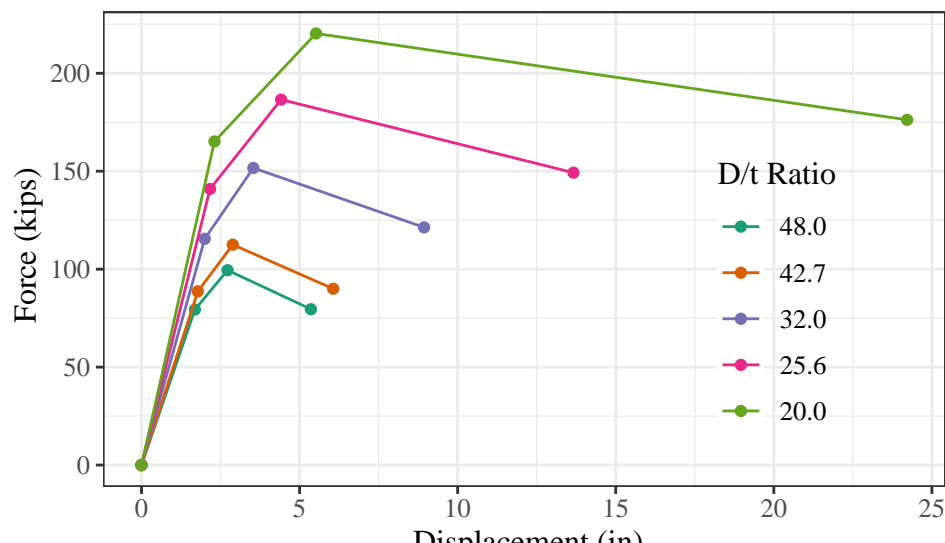
It is important to note that Equation 7.33 must only be used within the range of values of independent variables used in this study, i.e., for D/t ratios between 20 and 48, and axial load ratios below 10%.

7.7 Model Validation

The multilinear force versus displacement response of two column bridge piers with hollow circular steel sections can be developed using simple hand calculations by following



(a)



(b)

Figure 7.32 (a) Comparison of the proposed model with experimental results. (b) Variation of the force versus displacement behavior of hollow steel columns with the same diameter but different wall thickness.

Equations 7.7 through 7.34. Although more experimental results are warranted to validate the foregoing model, it is worthwhile to check if this model can provide a good approximation of the behavior of pier specimens tested as part of this study. The geometric and material properties used in tests 1 through 3 are nominally similar. Therefore, these properties were used to generate the idealized force versus displacement backbone envelope. A comparison of this idealized backbone with experimentally observed backbone curves is shown in Figure 7.32a. It can be seen that the idealized model provides a good approximation of the observed response. It must be noted that the linear strength degradation portion of the idealized curve is conservative initially but shifts to a non-conservative approximation at high ductility values. This occurs because of the linear regression fit used to define this portion of the curve and was intentional because these high ductility values are typically never considered in design.

The simplified model can also account for the behavior due to variation in D/t ratios. Figure 7.32b shows the different curves obtained by changing the column wall thickness in the model. For the same column diameter, larger wall thickness means a smaller D/t ratio, which leads to a more compact section. It can be seen that smaller D/t ratios delay local buckling and exhibit smaller post-buckling strength degradation.

7.8 Chapter Summary

The objective of this chapter was to develop a simple hand calculation based model to estimate the limit state displacements of two column steel bridge piers incorporating the GSS connection. Such a model becomes crucial for the displacement based seismic design of these systems. Important limit states that were identified as having structural conse-

quences were column yielding, column local buckling, and levels of strength degradation.

The model that was developed subsequently is semi-empirical in nature. It uses correction factors to adjust the top displacement of the system that can be nominally predicted by the application of the moment area method over the cantilever length of the column, i.e., integrating to evaluate the first moment of the area under the curvature profile. The correction factors were necessary because of the additional flexibility in the system that is not accounted for by column flexure. These components are related to 1) the cap beam flexibility and 2) the socket action.

First, finite element models were calibrated to simulate the results of the experimental large scale tests. These models were subsequently used to perform parametric studies that led to the development of empirical expressions for the correction factors. Last, the simplified model was used to estimate the response of the test specimens. It was observed that the model could estimate the complete cyclic response of the two column bridge pier specimens with reasonable accuracy.

CHAPTER

8

CONCLUSIONS AND RECOMMENDATIONS

The grouted shear stud (GSS) connection was developed as a ductile alternative to conventional directly welded connections in steel bridge substructures. It is a socket type connection in which the socket is formed by a pipe stub which is shop welded to the cap-beam. The steel pile-columns can be inserted into the socket and the annular region thus formed can be filled with high-strength cementitious grout to complete the connection. In addi-

tion to superior ductility capacity, the GSS connection provides other advantages such as potential use in accelerated bridge construction (ABC), and as a retrofitting option for seismically deficient bridges.

After passing the proof of concept phase, a few unanswered questions regarding the GSS connection remained before implementing it in practice. These questions, which formed the basis for this doctoral dissertation were the following.

1. Is the GSS connection durable in service?
2. How should one perform the structural design of the GSS connection?
3. What must be the procedure for seismic design of systems incorporating the GSS connection?

This chapter provides conclusions regarding each objective based on results from several experiments and computational simulations.

8.1 Durability of the GSS connection in Cold Climates

Although the GSS connection has been shown to exhibit exceptional structural performance under laboratory conditions, other issues required consideration before widespread deployment of the connection in practice. Since the Alaska Department of Transportation and Public Facilities (AKDOT) was interested in using this connection in their bridges, there was a need to investigate its long term durability in extreme cold climates. This project began with the motivation of investigating the durability of the GSS connection in cold

climates. Unlike other steel connection details, the GSS connection introduces a new variable, i.e., the cementitious grout. Cementitious materials are porous and have the propensity to crack under multiple cycles of freeze and thaw. Since studies on the freeze and thaw resistance of commercial cementitious grouts are few, such a study was undertaken.

The durability of the GSS connection could be viewed from two different perspectives. It could be concluded that the GSS connection is durable in a cold climate if either one of the following statements were true.

Statement 1: Commercial cementitious grouts are durable in cold climates.

Statement 2: Grout durability does not have a significant impact on the structural performance of the GSS connection.

The approach taken in the work described in this dissertation was to attempt to determine whether each of these statements was true or false.

8.1.1 Durability of Cementitious Grouts

Investigating the durability of all commercial cementitious grouts was as expensive as it was fruitless. First, there are a myriad of competing manufacturers that produce similar products. To procure each one of them was expensive. Second, the chemical composition of every grout is proprietary, and the grouts are constantly being modified by the manufacturers. Results obtained now may not reflect their characteristics after a few years. Third, standard durability tests on cementitious materials specific to cold climate exposure take an extremely long time to perform. Testing one batch of specimens according to ASTM C666 [Aste] may take up to 75 to 80 days to complete. With due consideration of all of the aforementioned issues, four commercial grouts meeting AKDOT specifications were cho-

sen to be investigated to obtain some information on the suitability of these grouts.

The chosen commercial grouts were tested to determine their vulnerability to freeze and thaw damage, and their propensity to cracking under restrained shrinkage. Although the question of whether cementitious grouts are durable in cold climates could not be conclusively answered, some important observations were made. Some grouts are indeed vulnerable to freeze and thaw degradation while others showed exceptional performance. However, material inconsistency was pervasive even among the grouts that performed well. The potential for restrained shrinkage cracking depends not only on the grout material, but also on the degree of restraint provided to it. The degree of restraint is specific to the practical application of the grout. In the case of the GSS connection, this restraint was found to be high enough to crack all of the grout materials that were tested. However, it was also found that the presence of shear studs within the GSS connection helps distribute the cracking by providing some reinforcement, and in turn reducing crack widths.

8.1.2 Structural Consequences of Grout Deterioration

Since the material level inquiry did not conclusively prove that all cementitious grouts are durable in cold climates, the study moved on to investigate the consequences of material durability on the structural performance of the GSS connection. Four large scale steel bridge pier specimens (tests 1 through 4) incorporating the GSS connection were structurally tested. To determine the structural consequences of grout deterioration, the performance of specimens with deteriorated GSS connections (test 2 and test 3) was compared to the performance of a control specimen (test 1). The control specimen had standard high strength grout in its GSS connections, while the remainder of the specimens

had grout mixed with expanded polystyrene (EPS) aggregates. The addition of EPS aggregates reduced the structural properties of the grout, such as its compressive strength and elastic modulus, simulating a GSS connection exposed to multiple years of service in cold climates.

Direct comparison between the global structural behavior of the bents with deteriorated connections and the control specimen suggested that grout deterioration may not have a significant impact on the capability of the GSS connection to successfully relocate the plastic hinge. Therefore, it was concluded that the GSS connection is durable in service.

8.2 Structural Design of the GSS Connection

The result that the GSS connection is not affected significantly by grout deterioration became evident after the first two large scale tests. Therefore, AKDOT wanted to use the remaining two large scale tests to answer a different question. To be able to optimally design the GSS connection for satisfactory performance, a need arose to better understand the force transfer mechanism within the GSS connection. Two large scale tests (tests 3 and 4), each varying a single parameter, were performed to obtain some information regarding the force transfer mechanism.

The GSS connections in test 3 used only 16, 1" shear studs per connection, which was a significant reduction from some of the earliest tests on GSS connections that contained 96, 3/4" shear studs per connection. The objective of test 3 was to determine if the number of shear studs has a significant role in transferring the forces from the column to the cap-beam. It was observed that the test 3 specimen performed similarly to all of the previous tests performed on steel bridge bents with the GSS connection. This led to the conclusion

that the number of shear studs may have less of an impact on the successful performance of the GSS connection than previously thought.

The GSS connections in test 4 used a reduced embedment length by shortening the socket depth. In all of the previous cases, the GSS connections used a socket depth equal to one and a half times the column diameter, i.e., 24". In test 4, the depth was reduced to one times the column diameter, i.e., 16". Results from test 4 showed that for a D/t ratio of 32 (all test columns had a D/t ratio of 32), an embedment length equal to the column diameter was insufficient in successfully forming the plastic hinge in the column. This test resulted in poor performance with significantly lower energy dissipation and a reduced maximum load. This observation led to the conclusion that the embedment length is an important parameter in the successful performance of the GSS connection. This conclusion also meant that the dominant moment resisting mechanism in the GSS connection is a pair of normal forces producing a couple opposing the bending moment demand in the connection.

Following this discovery, an attempt was made to develop an a priori force transfer model consistent with empirical observations. A theoretical truss mechanism based model was developed, which can estimate the total capacity of the GSS connection when the accompanying column is under flexure. When this model was used to predict the observations of tests 3 and 4, it produced results that were in agreement. Although further validation with experimental data is recommended, the model can still be used for designing the GSS connection in the interim because the assumptions underlying this model are conservative in nature.

8.3 Limit State Displacements of Bridge Piers with GSS Connections

To implement the GSS connection in seismic regions, it is imperative to have a consistent design procedure. The bridge engineering community in seismically active states in the US have either adopted or are in the process of adopting direct displacement based seismic design (DDBD) principles. DDBD emphasizes structural displacement as the primary design variable. Given a specific seismic hazard level, the objective of DDBD is to force the structure to undergo response that is pre-determined by the designer. For example, while designing a new bridge in Anchorage, Alaska, DDBD allows a designer to say that the columns in the critical pier will undergo local buckling under a 2500-year earthquake, but not for a 1000-year earthquake.

A crucial aspect in performing DDBD is the availability of models that can estimate the displacement, and in turn damage, of the given structure. Equally important is information that can characterize the effective stiffness of structures at various key limit states. Therefore, the objective of the last part of this study was to develop a model that can estimate the force versus displacement backbone response envelope of two-column steel bridge piers.

Global and local demand parameter measurements during the large scale tests were used to calibrate fiber-based finite element models. These models were able to replicate the complete non-linear cyclic behavior of two-column bridge pier systems. Utilizing information from existing literature, these finite element models were extended to account for variation in column D/t ratios. Subsequently, these models were used to perform a

parametric study to ascertain the contribution of different variables in the prediction of global displacement. The result is a set of equations that can estimate limit state force and displacement at important limit states of this system.

8.4 Recommendations for Connection Design and Maintenance

The recommendations provided in this section address two issues. The first is the issue of achieving the best cold climate durability of cementitious grouts and the GSS connection, by association. The second is the optimum design of the GSS connection. It must be noted that the design recommendations provided here are based on structural tests performed on bridge pier specimens with 16" column diameter and a D/t ratio of 32. However, the results can be reasonably extrapolated to other column diameters and D/t ratios, as long as these are not drastically different from the one tested experimentally. Recommendations for determining the number of shear studs and embedment length may be considered as minimum requirements.

8.4.1 GSS Durability Recommendations

1. When choosing a cementitious grout for application in the GSS connection or any other application in cold climates, it is recommended to use the manufacturer specified Durability Factor (DF) determined in accordance with ASTM C666 Procedure A [Aste] as an adequate indicator of its durability.

2. Excess water impairs the freeze and thaw resistance of cementitious grouts. Therefore, it is recommended that the amount of water mixed per bag of grout be kept to the bag labelled minimum for “flowable” consistency.
3. In the case of the GSS connection, a minimum 28-day grout compressive strength of 7500 psi for “flowable” consistency is sufficient for satisfactory structural performance.
4. Contrary to provisions in some commercial grouts, it is recommended to not extend the grout with pea-gravel aggregates. Extending grout with pea-gravel aggregates results in reduced workability of the wet mixture. Further addition of water to improve workability also results in segregation of the aggregates. Reduced workability and segregation are, of course, undesirable.

8.4.2 Design Recommendations

1. The predominant role of shear studs in the GSS connection is to resist pullout of the column from the socket under axial tensile demand (P_t), induced by the lateral loads on multi-column bridge piers. It is recommended that the number of shear studs required to resist this demand be calculated according to Equation 8.1. In Equation 8.1, n is the required number of shear studs on both the column and inside the stub, P_t is the maximum axial tension induced in any of the columns due to the maximum lateral load on the bridge bent at strength level (LRFD), A_s is the cross-section area of a single shear connector, and F_u is the ultimate tensile strength of the shear connector. C is a conservative constant that is based on engineering judgment. It is

recommended that the value of C be not less than 2.

$$n = C \frac{P_t}{0.6A_s F_u} \quad (8.1)$$

$$C \geq 2 \quad (8.2)$$

2. It is recommended to provide the column and the stub with at least 4 vertical lines of shear connectors at 90° angles to the adjacent lines. This arrangement will result in a total of 8 vertical lines of shear connectors in the GSS connection (4 on column and 4 on stub) at 45° angles to the adjacent lines. Provide at least 2 shear connectors per vertical line.
3. The socket depth (D_s) or the embedment length (L_e) is the most important design parameter of the GSS connection. It is recommended to provide an embedment length between 1.2 to 1.6 times the diameter of the connecting column (D_c), as shown in Equation 8.3.

$$1.2D_c \leq L_e \leq 1.6D_c \quad (8.3)$$

4. At the start of the design process, it is recommended to proportion the embedment length (L_e) as a function of the total cantilever height (L_{tc}), as shown in the equations

below. Here, L_{tc} is the distance of the expected point of contraflexure from the cap-beam soffit, calculated using Equation 8.5, where L_c is the clear cantilever length.

$$0.2L_{tc} \leq L_e \leq 0.3L_{tc} \quad (8.4)$$

$$L_{tc} = L_e + L_c \quad (8.5)$$

5. After sizing the columns, the total capacity of the GSS connection must be checked using the Equation 8.6, where V_c is the maximum shear force demand in the column, f'_{ca} is the average compressive strength of the grout, as discussed in Chapter 6, β_1 is the ACI stress block coefficient, and D is the column diameter.

$$V_c \leq \frac{0.85f'_{ca}\beta_1 D \left(\frac{L_e}{2} \right)}{\left(\frac{1}{2} + \frac{L_c + L_e \left(1 - \frac{\beta_1}{4} \right)}{L_e \left(1 - \frac{\beta_1}{2} \right)} \right)} \quad (8.6)$$

For typical values, $\beta_1 = 0.8$ and $L_e = 0.2L_{tc}$, the above equation reduces to Equation 8.7.

$$V_C \leq 0.008 f'_{ca} D L_{tc} \quad (8.7)$$

8.4.3 Maintenance Recommendation

After construction, it is recommended that the GSS connections be inspected regularly for loss of grout. In addition, cracks wider than 0.30 mm (0.012 in) are recommended to be repaired with epoxy injection. For excessive loss of grout, the void must be re-packed with grout of similar strength. Good bond between the old and new grout must be ensured.

8.5 Recommendations for Seismic Design

The recommendations provided in this section pertain to the seismic design of two-column steel bridge piers that utilize the GSS connection to connect columns to cap-elements. The displacement based seismic design procedure for bridges, as described in Priestley et al. [Pri07], is recommended. The work discussed in this dissertation investigated the estimation of limit state displacements for these piers.

1. A fiber-based computational model with appropriate values for input parameters, as described in Chapter 7, may be used to achieve accurate prediction of the complete non-linear cyclic response of the bridge piers with GSS connections.
2. For design, it is recommended to use the set of equations provided in Chapter 7 and Appendix A to estimate target displacements at key limit states of column yield, pile wall local buckling, and a desirable level of strength degradation.

3. It is recommended to use strain based limit states for the most accurate characterization of column damage. For pile wall local buckling strain limit, the British Standards [BS93] model, reproduced here in Equation 8.8, produced results that closely matched experimental observations. However, any state-of-the-art limit state model may be utilized.

$$\epsilon_b = 15 \left(\frac{D}{t} \right)^{-2} \quad (8.8)$$

where, ϵ_b is the strain limit for wall local buckling, D and t are the column diameter and wall thickness.

4. While estimating the structural displacement of the pier, it is important to consider additional flexibility in the system attributable to a non-rigid cap-beam and socket action inside the GSS connection. Between these two, the socket action has a much larger impact on the total system displacement.

BIBLIOGRAPHY

- [ACI19] ACI:318-19. "Building code requirements for structural concrete (ACI 318-19) and commentary". American Concrete Institute. 2019.
- [AKM18] Al-Kaseasbeh, Q. & Mamaghani, I. H. "Buckling Strength and Ductility Evaluation of Thin-Walled Steel Tubular Columns with Uniform and Graded Thickness under Cyclic Loading". *Journal of Bridge Engineering* **24**.1 (2018), p. 04018105.
- [Ae19] ASTM:A370-19e1. "Standard Test Methods and Definitions for Mechanical Testing of Steel Product". *A370-19e1*. Philadelphia, Pa.: ASTM, 2019.
- [Aub02] Auberg, R. "Application of CIF-Test in practise for reliable evaluation of frost resistance of concrete". *International RILEM Workshop on Frost Resistance of Concrete*. RILEM Publications SARL. 2002, pp. 255–267.
- [Bab05] Babu, D. S. et al. "Properties of lightweight expanded polystyrene aggregate concretes containing fly ash". *Cement and Concrete Research* **35**.6 (2005), pp. 1218–1223.
- [Bab06] Babu, D. S. et al. "Effect of polystyrene aggregate size on strength and moisture migration characteristics of lightweight concrete". *Cement and Concrete Composites* **28**.6 (2006), pp. 520–527.
- [Bag10] Bager, D. "Qualitative Description of the Micro-ice Body Freeze-thaw Damage Mechanism in Concrete. Freeze-thaw Testing Of Concrete–Input To Revision of CEN Test Methods". *Workshop proceeding From a Nordic Mini-seminar*. 2010, pp. 4–5.
- [BFY76] Bagon, C. & Frondistou-Yannas, S. "Marine floating concrete made with polystyrene expanded beads". *Magazine of Concrete Research* **28**.97 (1976), pp. 225–229.
- [Bjo05] Bjorhovde, R. "Realistic performance requirements for steel in structures". *Advances in Structural Engineering* **8**.3 (2005), pp. 203–215.
- [BS93] British Standards, I. "Code of practice for pipelinesPart 3. Pipelines subsea: Design, construction and installation" (1993).
- [Buc09] Bucher, B. E. "Shrinkage and shrinkage cracking behavior of cement systems containing ground limestone, fly ash, and lightweight synthetic particles" (2009).

- [Coo09] Cookson, K. A. "Seismic Performance of Steel Bridge Bent Welded Connections." (2009).
- [Fag77a] Fagerlund, G. "The critical degree of saturation method of assessing the freeze/thaw resistance of concrete". *Matériaux et Construction* **10**.4 (1977), pp. 217–229.
- [Fag77b] Fagerlund, G. "The international cooperative test of the critical degree of saturation method of assessing the freeze/thaw resistance of concrete". *Matériaux et Construction* **10**.4 (1977), pp. 231–253.
- [Ful10a] Fulmer, S. et al. "Ductility of welded steel pile to steel cap beam connections". *Structures Congress 2010*. 2010, pp. 216–227.
- [Ful15] Fulmer, S. et al. "Grouted shear stud connection for steel bridge substructures". *Journal of Constructional Steel Research* **109** (2015), pp. 72–86.
- [Ful10b] Fulmer, S. J. et al. *Ductility of welded steel column to steel cap beam connections*. Tech. rep. 2010.
- [Got06] Goto, Y. et al. "Stability and ductility of thin-walled circular steel columns under cyclic bidirectional loading". *Journal of structural engineering* **132**.10 (2006), pp. 1621–1631.
- [Gre14] Gresnigt, A. "Pipelines under imposed deformation Local buckling". *2nd Annual Global Forum on Pipeline Maintenance and Integrity Management, 18–19 September 2014, Amsterdam, the Netherlands*. Prospero. 2014.
- [Gri17] Grilli, D. et al. "Seismic performance of embedded column base connections subjected to axial and lateral loads". *Journal of Structural Engineering* **143**.5 (2017), p. 04017010.
- [Ham17] Hammett, S. "Theoretical Moment-Rotation Curve for Steel Piles Embedded in Concrete" (2017).
- [Han99] Handbook, P. D. *Precast and prestressed concrete*. 1999.
- [Har10] Harn, R. et al. "Proposed seismic detailing criteria for piers and wharves". *Ports 2010: Building on the Past, Respecting the Future*. 2010, pp. 460–469.
- [Har19] Harn, R. et al. "Proposed Pipe Pile Strain Limits for ASCE 61-19". *Ports 2019: Port Engineering*. American Society of Civil Engineers Reston, VA, 2019, pp. 437–448.

- [HW04] Hossain, A. B. & Weiss, J. "Assessing residual stress development and stress relaxation in restrained concrete ring specimens". *Cement and Concrete Composites* **26**.5 (2004), pp. 531–540.
- [HW06] Hossain, A. B. & Weiss, J. "The role of specimen geometry and boundary conditions on stress development and cracking in the restrained ring test". *Cement and Concrete Research* **36**.1 (2006), pp. 189–199.
- [Jan02] Janssen, D. "Requirements for a test of frost resistance of concrete". *International RILEM Workshop on Frost Resistance of Concrete*. RILEM Publications SARL. 2002, pp. 277–286.
- [Kha99] Khayat, K. et al. "High-performance cement grout for post-tensioning applications". *Materials Journal* **96**.4 (1999), pp. 471–477.
- [Kul09] Kulkarni, N. et al. "Displacement based seismic verification method for thin-walled circular steel columns subjected to bi-directional cyclic loading". *Engineering Structures* **31**.11 (2009), pp. 2779–2786.
- [Lar13] Larosche, A. et al. "Plain pile embedment for exterior bent cap connections in seismic regions". *Journal of Bridge Engineering* **19**.4 (2013), p. 04013016.
- [Lem98] Leming, M. L. et al. "Non-destructive determination of the dynamic modulus of concrete disks". *Materials Journal* **95**.1 (1998), pp. 50–57.
- [Li11] Li, W. et al. "Water absorption and critical degree of saturation relating to freeze-thaw damage in concrete pavement joints". *Journal of Materials in Civil Engineering* **24**.3 (2011), pp. 299–307.
- [Lit88] Litvan, G. G. *The mechanism of frost action in concrete: Theory and practical implications*. National Research Council Canada, Institute for Research in Construction, 1988.
- [Lit80] Litvan, G. "Freeze-thaw durability of porous building materials". *Durability of building materials and components*. ASTM International, 1980.
- [Man88] Mander, J. B. et al. "Theoretical stress-strain model for confined concrete". *Journal of structural engineering* **114**.8 (1988), pp. 1804–1826.

- [McK10] McKenna, F. et al. “Nonlinear finite-element analysis software architecture using object composition”. *Journal of Computing in Civil Engineering* **24**.1 (2010), pp. 95–107.
- [MM17] Mehta, P. K. & Monteiro, P. J. *Concrete Microstructure, Properties and Materials*. 2017.
- [MW06] Moon, J. H. & Weiss, J. “Estimating residual stress in the restrained ring test under circumferential drying”. *Cement and Concrete Composites* **28**.5 (2006), pp. 486–496.
- [Moo06] Moon, J.-H. et al. “Quantifying the influence of specimen geometry on the results of the restrained ring test”. *Journal of ASTM International* **3**.8 (2006), pp. 1–14.
- [Per91] Perry, S. et al. “Mix details and material behaviour of polystyrene aggregate concrete”. *Magazine of Concrete Research* **43**.154 (1991), pp. 71–76.
- [Pow60] Powers, T. C. *Physical properties of cement paste*. Tech. rep. 1960.
- [PB46] Powers, T. C. & Brownyard, T. L. “Studies of the physical properties of hardened Portland cement paste”. *Journal Proceedings*. Vol. 43. 9. 1946, pp. 101–132.
- [Pri03] Priestley. “Myths and Fallacies in Earthquake Engineering, Revisited: The Ninth Mallet Milne Lecture” (2003).
- [Pri07] Priestley, M. J. N. et al. *Displacement-Based Seismic Design of Structures*. First Edition. Pavia, ITALY: IUSS Press, 2007.
- [Pri00] Priestley, M. “Performance based seismic design”. *Bulletin of the New Zealand society for earthquake engineering* **33**.3 (2000), pp. 325–346.
- [RT94] Ravindrarajah, R. S. & Tuck, A. “Properties of hardened concrete containing treated expanded polystyrene beads”. *Cement and Concrete Composites* **16**.4 (1994), pp. 273–277.
- [Ric28] Richart, F. E. et al. *A study of the failure of concrete under combined compressive stresses*. Tech. rep. University of Illinois at Urbana Champaign, College of Engineering, 1928.

- [Set99] Setzer, M. "Micro ice lens formation and frost damage". *Proceedings of the International RILEM Workshop on Frost damage in concrete, Minneapolis, 28–30 June 1999*. 1999, pp. 1–15.
- [Set04] Setzer, M. et al. "Test methods of frost resistance of concrete: CIF-Test: Capillary suction, internal damage and freeze thaw test - Reference method and alternative methods A and B". *Materials and Structures* **37**.10 (2004), pp. 743–753.
- [Sha02a] Shama, A. A. et al. "Seismic investigation of steel pile bents: I. Evaluation of performance". *Earthquake spectra* **18**.1 (2002), pp. 121–142.
- [Sha02b] Shannag, M. J. "High-performance cementitious grouts for structural repair". *Cement and Concrete Research* **32**.5 (2002), pp. 803–808.
- [SS76] Shibata, A. & Sozen, M. A. "Substitute-structure method for seismic design in R/C". *Journal of the structural division* **102**.ASCE# 11824 (1976).
- [Asta] *Standard Test Method for Compressive Strength of Cylindrical Concrete Specimens*. Standard. West Conshohocken, PA: ASTM International, 2018.
- [Astb] *Standard Test Method for Compressive Strength of Hydraulic Cement Mortars (Using 2-in. or [50-mm] Cube Specimens)*. Standard. West Conshohocken, PA: ASTM International, 2016.
- [Astc] *Standard Test Method for Determining Age at Cracking and Induced Tensile Stress Characteristics of Mortar and Concrete under Restrained Shrinkage*. Standard. West Conshohocken, PA: ASTM International, 2018.
- [Astd] *Standard Test Method for Fundamental Transverse, Longitudinal, and Torsional Resonant Frequencies of Concrete Specimens*. Standard. West Conshohocken, PA: ASTM International, 2014.
- [Aste] *Standard Test Method for Resistance of Concrete to Rapid Freezing and Thawing*. Standard. West Conshohocken, PA: ASTM International, 2015.
- [Astf] *Standard Test Method for Soundness of Aggregates by Use of Sodium Sulfate or Magnesium Sulfate*. Standard. West Conshohocken, PA: ASTM International, 2018.
- [Tou99] Toumbakari, E.-E. et al. "Effect of mixing procedure on injectability of cementitious grouts". *Cement and Concrete Research* **29**.6 (1999), pp. 867–872.

- [UG98] Usami, T. & Ge, H. "Cyclic behavior of thin-walled steel structures - numerical analysis". *Thin-walled structures* **32**.1-3 (1998), pp. 41–80.
- [Xia06] Xiao, Y et al. "Experimental studies on seismic behavior of steel pile-to-pile-cap connections". *Journal of Bridge Engineering* **11**.2 (2006), pp. 151–159.

APPENDICES

APPENDIX

A

EQUATIONS FOR ESTIMATING THE
CYCLIC BACKBONE RESPONSE OF
TWO-COLUMN BRIDGE PIERS

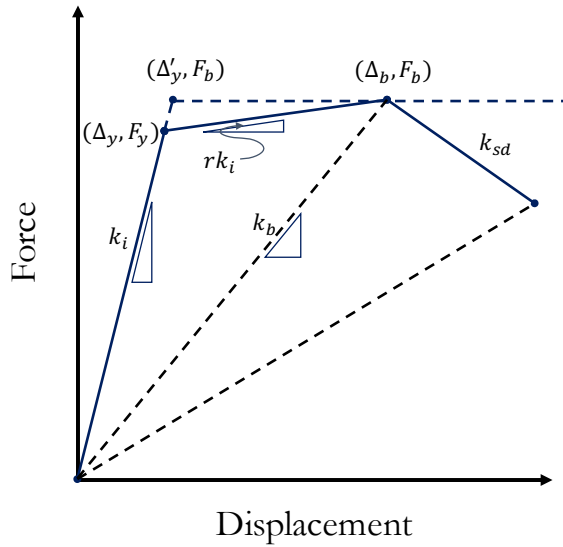


Figure A.1 Idealized force versus displacement response.

Yield Limit-State

$$\Delta_y = \gamma_{sc} \gamma_{cb} \Delta'_y \quad (\text{A.1})$$

$$\gamma_{cb} = 1.05 \left(\frac{1}{K_{rcb}} \right)^{0.92} \quad (\text{A.2})$$

$$\gamma_{sc} = 1.88 - 0.01 \left(\frac{D}{t} \right) \quad (\text{A.3})$$

$$\Delta'_y = \frac{\phi_y L_c^2}{3} \quad (\text{A.4})$$

$$\phi_y = \frac{2\epsilon_y}{D} \quad (\text{A.5})$$

$$F_y = n_c \frac{f_y S}{L_c} \quad (\text{A.6})$$

Buckling Limit-State

$$\Delta_b = \gamma_{sc} \gamma_{cb} \Delta'_b \quad (\text{A.7})$$

$$\gamma_{cb} = 0.65 \left(\frac{1}{K_{rcb}} \right)^{0.58} \left(\frac{D}{t} \right)^{0.14} \quad (\text{A.8})$$

$$\gamma_{sc} = 1.73 \quad (\text{A.9})$$

$$\Delta'_b = \Delta_e + \Delta_p \quad (\text{A.10})$$

$$\Delta_e = \frac{\phi'_y L_c^2}{3} \quad (\text{A.11})$$

$$\phi'_y = \phi_y \left(\frac{M_p}{M_y} \right) \quad (\text{A.12})$$

$$\Delta_p = L_p \left(\phi_b - \phi'_y \right) \left(L_c - \frac{L_p}{2} \right) \quad (\text{A.13})$$

$$\phi_b = \frac{b_c \epsilon_b}{D} \quad (\text{A.14})$$

$$b_c = 2.81 - 0.019 \left(\frac{D}{t} \right) \quad (\text{A.15})$$

$$\epsilon_b = 15 \left(\frac{D}{t} \right)^{-2} \quad (\text{A.16})$$

$$L_p = k_p L_c \quad (\text{A.17})$$

$$k_p \approx 0.035 \quad (\text{A.18})$$

$$F_b = F_y \left[1 + r \left(\frac{\Delta'_b}{\Delta'_y} - 1 \right) \right] \leq \frac{M_p}{L_c} \quad (\text{A.19})$$

$$r = 0.0136 \left(\frac{D}{t} \right) + 0.004 f_y - 0.35 \quad (\text{A.20})$$

Strength Degradation Rate

$$k_{sd} = 540 \left(\frac{D}{t} \right)^{-1.3} - 0.18 \left(\frac{P}{P_u} \right) - 11.3 \quad (\text{A.21})$$

$$\Delta_{sd-n} = \Delta_b - \frac{F_b L_e (1 - 0.01n)}{100 k_{sd}} \quad (\text{A.22})$$

Nomenclature

D = Column diameter

F_y = System force at yield limit-state

F_b = System force at local buckling limit-state

K_{rcb} = Cap beam relative stiffness

L_c = Column cantilever length

L_p = Plastic hinge length

M_p = Expected column maximum bending moment

M_y = Column yield moment

P = Column axial load

P_u = Column axial load capacity

S = Column section modulus

Nomenclature (Cont...)

- b_c = Dimensionless column curvature at local buckling
- f_y = Yield strength of steel
- k_p = Ratio of plastic hinge length to column cantilever length
- k_{sd} = Column strength degradation rate, % reduction per unit drift
- n = Strength reduction in terms of percentage of F_b
- n_c = Number of columns
- r = Column bi-linear factor
- t = Column wall thickness
- Δ_b = System displacement at column local buckling
- Δ'_b = Single column displacement at column local buckling
- Δ_e = Elastic component of column displacement
- Δ_p = Plastic component of column displacement
- Δ_{sd-n} = Displacement at n% strength reduction
- Δ_y = System yield displacement
- Δ'_y = Single column yield displacement
- ϵ_y = Column yield strain
- ϵ_b = Column strain at local buckling

Nomenclature (Cont...)

γ_{sc} = Socket connection flexibility coefficient

γ_{cb} = Cab beam flexibility coefficient

ϕ_b = Column maximum curvature at local buckling

ϕ_y = Column yield curvature

ϕ'_y = Equivalent column yield curvature

APPENDIX

B

MILL CERTIFICATES

1600

Tenaris

HILL TEST CERTIFICATE

Number:	83814552.0.1	Page:	1 / 6
Date:	March 11, 2014		

MAVERICK TUBE CORPORATION
Hawthorne Park
SUITE 100, MCKINNEY, TX 75071
817.748.4222, ext.
(800) 774.5018, fax

Customer:	SAGINAW PIPE COMPANY, INC. 1350 FIVE ST, SAGINAW, MI.	Customer's Order No.:	33814552.0.1
Manufacturing Process:	HTP	Customer's Order Date:	3/08/2014
Product Type:	Line Pipe	Customer's Reference:	55376
Standard or Specification:			
API SL:			

Dimensions:	Schedule:	Length:	Type:	Quantity:	Req. PT:	40561 LG	Nominal Weight:	32.65 LB/FT	TEST RESULTS										
									Ls	Sc	Type	Or	Specimen Condition:	Specimen Dimensions:	Test Temp:	Y.S.	UTS	Y.S. (%)	UTS (%)
12.523	34.00003	E1	12548	2	AM	SS	T	1,600	RT	62,670	70,980	0.65	2.0	26.0	43.7				
12645	34.00004	E1	12648	B	AM	SS	T	1,500	RT	59,470	71,160	0.82	2.0	28.0	46.0				
12728	34.00005	E1	12728	B	AM	SS	T	1,500	RT	59,480	67,510	0.87	2.0	29.0	44.7				
226134	34.00006	E1	226134	B	AM	SS	T	1,500	RT	67,470	74,100	0.91	2.0	29.0	45.3				

Specimen condition:	Specimen dimensions:	Test Temp:	Y.S.	UTS	Y.S. (%)	UTS (%)	Reduction:				
Ls	Sc	Type	Or	Specimen condition:	Specimen dimensions:	Test Temp:	Y.S.	UTS	Y.S. (%)	UTS (%)	Reduction:
AM	SS	AM	SS	AM	SS	AM	AM	AM	AM	AM	AM
AM	SS	AM	SS	AM	SS	AM	AM	AM	AM	AM	AM
AM	SS	AM	SS	AM	SS	AM	AM	AM	AM	AM	AM

U.T.S.: Ultimate tensile strength

Y.S.: Yield strength

RT: Room temperature

Specimen condition:
AM: As received
SS: Specimen prepared
AM: As machined

Loc. of sample:

Req. Max. Required minimum:

RT: Room temperature

AM: As received

SS: Specimen prepared

AM: As machined

SS: Specimen prepared

AM: As received

SS: Specimen prepared

AM: As machined

SS: Specimen prepared

AM: As received

SS: Specimen prepared

AM: As machined

SS: Specimen prepared

AM: As received

SS: Specimen prepared

AM: As machined

SS: Specimen prepared

AM: As received

SS: Specimen prepared

AM: As machined

SS: Specimen prepared

AM: As received

SS: Specimen prepared

AM: As machined

SS: Specimen prepared

AM: As received

SS: Specimen prepared

AM: As machined

SS: Specimen prepared

AM: As received

SS: Specimen prepared

AM: As machined

SS: Specimen prepared

AM: As received

SS: Specimen prepared

AM: As machined

SS: Specimen prepared

AM: As received

SS: Specimen prepared

AM: As machined

SS: Specimen prepared

AM: As received

SS: Specimen prepared

AM: As machined

SS: Specimen prepared

AM: As received

SS: Specimen prepared

AM: As machined

SS: Specimen prepared

AM: As received

SS: Specimen prepared

AM: As machined

SS: Specimen prepared

AM: As received

SS: Specimen prepared

AM: As machined

SS: Specimen prepared

AM: As received

SS: Specimen prepared

AM: As machined

SS: Specimen prepared

AM: As received

SS: Specimen prepared

AM: As machined

SS: Specimen prepared

AM: As received

SS: Specimen prepared

AM: As machined

SS: Specimen prepared

AM: As received

SS: Specimen prepared

AM: As machined

SS: Specimen prepared

AM: As received

SS: Specimen prepared

AM: As machined

SS: Specimen prepared

AM: As received

SS: Specimen prepared

AM: As machined

SS: Specimen prepared

AM: As received

SS: Specimen prepared

AM: As machined

SS: Specimen prepared

AM: As received

SS: Specimen prepared

AM: As machined

SS: Specimen prepared

AM: As received

SS: Specimen prepared

AM: As machined

SS: Specimen prepared

AM: As received

SS: Specimen prepared

AM: As machined

SS: Specimen prepared

AM: As received

SS: Specimen prepared

AM: As machined

SS: Specimen prepared

AM: As received

SS: Specimen prepared

AM: As machined

SS: Specimen prepared

AM: As received

SS: Specimen prepared

AM: As machined

SS: Specimen prepared

AM: As received

SS: Specimen prepared

AM: As machined

SS: Specimen prepared

AM: As received

SS: Specimen prepared

AM: As machined

SS: Specimen prepared

AM: As received

SS: Specimen prepared

AM: As machined

SS: Specimen prepared

AM: As received

SS: Specimen prepared

AM: As machined

SS: Specimen prepared

AM: As received

SS: Specimen prepared

AM: As machined

SS: Specimen prepared

AM: As received

SS: Specimen prepared

AM: As machined

SS: Specimen prepared

AM: As received

SS: Specimen prepared

AM: As machined

SS: Specimen prepared

AM: As received

SS: Specimen prepared

AM: As machined

SS: Specimen prepared

AM: As received

SS: Specimen prepared

AM: As machined

SS: Specimen prepared

AM: As received

SS: Specimen prepared

AM: As machined

SS: Specimen prepared

AM: As received

SS: Specimen prepared

AM: As machined

SS: Specimen prepared

AM: As received

SS: Specimen prepared

AM: As machined

SS: Specimen prepared

AM: As received

SS: Specimen prepared

AM: As machined

SS: Specimen prepared

AM: As received

SS: Specimen prepared

AM: As machined

SS: Specimen prepared

AM: As received

SS: Specimen prepared

AM: As machined

SS: Specimen prepared

AM: As received

SS: Specimen prepared

AM: As machined

SS: Specimen prepared

AM: As received

SS: Specimen prepared

AM: As machined

SS: Specimen prepared

AM: As received

SS: Specimen prepared

AM: As machined

SS: Specimen prepared

AM: As received

SS: Specimen prepared

AM: As machined

SS: Specimen prepared

AM: As received

SS: Specimen prepared

AM: As machined

SS: Specimen prepared

AM: As received

SS: Specimen prepared

AM: As machined

SS: Specimen prepared

AM: As received

SS: Specimen prepared

AM: As machined

SS: Specimen prepared

AM: As received

SS: Specimen prepared

AM: As machined

SS: Specimen prepared

AM: As received

SS: Specimen prepared

AM: As machined

SS: Specimen prepared

AM: As received

SS: Specimen prepared

AM: As machined

SS: Specimen prepared

AM: As received

SS: Specimen prepared

AM: As machined

SS: Specimen prepared

AM: As received

SS: Specimen prepared

AM: As machined

SS: Specimen prepared

AM: As received

SS: Specimen prepared

AM: As machined

SS: Specimen prepared

AM: As received

SS: Specimen prepared

AM: As machined

SS: Specimen prepared

AM: As received

SS: Specimen prepared

AM: As machined

SS: Specimen prepared

AM: As received

SS: Specimen prepared

AM: As machined

SS: Specimen prepared

AM: As received

SS: Specimen prepared

AM: As machined

SS: Specimen prepared

AM: As received

SS: Specimen prepared

AM: As machined



MILL TEST CERTIFICATE

Number:	83614552.0.1
Page:	2 / 6

Date:	March 11, 2014
-------	----------------

Customer's Works Order No:
48576

GARRETT PIPE CORPORATION

Hannan Plant

SHERMAN COUNTY RD 667

BLYTHEVILLE, AR 72315

(870) 776-5003

(870) 776-5006 fax

Customer: SAGINAW PIPE COMPANY, INC. 1986 HWY 31 S, SAGINAW, AL.

Customer Order Item: 311692313010

Customer's Reference: 48576

Customer: SAGINAW PIPE COMPANY, INC. 1986 HWY 31 S, SAGINAW, AL.
311692313010

Customer Order Item: 311692313010

Customer's Reference: 48576

35137

HFW

Manufacturing Process:

API SL

Standard or Specification:

Dimensions:

16,000 x 0.350 14

Grade:

N/A

Length:

N/A

Surface:

N/A

Product Type:

Line Pipe

Line:

N/A

Size:

N/A

Grade:

N/A

Steel Grade:

X52M PSI. 2

Quantity: 9 PCS

400 FT

40518 LS

UTS: 52.85 LB/FT

Wt. Wgt:

Plain End Bevelled

Nominal Weight:

N/A

Surface:

Bare

Ends:

N/A

Base:

N/A

Bottom:

N/A

Top:

Tenaris

MILL TEST CERTIFICATE

Number:	Page:
33814552.0.1	3 / 6

MASTERCUT TUBE CORPORATION
National Plant
SAVANNAH COUNTY RD 667
BUTTERVILLE, AR 72315
(873) 778-5210 Tel
(873) 778-5211 Fax

Customer: SAGINAW PIPE COMPANY, INC. 1989 Hwy 31 S, SAGINAW, AL,

25137

Customer's Order No.:

3103026345010

Customer's Reference:

45578

Manufacturing Process:
API SL
HPW

Product Type:
Line Pipe

Spec Grade:

XSEMPSL2

Dimensions:

Schedule:

Length:

Sample Random

Quantity: 9 PCS

489 FT

46518 LS

Max. Weight:

32.85 LB/FT

Min. Weight:

30.00 LB/FT

Max. Diameter:

1.15 IN

Min. Diameter:

1.14 IN

Max. Wall Thickness:

0.15 IN

Min. Wall Thickness:

0.14 IN

Max. Length:

489 FT

Min. Length:

489 FT

Max. Thickness:

0.15 IN

Min. Thickness:

0.14 IN

Max. Diameter:

1.15 IN

Min. Diameter:

1.14 IN

Max. Wall Thickness:

0.15 IN

Min. Wall Thickness:

0.14 IN

Max. Length:

489 FT

Min. Length:

489 FT

Max. Thickness:

0.15 IN

Min. Thickness:

0.14 IN

Max. Diameter:

1.15 IN

Min. Diameter:

1.14 IN

Max. Wall Thickness:

0.15 IN

Min. Wall Thickness:

0.14 IN

Max. Length:

489 FT

Min. Length:

489 FT

Max. Thickness:

0.15 IN

Min. Thickness:

0.14 IN

Max. Diameter:

1.15 IN

Min. Diameter:

1.14 IN

Max. Wall Thickness:

0.15 IN

Min. Wall Thickness:

0.14 IN

Max. Length:

489 FT

Min. Length:

489 FT

Max. Thickness:

0.15 IN

Min. Thickness:

0.14 IN

Max. Diameter:

1.15 IN

Min. Diameter:

1.14 IN

Max. Wall Thickness:

0.15 IN

Min. Wall Thickness:

0.14 IN

Max. Length:

489 FT

Min. Length:

489 FT

Max. Thickness:

0.15 IN

Min. Thickness:

0.14 IN

Max. Diameter:

1.15 IN

Min. Diameter:

1.14 IN

Max. Wall Thickness:

0.15 IN

Min. Wall Thickness:

0.14 IN

Max. Length:

489 FT

Min. Length:

489 FT

Max. Thickness:

0.15 IN

Min. Thickness:

0.14 IN

Max. Diameter:

1.15 IN

Min. Diameter:

1.14 IN

Max. Wall Thickness:

0.15 IN

Min. Wall Thickness:

0.14 IN

Max. Length:

489 FT

Min. Length:

489 FT

Max. Thickness:

0.15 IN

Min. Thickness:

0.14 IN

Max. Diameter:

1.15 IN

Min. Diameter:

1.14 IN

Max. Wall Thickness:

0.15 IN

Min. Wall Thickness:

0.14 IN

Max. Length:

489 FT

Min. Length:

489 FT

Max. Thickness:

0.15 IN

Min. Thickness:

0.14 IN

Max. Diameter:

1.15 IN

Min. Diameter:

1.14 IN

Max. Wall Thickness:

0.15 IN

Min. Wall Thickness:

0.14 IN

Max. Length:

489 FT

Min. Length:

489 FT

Max. Thickness:

0.15 IN

Min. Thickness:

0.14 IN

Max. Diameter:

1.15 IN

Min. Diameter:

1.14 IN

Max. Wall Thickness:

0.15 IN

Min. Wall Thickness:

0.14 IN

Max. Length:

489 FT

Min. Length:

489 FT

Max. Thickness:

0.15 IN

Min. Thickness:

0.14 IN

Max. Diameter:

1.15 IN

Min. Diameter:

1.14 IN

Max. Wall Thickness:

0.15 IN

Min. Wall Thickness:

0.14 IN

Max. Length:

489 FT

Min. Length:

489 FT

Max. Thickness:

0.15 IN

Min. Thickness:

0.14 IN

Max. Diameter:

1.15 IN

Min. Diameter:

1.14 IN

Max. Wall Thickness:

0.15 IN

Min. Wall Thickness:

0.14 IN

Max. Length:

489 FT

Min. Length:

489 FT

Max. Thickness:

0.15 IN

Min. Thickness:

0.14 IN

Max. Diameter:

1.15 IN

Min. Diameter:

1.14 IN

Max. Wall Thickness:

0.15 IN

Min. Wall Thickness:

0.14 IN

Max. Length:

489 FT

Min. Length:

489 FT

Max. Thickness:

0.15 IN

Min. Thickness:

0.14 IN

Max. Diameter:

1.15 IN

Min. Diameter:

1.14 IN

Max. Wall Thickness:

0.15 IN

Min. Wall Thickness:

0.14 IN

Max. Length:

489 FT

Min. Length:

489 FT

Max. Thickness:

0.15 IN

Min. Thickness:

0.14 IN

Max. Diameter:

1.15 IN

Min. Diameter:

1.14 IN

Max. Wall Thickness:

0.15 IN

Min. Wall Thickness:

0.14 IN

Max. Length:

489 FT

Min. Length:

489 FT

Max. Thickness:

0.15 IN

Min. Thickness:

0.14 IN

Max. Diameter:

1.15 IN

Min. Diameter:

1.14 IN

Max. Wall Thickness:

0.15 IN

Min. Wall Thickness:

0.14 IN

Max. Length:

489 FT

Min. Length:

489 FT

Max. Thickness:

0.15 IN

Min. Thickness:

0.14 IN

Max. Diameter:



MILL TEST CERTIFICATE

Number:	63814552.0.1	Page:	4 / 6
Date:	March 11, 2014	Customer's Reference:	43578

MANFREDI TUBE CORPORATION

Hickman Plaza

SAU N COUNTY RD 987

BLUFFVILLE, AR 72315

(873) 735-5000 tel

(873) 735-5005 fax

Customer: SAGINAW PIPE COMPANY, INC. 1980 Hwy 31 S, SAGINAW, AL, 35137	Customer's Order Number 310028345210
Manufacturing Process: API SL	Product Type: Line Pipe

Standard or Specification: ASME PSLL 2	Steel Grade: X52A PSLL 2
Dimensions: 16.000 x 6.500 in	Schedule: Welded Random

Length: 408 FT	Quantity: 9 PCS
Weight: 40518 LB	Nominal Weight: 82.65 LB/FT

Ends: Plain End Bevelled	Surface: NA
Specimen Preparation: Not Specified	Specimen Preparation: Not Specified

4.14. As manufactured
Avg. Average
B: Body
Loc. location of sample

Max. Measurement
Min. Minimum

Var. Variation
Var. Variation

Test: Charpy V	Temp: 32	Orientation: T	Ugt: F	Int. Min. Res.: 11	Sugt: Min. Avg.: 18	Int. Min. Recd.:	Shear area %	Req. Min. Avg.: 4	Results:						
									1	2	3	Avg.	1	2	3
Heat #:	Sample #:	Lot #:													
120238	3450083	120238	B	AM	32	34	215.3	214.3	216.5	216.2	105	130	100	100	100
120648	3406091	120648	B	AM	32	34	210.0	211.8	206.7	100.0	160	100	100	100	100
121259	3436580	121259	B	AM	32	34	204.2	206.0	206.6	100	160	100	100	100	100
	3405095	229434	9	AM	32	34	218.1	218.3	216.9	216.5	100	150	100	100	100

Ind. Min. Res: Individual Minimum Required

SC: Specimen composition

T.T: Test temperature

Temp: Temperature

Loc. location of sample

Req. Min. Avg. Required minimum average

Avg. Average

B: Body

This certificate is issued by a company and is signed with electronic signature. On the original certificate the handwritten green colored "Tenaris" is stamped. In case the owner of the original certificate might require a copy of it, he must obtain the certificate by the original company. It is assumed that responsibility for any informal or unauthorized use, Any violation of the certification will be subject to the law.

Tenaris

MILL TEST CERTIFICATE

Number:	83814552.01	Page:	5 / 6
Date:	March 11, 2014		

MAVERICK TUBE CORPORATION
Harrison Penn
SEGUIN COUNTY RD 517
SALTVILLE, AR 72115
(870) 776-2121 ext
(870) 776-6233 fax

Customer: SAGINAW PIPE COMPANY, INC. 1950 HWY 31 S, SAGINAW, AL,
151-37

Manufacturing Process: FHW
Standard or Specification: API 5L

Schedule: N/A
Length: Triple Random
Diameter: 3 PCS
488 FT
49318 LB
62.85 LAFT

Customer's Order Ref#:
210032635050

Customer's Reference#:
45576

Product Type:
Line Pipe

Steel Grade:
X70M PSL 2

Ends:
Plain End Beveled

Nominal Weight:

Manufacturer's Works Order #: N/A

Surface:
Bare

Material Weight:

Customer's Order Ref#:

Sample #	Lot N°	Sample N°	Regrd	Heat N°	Lot N°	Sample N°	Regrd
12058	120519	348603	Good	125545	126448	348591	Good

Sample #	Lot N°	Sample N°	Regrd	Heat N°	Lot N°	Sample N°	Regrd
				127289	127285	348500	Good

Customer's Order Ref#:

Pressure	Time	Results
Unit	Value	Seconds

Customer's Order Ref#:

Customer's

Tenaris

MILL TEST CERTIFICATE

Number:	83814552.01	Page:	6 / 6
Date:	March 11, 2014		

MAVERICK TUBE CORPORATION
Hannan Pipe
ROCK COUNTY, WI 53572
BLAUGRUND, WI 53516
(608) 776-5000 ext.
(608) 776-5005 fax

Customer: SAGINAW PIPE COMPANY, INC. 1380 HWY 31 S, SAGINAW, AL, 35137	Customer's Order Item: 315E2253/3254	Customer's Reference: 45573	Manufacturer's Works Order No.: N/A
Manufacturing Process: API 5L	Product Type: Line Pipe	Steel Grade: X52M PSL2	Ends: Plain End Bevelled
Dimensions: 48.400 x 0.500 in	Schedule: N/A	Quantity: 9 PCS	Nominal Weight: 32.85 LB/FT
	Length: Triple Random	488 FT	48518 LB

Steel Vendor Name and Remanufactured
126288 NUCOR STEEL HICKMAN ARMORED AR Melted and Remanufactured in USA

Steel Vendor Name and Remanufactured
126288 NUCOR STEEL HICKMAN ARMORED AR Melted and Remanufactured in USA

SUMMARY REPORT

Heat #	Quantity	Length	Weight	Heat #	Quantity	Length	Weight
126288	4	208.1	17,243.316	127289	2	193.359	5,810.605
126288	2	110.450	9,155.882	126288	1	52.001	4,308.659

This is to certify that the product described here was manufactured, sampled, tested, and inspected in accordance with purchaser order requirements. This certificate is not a declaration of origin but may be used as a declaration of origin.

CUSTOMER / THIRD PARTY

TENARIS QUALITY DEPARTMENT SIGNATURE

INSPECTION COMPANY
DEPARTAMENTO DE INSPECCIÓN

Company Name: N/A
Employee Name: N/A

QUALITY CERTIFICATION DEPT.

Robert Semmel

Markus Schmid
J. Miller

CHIEF OF QUALITY CERTIFICATION DEPT.

Jeff Hollingshead

This document is issued by a compensated system and is valid with sufficient validation. Only the original certificate will receive green colored thermal stamp. In case the owner of the original certificate would request a copy of it, he must allow to reissue it to the original pipe holder upon request the responsibility for any damage or loss is borne. Any alteration made to this document will be voided and the box.

24th
69
so good to see
CERTIFIED

AMERICAN STEEL PIPE

A division of American Cast Iron Pipe Co.,
P.O. Box 2727, Birmingham, AL 35202-2727
QUALIFICATION REPORT OF SHIPMENT

DATE: 19/JAN/2011

CUSTOMER ADDRESS: SAGINAW PIPE INCORPORATED
P O BOX 8
SAGINAW AL 35137

Customer Order Number 38706
MRG Order Number S109332

SPECIAL NOTES

REVISED MTR WITH A500 GRADE B & C SPECIFICATION ADDED.

PIPE FROM LINES 1, 2 AND 3 WILL ALSO MEET ASTM A53-01 GRADE B,
AND ASME SA53-04 GRADE B. PIPE FROM LINES 1, 2, AND 3 WILL ALSO MEET

ASTM A500 GRADE B & C.

PIPE WERE NDT TESTED USING AN ULTRASONIC TEST METHOD CALIBRATED ON ID & OD N-10 NOTCHES.
HYDROSTATIC TEST DURATION 10 SECONDS. MAX ALLOWABLE POM .25.
MINIMUM WELD SEAM ANNEAL TEMPERATURE 1600 DEGREES F FOR ALL PIPE.

CHARPY ACCEPTANCE CRITERIA MIN. ENERGY 15/HEAT, MIN. SHEAR AREA N/A.

LINE	PIECES	FOOTAGE	SIZE	WALL	SHIPMENT DESCRIPTION		SPECIFICATIONS	GRADE
					SHIPS NO	1-22		
1	46	3010.5	20.00	.375	ERW API LINE PIPE		API 5L, PSL2	SMX42M
2	71	4866.7	24.00	.500	DITTO			X52M
3	4	126.5	24.00	.500	DITTO			X52M

All tests are from the body of the pipe in the transverse direction unless otherwise noted.
Standard tensile gage length 1-1/2" x 2".

HEAT	C	MN	P	S	CB	SI	TI	CU	NI	MO	CR	V	AL	B	N	C.E.	Coil
N94193	*	L1															PIPE
H=	0.050	0.650	0.006	0.004	0.013	0.193	0.010	0.090	0.030	0.010	0.020	0.002	0.024	0.001	0.068	0.096	0.001
P=	0.063	0.660	0.005	0.006	0.012	0.187	0.009	0.080	0.042	0.010	0.007	0.002	0.022	0.000	0.000	0.108	0.012
M=Weld Ten.	69.4	Ksi	Ten.	65.5	Ksi	Yield	53.2	Ksi	%EL	43.0	Rb	77	Hydro:	1420	Psi	RUN:	37-0
V/T RATIO	=	0.81															

Attachments

PAGE 1
Continued

ISO 9001:2000
CERTIFIED

CUSTOMER NAME: SAGINAW PIPE INCORPORATED

Customer Order Number
38708

Date: 19/JAN/2011
MRG Order Number
S109332

ITEM C MN P S CB SI TI CU NI MO CR V AL B N C.E. Coil

N94193 * LINE 1 EDITION REFERENCE 4 Yield Strength by Strap
H= 0.050 0.550 0.006 0.004 0.013 0.193 0.010 0.090 0.030 0.010 0.020 0.002 0.024 0.001 0.0068 0.096 0.002
P= 0.053 0.661 0.005 0.005 0.014 0.185 0.009 0.081 0.042 0.011 0.010 0.002 0.022 0.000 0.000 0.098 /
M=Weld Ten. 00.0 ksi Ten. 00.0 ksi Yield 00.0 ksi %EL 00.0 RB 00 Hydro: 1420 Psi RUN: 37-0

V/T RATIO = 0.00

N94192 * LINE 1 EDITION REFERENCE 4 Yield Strength by Strap
H= 0.050 0.680 0.006 0.003 0.014 0.184 0.010 0.090 0.040 0.010 0.030 0.002 0.029 0.001 0.074 0.098 0.003
P= 0.051 0.688 0.005 0.004 0.013 0.175 0.009 0.083 0.044 0.011 0.014 0.002 0.027 0.000 0.000 0.098 06/11
M=Weld Ten. 69.4 ksi Ten. 66.5 ksi Yield 53.9 ksi %EL 44.5 RB 94 Hydro: 1420 Psi RUN: 37-0

V/T RATIO = 0.81

N94192 * LINE 1 EDITION REFERENCE 4 Yield Strength by Strap
H= 0.050 0.680 0.006 0.003 0.014 0.184 0.010 0.090 0.040 0.010 0.030 0.002 0.029 0.001 0.074 0.098 0.003
P= 0.051 0.688 0.005 0.004 0.013 0.175 0.009 0.083 0.044 0.011 0.014 0.002 0.027 0.000 0.000 0.098 06/11
M=Weld Ten. 00.0 ksi Ten. 00.0 ksi Yield 00.0 ksi %EL 00.0 RB 00 Hydro: 1420 Psi RUN: 37-0

V/T RATIO = 0.00

N04919 * LINE 1 EDITION REFERENCE 4 Yield Strength by Strap
H= 0.050 0.680 0.008 0.003 0.014 0.206 0.010 0.120 0.040 0.010 0.050 0.002 0.025 0.001 0.077 0.101 0.009
P= 0.059 0.713 0.008 0.005 0.016 0.195 0.010 0.112 0.048 0.015 0.031 0.002 0.024 0.000 0.000 0.110 09/18
M=Weld Ten. 72.6 ksi Ten. 65.3 ksi Yield 50.3 ksi %EL 47.0 RB 80 Hydro: 1420 Psi RUN: 37-0
V/T RATIO = 0.77

PAGE 2
Continued

Attachments
Issue No.: 6

Form Date: 10/18/2004

QD-AW3P055

200074206
CERTIFIED

CUSTOMER NAME: SAGINAW PIPE INCORPORATED

Customer Order Number 38708
MFG Order Number S109332

Date: 19/JAN/2011

EDITION REFERENCE 4

HEAT	C	MN	P	S	CB	SI	TI	CT	NT	NO	CR	V	AL	B	N	C.E.	Coil	Pipe	
N04913	*	LINE 1																	

H= 0.050 0.680 0.008 0.003 0.014 0.206 0.010 0.120 0.040 0.010 0.050 0.002 0.025 .0001 .0077 0.101 0010
P= 0.061 0.718 0.008 0.005 0.017 0.197 0.010 0.114 0.050 0.015 0.034 0.002 0.024 .0000 .0000 0.113 /
M=Weld Ten. 00.0 ksi Ten. 00.0 ksi Yield 00.0 ksi SEL 00.0 RB 00 Hydro: 1420 Psi RUN: 37-0

Y/T RATIO = 0.00

BOX7622 * LINE 2 ✓

EDITION REFERENCE 4

Yield Strength by Strap
H= 0.060 1.160 0.008 0.003 0.028 0.210 0.001 0.230 0.090 0.022 0.050 0.018 0.032 .0002 .0080 0.145 0008
P= 0.033 1.146 0.009 0.007 0.020 0.201 0.003 0.219 0.088 0.024 0.033 0.020 0.028 .0000 0.000 0.115 04/08
M=Weld Ten. 79.8 ksi Ten. 76.2 ksi Yield 61.1 ksi SEL 41.0 RB 92 Hydro: 1960 Psi RUN: 41-0

Y/T RATIO = 0.80

BOX7622 * LINE 2 ✓

EDITION REFERENCE 4

Yield Strength by Strap
H= 0.060 1.160 0.008 0.003 0.028 0.210 0.001 0.230 0.090 0.022 0.050 0.018 0.032 .0002 .0080 0.145 0009
P= 0.035 1.150 0.009 0.007 0.021 0.196 0.003 0.221 0.089 0.026 0.038 0.022 0.031 .0000 .0000 0.117 /
M=Weld Ten. 00.0 ksi Ten. 00.0 ksi Yield 00.0 ksi SEL 00.0 RB 00 Hydro: 1960 Psi RUN: 41-0

Y/T RATIO = 0.00

BOX8269 * LINE 2

EDITION REFERENCE 4

Yield Strength by Strap
H= 0.061 1.171 0.009 0.003 0.031 0.189 0.001 0.225 0.080 0.022 0.060 0.017 0.030 .0001 .0100 0.145 0001
P= 0.054 1.126 0.009 0.005 0.019 0.171 0.003 0.202 0.083 0.024 0.037 0.019 0.023 .0000 .0000 0.133 05/09
M=Weld Ten. 83.4 ksi Ten. 78.6 ksi Yield 63.3 ksi SEL 41.0 RB 88 Hydro: 1960 Psi RUN: 46-0

Y/T RATIO = 0.81

Attachments

PAGE 3
Continued

Form Date: 10/18/2004

QD-AM3F055

Issue No.: 6

SO 9007-2008
CERTIFIED

CUSTOMER NAME: SAGINAW PIPE INCORPORATED

Customer Order Number: 38708
MFG Order Number: S109332
Date: 19/JAN/2011

HEAT	C	MN	P	S	CB	SI	TI	CU	NI	MO	CR	V	AL	B	N	C.E.	COIL	
BOX8269	*	LINE 2																Pipe
H=	0.061	1.171	0.009	0.003	0.031	0.189	0.001	0.225	0.080	0.022	0.060	0.017	0.030	0.001	0.0100	0.145	0002	
P=	0.050	1.134	0.011	0.006	0.023	0.179	0.003	0.213	0.085	0.023	0.043	0.020	0.029	0.000	0.0000	0.130	/	
M=Weld Ten.	00.0	ksi	Ten.	00.0	ksi	Yield	00.0	ksi	#EL	00.0	RB	00	Hydro:	1960	Psi	RUN: 46-0		
Y/T RATIO	=	0.00																

BOX8270 * LINE 2

EDITION REFERENCE 4

Yield Strength by Strap

H= 0.066 1.139 0.009 0.003 0.029 0.186 0.001 0.210 0.080 0.026 0.040 0.016 0.028 .0002 .0110 0.147 0004
P= 0.058 1.099 0.010 0.005 0.021 0.173 0.003 0.197 0.083 0.026 0.025 0.019 0.030 .0000 .0000 0.135 05/09

M=Weld Ten. 89.1 ksi Ten. 79.5 ksi Yield 62.5 ksi #EL 40.0 RB 91 Hydro: 1960 Psi RUN: 46-0

Y/T RATIO = 0.79

BOX8270 * LINE 2

EDITION REFERENCE 4

Yield Strength by Strap

H= 0.066 1.139 0.009 0.003 0.029 0.186 0.001 0.210 0.080 0.026 0.040 0.016 0.028 .0002 .0110 0.147 0005
P= 0.057 1.105 0.010 0.005 0.020 0.175 0.003 0.197 0.083 0.026 0.022 0.019 0.027 .0000 .0000 0.134 /
M=Weld Ten. 00.0 ksi Ten. 00.0 ksi Yield 00.0 ksi #EL 00.0 RB RUN: 46-0

Y/T RATIO = 0.00

BOX8268 * LINE 2
EDITION REFERENCE 4
Yield Strength by Strap
H= 0.065 1.111 0.009 0.003 0.027 0.181 0.001 0.215 0.080 0.024 0.040 0.015 0.033 .0001 .0110 0.144 0007
P= 0.061 1.092 0.009 0.005 0.018 0.161 0.003 0.197 0.085 0.024 0.026 0.018 0.033 .0000 .0000 0.137 05/08
M=Weld Ten. 82.0 ksi Ten. 77.5 ksi Yield 64.0 ksi #EL 39.5 RB 89 Hydro: 1960 Psi RUN: 46-0
Y/T RATIO = 0.83

Attachments

PAGE 4

Continued

Issue No.: 6

Form Date: 10/18/2004

OD-AW3F055



CERTIFIED

CUSTOMER NAME: SAGINAW PIPE INCORPORATED

Customer Order Number
38708
Date: 19/JAN/2011
MFG Order Number
S109332

HEAT	C	MN	P	S	CB	SI	TI	CU	NI	MO	CR	V	AL	B	N	C.E.	Coil
------	---	----	---	---	----	----	----	----	----	----	----	---	----	---	---	------	------

BOX8268 * LINE 2
H= 0.065 1.111 0.009 0.003 0.027 0.181 0.001 0.215 0.080 0.024 0.040 0.015 0.033 0.001 0.010 0.144 0.008
P= 0.053 1.096 0.010 0.005 0.020 0.163 0.003 0.198 0.086 0.024 0.029 0.019 0.032 0.000 0.000 0.130 /
M=Weld Ten. 00.0 ksi Ten. 00.0 ksi Yield 00.0 ksi %EL 00.0 RB 00 Hydro: 1960 Psi RUN: 46-0

A0X3449 * LINE 2
EDITION REFERENCE 4
H= 0.063 1.153 0.010 0.003 0.029 0.191 0.001 0.235 0.080 0.020 0.060 0.016 0.030 0.001 0.010 0.147 0.009
P= 0.048 1.136 0.012 0.005 0.021 0.178 0.003 0.229 0.082 0.021 0.048 0.019 0.028 0.000 0.000 0.129 09/11
M=Weld Ten. 82.0 ksi Ten. 78.6 ksi Yield 64.8 ksi %EL 41.0 RB 88 Hydro: 1960 Psi RUN: 46-0

A0X3449 * LINE 2
EDITION REFERENCE 4
H= 0.063 1.153 0.010 0.003 0.029 0.191 0.001 0.235 0.080 0.020 0.060 0.016 0.030 0.001 0.010 0.147 0.009
P= 0.048 1.131 0.012 0.006 0.021 0.181 0.003 0.225 0.083 0.021 0.046 0.018 0.028 0.000 0.000 0.129 /
M=Weld Ten. 80.0 ksi Ten. 78.0 ksi Yield 60.0 ksi %EL 00.0 RB 00 Hydro: 1960 Psi RUN: 46-0

A0X3450 * LINE 2
EDITION REFERENCE 4
H= 0.065 1.161 0.009 0.003 0.030 0.193 0.001 0.206 0.080 0.022 0.050 0.018 0.027 0.001 0.010 0.147 0.013
P= 0.053 1.110 0.010 0.006 0.021 0.172 0.003 0.196 0.080 0.023 0.028 0.019 0.025 0.000 0.000 0.130 04/08
M=Weld Ten. 82.7 ksi Ten. 78.5 ksi Yield 64.9 ksi %EL 43.0 RB 90 Hydro: 1960 Psi RUN: 46-0

Attachments

Issue No.: 6

Form Date: 10/18/2004

QD-AW3F055

PAGE 5
Continued

ISO 9001:2000
CERTIFIED

CUSTOMER NAME: SAGINAW PIPE INCORPORATED

Customer Order Number
38708
MFG Order Number
S109332
Date: 19/JAN/2011

EDITION REFERENCE 4
H= 0.051 1.127 0.010 0.005 0.020 0.176 0.003 0.197 0.079 0.021 0.034 0.019 0.024 0.000 0.000 0.129 /
P= 0.047 0.913 0.006 0.005 0.049 0.214 0.015 0.015 0.021 0.006 0.002 0.005 0.035 0.000 0.000 0.102 07/12
M=Weld Ten. 75.8 ksi Ten. 75.8 ksi Yield 62.9 ksi SEL 44.5 RB 87 Hydro: 1960 Psi RUN: 19-0
Y/T RATIO = 0.83

Pipe

HEAT	C	MN	P	S	CB	ST	TI	CU	NI	MO	CR	V	AL	B	N	C.E.	Coil
A0X3450	*	LINE 2															
H=	0.065	1.161	0.009	0.003	0.030	0.193	0.001	0.206	0.080	0.022	0.050	0.018	0.027	0.001	0.100	0.147	0014
P=	0.051	1.127	0.010	0.005	0.020	0.176	0.003	0.197	0.079	0.021	0.034	0.019	0.024	0.000	0.000	0.129	/
M=Weld Ten.	00.0	ksi	Ten.	00.0	ksi	Yield	00.0	ksi	SEL	00.0	RB	00	Hydro:	1960	Psi	RUN:	46-0
Y/T RATIO	=	0.00															

013532 * LINE 3

EDITION REFERENCE 4
H= 0.045 0.887 0.006 0.000 0.048 0.210 0.018 0.017 0.008 0.002 0.019 0.002 0.033 0.000 0.062 0.099 0.005

Yield Strength by Strap

P= 0.046 0.918 0.006 0.005 0.050 0.218 0.016 0.015 0.022 0.005 0.004 0.004 0.005 0.036 0.000 0.000 0.101 /
M=Weld Ten. 00.0 ksi Ten. 00.0 ksi Yield 00.0 ksi SEL 00.0 RB 00 Hydro: 1960 Psi RUN: 19-0

Yield Strength by Strap

027738 * LINE 3

EDITION REFERENCE 4
H= 0.031 0.866 0.006 0.000 0.047 0.203 0.016 0.026 0.007 0.002 0.021 0.001 0.035 0.000 0.049 0.084 0001

Yield Strength by Strap

P= 0.053 0.880 0.006 0.004 0.047 0.210 0.014 0.023 0.019 0.005 0.002 0.003 0.035 0.001 0.000 0.107 07/14
M=Weld Ten. 77.4 ksi Ten. 76.3 ksi Yield 63.6 ksi SEL 45.5 RB 85 Hydro: 1960 Psi RUN: 19-0

Yield Strength by Strap

Y/T RATIO = 0.83

EDITION REFERENCE 4
H= 0.031 0.866 0.006 0.000 0.047 0.203 0.016 0.026 0.007 0.002 0.021 0.001 0.035 0.000 0.049 0.084 0001
P= 0.053 0.880 0.006 0.004 0.047 0.210 0.014 0.023 0.019 0.005 0.002 0.003 0.035 0.001 0.000 0.107 07/14
M=Weld Ten. 77.4 ksi Ten. 76.3 ksi Yield 63.6 ksi SEL 45.5 RB 85 Hydro: 1960 Psi RUN: 19-0

Attachments

PAGE 6
Continued

Issue No.: 6

Form Date: 10/18/2004

QD-AW3F055

SO 9007:2008
CERTIFIED

CUSTOMER NAME: SAGINAW PIPE INCORPORATED

Customer Order Number 38708

Date: 19/JAN/2011
MFG Order Number S109332

HEAT	C	MN	P	S	CB	SI	TI	CU	NI	MO	CR	V	AL	B	N	C.E.	Coil	Pipe
027738	* LINE 3																	Yield Strength by Strap
H=	0.031	0.866	0.006	0.000	0.047	0.203	0.016	0.026	0.007	0.002	0.021	0.001	0.035	0.000	0.049	0.084	0.002	
P=	0.043	0.891	0.006	0.005	0.048	0.210	0.014	0.022	0.019	0.005	0.002	0.004	0.036	0.000	0.096	0.100	/	RUN: 19-0
M=Weld Ten.	00.0	ksi	Ten.	00.0	ksi	Yield	00.0	ksi	SEL	00.0	RB	00	Hydro:	1960	PSI			
Y/T RATIO	=	0.00																

EDITION REFERENCE 4

Yield Strength by Strap

PIPE

Attachments

PAGE 7

Continued

Form Date: 10/18/2004

OD-AW3#055

Issue No.: 6



CERTIFIED

CUSTOMER NAME: SAGINAW PIPE INCORPORATED
Charpy "V" Notch Tests

Customer Order Number
38708

Date: 19/JAN/2011
MFG Order Number
S109332

HEAT NO.	SIZE	TEMP	ENERGY (FT./LBS.)	Avg.	Fracture Appearance (% Shear Area) Avg.	Line #
N94193	.750	32	200.0	196.0	100	100
N94192	.750	32	202.0	198.0	100	100
N04919	.750	32	200.0	198.0	100	100
X B0V7622-	.750	32	193.0	206.0	100	100
B0X8269-	.750	32	216.0	214.0	100	100
B0X8270-	.750	32	112.0	214.0	100	100
B0X8268-	.750	32	208.0	210.0	100	100
A0X3449-	.750	32	206.0	198.0	100	100
A0X3450-	.750	32	206.0	206.0	100	100
013532-	.750	14	221.0	223.0	100	100
027738-	.750	14	213.0	218.0	100	100
ALL HEAT AVERAGE				204.0	100.0	

Additional Charpy "V" Notch Tests

013532 -W W	.750	14	219.0	209.0	210.0	212.7	100	100	100.0	3
027738 -W W	.750	14	222.0	224.0	224.0	223.3	100	100	100.0	3

PAGE 8
Continued

Issue No.: 6

Form Date: 10/18/2004

OD-AW3F055



CUSTOMER NAME: SAGINAW PIPE INCORPORATED

Customer Order Number
38708

Date: 19/JAN/2011
MFG Order Number
SI09332

Legend Analyses:
A-Z - Additional Testing R - Retest
H - Heat Analysis L - Longitudinal
P - Product Analysis T - Transitional
M - Mechanical Properties W - Weld Line

Hydrostatic Test: OK
Flattening Test: OK

EDITION REFERENCE 1: API 5L 41ST EDITION 4/1/1995
EDITION REFERENCE 2: API 5L 42ND EDITION 7/1/2000
EDITION REFERENCE 3: API 5L 43RD EDITION 10/4/2004
EDITION REFERENCE 4: API 5L 44TH EDITION 10/1/2008
EDITION REFERENCE 5: ASTM/ASME ANNUAL BOOK OF STANDARDS SECT.1, VOL 01.01

* Manufactured and Melted in the USA.

We hereby certify that the above figures are correct as contained in the records of this company, and that the pipe were manufactured, tested and inspected in compliance with the latest edition of the applicable specification, in Birmingham, Alabama, U.S.A.

Noel A. Gordon
Manager of Quality Assurance - Steel Pipe

PAGE 9

End Of Report

Issue No.: 6

Form Date: 10/18/2004

QD-AW3FOSS

APPENDIX

C

WELD SPECIFICATION DETAILS

Table 3.7
Prequalified WPS Requirements^f (see 3.7)

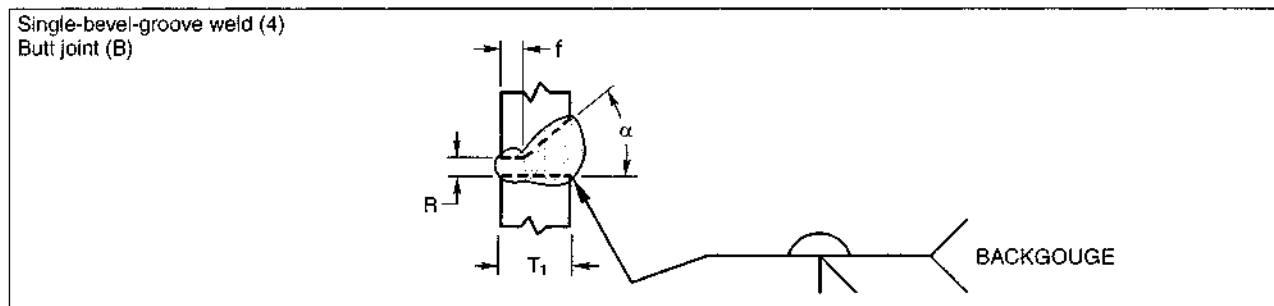
Variable	Position	Weld Type	SMAW	SAW ^d			GMAW/ FCAW ^g	
				Single	Parallel	Multiple		
Maximum Electrode Diameter	Flat	Fillet ^a	5/16 in [8.0 mm]	1/4 in [6.4 mm]			1/8 in [3.2 mm]	
		Groove ^a	1/4 in [6.4 mm]					
		Root pass	3/16 in [4.8 mm]					
Maximum Current	Horizontal	Fillet	1/4 in [6.4 mm]	1/4 in [6.4 mm]			1/8 in [3.2 mm]	
		Groove	3/16 in [4.8 mm]	Requires WPS Qualification Test				
Maximum Root Pass Thickness ^d	Vertical	All	3/16 in [4.8 mm] ^b				3/32 in [2.4 mm]	
	Overhead	All	3/16 in [4.8 mm] ^b				5/64 in [2.0 mm]	
Maximum Single Pass Fillet Weld Size ^c	All	All	Fillet	1000 A	1200A	Unlimited	Within the range of recommended operation by the filler metal manufacturer	
		Groove weld root pass with opening	Within the range of recommended operation by the filler metal manufacturer	700A				
		Groove weld root pass without opening		600A				
		Groove weld fill passes		900A				
		Groove weld cap pass		1200A				
		Unlimited						
Maximum Fill Pass Thickness	All	Flat	3/8 in [10 mm]	Unlimited			3/8 in [10 mm]	
		Horizontal	5/16 in [8 mm]				5/16 in [8 mm]	
		Vertical	1/2 in [12 mm]				1/2 in [12 mm]	
		Overhead	5/16 in [8 mm]				5/16 in [8 mm]	
Maximum Single Pass Layer Width	All	All	3/16 in [5 mm]	1/4 in [6 mm]	Unlimited		1/4 in [6 mm]	
Maximum Single Pass Fillet Weld Size ^c	Fillet	Flat	3/8 in [10 mm]	Unlimited			1/2 in [12 mm]	
		Horizontal	5/16 in [8 mm]	5/16 in [8 mm]	5/16 in [8 mm]	1/2 in [12 mm]	3/8 in [10 mm]	
		Vertical	1/2 in [12 mm]				1/2 in [12 mm]	
		Overhead	5/16 in [8 mm]				5/16 in [8 mm]	
Maximum Single Pass Layer Width	All (for GMAW/ FCAW) F & H (for SAW)	Root opening > 1/2 in [12 mm], or	Any layer of width w	Split layers	Laterally displaced electrodes or split layer	Split layers	Split layers	
		Any layer of width w		Split layers if w > 5/8 in [16 mm]	Split layers with tandem electrodes if w > 5/8 in [16 mm]	If w > 1 in [25 mm], split layers	(Note e)	

^a Except root passes.^b 5/32 in [4.0 mm] for EXX14 and low-hydrogen electrodes.^c See 3.7.3 for requirements for welding unpainted and exposed ASTM A 588.^d See 3.7.2 for width-to-depth limitations.^e In the F, H, or OH positions for nontubulars, split layers when the layer width w > 5/8 in [16 mm]. In the vertical position for nontubulars or the flat, horizontal, vertical, and overhead positions for tubulars, split layers when the width w > 1 in [25 mm].^f Shaded area indicates nonapplicability.^g GMAW-S shall not be prequalified.

See Notes on Page 77

				Tolerances	
				As Detailed (see 3.13.1)	As Fit-Up (see 3.13.1)
Single-bevel-groove weld (4)	T-joint (T)	Corner joint (C)		R = +1/16, -0	+1/4, -1/16
				$\alpha = +10^\circ, -0^\circ$	$+10^\circ, -5^\circ$

Welding Process	Joint Designation	Base Metal Thickness (U = unlimited)		Groove Preparation		Allowed Welding Positions	Gas Shielding for FCAW	Notes
		T ₁	T ₂	Root Opening	Groove Angle			
SMAW	TC-U4a	U	U	R = 1/4	$\alpha = 45^\circ$	All	—	e, g, j, k
				R = 3/8	$\alpha = 30^\circ$	F, V, OH	—	e, g, j, k
GMAW FCAW	TC-U4a-GF	U	U	R = 3/16	$\alpha = 30^\circ$	All	Required	a, g, j, k
				R = 3/8	$\alpha = 30^\circ$	F	Not req.	a, g, j, k
				R = 1/4	$\alpha = 45^\circ$	All	Not req.	a, g, j, k
				R = 3/8	$\alpha = 30^\circ$	F	—	g, j, k
				R = 1/4	$\alpha = 45^\circ$		—	
SAW	TC-U4a-S	U	U					



Welding Process	Joint Designation	Base Metal Thickness (U = unlimited)		Groove Preparation		Allowed Welding Positions	Gas Shielding for FCAW	Notes
		T ₁	T ₂	Root Opening	Tolerances			
SMAW	B-U4b	U	—	R = 0 to 1/8 f = 0 to 1/8 $\alpha = 45^\circ$	$+1/16, -0$ $+1/16, -0$ $+10^\circ, -0^\circ$	All	—	c, d, e, j
GMAW FCAW	B-U4b-GF	U	—	R = 0 f = 1/4 max. $\alpha = 60^\circ$	± 0 $+0, -1/8$ $+10^\circ, -0^\circ$	All	Not required	a, c, d, j
SAW	B-U4b-S	U	—	R = 0 f = 1/4 max. $\alpha = 60^\circ$	$\pm 1/16$ $10^\circ, -5^\circ$	F	—	c, d, j

**Figure 3.4 (Continued)—Prequalified CJP Groove Welded Joint Details
(see 3.13) (Dimensions in Inches)**

WELDING PROCEDURE SPECIFICATION (WPS) Yes
PREQUALIFIED _____ QUALIFIED BY TESTING _____
or PROCEDURE QUALIFICATION RECORDS (PQR) Yes

Company Name _____
 Welding Process(es) _____
 Supporting PQR No.(s) _____

Identification # _____
 Revision _____ Date _____ By _____
 Authorized by _____ Date _____
 Type—Manual Semiautomatic
 Mechanized Automatic

JOINT DESIGN USED

Type:
 Single Double Weld
 Backing: Yes No
 Backing Material:
 Root Opening _____ Root Face Dimension _____
 Groove Angle: _____ Radius (J-U) _____
 Back Gouging: Yes No Method _____

POSITION
 Position of Groove: _____ Fillet: _____
 Vertical Progression: Up Down

BASE METALS

Material Spec. _____
 Type or Grade _____
 Thickness: Groove _____ Fillet _____
 Diameter (Pipe) _____

ELECTRICAL CHARACTERISTICS

FILLER METALS
 AWS Specification _____
 AWS Classification _____

SHIELDING
 Flux _____ Gas _____
 Composition _____
 Electrode-Flux (Class) _____ Flow Rate _____
 Gas Cup Size _____

TECHNIQUE
 Stringer or Weave Bead: _____
 Multi-pass or Single Pass (per side) _____
 Number of Electrodes _____
 Electrode Spacing Longitudinal _____
 Lateral _____
 Angle _____
 Contact Tube to Work Distance _____
 Peening _____
 Interpass Cleaning: _____

PREHEAT
 Preheat Temp., Min. _____
 Interpass Temp., Min. _____ Max. _____

POSTWELD HEAT TREATMENT
 Temp. _____
 Time _____

WELDING PROCEDURE

Pass or Weld Layer(s)	Process	Filler Metals		Current		Volts	Travel Speed	Joint Details
		Class	Diam.	Type & Polarity	Amps or Wire Feed Speed			

**NORTH CAROLINA DEPARTMENT OF TRANSPORTATION
MATERIALS AND TESTS UNIT, STRUCTURAL MATERIALS GROUP**



1801 Blue Ridge Road, Raleigh, NC 27607
Tel: 919-329-4000 Fax: 919-733-8742

INSPECTION REPORT

Contract / Project Number:	N/A	NCSU:	Arjun Jayaprakash
County:	N/A	Contractor:	BAE Research Shop
Division:	N/A	M&T Inspector/Representative:	Michael Pulley

Reason for Inspection:	<input type="checkbox"/>	Material Inspection	
	<input checked="" type="checkbox"/>	Welding Inspection	
	<input type="checkbox"/>	Field Audit	
	<input checked="" type="checkbox"/>	Other (Explain):	

Inspection Start Time:	8:00 AM	Inspection performed in accordance to - AWS D1.1 2015 - Structural Welding Code - Steel
Inspection End Time:	3:00 PM	
Date of Inspection:	7/10/18 to 7/12/18	

Personnel Present During Inspection (If Any)	Company	Title
Arjun Jayaprakash	NCSU	NCSU Graduate Student
Joe Blalock	NCSU BAE Research Shop	Welder
Neil Bain	NCSU BAE Research Shop	Supervisor

INSPECTION DETAILS

Traveled to NCSU and met with Arjun Jayaprakash, and Joe Blalock. Arjun explained how the GSS Specimen should be assembled. During the welding process the following information was documented:

Welder - Miller Goldstar 302

Filler Metal - Lincoln Excalibur E7018 MR 1/8" and 5/32"

Polarity - DCEP

Amperes - 123 to 130 amps for 1/8" electrodes and 171 to 181 amps for 5/32" electrodes

Weld Groove - TC-U4a

Welder Qualification - Joe Blalock, Process - SMAW, Position - 3G & 4G, Filler Metal Classification - E7018, Groove thickness qualified 1/8" to Unlimited

7/10/18 - The inspection performed included material inspection, TC-U4a groove inspection, and material fit-up on the north and south GSS connections. The groove angle and fit-up was found to be acceptable. The root opening on the north connection was 3/16" to 1/2". The root opening on the south connection was 3/16" to 5/16". An in process welding inspection was performed on the north connection. E7018 1/8" electrodes were used. At the end of the day, the groove weld was 75% complete.

INSPECTION DETAILS (Continued)

7/11/18 - An in process inspection of the welding on the north connection was continued. At 11:00 am the welder changed to E7018 5/32" electrodes. The north connection weld was completed at 2:30 pm. A final visual weld inspection was performed on the north connection weld. The welding was found to be visually acceptable. At 2:45 pm welding was started on the south connection. E7018 1/8" electrodes were used on the root pass at 120 amps. After the root pass was completed the welder switched back to the E7018 5/32" electrodes and 175 amps. At the end of the day approximately 10% of the south connection weld was complete.

7/12/18 - An in process inspection of the welding on the south connection was continued. E7018 - 5/32" electrodes were used at 175 amps. The south connection weld was completed at 2:40 pm. A final visual weld inspection was performed. All of the welding on the north and south connection welds were found to be visually acceptable.

GSS Specimen



INSPECTION DETAILS (Continued)

North Connection fit-up



South Connection Fit-up



INSPECTION DETAILS (Continued)

North connection root pass



Completed weld North Connection



INSPECTION DETAILS (Continued)

Completed South Connection Weld

